# The Impact of Sensor Characteristics and Data Availability on Remote Sensing Based Change Detection

Dissertation
zur
Erlangung des Doktorgrades (Dr. rer. nat.)
der
Mathematisch-Naturwissenschaftlichen Fakultät
der
Rheinischen Friedrich-Wilhelms-Universität Bonn

vorgelegt von

Frank Thonfeld

aus Rodewisch

Bonn, Juli 2014

Angefertigt mit Genehmigung der Mathematisch-Naturwissenschaftlichen Fakultät
der Rheinischen Friedrich-Wilhelms-Universität Bonn

1. Gutachter: Prof. Dr. Gunter Menz
2. Gutachter: Prof. Dr. Christiane Schmullius

Tag der Promotion: 25. September 2014

Erscheinungsjahr: 2014

to my cousin Heidi

## Acknowledgments

First of all I thank all the people that have been involved in the thesis itself (although some of them are not aware of that). Going long time back, I once got the opportunity to work in the Enviland2 project. I was allowed to work on change detection. More or less this was the starting point of what ended up in this thesis. I thank Gunter Menz for supervising my work and providing me with such an interesting topic. He was always open to new ideas and supported my work entirely. I still enjoy his spontaneous ideas (also beyond work). I also want to thank Christiane Schmullius who once drew my interest to remote sensing and who supported my change to Bonn. I thank Matthias Braun who was also involved in the Enviland2 project and, as former ZFL coordinator, taught me many things. Looking back I appreciate the patience of Sascha Klemenjak who showed me the first steps of programming. It was mainly Hannes Feilhauer who brought me to R and climbing. Both are essential for this thesis. I thank Mort Canty for his advice, his support, and his great ideas (and for his freely accessible software tools, the many high-level IDL courses,…). Free software was fundamental for my work, and I am happy that I was provided with the LEDAPS software – many thanks to Jeff Masek. Fmask is free as well – thanks to Zhe Zhu and Curtis Woodcock. I also appreciated very much the discussions with Mike Wulder and Jan Verbesselt about forests in Canada and time series processing. A great experience was the field trip to Vancouver Island. In fact, Livia and Susan spent their holidays with me – thanks for a cool time.

I am also grateful to the (meanwhile many) ZFL & RSRG people that I met over the years. In particular, I thank Ellen, Sabine, Bärbel and Tomek for their everyday assistance and help, and the Enviland2 gang (Antje, Frauke, Ingo, Ben, Benjamin, Johann, Angela, Edda) for the great time. I think I have to apologize for my noisy and grumbling programming style – the anger when things failed, the joy when things worked well. I also thank all the pre-, non- and post-Enviland ZFLers. They always gave/give me a good feeling. I enjoy the many discussions, Thursday morning meetings, and lunch breaks. One major outcome of this thesis is that I made a couple of new friends – and hopefully didn't lose too many.

Of course, I thank the friends who proofread this thesis – Birte, Uli, Hannes!

Finally, I thank my family for their continuous support, their belief in me, and a perfect childhood. Unfortunately, my grandparents cannot share the moment of finishing this PhD with me. Nevertheless, I am well aware that their love and support shaped me and my life. Last but not least, I thank Livia for a great time, patience (a word she actually does not know), and support.

## Table of Contents

## List of Figures

## List of Tables

## Acronyms and Abbreviations

| | |
|---|---|
| ACCA | Automated Cloud Cover Assessment |
| AO | Announcement of Opportunity |
| ALOS | Advanced Land Observing Satellite |
| ASAR | Advanced Synthetic Aperture Radar |
| AVHRR | Advanced Very High Resolution Radiometer |
| BIC | Bayesian Information Criterion |
| BFAST | Breaks For Additive Season and Trend |
| CDR | Landsat Climate Data Record |
| CVA | Change Vector Analysis |
| DOY | Day Of Year |
| DEM | Digital Elevation Model |
| DLR | Deutsches Zentrum für Luft- und Raumfahrt e.V. |
| DN | Digital Number |
| DSM | Digital Surface Models |
| DI | Disturbance Index |
| ERS | European Remote Sensing satellite |
| ESA | European Space Agency |
| ETM+ | Enhanced Thematic Mapper + |
| EVI | Enhanced Vegetation Index |
| EWDI | Enhanced Wetness Difference Index |
| FAPAR | Fraction of Absorbed Photosynthetically Active Radiation |
| Fmask | Function of mask |
| FWHM | Full Width at Half Maximum |
| GLP | Global Land Project |
| IFI | Integrated Forest Index |
| IFOV | Instantaneous Field Of View |
| IGBP | International Geosphere-Biosphere Program |
| IHDP | International Human Dimensions Program |
| IR-MAD | Iteratively Re-weighted Multivariate Alteration Detection |
| JERS | Japanese Earth Resources Satellite |
| K-S test | Kolmogorov-Smirnov test |
| LST | Land Surface Temperature |
| LCM | Land-cover Change Mapper |
| LDCM | Landsat Data Continuity Mission |
| LEDAPS | Landsat Ecosystem Disturbance Adaptive Processing System |
| LPGS | Landsat Level 1 Product Generation System |
| LAI | Leaf Area Index |
| LiDAR | Light Detection and Ranging |
| LOESS | LOcally wEighted regreSsion Smoother |
| MERIS | Medium Resolution Imaging Specrometer |

| | |
|---|---|
| MIR | mid-infrared |
| MODIS | Moderate Resolution Imaging Spectroradiometer |
| MOSUM | MOving SUM |
| MSS | Multi-Spectral Scanner |
| MAD | Multivariate Alteration Detection |
| NOAA | National Oceanic and Atmospheric Administration |
| NC | No Change |
| NIR | near-infrared |
| NBR | Normalized Burn Ratio |
| NDBI | Normalized Difference Built-up Index |
| NDII | Normalized Difference Infrared Index |
| NDMI | Normalized Difference Moisture Index |
| NDVI | Normalized Difference Vegetation Index |
| OLI | Operational Land Imager |
| PA | Producer Accuracy |
| PALSAR | Phased Array type L-band Synthetic Aperture Radar |
| PCA | Principal Component Analysis |
| PIF | Pseudo-Invariant Features |
| RCM | Radarsat Constellation Mission |
| RCVA | Robust Change Vector Analysis |
| RESA | RapidEye Science Archive |
| SAR | Synthetic Aperture Radar |
| SLC | Scan Line Corrector |
| SWIR | shortwave-infrared |
| SRTM | Shuttle Radar Topography Mission |
| SNR | Signal-to-Noise Ratios |
| STL | Seasonal-Trend decomposition based on LOESS |
| TC | Tasseled Cap |
| TCA | Tasseled Cap Angle index |
| TCD | Tasseled Cap Distance |
| TIC | Temporally Invariant Clusters |
| TM | Thematic Mapper |
| TIR | thermal infrared |
| TOA | Top of Atmosphere |
| UA | User Accuracy |
| UTC | Universal Time, Coordinated |
| USGS | United States Geological Survey |
| VCF | Vegetation Continuous Filed |
| VIS | visible |
| WELD | Web-Enabled Landsat Data |
| WRS-2 | World Reference System-2 |

## Summary

Land cover and land use change are among the major drivers of global change. In a time of mounting challenges for sustainable living on our planet any research benefits from interdisciplinary collaborations to gain an improved understanding of the human-environment system and to develop suitable and improve existing measures of natural resource management. This includes comprehensive understanding of land cover and land use changes, which is fundamental to mitigate global change. Remote sensing technology is essential for the analyses of the land surface (and hence related changes) because it offers cost-effective ways of collecting data simultaneously over large areas. With increasing variety of sensors and better data availability, the application of remote sensing as a means to assist in modeling, to support monitoring, and to detect changes at various spatial and temporal scales becomes more and more feasible. The relationship between the nature of the changes on the land surface, the sensor properties, and the conditions at the time of acquisition influences the potential and quality of land cover and land use change detection. Despite the wealth of existing change detection research, there is a need for new methodologies in order to efficiently explore the huge amount of data acquired by remote sensing systems with different sensor characteristics. The research of this thesis provides solutions to two main challenges of remote sensing based change detection.

First, geometric effects and distortions occur when using data taken under different sun-target-sensor geometries. These effects mainly occur if sun position and/or viewing angles differ between images. This challenge was met by developing a theoretical framework of bi-temporal change detection scenarios. The concept includes the quantification of distortions that can occur in unfavorable situations. The invention and application of a new method – the Robust Change Vector Analysis (RCVA) – reduced the detection of false changes due to these distortions. The quality and robustness of the RCVA were demonstrated in an example of bi-temporal cross-sensor change detection in an urban environment in Cologne, Germany. Comparison with a state-of-the-art method showed better performance of RCVA and robustness against thresholding.

Second, this thesis provides new insights into how to optimize the use of dense time series for forest cover change detection. A collection of spectral indices was reviewed for their suitability to display forest structure, development, and condition at a study site on Vancouver Island, British Columbia, Canada. The spatio-temporal variability of the indices was analyzed to identify those indices, which are considered most suitable for forest monitoring based on dense time series. Amongst the indices, the Disturbance Index (DI) was found to be sensitive to the state of the forest (i.e., forest structure). The Normalized Difference Moisture Index (NDMI) was found to be spatio-temporally stable and to be the most sensitive index for changes in forest condition. Both indices were successfully applied to detect abrupt forest cover changes. Further, this thesis demonstrated that relative radiometric normalization can obscure actual seasonal variation and long-term trends of spectral signals and is therefore not recommended to be incorporated in the time series pre-processing of remotely-sensed data. The main outcome of this part of the presented research is a new method for detecting discontinuities in time series of spectral indices. The method takes advantage of all available information in terms of cloud-free pixels and hence

increases the number of observations compared to most existing methods. Also, the first derivative of the time series was identified (together with the discontinuity measure) as a suitable variable to display and quantify the dynamic of dense Landsat time series that cannot be observed with less dense time series. Given that these discontinuities are predominantly related to abrupt changes, the presented method was successfully applied to clearcut harvest detection. The presented method detected major events of forest change at unprecedented temporal resolution and with high accuracy (93% overall accuracy).

This thesis contributes to improved understanding of bi-temporal change detection, addressing image artifacts that result from flexible acquisition features of modern satellites (e.g., off-nadir capabilities). The demonstrated ability to efficiently analyze cross-sensor data and data taken under unfavorable conditions is increasingly important for the detection of many rapid changes, e.g., to assist in emergency response.

This thesis further contributes to the optimized use of remotely sensed time series for improving the understanding, accuracy, and reliability of forest cover change detection. Additionally, the thesis demonstrates the usability of and also the necessity for continuity in medium spatial resolution satellite imagery, such as the Landsat data, for forest management. Constellations of recently launched (e.g., Landsat 8 OLI) and upcoming sensors (e.g., Sentinel-2) will deliver new opportunities to apply and extend the presented methodologies.

## Zusammenfassung

Landbedeckungs- und Landnutzungswandel gehören zu den Haupttriebkräften des Globalen Wandels. In einer Zeit, in der ein nachhaltiges Leben auf unserem Planeten zu einer wachsenden Herausforderung wird, profitiert die Wissenschaft von interdisziplinärer Zusammenarbeit, um ein besseres Verständnis der Mensch-Umwelt-Beziehungen zu erlangen und um verbesserte Maßnahmen des Ressourcenmanagements zu entwickeln. Dazu gehört auch ein erweitertes Verständnis von Landbedeckungs- und Landnutzungswandel, das elementar ist, um dem Globalen Wandel zu begegnen. Die Fernerkundungstechnologie ist grundlegend für die Analyse der Landoberfläche und damit verknüpften Veränderungen, weil sie in der Lage ist, große Flächen gleichzeitig zu erfassen. Mit zunehmender Sensorenvielfalt und besserer Datenverfügbarkeit gewinnt Fernerkundung bei der Modellierung, beim Monitoring sowie als Mittel zur Erkennung von Veränderungen in verschiedenen räumlichen und zeitlichen Skalen zunehmend an Bedeutung. Das Wirkungsgeflecht zwischen der Art von Veränderungen der Landoberfläche, Sensoreigenschaften und Aufnahmebedingungen beeinflusst das Potenzial und die Qualität fernerkundungsbasierter Landbedeckungs- und Landnutzungsveränderungs-detektion. Trotz der Fülle an bestehenden Forschungsleistungen zur Veränderungsdetektion besteht ein dringender Bedarf an neuen Methoden, die geeignet sind, das große Aufkommen von Daten unterschiedlicher Sensoren effizient zu nutzen. Die in dieser Abschlussarbeit durchgeführte Forschung befasst sich mit zwei aktuellen Problemfeldern der fernerkundungsbasierten Veränderungsdetektion.

Das erste sind die geometrischen Effekte und Verzerrungen, die auftreten, wenn Daten genutzt werden, die unter verschiedenen Sonne-Zielobjekt-Sensor-Geometrien aufgenommen wurden. Diese Effekte treten vor allem dann auf, wenn unterschiedliche Sonnenstände und/oder unterschiedliche Einfallswinkel der Satelliten genutzt werden. Der Herausforderung wurde begegnet, indem ein theoretisches Konzept von Szenarien dargelegt wurde, die bei der bi-temporalen Veränderungsdetektion auftreten können. Das Konzept beinhaltet die Quantifizierung der Verzerrungen, die in ungünstigen Fällen auftreten können. Um die Falscherkennung von Veränderungen in Folge der resultierenden Verzerrungen zu reduzieren, wurde eine neue Methode entwickelt – die *Robust Change Vector Analysis (RCVA)*. Die Qualität der Methode wird an einem Beispiel der Veränderungsdetektion im urbanen Raum (Köln, Deutschland) aufgezeigt. Ein Vergleich mit einer anderen gängigen Methode zeigt bessere Ergebnisse für die neue RCVA und untermauert deren Robustheit gegenüber der Schwellenwertbestimmung.

Die zweite Herausforderung, mit der sich die vorliegende Arbeit befasst, betrifft die optimierte Nutzung von dichten Zeitreihen zur Veränderungsdetektion von Wäldern. Eine Auswahl spektraler Indizes wurde hinsichtlich ihrer Tauglichkeit zur Erfassung von Waldstruktur, Waldentwicklung und Waldzustand in einem Untersuchungsgebiet auf Vancouver Island, British Columbia, Kanada, bewertet. Um die Einsatzmöglichkeiten der Indizes für dichte Zeitreihen bewerten zu können, wurde ihre raum-zeitliche Variabilität untersucht. Der *Disturbance Index (DI)* ist ein Index, der sensitiv für das Stadium eines Waldes ist (d. h. seine Struktur). Der *Normalized DIfference Moisture Index (NDMI)* ist raum-zeitlich stabil und zudem am sensitivsten für

Veränderungen des Waldzustands. Beide Indizes wurden erfolgreich zur Erkennung von abrupten Veränderungen getestet. In der vorliegenden Arbeit wird aufgezeigt, dass die relative radiometrische Normierung saisonale Variabilität und Langzeittrends von Zeitreihen spektraler Signale verzerrt. Die relative radiometrische Normierung wird daher nicht zur Vorprozessierung von Fernerkundungszeitreihen empfohlen. Das wichtigste Ergebnis dieser Studie ist eine neue Methode zur Erkennung von Diskontinuitäten in Zeitreihen spektraler Indizes. Die Methode nutzt alle wolkenfreien, ungestörten Beobachtungen (d. h. unabhängig von der Gesamtbewölkung in einem Bild) in einer Zeitreihe und erhöht dadurch die Anzahl an Beobachtungen im Vergleich zu anderen Methoden. Die erste Ableitung und die Messgröße zur Erfassung der Diskontinuitäten sind gut geeignet, um die Dynamik dichter Zeitreihen zu beschreiben und zu quantifizieren. Dies ist mit weniger dichten Zeitreihen nicht möglich. Da diese Diskontinuitäten im Untersuchungsgebiet üblicherweise abrupter Natur sind, ist die Methode gut geeignet, um Kahlschläge zu erfassen. Die hier dargelegte neue Methode detektiert Waldbedeckungsveränderungen mit einzigartiger zeitlicher Auflösung und hoher Genauigkeit (93% Gesamtgenauigkeit).

Die vorliegende Arbeit trägt zu einem verbesserten Verständnis bi-temporaler Veränderungsdetektion bei, indem Bildartefakte berücksichtigt werden, die infolge der Flexibilität moderner Sensoren entstehen können. Die dargestellte Möglichkeit, Daten zu analysieren, die von unterschiedlichen Sensoren stammen und die unter ungünstigen Bedingungen aufgenommen wurden, wird zukünftig bei der Erfassung von schnellen Veränderungen an Bedeutung gewinnen, z. B. bei Katastropheneinsätzen.

Ein weiterer Beitrag der vorliegenden Arbeit liegt in der optimierten Anwendung von Fernerkundungszeitreihen zur Verbesserung von Verständnis, Genauigkeit und Verlässlichkeit der Waldveränderungsdetektion. Des Weiteren zeigt die Arbeit den Nutzen und die Notwendigkeit der Fortführung von Satellitendaten mit mittlerer Auflösung (z. B. Landsat) für das Waldmanagement. Konstellationen kürzlich gestarteter (z. B. Landsat 8 OLI) und zukünftiger Sensoren (z. B. Sentinel-2) werden neue Möglichkeiten zur Anwendung und Optimierung der hier vorgestellten Methoden bieten.

# 1 Introduction

## 1.1 Land Use/Land Cover Change and Remote Sensing Based Change Detection

Over the past decades science put an emphasis on analysis of the land surface because it is seen as important agent of our life. People have understood that human activities on the land surface are affecting feedbacks to the Earth system and that the human-environment system responds to global change. The land related science disciplines have been fostered to establish integrated science. The Global Land Project (GLP) has been set up to contribute to the goals of the International Geosphere-Biosphere Program (IGBP) and the International Human Dimensions Program (IHDP). Better understanding of the coupled human-environment system is part of its science plan (http://www.globallandproject.org/). Sound scientific understanding is accompanied by monitoring programs. The key variables of land science are land cover and land use. Best understanding is gained by taking them literally: land cover is defined by "the attributes of the Earth's land surface and immediate subsurface, including biota, soil, topography, surface and groundwater, and human (mainly built-up) structures" (Lambin et al., 2006). Land use is defined "as the purposes for which humans exploit the land cover" (Lambin et al., 2006). Hence, related change *is* related to clearly defined categories, namely land cover and land use.

Human-induced land cover change is widely considered as primary driver of species endangerment and biodiversity decline (Hansen et al., 2001). Land use and land cover changes and related land-climate interactions also affect climate change (Stocker et al., 2013). As most land cover can be well detected by means of remote sensing, this technology is essential for analyses of the land surface. Relating land use decisions to remote sensing observations and vice versa is often challenging. Land use decisions, however, control ecosystem responses – intended or not (DeFries et al., 2004). Comprehensive understanding of land cover and land use changes is fundamental to fully conceive global change.

A philosophical discussion about what constitutes change is far beyond the scope of this thesis. Nevertheless, it is crucial to get knowledge of the term in the context of remote sensing. From a technical perspective, remote sensing change detection is – at least in part – the identification of differences between images. Hence, changes can be seen as differences between images. When applying remote sensing to scientific research questions, one is interested in changes on the ground rather than on differences between images. What can be seen as a change on the ground is usually closely related to processes and their driving forces, e.g., phenology is driven by light, temperature, as well as water and nutrient availability and is associated with greening, flowering, or browning. Generally, these changes can be measured in terms of intensity, frequency, spatial and temporal extent, spatial and temporal stability, and pace. Remote sensing is capable of addressing large areas within short time, which is advantageous when working in areas difficult to access, large areas or hazardous areas (e.g., nuclear sites, emergency sites). The simultaneous view of large areas cannot be achieved by means of field methods. Furthermore, remote sensing is the physically and chemically based measurement of reflectance and irradiance (or backscatter) in discrete wave lengths, which allows for the application of transferable principles. Measuring

change with remote sensing data of only one acquisition requires detailed knowledge of the study site so that the features on the (change) image can be related to processes on the ground.
Singh's (1989) definition terms change detection as "the process of identifying differences in the state of an object or phenomenon by observing it at different times". Coppin et al. (2004) define change detection as similarly "the quantification of temporal phenomena from multi-date imagery". Hecheltjen et al. (2014) define change detection as a sequence of processing steps including pre-processing, change extraction, thresholding, change labeling, and accuracy assessment. Some of these may be omitted depending on the goal of the study, data, and method. It is obvious that changes can only be detected in remote sensing data when a change on the ground causes changes in the spectral response (Singh, 1989). For long time remote sensing analysts were mainly interested in what is known as conversion, i.e. the replacement of one land use class by another (Coppin et al., 2004). Changes due to phenological changes of vegetation were frequently ignored, and it was seen as prerequisite to avoid such changes by carefully selecting the images used for change detection. However, there are many more phenomena that reflect change as natural dynamics. Phenological changes often show seasonal patterns, frequently related to latitude. Plants develop over time, plant communities as well. They change arrangement and composition until the process of succession ends up in a climax stage. This development, however, is nothing linear as will be shown later. Rather little attention has been spend on other cyclic changes that occur on ground such as thermal expansion of constructions, i.e. bridges and buildings. Although these changes are in the range of millimeters it is possible to measure them with appropriate methods, e.g., SAR (Synthetic Aperture Radar) remote sensing (Gernhardt and Bamler, 2012). The measurement of motion is another change detection application – rather literally than broadly accepted as remote sensing change detection. Motion detection can be conducted with optical data in some cases, e.g. glacier monitoring (Herman et al., 2011). However, it is the SAR characteristics including its high precision that lead to remote sensing applications such as ground subsidence monitoring (Strozzi et al., 2003; Wegmüller et al., 2010). Most motion and velocity measurement approaches are based on SAR data. Small scale motions and other motion related processes such as glacier movement, ground subsidence due to ground water extraction and subrosion or moving target detection have not been included in the well established change detection reviews (e.g., Coppin et al., 2004; Lu et al., 2004; Radke et al., 2005; Singh, 1989). However, the above examples can be attributed to changes on the ground which justifies to consider them in remote sensing change detection reviews. It is yet unknown if they have not been reviewed for so long simply because they are rather new or because they are not seen under the umbrella of change detection. The reason may be the huge variety of changes that occur on the ground. Any change that can be measured with remote sensor data can be subject of change detection studies. Most reviews focus on specific applications, e.g., ecosystem change (Coppin et al. 2004). Recent reviews direct towards object-based methods (Hussain et al., 2013) or include SAR methods as well as time series analysis (Hecheltjen et al., 2014). A comprehensive work about enhanced SAR change detection methods is presented by Schmitt (2012) and Schmitt et al. (2010). Most of the reviews reflect the long history of bi-temporal methods. Recent advances in medium and high resolution remote sensing focus on time series analysis, i.e., trend

analysis (Dubovyk et al., 2013a) or time series reconstruction by segmented regression modeling (Kennedy et al., 2010).

The user may direct the results of a study by selecting appropriate images, acquisition dates, acquisition parameters, preprocessing steps and change detection methods. Frequently, detected changes are a composition of "real" and "false" changes, the latter often being undesired changes rather than "false". However, there are a lot of factors that have to be considered to reduce false alarms. A technically perfect change detection result may not be the perfect result for the user. For any user it would be helpful to have an indication how the changes have to be interpreted. This can be understand twofold: a) knowledge of the underlying processes to be explored and of the factors potentially affecting the results is essential; b) real changes need to be assigned a label in order to understand their meaning. This process is also known as change labeling. Change labeling may be conducted in several ways and at different stages of the change detection process (Hecheltjen et al., 2014). Probably the most popular labeling approach is classification. For several applications a change/no-change distinction is sufficient. Some methods are specifically applied to a pre-defined land cover. Hence, classification of the change is not needed. Besides the many methods that exist for change detection (e.g., Coppin et al.2004, Hecheltjen et al. 2014) there are many applications of remote sensing change detection that are sometimes unique tools for policy makers, geographers or ecologists. Regardless of temporal or spatial scales these applications are among others agricultural expansion (Arvor et al., 2012), damage assessment (Klonus et al., 2012), land degradation (Dubovyk et al., 2013b), earthquake reconstruction (Massonnet et al., 1993), fire scar detection (Vogelmann et al., 2011), flood detection (Gianinetto and Villa, 2007), forest change detection (Desclée et al., 2004) and forest monitoring (Kennedy et al., 2010), glaciology (Fallourd et al., 2011), mass movement assessment (Strozzi et al., 2005), mining monitoring (Sen et al., 2012), oil spill monitoring (Leifer et al., 2012), subsidence monitoring (Strozzi et al., 2003), urban change detection (Thonfeld and Menz, 2011), volcanic activity monitoring (Agustan et al., 2012), wetland monitoring (Landmann et al., 2013), and land cover/land use map update (Xian et al., 2009). These applications are often part of climate change or global change studies. Many local, site-specific studies are not termed change detection application. But since they are using multi-date imagery to study variation or dynamics of phenomena they must be considered as such according to Singh's (1989) definition.

## 1.2 Factors Affecting Remote Sensing Based Change Detection

As can be seen from the manifold applications mentioned above as well as the numerous indicated methods there are various dimensions of remote sensing change detection. Notwithstanding the many publications and research projects that dealt with remote sensing change detection it is important to disassemble the complex construction and reflect some recent developments. In order to be able to detect changes on the ground, several requirements have to be met:

1) Changes on the ground must be characterized in a way that is visible for a remote sensing system.

2) The selected remote sensing system has to be configured in a way that enables the recognition of those changes.
3) The external acquisition conditions must allow for the detection of changes.

What seems obvious reveals opportunities and limitations of remote sensing change detection. In the following, the three requirements are clarified.

### 1.2.1 Change Properties

Changes on the ground may be differentiated according to temporal and spatial properties, and according to the spectral response they cause. The drivers of changes are manifold. There are natural drivers of land use and land cover change such as weather phenomena, phenology (which causes seasonal patterns), animals (from insects to large herbivores), geomorphology and geology, natural events and climate (Dardel et al., 2014), and there are human activities operating as drivers such as mining, forest management (including deforestation, afforestation, reforestation), urbanization, agricultural expansion, land abandonment, land reforms and latent impacts (e.g., Hostert et al., 2011). The causal agents of changes are often ambiguous, complex, and globally interlinked (Lambin et al., 2001; Rindfuss et al., 2004). Frequently, climate induced land cover modification and human driven land use change interact (Lambin et al., 2003; Stellmes et al., 2013). The results on the ground – the changes – may be characterized by temporal, spatial, and spectral aspects. The latter is mandatory for remote sensing.

#### 1.2.1.1 Temporal Aspects

Coppin et al. (2004) introduced modification and conversion as two basic process characteristics: Modification is the subtle change affecting the character of one land cover without impact on its classification. Conversion is the (permanent) replacement of one land cover or land use by another. The changes themselves may be fast and abrupt or slow and gradual. An example for abrupt changes is clear-cut harvesting of forests, an example of gradual changes is biomass accumulation. There are also differences in the time a process takes effect and in the time the results of these processes are (spectrally) visible: Floods last from only few hours to several days, sometimes weeks. Once they disappeared, the landscape regenerates relatively quick. Fires last only few days. Their scars often recover slowly, being visible for many years. The construction of a new building on a place that was previously covered by natural surfaces such as forests, grassland or bare soil takes few months but lasts years or decades. Its condition, however, may change steadily (e.g., corrosion of the roof material). The removal of trees in a forest is an example for modification when the forest itself remains a forest. The process of deforestation, i.e., the clearing of a forest and replacement by other land uses, is an example for conversion.
Consequently, remote sensing data have to be acquired at specific times in order to capture the initial situation and the subsequent changes. Floods, for instance, will be missed when adequate data are not available. Changes due to flooding are "elastic", i.e., an observed area is temporarily changed and returns to its initial condition after relatively short terms. Although floods may have

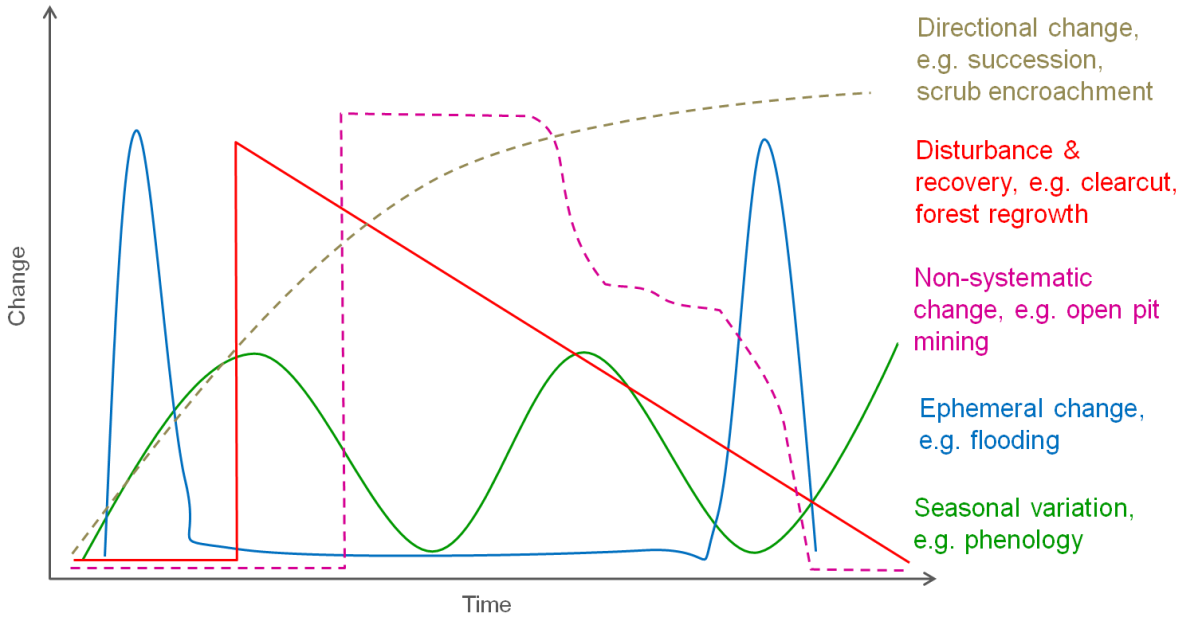


Fig. 1.2.1: Generalized representation of selected changes.

dramatic impact on infrastructure and ecosystems, they can only be captured within a short time (e.g., days up to weeks). Hence, flood monitoring is very sensitive to timing of the evaluable observations. Clouds may obscure optical images and are hence not evaluable. Quantification of a flood extent requires timely data. Another extreme related to timing are fires. Fires themselves are only visible with thermal sensors. Their legacy will be visible even after years. For the quantification of the extent of fires scars, timing of data acquisition is less critical. The temporal properties of some changes are generalized in Fig. 1.2.1. The change dimension may be a spectral value, index or quantity. The changes are only perceivable for a limited time, depending on the nature of change. Appropriate process characterization is only possible when a sufficient number of adequate observations is available.

Temporal aspects of change are its persistence (e.g., consistent growth) and reoccurrence (e.g., regularly reoccurring phenomena such as tides and the time lag between each repetition), timing and duration (e.g., start, end of an ephemeral change event and time in between), and its legacy (i.e., the time the result of a change is perceivable and ecologically/economically active).

### 1.2.1.2 Spatial Aspects

Some changes, especially human caused changes, appear in regular patterns, e.g., forest clearing, phenological patterns due to the geometric arrangement of agricultural fields, and urban structures. Consequently, extent, shape, size, stability over time, distribution, and arrangement of changes may be characteristic for certain phenomena. Natural changes are often more scattered and less distinct in their spatial distribution. The way spatial characteristics may be observed depends on the scale. Spatial attributes of an entity change when a land cover (or land use) becomes a different category. Spatial entities may be artificially defined categories such as administrative units, or homogeneous patches, or image objects. Expansion, shrinking and modification of shape are also spatial characteristics of change. A shift in position is also a spatial

process. Fragmentation or clustering are spatial processes that are particularly important in landscape ecology (Turner, 1989). The spatial entity of remote sensing images, however, is usually a pixel from which image objects may be derived. Their size is usually fixed. The examination of a particular pixel does not allow for the detection of spatially relevant changes except for the change of land cover category. Spatial processes are revealed when pixel based results are brought to spatial context (Blaschke, 2010; Chen et al., 2012).

#### 1.2.1.3 Spectral and Textural Aspects

Texture is closely related to spatial scale and thus to sensor resolution. However, when spectral properties of a land cover (more precisely of a pixel) do not change substantially although the land cover itself has changed, texture may be a means to detect the changes on the ground. An example are buildings after earthquake damage (Klonus et al., 2012).
Spectral properties are often more pronounced and less scale dependent than textural properties. To detect changes on the ground, changes in the textural or spectral properties of a surface (i.e., reflectance, backscatter and/or irradiance) are required. Frequently, the processes causing changes in the signal detected at a sensor are not linearly related to that signal. That means that many subtle processes such as maturation of a forest are not explicitly displayed by its spectral response. Consequently, only some forest growth stages may be captured adequately. Basically, all land cover changes that are perceivable by humans are detectable by technical instruments. It's the configuration of the devices that limits detectability with remote sensors.

### 1.2.2 Sensor Properties

Besides the change properties, the sensor characteristics are important factors that affect change detection and change understanding. Since the sensor system configuration is the limiting part, the following sensor properties refer essentially to characteristics that cause challenges. The affect change detection and are often primary sources of false detections.

#### 1.2.2.1 Temporal Resolution

The term temporal resolution characterizes the repetition rate of a sensor, i.e., the time it takes for a satellite to return to the same location on the Earth's surface. Many satellites such as the well-known Landsat satellites are nadir-looking with a fixed acquisition frame and regular revisit time – in case of the current Landsat 8 the repetition interval is 16 days. The repetition interval results from the satellite orbit, swath width, and off-nadir capabilities (Coops et al., 2007). With off-nadir capacity the repetition rate can be drastically reduced. Many of the recent (spatial high resolution) sensors have off-nadir capacities and thus are able to scan an area on Earth every day or every two days. A selection of sensors is shown in Fig. 1.2.2 confirming that only few systems have fixed viewing angles, e.g., the Landsat satellites. During the last decades, among the optical satellite sensors with spatial resolution better than 100 m the number of sensors with off-nadir capabilities has been increasing. The future Sentinel-2 satellites (not shown here) will operate as global monitoring systems with a fixed viewing angle as well (Drusch et al., 2012).

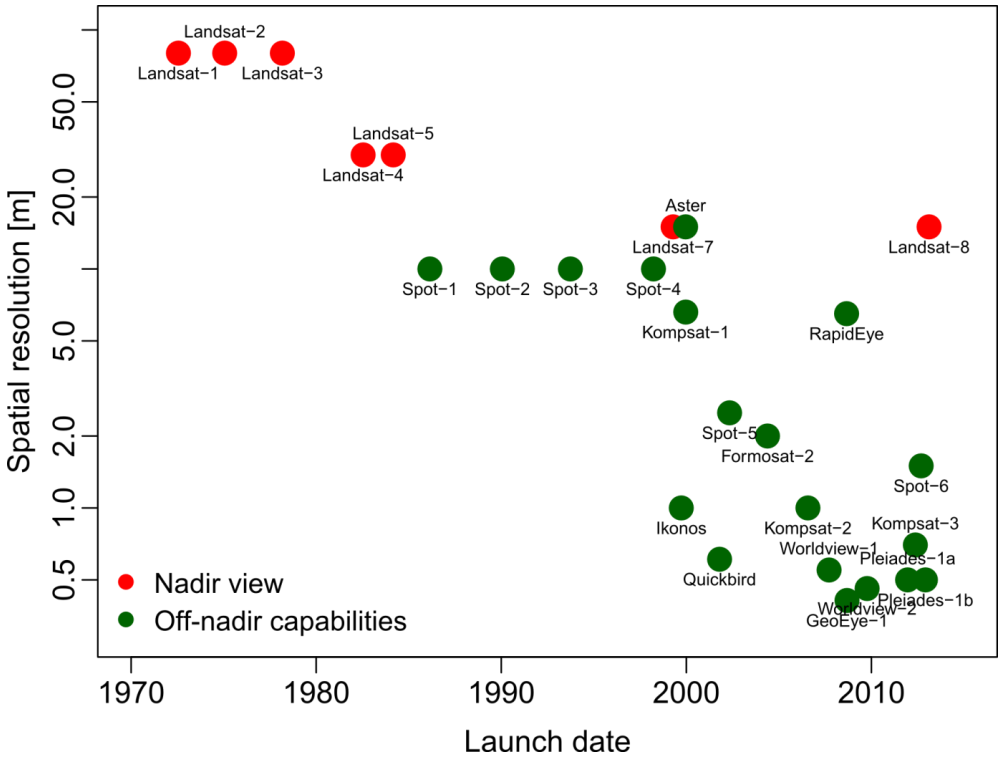


Fig. 1.2.2: Selection of sensors with spatial resolution better than 100 m launched during the last decades and their off-nadir capabilities.

Frequently, off-nadir capabilities are at the expense of reduced coverage of neighboring areas for a elongated period. Some coarse and medium resolution sensors with sufficiently high repetition rates allow for the generation of composite products such as the Moderate Resolution Imaging Spectroradiometer (MODIS) 16-day NDVI composites (van Leeuwen et al., 1999) and the Web-Enabled Landsat Data (WELD) products (Hansen et al., 2014; Roy et al., 2010).

From an application perspective it is important to differentiate between the repetition rate of one single sensor onboard a single satellite and of satellite constellations. RapidEye, for instance, is an optical satellite system consisting of five identical sensors that operate in a constellation that allows for frequent repetitions (Tyc et al., 2005).

Timing of image acquisition is crucial for many applications. Some phenological features (e.g., greening, browning) or disturbance agents (e.g., fire, defoliating insects) may have specific biowindows (Coops et al., 2007). Images must be acquired during these biowindows to detect the specific phenomenon (Wulder et al., 2004a). Timing also depends on the nature of process to be observed, as shown above. It is commonly accepted that monitoring forest change before and after a disturbance event, for example, should be conducted with anniversary images, i.e., images taken in the same season over a series of years (Coops et al., 2007). Anniversary dates are recommended to ensure phenological stability over successive years (Lunetta et al., 2004). Illumination conditions vary over the course of a year resulting in reduced image quality. Consequently, researchers try to prevent the use of off-season images and rather switch to other years (Wulder et al., 2004b). Summer or winter scenes are to be preferred because of their phenological stability (Häme, 1991). However, the use of winter acquisitions is often limited by various other phenomena such as snow cover, low sun angles resulting in large shadow

proportions, and leaf-off conditions. In regions without regular seasonal pattern it may be even more difficult to find appropriate datasets with comparable phenological conditions. Accuracy of several applications may be improved by considering different phenological situations, e.g., leaf-on and leaf-off conditions (Dymond et al., 2002). For bi-temporal change detection studies the time difference between the two images as well as the time lag between an observed event and the image acquisitions are important factors. The larger the time span the higher the probability of missing targeted changes and simultaneously including additional, undesired changes.
Acquisition time during a day is also affecting change detection. The MODIS sensors on TERRA and AQUA satellites take images at different times – the former in the morning, the latter in the afternoon. Diurnal variation of vegetation indices corresponding to ground measurements was found for several sensors (Fensholt et al., 2006; Uudus et al., 2013). Consequently, day time may affect change detection results. Atmospheric distortions are generally more pronounced in the afternoon, advocating morning acquisitions. Large regions of the world have strong daylight variation over the course of a year, e.g., the polar regions. Optical remote sensing is of limited use in these regions. Day length is closely related to illumination conditions. Shadow length of tall targets like trees or buildings varies considerably in the course of a day and also over a year. Since SAR are active systems, they are not affected by daylight at all. There are, however, radar shadows caused by its side-looking geometry which do not contain any information. For several SAR applications similar acquisition geometries are mandatory, e.g., SAR interferometry (Bamler and Hartl, 1998; Rosen et al., 2000).
In change detection studies, the repetition rates of sensors reflects only little its suitability. Rather, the time between usable acquisitions and the discrepancy from the change event are crucial. In case of long-term changes, the availability of multiple consistent observations is crucial. Although the term temporal resolution refers to the repetition rate of sensors, the time domain also includes the length of time series. Long-term processes may only be monitored when the process is at least partly covered by satellite observations. Many studies exploring environmental trends and change history rely on MODIS data and consequently cover only a short period of time (Pouliot et al., 2014; Sulla-Menashe et al., 2013). Other studies combine sensors to extend time series (e.g., Fensholt et al., 2009). Recent studies take advantage of the Landsat legacy which dates back as far as to the early 1970s and provides consistent datasets at 30 m spatial resolution (Markham and Helder, 2012)

#### 1.2.2.2 Spatial Resolution

Spatial resolution is defined by the Instantaneous Field Of View (IFOV), i.e. the area on the ground that is integrated in one measurement of a detector of the sensor. It is not identical with pixel size. The pixel size results from the processing of the raw data. Spatial resolution has major impact on the scale at which phenomena, structures, and processes, can be observed. High spatial resolution may provide detailed information on real world objects such as single trees or buildings. Usually, these sensors have limited spatial coverage. Change detection of large areas with sensors with small spatial coverage (some tens of km) is tedious and often hampers operational implementation. Thus, spatial coverage should be considered in change detection

studies as well. The swath width is limited by the sensor configuration. Sensors with large swath widths (up to several thousands of km) have lower spatial resolution (in the range of 250 m to several km) but short revisit times, e.g., National Oceanic and Atmospheric Administration Advanced Very High Resolution Radiometer (NOAA AVHRR), MODIS, Medium Resolution Imaging Specrometer (MERIS), and SPOT VEGETATION. Their spatial resolution is beyond the scale at which most processes dominate. Furthermore, the large spatial coverage with one data take is at the expense of varying viewing angles. Processes and their recognition are scale-dependent (Turner et al., 1989). Systems like Landsat operate on medium spatial resolution (e.g., Landsat with 30 m) and moderate swath widths (e.g., Landsat with 185 km). They operate with constant viewing angles and acquire data over several hundreds of kilometers or continuously. The 30 m spatial resolution is appropriate for most processes on the ground. Cross-sensor change detection of sensors with different spatial resolution is rarely applied.

#### 1.2.2.3 Spectral Resolution

Spectral resolution is defined by the part of the electromagnetic spectrum that is covered by each spectral band of a sensor, i.e. coverage, number of bands and their widths. The coverage is defined by the center wavelengths $\lambda$ and their Full Width at Half Maximum (FWHM). In this definition, thermal resolution is also included, i.e. the ability to measure temperature in selected bands of the thermal infrared part of the electromagnetic spectrum. All surfaces show characteristic spectral response. The more bands are available to measure spectral response and the finer their definition, the more precise the characterization of the observed surface. Unfortunately, there are constraints in the band definition, mostly related to the energy that must be received at the detector to detect distinct signals. As a trade-off, most spatial high resolution sensors have only broad spectral bands. Due to high production costs of shortwave-infrared (SWIR), mid-infrared (MIR), and thermal infrared (TIR) sensors, many commercial sensors lack of spectral bands beyond the visible (VIS) and near-infrared (NIR) spectral regions. Limited spectral coverage may affect a sensor's capability to assess particular phenomena such as floristic gradients (Feilhauer et al., 2013). Most optical instruments cover the VIS and NIR spectral regions. Many spectral indices are defined for the bands of these regions, e.g., the Normalized Difference Vegetation Index (NDVI) (Tucker, 1979). It has been shown, however, that spectral indices calculated from different sensors are not identical (Tüshaus et al., 2014). Sometimes scaling has to be applied to adjust different sensors (Pflugmacher et al., 2012). However, change detection based on spectral data (as opposed to post-classification comparison) requires identical (or at least similar) spectral bands for all acquisitions. Hyperspectral sensors have good spectral resolution compared to multispectral sensors but lack of spatial coverage and usually have smaller Signal-to-Noise Ratios (SNR). The full spectral range of a sensor can only be exploited if all images used for change detection have comparable spectral coverage. As the number of (space-borne) hyperspectral systems is very small, they currently play a minor role in change detection.
SAR systems usually operate with one frequency, i.e., radiation is transmitted at a defined wavelength; the received backscatter is measured. Once originated in military applications, the frequencies are still named with letters. The most important frequencies – because run in space

missions – are L-band (20 cm), C-band (5 cm) and X-band (3 cm). In the past there have been several L-band missions such as Seasat, JERS, and ALOS with the Phased Array type L-band Synthetic Aperture Radar (PALSAR). Its successor, ALOS-2 has been launched recently. There is a long tradition of European C-band missions with ERS-1/2, Envisat Advanced Synthetic Aperture Radar (ASAR) and the recently launched Sentinel-1. The C-band is also popular amongst the Canadian space program since it is operated onboard Radarsat-1/2 and their successors, the Radarsat Constellation Mission (RCM). The first civil satellite-based X-band missions are the German TerraSAR-X and TanDEM-X missions. When speaking about SAR, polarization is another important characteristic that has to be taken into account. Only few systems provide fully polarimetric data. Dual polarized modes are operational. Polarimetric data is still rarely used for change detection but provides great potential for automation (e.g., Conradsen et al., 2003; Thonfeld et al., 2013).

#### 1.2.2.4 Radiometric Resolution

Radiometric resolution describes the ability of a detector to distinguish its measurements. The higher the radiometric resolution the finer is the discrimination of detected signals. This leads to an individual dynamic range of each sensor. Common dynamic ranges are 8 bit (e.g. Landsat 5 TM & ETM+) or more, often saved in 16 bit format. Radiometric properties also include the sensitivity of a sensor to extreme measurements. Powerful instruments do not saturate and thereby offer suitable SNR. Changes beyond the saturation level may not be detected adequately.
The SNR plays a crucial role for the detection of changes with remote sensing data. It often determines the choice of sensor configuration since the choice of spatial and spectral resolution depends on the energy received at the sensor. Although SNR is important for the ability of a sensor to provide reliable measurements this is a given property that cannot be improved or corrected by the user. New sensors such as Landsat 8 Operational Land Imager (OLI) have typically a good SNR. The OLI instrument, for example, exceeds its precursors, thereby providing opportunities for unprecedented applications (Roy et al., 2014).

#### 1.2.2.5 Off-Nadir Capability and Changing Look Angles

As mentioned above, many recent sensors have off-nadir capabilities. Despite the advantage of increasing the repetition rate, this leads also to new methodological problems in change detection studies, e.g. Bidirectional Reflectance Distribution Function (BRDF) effects, and scene-specific layover of protruding objects. Another consequence of off-nadir capability is that when a sensor is tilted to increase the temporal resolution for one specific location it cannot capture the current nadir location at the same time. That means that the potential temporal resolution at the omitted location is decreased. The enhanced flexibility – which is essential for emergency response and other time critical applications – is at the expense of other regions.
Similarly, look angle dependent phenomena occur in SAR images. The layover, foreshortening and radar shadow phenomena largely depend on the depression angle (complementary to the look angle) of the sensor. If different depression angles are used, the aforementioned phenomena

are individual in each image and hamper change detection. The use of different depression angles may lead to detection of false alarms that are caused by image distortions and SAR effects rather than real changes. Indeed, the interaction of transmitted radiation with features on the ground depends among others on the local incidence angle rather than look angle. Scattering processes are incidence angle dependent (Ulaby et al., 1986). Consequently, backscatter mechanisms may change with changing incidence angles although the observed object remains unchanged. To achieve good change detection results, constant acquisition geometries are appreciated.

#### 1.2.2.6 Data Availability

Among the various factors affecting remote sensing change detection, data availability is probably the most critical one. Data availability does not only account for the sensors' capabilities to acquire data, their life history or the number of cloud free observations. It also comprises data access (Wulder et al., 2012). The opening of the Landsat archive in 2008 (Woodcock et al., 2008) was the starting point of a new era (indeed, the opening was triggered by the open data policy of Brazil). Some years ago one Landsat scene was at a cost of $4400 caused by commercial operations. With the launch of Landsat-7 in 1999 USGS inherited all operations and consequently the costs decreased to $600 per scene (Wulder et al., 2012). It is not surprising that there was only very limited benefit of the valuable Landsat records. After the opening of the archive the number of downloaded scenes increased drastically (Wulder et al., 2012). The advance by opening the Landsat archive was not only the establishment of an efficient interface to screen data, it was furthermore the change in data policy that allowed data access free of charge. Large-scale as well as long-term (change) studies are now feasible at a unprecedented spatial and temporal resolution; standardized products such as monthly or seasonal composites will be operational globally in the near future (Roy et al., 2014, 2010). A new level of information retrieval has emerged. Yet, there are limited efforts to relate observed spatio-temporal patterns to processes on the ground. Data exploration is also just at a starting point as can be seen from the very limited number of publications that account for exhaustive datasets (e.g., Zhu and Woodcock, 2014).

#### 1.2.2.7 Other Factors

Although not restricted to the platform itself, there exist additional properties that may limit the use of sensors. Those properties comprise among others downlink capability and processing time which may be important for near-real time processing and may become a bottleneck. Another issue is the processing of big data (Madden, 2012) which seems discouraging for working with comprehensive datasets.

### 1.2.3 Data Acquisition Conditions

The previous sections summarized the most important change properties – their interaction characterizes changes – and the most important sensor related properties. An adequate sensor configuration allows for the detection of changes at an acceptable false alarm rate. There are,

however, external factors that affect remote sensing change detection. These external factors – acquisition conditions – mainly refer to atmospheric properties during image acquisition. Atmosphere and all other spheres between Earth and sensor often experience much faster changes than processes on Earth take place. Thus, atmospheric conditions are hardly equal for multiple image takes. To assure proper change detection results, acquisition conditions have to be equalized. In optical data, haze can be corrected (Richter, 1996). Clouds, however, obscure the ground in optical imagery. SAR images are not completely unaffected by atmospheric conditions (Danklmayer et al., 2009), but they are much less sensitive to weather conditions and other atmospheric phenomena than optical systems. High frequency SAR systems (e.g. X-band) are sensitive to heavy rains and atmospheric distortions. Longer wavelength SAR (e.g., C- and L-band) are virtually insensitive to clouds.

Acquisition conditions also refer to illumination conditions including BRDF effects. These effects play a minor role in change detection studies with identical orbits, nadir viewing sensors with narrow viewing angles, and data taken in the same season. But they are critical when wide-swath sensors (e.g., MERIS) are used. Some data products are distributed as BRDF-corrected (e.g., MODIS) facilitating data exploration.

Acquisition conditions include also state and condition of the observed study site at the time of acquisition, including tidal stage, soil moisture, and phenology (Jensen, 1996). They may limit the usability of remote sensing means or stimulate the development of adequate methods.

## 1.3 Scope, Aim, and Research Objectives

The previous sections shortly reviewed the interrelationship of nature of change, sensor properties, and external constraints. Among the limiting factors of remote sensing change detection the sensor properties are probably those that leave most ground for research and improvement. Although the number of studies using multi-temporal data (i.e., more than two images) is increasing, bi-temporal change detection is still an adequate means to uncover many change types. Flood detection, urban expansion, emergency response, and others are typical bi-temporal applications. Even if time series can provide more comprehensive monitoring and process understanding capabilities, bi-temporal datasets are often preferred for these applications due to shorter processing time, data suitability, and efficiency. If a dataset of two images is considered the minimum requirement for change detection than using all data can be considered as the other extreme. Each single cloud free, non-contaminated pixel provides spectral information of a defined location of our planet. Disregarding some of this information means loss of precious observations – limiting our understanding of spectral trends that may be related to processes on the ground. A huge benefit of improved understanding can be assumed from exploring all information we can get. If this information is not perfect, we should aim at finding methods that enable us to deal with imperfect data. Both approaches – bi-temporal change detection and analysis of dense time-series – are addressed in different ways in this thesis. The two main aims of this research were therefore:

1) to contribute to a more accurate estimation of land use/land cover changes by accounting for the effects of variable sun-target-sensor geometries. In a generalized form, these effects are of spatial nature. Thus, the first part of the thesis deals with the spatial domain of remote sensing based change detection. However, effects of spectral, radiometric and temporal resolution are inherently linked to variations and changes in the spatial domain.

2) to contribute to a better understanding of forest dynamics by providing a new approach of remotely sensed data exploration. The novelty of the approach is to use all available observations, thereby increasing the temporal resolution compared to existing methods. Thus, the second part of the thesis refers to the temporal domain.

Pursuing these aims leads to several research questions. For the first aim these are:

1a. Which sun-target-sensor constellations can occur in remote sensing and how do they affect change detection?

1b. How can the effects of different sun-target-sensor constellations be reduced?

The objective of the first part of this thesis is the enhancement of bi-temporal change detection methods. The previously described off-nadir capabilities of high spatial resolution sensors allow for flexible use of the sensors, while this means that different acquisition geometries also need to be taken into consideration in the analysis and interpretation. The main objective of the first section of the thesis is thus to provide a theoretical concept of bi-temporal change detection scenarios including the quantification of distortions that can occur in unfavorable situations. To address research question 1b, a new method capable of reducing the detection of false changes is introduced. The requirements that have to be fulfilled include robustness against distortions that result from different sun-target-sensor geometries and use of all spectral bands to enhance understanding of the nature of change.
The main objective of the second part of this thesis is to demonstrate the continuing legacy of Landsat data and the value of long-term Landsat time series for forest monitoring. This area of research has already been thoroughly explored, as a keyword search of *forest monitoring* in the *Remote Sensing of Environment* journal revealed (2534 hits as of 8th July 2014). Although many recent studies built upon (Landsat) time series (Cohen et al., 2010; Griffiths et al., 2012; Kennedy et al., 2010; Meigs et al., 2011; Powell et al., 2010; Schroeder et al., 2011), there are only few studies that take advantage of all available data in the archives (Zhu and Woodcock, 2014; Zhu et al., 2012). However, despite the knowledge in this field there is still space and urgent need for research for a comprehensive understanding of the environment, which can only be achieved when all temporal scales are addressed, i.e., long-term trends, seasonal variation, shifts in seasonal variation, abrupt changes, and subtle changes. The research questions to achieve the second aim of this thesis are therefore:

2a. Which spectral indices are suitable for forest cover change characterization?

2b. How suitable are selected spectral indices for dense time series?

2c. How does radiometric normalization affect time series of spectral indices?

2d. How can forest development and forest cover change be characterized by means of dense Landsat time series?

To address research question 2a selected spectral indices are to be reviewed. Emphasis is on their relationship to forest development, particularly conifer forests. The assessment of spatio-temporal variability of spectral indices is subject of research question 2b. The objective is to identify those spectral indices that reflect structural changes in conifer forests and that respond sensitively on subtle changes. At the same time it is required that the indices are invariant to changing illumination as varying sun positions during the course of a year are occurring when using off-seasonal observations. Answering research question 2c is essential for the analysis of time series of remote sensing data. There are several studies that addressed this question for early data (Schroeder et al., 2006; Vicente-Serrano et al., 2008). However, the implications of radiometric normalization on dense time series including off-seasonal data have not yet been addressed. Research question 2d is based on the solutions of research questions 2a-2c. The related objectives include exploring features that describe time series properties that are related to forest structure, and presenting a new method allowing for the detection of abrupt changes (e.g., clearcut harvest).

## 1.4 Structure of the Thesis

Given the two aims and the six research questions, the thesis is structured as follows: Section 2 is related to research questions 1a and 1b. In Section 2, a new bi-temporal change detection method, Robust Change Vector Analysis (RCVA), which is efficient in cross-sensor change detection of spatial high resolution images with different viewing geometries, is introduced. Section 3 addresses research questions 2a-2d and presents the optimized exploitation of the Landsat archive. In that Section, a description of the study site including Landsat derived cloud statistics (Section 3.1) is given and followed by a general explanation of forest dynamics in the study region (Section 3.2). Section 3.3 presents a review of a collection of selected spectral indices and their suitability for forest monitoring. An emphasis is set on the time series generation of the Disturbance Index (DI) by Healey et al. (2005) and the intra-annual spatio-temporal variation of the selected indices. Research questions 2a and 2b are addressed in this Section.
Section 3.4 discusses the state of the art of the preprocessing for time series analysis. The potential of radiometric normalization as a tool to generate consistent datasets is assessed (research question 2c). A new method for the detection of forest harvest events with an improved temporal accuracy is presented in Section 3.5, addressing research question 2d. Section 4 summarizes the key findings of this research, demonstrates the major contributions and significance of this research, and discusses (current) limitations.

# 2 Development of a New Robust Change Vector Analysis (RCVA) Method for Multi-Sensor High Resolution Optical Data

## 2.1 Introduction

Environmental change detection is a key application of remote sensing technology (Hecheltjen et al., 2014). With increasing availability of multi-sensor imagery, the variety of application fields and methods continues to grow. Comprehensive reviews of change detection techniques can be found in (Coppin et al., 2004; Hecheltjen et al., 2014; Lu et al., 2004; Radke et al., 2005; Singh, 1989). In general, change detection techniques utilize either a bi-temporal or a multi-temporal approach. The focus here is on bi-temporal change detection.

Environmental change detection using multi-sensor imagery features some attendant challenges as the multi-temporal image suite can include a number of error sources which may lead to the identification of spurious changes. These error sources can be related to the sensor properties or to environmental conditions. The latter include atmospherics, vegetation phenology, soil moisture, and tidal stage; all of which can interact and impact the change detection process in various ways (Jensen, 1996). A bi-temporal change detection approach utilizes one initial-state image and one final-state image. Coppin et al. (2004) recommend using anniversary data to minimize differences in reflectance caused by varying phenological conditions and different sun position. Due to their phenological stability, summer or winter scenes should be preferred for bi-temporal change detection (Häme, 1991). However, the use of winter acquisitions may be limited by other phenomena such as snow cover, low sun angles (resulting in large shadow proportions), and leaf-off conditions. In regions without regular seasonal patterns, identifying appropriate datasets may be even more challenging.

Off-nadir capabilities of modern satellite sensors enable frequent repeat monitoring, sometimes even daily revisits. This allows for the identification and assessment of rapid changes due to floods, earthquakes, tsunamis, fires, and urban infrastructure construction and damage. Utilizing anniversary data is inappropriate for these applications. Along with specific environmental conditions that impact the change detection process and may be captured in any image data, off-nadir imagery typically includes additional unique characteristics. Due to differing viewing angles, off-nadir images may capture surface geometric phenomena such as horizontal layover of protruding objects, including buildings and trees (Im and Jensen, 2005). Shadow effects also impede change detection, especially under different sun positions and with increasing spatial resolution. Shadow modeling and elimination is difficult without accurate Digital Surface Models (DSM) that perfectly match the geometry of the spectral image.

The majority of established change detection methods require high geometric registration accuracy at subpixel level as image misregistration may cause image object properties to be evaluated at incorrect locations. This can lead to identification of spurious changes as well as the failure to identify genuine changes due to even slight dislocations of image objects (Townshend et al., 1992). Due to arbitrary platform shifts between different acquisitions, the footprints of coincident pixels of images from the same sensor are not necessarily identical, thus further

complicating exact registration (Bruzzone and Cossu, 2003). Several studies have attempted to quantify the impact of misregistration on change detection (e.g., Dai and Khorram, 1998; Townshend et al., 1992). In addition, Chen et al. (2014) examined misregistration effects on object-based change detection and concluded that even subpixel registration errors can result in substantial overestimation of change. A number of methods have also been developed to reduce the effects of registration noise in remote sensing change detection (Bruzzone and Cossu, 2003; Gong et al., 1992; Stow, 1999). Additional techniques may be required to reduce other undesired effects.

For many fast response applications (such as emergency services) scene selection will prefer data availability over perfect image conditions to insure appropriate temporal coverage. These circumstances require a change detection approach that is capable of utilizing data which have been acquired under varying sun position and viewing angles as well as differing atmospheric and phenological conditions. When using data acquired by multiple sensors, differences in spatial, spectral, and radiometric resolution must be considered, as well.

Most change detection algorithms were developed to identify changes in medium to coarse resolution imagery (Coppin et al., 2004). For many remote sensing applications with high spatial resolution data the paradigm moved from per-pixel analysis to object-oriented approaches (Blaschke, 2010). Object-oriented techniques allow for the segmentation of image objects and thus the representation of real world objects (Benz et al., 2004). Those approaches have also found their way to change detection procedures (e.g., Chen et al., 2014, 2012; Desclée et al., 2006; Hall and Hay, 2003; Hussain et al., 2013; Walter, 2004). The creation of meaningful image objects does not eliminate the aforementioned geometric distortions, sun position effects or shadow effects. Thus, several methods were developed to consider the pixel neighborhood (Bruzzone and Cossu, 2003; Castilla et al., 2009; Gong et al., 1992; Im and Jensen, 2005). The Land-cover Change Mapper (LCM) technique (Castilla et al., 2009) is simple, fast and accurate. This procedure utilizes a single image spectral band and generates a vector dataset with change objects of a predefined minimum mapping unit. The LCM tool was designed for analysis of forest cover change, which can be successfully performed when an appropriate single image band is selected. The procedure is also more efficient as spectral change has to be calculated for only one band. Constraining the LCM procedure to a single spectral band limits information content inherent in the data and the method is not appropriate to identify multiple changes that may occur. The extension of the LCM method to incorporate multiple spectral bands allows for the discrimination of different change types.

Of the numerous change detection methods that have been developed and tested, relatively few go beyond the simple discrimination of changed and unchanged features (Hecheltjen et al., 2014). Change Vector Analysis (CVA) (Malila, 1980) is a widely used and robust method which produces two types of change information: 1) change *magnitude* which represents the intensity of change; and, 2) change *direction* which provides information about the spectral behavior of the change vector. Although change direction information is sometimes disregarded in change detection applications, some studies have examined it and documented its efficiency (Allen and Kupfer, 2000; Chen et al., 2003; Johnson and Kasischke, 1998; Landmann et al., 2013). Bovolo and Bruzzone (2007) provide a comprehensive theoretical framework for CVA.

In the work summarized here we focus upon the fundamental concept of considering pixel neighborhood in the change detection methodology. This approach is extended to a new, more robust CVA-based change detection method which we term *Robust Change Vector Analysis (RCVA)*.
The study has three main objectives: 1) to present the conceptual basis of pixel neighborhood in change detection and to consider how this attribute may be used to reduce overestimation of spurious changes in the detection process; 2) to describe in detail the RCVA method; and, 3) to demonstrate the effectiveness of RCVA in comparison to conventional CVA.

## 2.2 Methods

### 2.2.1 Problem Formulation

Off-nadir sensing is a common capability in recent satellite sensor systems. It is understood that sensor viewing angle has a significant effect on orthorectified imagery (Aguilar et al., 2013; Toutin, 2004). Assuming identical environmental conditions of atmospherics, phenology, and soil moisture for both image sets used in a bi-temporal change detection, sun-target-sensor geometry becomes the critical variable producing distortions in the satellite imagery.
In general, four sun-target-sensor geometry scenarios may occur (as illustrated in Fig. 2.2.1):

1) Viewing geometries -- sensor position, viewing angle, and sun position -- are identical in both images (Fig. 2.2.1a). Chances of realizing this "ideal" case are greatest when anniversary data are acquired under the same sensor parameters, including identical overflight times. Horizontal layover (if present) and shadow effects are identical and would not cause spurious changes. Scan lines would be identical in both images within image areas that covered ground locations where no real land cover changes were present.

2) Viewing geometries are identical, but the sun position is different (Fig. 2.2.1b). This is the typical case for nadir-viewing systems such as Landsat. Per-pixel based change detection techniques may be adequate for use under this scenario, because pseudo changes caused by differing sun-sensor-geometries are insignificant. Differing sun positions may, however, affect shadow proportions in the images. Different sun-target-sensor constellations may also cause significant differences in the composition of mixed pixels within the images.

3) Sun position is identical for both acquisitions, but viewing geometries differ (Fig. 2.2.1c). This exceptional scenario may only occur when off-nadir sensors are used at anniversary dates. Shadow proportions may differ dependent on the three-dimensional appearance of the objects on the ground. Scan lines will differ noticeably since identical objects are recorded from different positions.

4) Viewing geometries and sun positions both differ between the two input datasets (Fig. 2.2.1d). This scenario is the most common for all off-nadir viewing sensors and multi-sensor change detection. It occurs when non-anniversary data are used and the viewing geometries differ. Distortions are most complex in imagery acquired under this scenario.

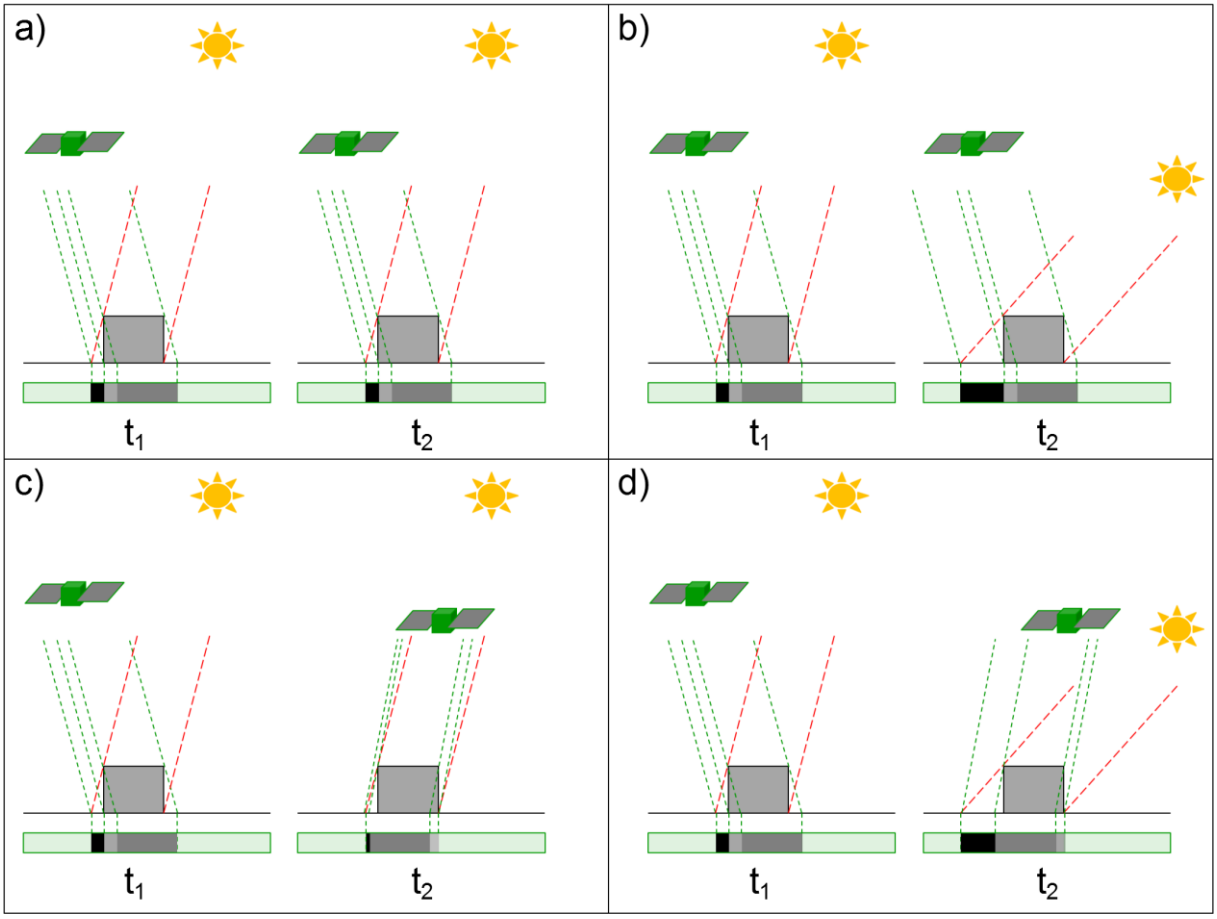


Fig. 2.2.1: Four scenarios of sun-target-sensor constellations and resulting differences between two image acquisitions at $t_1$ and $t_2$: a) identical sun-target-sensor geometries; b) identical target-sensor geometries, different sun angles; c) identical sun angles, different target-sensor geometries; and, d) different target-sensor geometries, different sun angles. The effects in satellite images are diagramed as representative scan lines shown at the bottom of each graphic. No changes on the ground have occurred in any of the examples. The differences shown in scenario b) to d) are of particular interest.

Change detection algorithms calculate differences among images rather than direct changes on the ground. It is necessary to implement algorithms that are capable of detecting only those differences between images that can be correlated to changes on the ground. Fig. 2.2.1 illustrates how target object information (e.g., a building, indicated by its roof) can be identified in imagery acquired under all four described constellations. Visibility of targets may be limited by layover of larger objects. This can be an acute effect in city environments with very tall buildings. If layover effects are not present, the roof will be depicted in each scenario, though in different locations, as shown in Fig. 2.2.1c and d, which illustrate scenarios in which $t_1$ and $t_2$ sensor positions vary. Per-pixel based change detection approaches are not adequate to account for the distortion within imagery of tall topographic features such as buildings or trees, because these features are not consistently spatially rendered within each image. The layover effect can be considered as a unique type of registration noise that typically adds additional image distortion. An example of this occurs when portions of walls or other objects that are not visible in $t_1$ images are visible in $t_2$

imagery (and vice versa). These artifacts cause pseudo-changes. Consideration of pixel neighborhood is appropriate for settings -- including urban environments -- that are dominated by distinct three-dimensional surfaces and/or characterized by frequent topographic changes.

### 2.2.2 Quantification of distortions

The scenarios illustrated in Fig. 2.2.1 show sun-target-sensor geometries reduced to a plane dimension. The resulting layover angles can be calculated from sun and sensor positions through simple trigonometric functions. Three major effects are important in quantifying layover.
The first effect involves relationships among object height *h* (the height of the observed target on the ground), the viewing angle in the plane θ and the distortion on the ground *a*:

$$a = \tan(\theta)\, h. \tag{1}$$

The resulting effect is shown in Fig. 2.2.2a. It occurs in any off-nadir image as well as in the off-nadir (far-range) portions of nadir images. Angles shown in Fig. 2.2.2 are not necessarily equal to the sensor viewing angle as the figure depicts a plane view. To derive the actual viewing angles, the sensor position must be taken into account. However, the effective displacement shown in Fig. 2.2.1 and Fig. 2.2.2 is relevant to quantify displacement on the ground. The left portions of Fig. 2.2.2a-c show distortions (quantified by color) according to object height and viewing angle of a single observation.
The second effect is relevant when two different acquisitions are compared, and additional complicating issues may occur (see again Fig. 2.2.1). The combination of two individual image acquisitions may result in relative artifacts between the two images. This second effect is derived as a function of the relationship between the viewing angles θ and θ` of two images, their respective differences, and the relative displacement of an object or building of static height (a 10 m value is shown in Fig. 2.2.2b). This can be calculated as follows:

$$a = \tan(\theta)h - \tan(\theta`)h. \tag{2}$$

The relative displacement of an object between to images is low if the viewing angles are similar and large if the viewing angles differ markedly. This is quantified by the colors in the left panel of Fig. 2.2.2b.
The third effect is that the displacement for a fixed difference of viewing angles is smaller for narrow nadir angles than for wider angles (Fig. 2.2.2c). Distortions are greater in an image pair with 25° and 15° viewing angles, respectively, than in an image pair with 10° and 0° viewing angles, although the angular difference is 10° for both. Thus, in order to reduce distortions between images, viewing angle differences should be minimized. Additionally, imaging angles close to nadir reduce geometric distortions of objects on the ground. The left panel in Fig. 2.2.2c plots the viewing angle of an image that is closer to nadir on the abscissa with building height on the ordinate. The viewing angle of the second image is 10° larger than θ. The colors quantify distortions of an object with height *h*.

These geometric relationships lead to two idealized situations, under which sun position is disregarded and all other conditions are held constant: 1) Geometric distortions are not present in imagery in nadir view; and, 2) Distortions are similar in two images when their off-nadir viewing angles are identical.

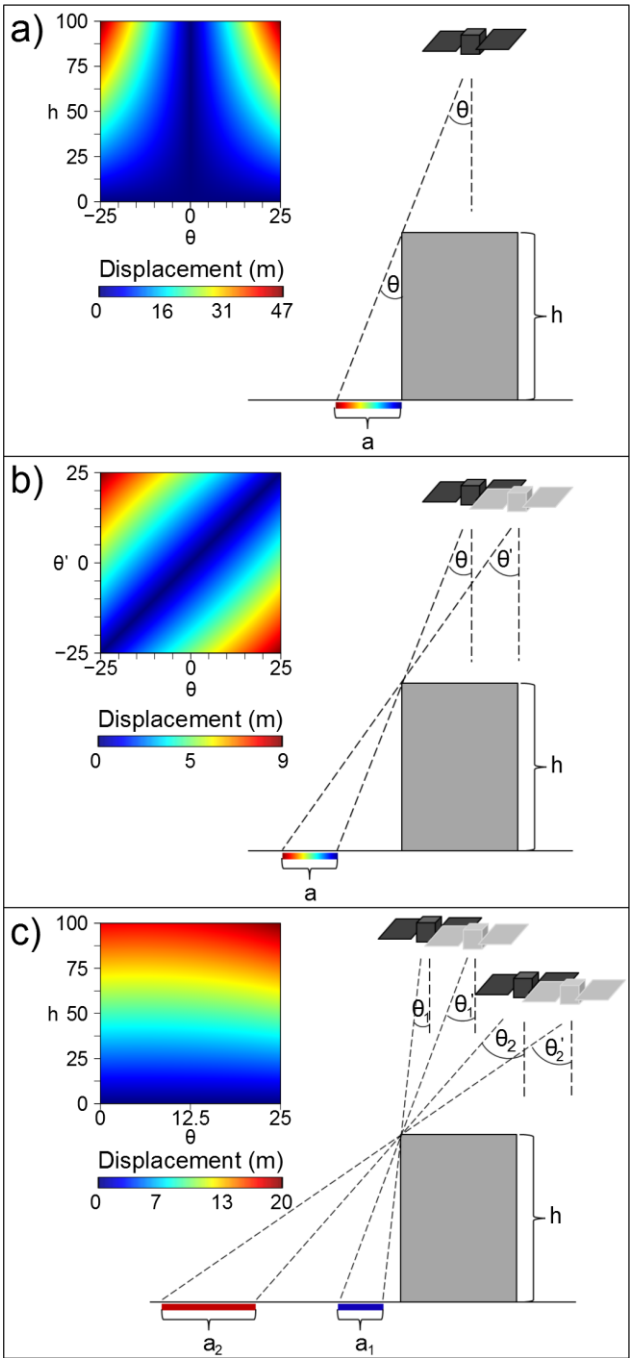


Fig. 2.2.2: a) Displacement of an object on the ground in relation to the sensor viewing angle and object height in a single image; b) Relative displacement of an object 10 m in ground height in relation to the viewing angles of two images acquired with different viewing angles; c) Relative displacement of an object on the ground in relation to the viewing angle of one image and object height. The viewing angle difference is 10° for both image pairs. Distortion is reduced in the close-to-nadir image pair. Distortions (in meters) are quantified by colors at the left in each graphic. Distortion effects are projected on a plane in all examples.

Sun position effects follow the same mathematical principles. Sun azimuth (a function of calendar date and time of day) affects shadow orientation; sun elevation affects shadow length. Differences in sun position at the time of imaging lead to different shadow patterns in the imagery. These differences can be addressed in a number of ways. Appropriate scenes with similar viewing conditions may be selected, or shadows may be recognized and eliminated by preprocessing (Chen et al., 2007; Sarabandi et al., 2004; Teke et al., 2011). Failure to account for image viewing geometry and sun position will lead to obvious distortions within images covering locations characterized by pronounced relief. Correcting image distortions and shadow effects introduced by differing viewing geometries can be challenging, particularly when no adequate ancillary DSM is available.

Although various sensors have off-nadir viewing capabilities at angles of 45° or more, angles exceeding 25° are rarely used (Dial et al., 2003). It can be shown that even low objects will produce a relative displacement in the order of one pixel or more when spatially very-high resolution (5 m or less) off-nadir sensors (e.g., Ikonos, Quickbird, Worldview-2, RapidEye, Spot-6) are used. The effects of such object displacement are increased as reflectance from neighboring pixels is integrated within the image. When buildings and other objects are depicted off-nadir, distinct materials may be rendered in the image that are not detectable by the sensor under nadir conditions, where only the top surface of an object or the roof of a building contributes to the reflectance signal. Accurate displacement values are quantified in color-cube at the left of Fig. 2.2.2a-c.

### 2.2.3 Proposed Method

We have seen that it is feasible to consider pixel neighborhood in change detection studies based on very-high spatial resolution data. We will now describe the RCVA technique we propose to overcome spurious changes which may occur in the change detection process. This methodology includes four components:

1. standard geometric and radiometric preprocessing adjustments (discussed in detail in Section 2.2.3.1)
2. the new robust change detection procedure itself (Section 2.2.3.2);
3. thresholding to derive a change/no-change mask (Section 2.2.3.3); and,
4. the identification of change classes.

The processing workflow is diagrammed in Fig. 2.2.3.

#### 2.2.3.1 Preprocessing

The RCVA method has been developed to overcome image geometric distortion and misregistration. However, an accurate orthorectification of the imagery is still required. When using any pixel-based approach such as RCVA, adjustment of pixel size is also necessary. The optimum approach for radiometric preprocessing in RCVA is evaluated under the assumption of

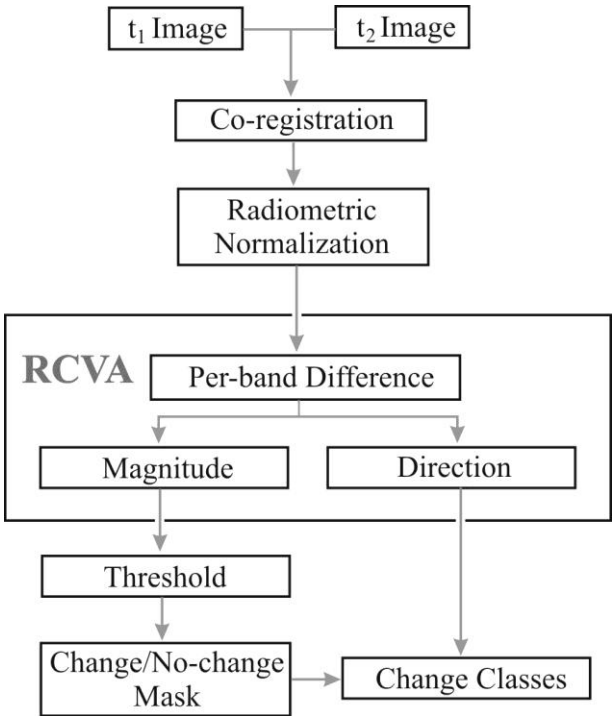


Fig. 2.2.3: Proposed RCVA processing flow.

relative distortions between the images. Numerous studies prescribe the application of radiometric correction in change detection studies (Collins and Woodcock, 1996; Schroeder et al., 2006; Song et al., 2001). These studies conclude that relative atmospheric correction performs as well as absolute correction but is typically easier to apply. Absolute atmospheric correction methods are required when biophysical parameters are to be calculated. Relative atmospheric correction methods are usually sufficient to achieve a "common radiometric scale" (Song et al., 2001) which is needed for change detection. A fully automatic method for radiometric normalization (relative atmospheric correction) is the Iteratively Re-weighted Multivariate Alteration Detection (IR-MAD) (Canty and Nielsen, 2008). The method iteratively identifies unchanged pixels which are used to set up an equation determining a linear relationship between the two images. The images are subsequently normalized by means of orthogonal linear regression. Distortions are expected to occur only in regions with pronounced three-dimensional surfaces which are not adequately captured by the Digital Elevation Model (DEM) during orthorectification. In image regions where the DEM equals the DSM, no distortions are expected. Since RCVA is designed for use with high spatial resolution data, unchanged pixels are assumed to be components of larger homogeneous objects; this supports the use of IR-MAD or similar radiometric normalization procedures.

As stated previously, change detection is the process of identifying differences between images. Even when data acquired by the same sensor are used, there are small differences originating from sensor degradation. When using different sensors the amount of systematic errors is increased due to distinct spectral response curves. Although not commonly applied, change detection using multi-sensor data is possible when similar spectral bands are used. Relative radiometric normalization procedures such as IR-MAD can equalize sensor variations sufficiently to allow comparison of images acquired by different sensors.

#### 2.2.3.2 Robust Change Vector Analysis (RCVA)

The proposed method is based on CVA (Malila, 1980). This method performs change detection by differencing the spectral vectors of identical pixels in two co-registered multispectral images. The difference vector for all spectral bands can be described by its magnitude and its direction. Change magnitude – a measure of change intensity – is expressed as the Euclidean distance in the multidimensional feature space, calculated from the differences in each spectral band:

$$x_{diff_i} = x_{2_i} - x_{1_i} \tag{3}$$

$$m = \sqrt{\sum_{i=1}^{n} x_{diff_i}{}^2}, m \in [0, \max(m)] \tag{4}$$

where:

$x_{1i}$ and $x_{2i}$ = the digital number (DN) of band $i$ in images 1 and 2, respectively;
$x_{diffi}$ = the difference of each band $i$;
$m$ = magnitude;
$n$ = number of bands.

Change direction can be calculated in four ways:

1) sector-coding (Michalek et al., 1993);
2) vector direction cosines (Chen et al., 2003);
3) Principal Component Analysis (PCA) in the multi-temporal domain (Lambin and Strahler, 1994), and;
4) direction in polar domain (Allen and Kupfer, 2000).

The last method results in a single vector projected on all axes of the feature space. A systematic approach to representing changes in the polar domain is given by (Bovolo and Bruzzone, 2007). Change direction does not provide from/to classes. It rather indicates the direction of change, e.g. in terms of spectral response increase or decrease in a given image band over time. Since we seek to exploit all available spectral information, we adopt the methodology described by Bovolo et al. (2010), who extended the polar domain approach to represent higher dimensional feature spaces in two dimensions (5):

$$\alpha = \cos^{-1}\left[\frac{1}{\sqrt{n}}\left(\frac{\sum_{i=1}^{n} x_{diff_i}}{\sqrt{\sum_{i=1}^{n} x_{diff_i}{}^2}}\right)\right], \alpha \in [0, \pi] \tag{5}$$

where:

$a$ = direction expressed as multi-dimensional angle.

Again, due to positional inaccuracies and geometric distortions, it is unlikely that corresponding pixels will contain the spectral information of identical ground areas despite adequate image co-registration. It is further assumed that the corresponding ground information of a pixel with position $j,k$ in image $x_1$ is contained either in the corresponding $x_2(j,k)$ pixel, or in one of the pixels in the adjacent neighborhood. Accordingly, differences caused by geometric distortions and image misregistration can be eliminated. Differences due to shifts of the instantaneous field of view can also be minimized by the consideration of the pixel neighborhood in the change detection process.

Dai and Khorram (1998) showed that precise image registration is required to achieve accurate results in per-pixel change detection, especially when using high spatial resolution imagery. This conclusion weighs against the use of per-pixel approaches in general. A number of methods have been developed to account for pixel neighborhood:

1) filtering of the difference image to reduce registration noise (Gong et al., 1992);
2) estimating the registration noise from the contextual information in a quantized magnitude-direction space and subsequent consideration of registration noise probability for the final change/no-change decision (Bruzzone and Cossu, 2003);
3) calculating multiple correlation images in several neighborhood configurations with subsequent classification of from/to changes (Im and Jensen, 2005), and;
4) calculating the least difference of a single band in a predefined neighborhood (Castilla et al., 2009).

Object-based approaches are sometimes preferred, as "sliver" polygons that show spurious changes may be distinguished from real change polygons by GIS analyses (Chen et al., 2012). However, the per-pixel method described by Castilla et al. (2009) is efficient and effective and does not require additional analyses. It proceeds under the basic assumption that a pixel $x_2(j\pm w,k\pm w)$ showing the least spectral variance to $x_1(j,k)$ is the pixel containing most of the corresponding ground information of $x_1(j,k)$. In order to derive additional information about the nature of changes, we extended this approach to multiple bands and compute the least difference of each pixel in all bands in a moving window $2w+1$ in size (6, 7). Each change detection method is expected to produce identical results when the images of $t_1$ and $t_2$ are exchanged. This logical assumption cannot be fulfilled when the smallest deviation in the specified neighborhood (the smallest absolute of the differences) is computed. The computation of $x_1(j,k)$-$x_2(j\pm w,k\pm w)$ under this condition would produce a result at variance with $x_2(j,k)$-$x_1(j\pm w,k\pm w)$. The calculation of the robust difference must therefore be performed in two steps. In the first step, difference images are calculated considering pixel neighborhood for subtracting $t_1$ from $t_2$ and vice versa:

$$x_{diffa_i}(j,k) = \min_{(p\in[j-w,j+w],q\in[k-w,k+w])} \{(x_{2i}(j,k) - x_{1i}(p,q)) \geq 0\} \quad (6)$$

$$x_{diffb_i}(j,k) = \min_{(p\in[j-w,j+w],q\in[k-w,k+w])} \left\{ \left( x_{1_i}(j,k) - x_{2i}(p,q) \right) \geq 0 \right\} \tag{7}$$

Equations (6) and (7) specify that all negative differences are set to 0. Only an increase in reflectance of a pixel (expressed in DN value) can be computed correctly with this method. To overcome this effect, and to ensure exchangeability of $t_1$ and $t_2$ without loss of information, we combine the difference images of $x_1$-$x_2$ and $x_2$-$x_1$ in a second calculation as follows:

$$x_{diff\,i}(j,k) = \begin{cases} x_{diffa_i} > 0 \Rightarrow x_{diffa_i} \\ x_{diffa_i} = 0 \Rightarrow 0 - x_{diffb_i} \end{cases} \tag{8}$$

Change magnitude and direction are now calculated from the robust differences according to (4) and (5), respectively.

### 2.2.3.3 Change Separation

A crucial step in change detection analysis is the change/no-change decision which usually requires thresholding. Change magnitude and direction are equally important, but for practical reasons a threshold separating change from no-change pixels is frequently applied to the magnitude variable (Bovolo et al., 2010). There are numerous thresholding techniques (Bazi et al., 2007; Coudray et al., 2010; Otsu, 1979; Rogerson, 2002; Rosin and Ioannidis, 2003; Rosin, 2001, 1998; Sezgin and Sankur, 2004). The generalized magnitude histogram of the CVA has two peaks, a pronounced peak close to zero indicating the center of the no-change marginal distribution, and a less distinct peak indicating the center of the change marginal distribution (Fig. 2.2.4).
An offset from zero can frequently be observed in magnitude histograms (Bruzzone and Prieto, 2000). This results from differences between the $t_1$ and $t_2$ images that cannot be attributed to changes on the ground. No such offset is visible in the RCVA histogram. The peak of the no-change marginal distribution is at zero. Courses of the RCVA and CVA histograms are similar

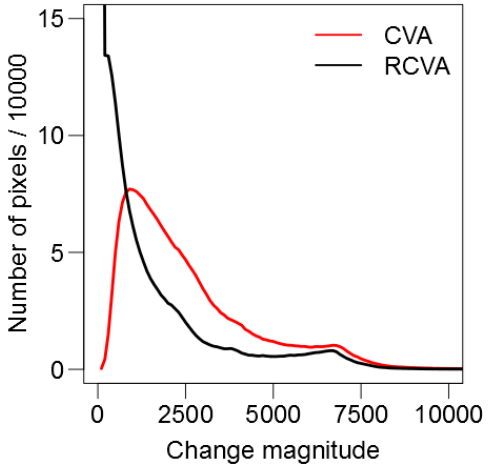


Fig. 2.2.4: Histograms of CVA and RCVA change magnitude. For visualization purposes magnitude values above approximately 10,000 are not plotted; the maximum value derived in this example was approximately 90,000.

beyond the respective peaks; the RCVA histogram is shifted towards the zero value and shows a steeper decrease from the no-change peak.
A change/no-change mask is derived by choosing and applying a thresholding procedure on the magnitude image (Bazi et al., 2007; Coudray et al., 2010; Otsu, 1979; Rosin, 2001). A primary goal of this study is to demonstrate the effectiveness of RCVA rather than to test thresholding methods. The thresholding technique selected for use had to meet some relatively straightforward requirements: it had to be fast, easy to implement, and robust against data range and large magnitude values. It also had to produce reasonable results. Prior tests revealed that the Otsu method best met these requirements. The binary mask generated based on the Otsu thresholding technique is also subsequently used for the direction image. From/to class labeling was not performed in this study, as our focus was on the change detection algorithm itself.

#### 2.2.3.4 Validation

Validation of change detection results can be challenging. Reference data is required for both image acquisitions and is often unavailable. When analyzing spontaneous or continuous changes, in particular, acquisition *in situ* ancillary data is sometimes not possible. In many change detection scenarios, archived images are the only available reference data and can only be utilized as before-event information. Backdating of reference data, therefore, can only be made based directly on the imagery itself. However, visual interpretation and relative performance evaluation of different algorithms can be performed in any case.
For this study, our validation procedure included three elements:

1) Results of the change detection procedures were visually interpreted and qualitatively evaluated;
2) The relative performance of CVA and RCVA was quantitatively compared; and,
3) Robustness of the two approaches was evaluated with the emphasis on dislocated pixels and geometric effects.

a) Visual interpretation
Images acquired by RapidEye and Kompsat-2 satellites were tested as input data for both CVA and RCVA. In addition to quantitative statistical measures, a credible visual impression is also an important measure of the performance of a change detection algorithm. It was therefore important to compare CVA and RCVA results visually. A common technique for visual comparison is to generate Red/Green/Blue (RGB) composite images with the change image rendered in red, the $t_1$ image in green and the $t_2$ image in blue (Castilla et al., 2009). In addition, displaying the near infra-red (NIR) image bands allows the visual evaluation to be more readily focused on changes related to vegetation as well as conversions to or from vegetation classes. When rendered in this band combination, no-change areas display as gray levels ranging from white to black. Gradual changes such as greening vegetation appear as shades of blue-green, and strong changes appear as either pink (reflecting increases in NIR response) or yellow (as NIR band response decreases). Spurious changes along edges of buildings can also be readily identified

in such RGB composites. Visual comparisons of CVA and RCVA magnitude and direction images reinforce the advantages and disadvantages of each change detection method. The scattergrams of CVA and RCVA results may be displayed as polar plots according to Bovolo et al. (2010).

b) Relative performance test of CVA and RCVA

For a relative performance estimation of the CVA and the proposed RCVA method we used the RCVA method as a benchmark and masked the result according to the Otsu threshold technique (Otsu, 1979). CVA and RCVA magnitude images have different data distributions (Fig. 2.2.4), and use of an identical threshold would not be optimal for both methods. We used the RCVA threshold as benchmark, applied it to the CVA result, increased the threshold stepwise to create a binary CVA magnitude mask for each step, and calculated the difference to the binary RCVA mask. Using this procedure, it was possible to identify the CVA result threshold that maximized true positives and minimized false negatives. This threshold is considered to produce the most comparable results, as the differences between CVA and RCVA masks are minimized. This threshold was then used for the CVA magnitude image to separate change from no-change areas. The magnitude masks with individual thresholds that represent highest correlation were used to qualitatively assess change detection performance. The RCVA results masked according to optimal thresholds could thus be compared with the adequate CVA result with the adjusted threshold. This test was repeated with the CVA threshold as the benchmark and the RCVA result being adjusted.

c) Test of spatial robustness

We proposed RCVA as a method of reducing spurious changes which originate from image acquisition geometry, sensor differences and associated effects (Section 2.2.1 and Section 2.2.2). Robustness is an important criterion in evaluating change detection techniques; a change detection method should not detect changes where none have occurred. As a test for spatial robustness the $t_2$ image was spatially offset, or dislocated by a single pixel in each direction and reproduced. This process generated a sequence of nine alternative $t_2$ images, including one duplicate of the original $t_2$ image. This duplicate image (the fifth produced in the series) has no x or y pixel offset and logically should include the fewest positional errors (Fig. 2.2.5). CVA and RCVA were then applied to each of the nine offset images paired with the original $t_1$ image.

The results of CVA and RCVA were then compared. This comparison was conducted in two ways. For the first test, radiometric normalization was implemented prior to image offset. In the second, the image was first geometrically offset and then radiometrically normalized.

In the first test, following normalization and dislocation, a threshold was calculated for the center (zero-dislocation) image change magnitude derived from both CVA and RCVA. Thresholds were then calculated for the results of CVA and RCVA using the eight offset images. These thresholds minimized differences from the center image masks, employing the stepwise procedure described above. This approach ensures that the differences between the results are due solely to the change detection procedure and are not caused by other processing steps. The change/no-change masks of the center magnitude images were subsequently compared to the masks of the

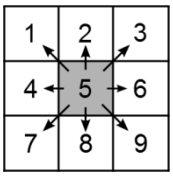


Fig. 2.2.5: Scheme of the dislocation experiment for the evaluation of spatial robustness. Numbers 1 to 9 indicate the nine dislocated (offset) $t_2$ pixels and their relative position in relation to the associated $t_1$ pixel shown in gray. "Offset" pixel 5 is expected to exhibit least positional error compared to the $t_1$ center pixel.

dislocated images showing the smallest deviation. For the second test, the $t_2$ image was dislocated and an additional series of nine offset images was derived. Radiometric normalization was then applied to each of the dislocated images and the center image, individually. Thresholds were calculated in the same manner as in the first experiment: thresholds of the center magnitude images were determined with the Ostu method, and the thresholds of the dislocated images were calculated stepwise to ensure the smallest deviation from the benchmark mask of the center image. This approach ensures optimal results for each image pair and accounts for differences that may result from the radiometric normalization procedure. Both tests were run for the RCVA mask and the CVA mask.

## 2.3 Data and Study Site

Our study site includes parts of the city of Cologne, North Rhine-Westphalia, Germany. The site covers an area of 8.25 x 4.25 km². It is composed of several land use types including densely populated urban areas, rural settlements, industrial districts, transportation infrastructure, parks and recreation areas, water bodies, and agricultural fields. This mixture of land cover types is very common in central Europe. The site was chosen primarily because ongoing change can be expected in such environments. Changes are expected in vegetation phenology, agricultural crop type, along with building construction, destruction and reconstruction. Even more subtle changes -- such as those caused by vehicle movement occurring between image acquisitions -- may be expected.

A RapidEye scene from May 24, 2009 and a Kompsat-2 image acquired on June 4, 2010 were used for this analysis. The sun-target-sensor geometries of the two images differ considerably. Although the image dates are close to the anniversary, the images show a two and a-half hour difference in acquisition time. In addition, orbital parameters of the two sensors vary: RapidEye orbits on a descending path, the path of Kompsat-2 is ascending. This leads to a rather complex sun-target-sensor constellation (Fig. 2.3.1). As shown in Fig. 2.3.1, distinct viewing angles θ and θ` and azimuth angles *a* and *a*` caused by the different overflight paths and times lead to dislocation of identical features and to different shadow proportions and positions. RapidEye and Kompsat-2 also have distinct spectral coverage and spatial resolution characteristics (Tab. 2.3.1). Correlated image bands with similar spectral definitions (blue, green, red, and near infrared) were selected for use in the analysis. The Kompsat-2 panchromatic band and the red-edge band of RapidEye were not utilized.

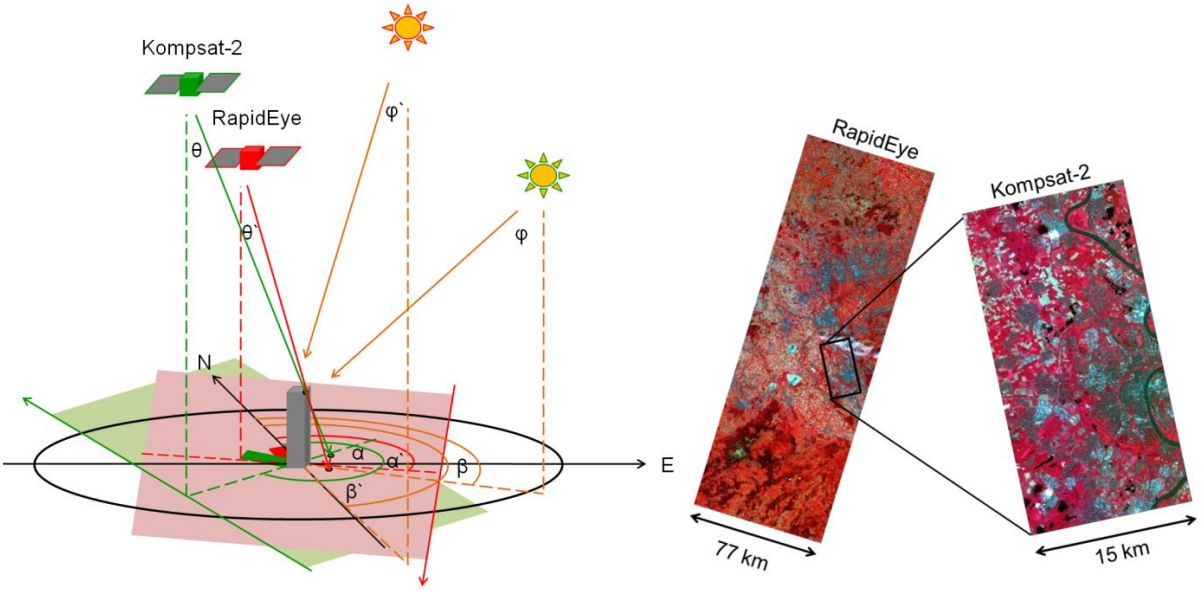


Fig. 2.3.1: Acquisition constellation of Kompsat-2 and RapidEye (at left) and corresponding scene ground coverage geometry (on right), displaying the RapidEye and the smaller Kompsat-2 footprints over the city of Cologne, Germany. Images are composites of RGB = NIR, red, green. Note the different viewing angles θ and θ`, sensor azimuth angles *a* and *a`* and the corresponding sun zenith angles φ and φ` and sun azimuth angles β and β`of the two sensors.

The images were orthorectified using a 10 m resolution DEM. The Kompsat-2 data were orthorectified at its original 4 m pixel size. To conduct a pixel-by-pixel comparison, the RapidEye image was resampled from the original 6.5 m spatial resolution to 4 m resolution by nearest-neighbor interpolation. As RCVA accounts for pixel neighborhood, it was feasible to reduce the pixel size of the RapidEye data. The difference in spatial resolution between the two images is less than the pixel size of the higher resolution Kompsat-2 data. Differences in spatial resolution are thus expected to be resolved when pixel neighborhood effects are considered. The RapidEye image acquired on May 24, 2009 was used as the $t_1$ "before-change" image. The June 4, 2010 Kompsat-2 image was used as the $t_2$ "after-change" image. The Kompsat-2 image was radiometrically normalized to the RapidEye image using IR-MAD. Test statistics of this

Tab. 2.3.1: Sensor and acquisition characteristics of Kompsat-2 and RapidEye.

| | **Kompsat-2** | **RapidEye** |
|---|---|---|
| date of acquisition | 2010/04/06 | 2009/24/05 |
| acquisition time (UTC) | 08:57:35 | 11:29:16 |
| off-nadir angle | 10,19° (east) | 8,28° (east) |
| orbit | ascending | descending |
| spatial resolution | 4 m (1 m pan) | 6,5 m |
| blue | 450-520[a] | 440-510[a] |
| green | 520-600[a] | 520-590[a] |
| red | 630-690[a] | 630-685[a] |
| red edge | - | 690-730[a] |
| nir | 760-900[a] | 760-850[a] |
| pan | 500-900[a] | - |
| data range | 10 bit | 12 bit |

* wavelength in nm

procedure confirmed high quality normalization for all multispectral bands resulting from the orthogonal linear regression.

## 2.4 Results

### 2.4.1 Visual Interpretation

Fig. 2.4.1 shows that CVA (Fig. 2.4.1c, g, k) and RCVA (d, h, l) results are generally correlated. Pink and yellow colors in the output image composites indicate distinct changes identified in the NIR image spectral bands. These can be interpreted as the effects of the construction and removal of buildings in the area. The CVA results also show pronounced pink and yellow edges along buildings. These are assessed as artifacts of the input images' varying spatial resolution as well as spurious changes resulting from differing image acquisition geometries. These spurious changes are largely eliminated with the RCVA method. This "cleaning" effect can be best observed in the dense urban area (Fig. 2.4.1k, l).

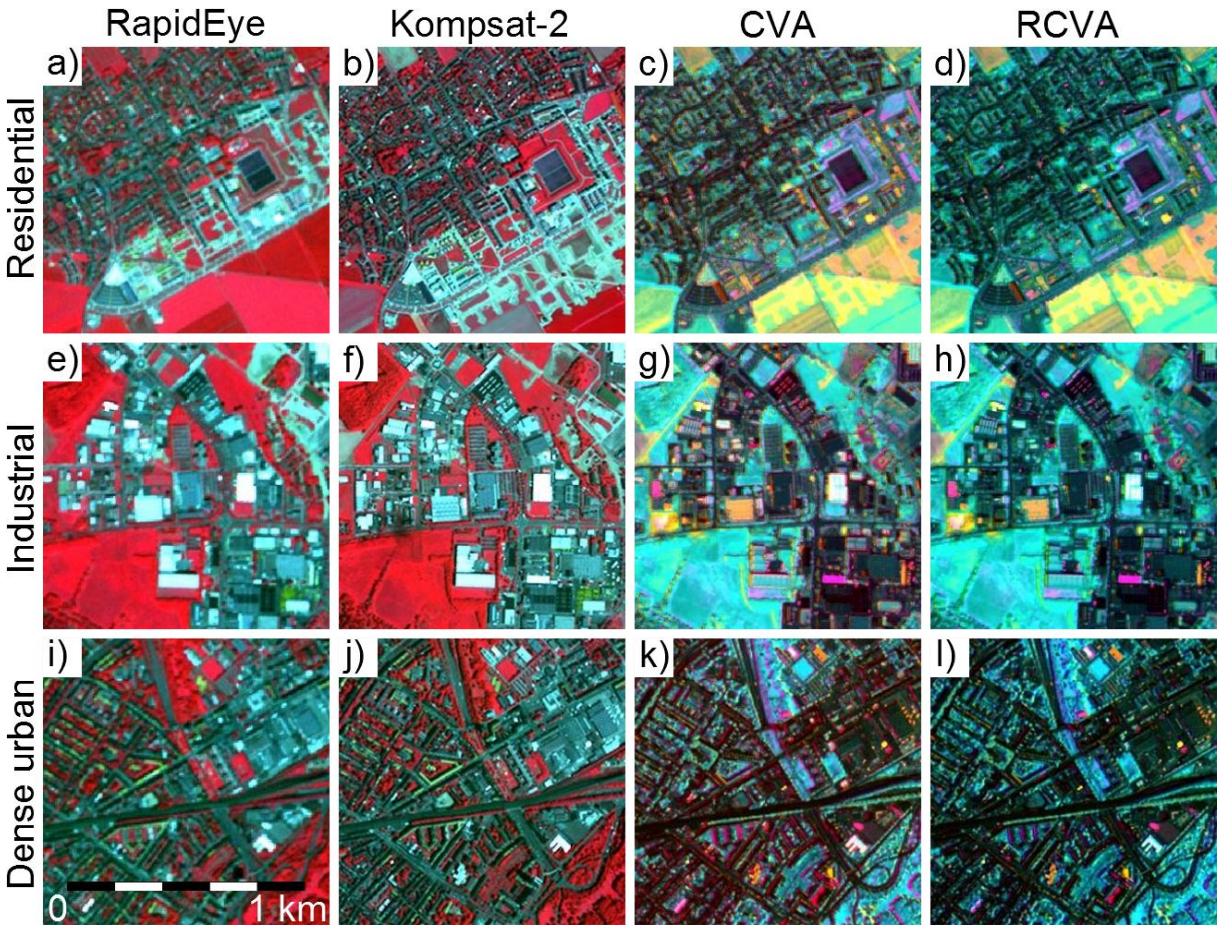


Fig. 2.4.1: From left to right: RapidEye 2009/24/05 image (NIR-red-green); Kompsat-2 2010/04/06 image (NIR-red-green); RGB images composited by rendering change magnitude in red, RapidEye NIR band in green and Kompsat-2 NIR band in blue; RGB composites with identical image bands used in CVA composite along with the addition of robust change magnitude results in red. Three different examples are presented: residential areas (Frames a-d), industrial district (Frames e-h), and dense urban area (Frames i-l).

Fig. 2.4.2 shows the magnitude (a, b) and direction (e, f) bands of CVA and RCVA masked by the threshold derived from the RCVA magnitude. Thus, identical change areas are ensured and only differences of magnitude and direction in the change areas are displayed. Very little difference is visible through simple visual comparison of the corresponding magnitude and direction images. However, the difference images between the CVA and RCVA results reveal slight differences (Fig. 2.4.2c, g). Distinct differences are displayed in bright tones. Differences are most evident along the edges of larger homogeneous objects such as agricultural fields. A profile along the red line is visualized in Fig. 2.4.2d, h, respectively. Change magnitude is a data dependent measure. Change magnitude values are influenced by data range, number of spectral bands, spectral band coverage, and the nature of change. If identical spectral bands are used to compute CVA and RCVA, the directional components of the change detection results should be similar. The difference image of RCVA and CVA (Fig. 2.4.2g) shows masked no-change areas in gray. Bright image tones indicate higher CVA direction values, dark tones correspond to higher RCVA direction values. Once again, the most distinct differences are apparent along edges of larger homogeneous objects. The profiles along the red lines shown in Fig. 2.4.2d, h confirm this visual interpretation.

The distribution of "no-change" pixels resulting from CVA and RCVA analyses are displayed as polar plots in Fig. 2.4.3. A comparison of these graphs shows that general distributions of CVA and RCVA pixels are similar in both results, although RCVA no-change pixels are clustered more at the plot origin than CVA no-change pixels.

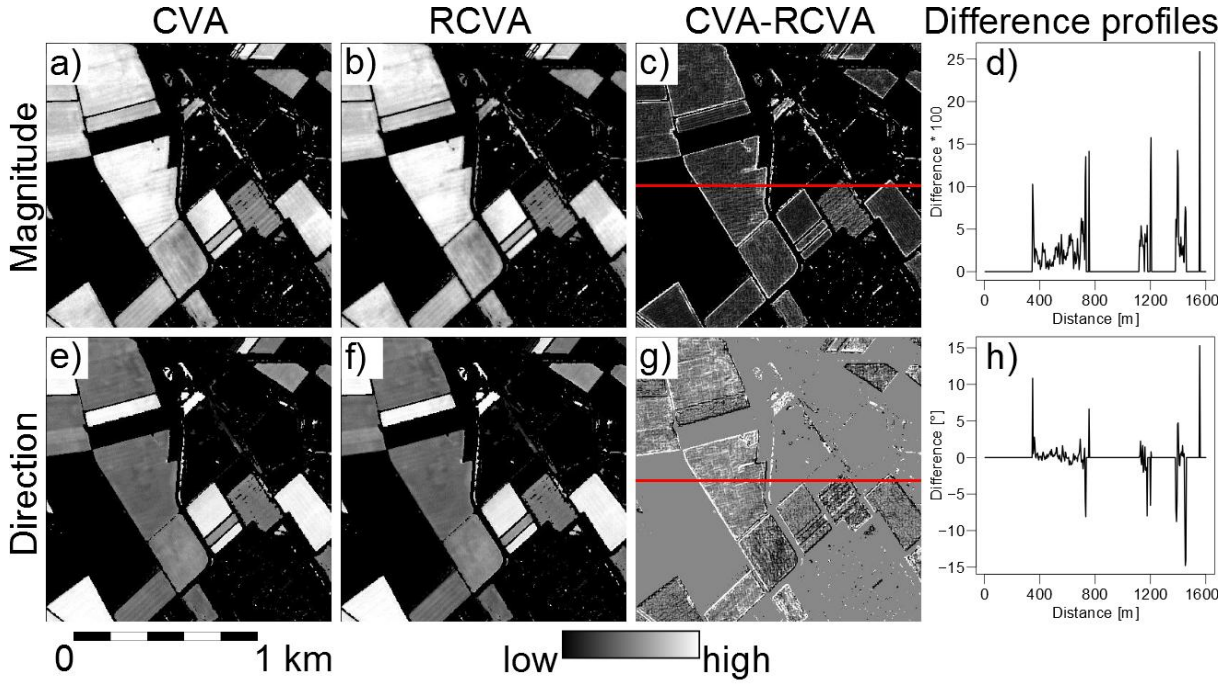


Fig. 2.4.2: Comparison of CVA and RCVA results. Magnitude images for CVA (a) and RCVA (b), the CVA / RCVA difference image (c), and profile of the magnitude difference image (d) indicated by the red line in (c). Direction images for CVA (e) and RCVA (f), the CVA / RCVA difference image (g), and profile of the direction difference image (h) indicated by the red line in g. In (g) masked zero values are shown in gray, positive change values are rendered in bright tones, negative values appear as darker tones.

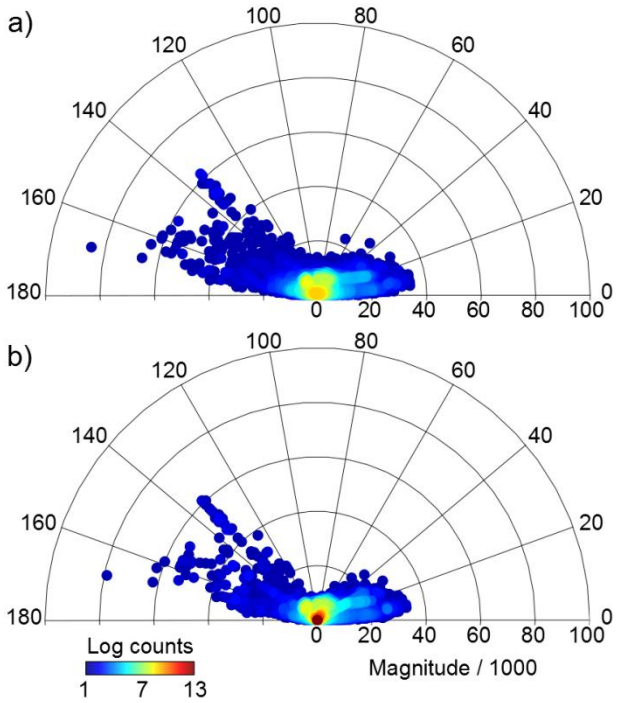


Fig. 2.4.3: Polar plots of a) CVA, and b) RCVA results.

### 2.4.2 Relative Performance Test of CVA and RCVA

RCVA detects change by calculating the least difference in a moving window. This results in a shift of the peak of the resulting change magnitude histogram towards zero (Fig. 2.2.4). The decrease of the histogram is much steeper than that of the CVA magnitude histogram. Accordingly, the change and no-change segments of the RCVA histogram show less overlap than in the CVA based histogram. The threshold of the RCVA magnitude is generally lower than that of CVA magnitude using identical input data.

The results of the stepwise threshold adjustment are shown in Fig. 2.4.4. In this figure, the red x indicates the CVA threshold value that produces the mask with least deviation from the RCVA benchmark mask – the optimal threshold was a value of 4550. This quantitative analysis showed that the CVA mask related to that optimal threshold had a relative error of 4.45%, with 2.10% false positives and 2.35% false negatives. In a second run CVA was used as benchmark and RCVA threshold was adjusted (Fig. 2.4.5). Least differences occurred with a threshold of 2900. The RCVA mask with least deviation from the CVA benchmark mask has a relative error of 6.09% with 0.69% false positives and 5.40% false negatives.

Visual interpretations of the adjusted threshold masks reveal that the mask based on RCVA depicts a more comprehensive result. Fewer true changes are missed using RCVA and spurious changes are minimized (Fig. 2.4.6).

In Fig. 2.4.6, frames a and b display rural subscenes from the study site. In this case, the RCVA mask was used as benchmark and CVA thresholds were adjusted. The CVA mask shown in Fig. 2.4.6c is the mask with least deviation from the benchmark RCVA mask (Fig. 2.4.6d). The large agricultural field shown in the subscene center is not adequately captured by the CVA result (Fig. 2.4.6c). In comparison, the RCVA mask accurately depicts the changes on the ground.

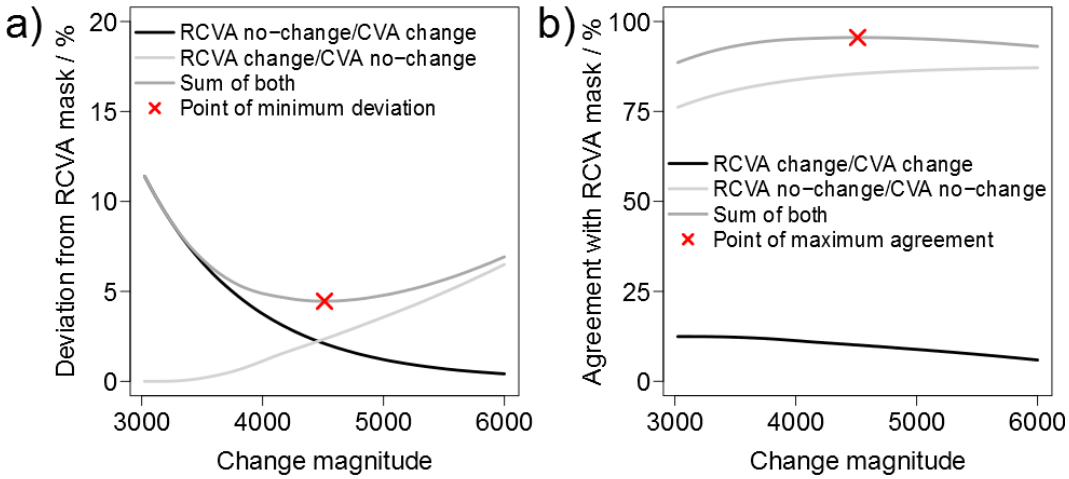


Fig. 2.4.4: Change magnitude histograms - threshold calculated for RCVA used as benchmark, CVA threshold stepwise adjusted. a) False positives and false negatives as a function of threshold. b) True positives and true negatives as a function of threshold. **X** in each plot indicates the threshold value where the mask with least deviation to the benchmark is created.

An industrial location is shown in Fig. 2.4.6e and f. For this setting, several spurious changes appear within the CVA-based mask (Fig. 2.4.6g). Spurious changes are largely removed in the RCVA-based mask, while real ground changes are identified (Fig. 2.4.6h).
In Fig. 2.4.7 the same subscenes are presented, with the CVA based threshold as benchmark and the RCVA threshold being adjusted. The CVA results in the rural subscene (Fig. 2.4.7a) and the industrial example (Fig. 2.4.7c) appear more credible and sound than the CVA results shown in Fig. 2.4.6c and g, and fewer true ground changes are missed. However, this improvement is at the expense of additional spurious changes. The RCVA results for the rural and industrial examples illustrated here are comparable to those shown in Fig. 2.4.6; only a small number of additional spurious changes appear. These conclusions are significant when the results of the spatial robustness test are visually interpreted.

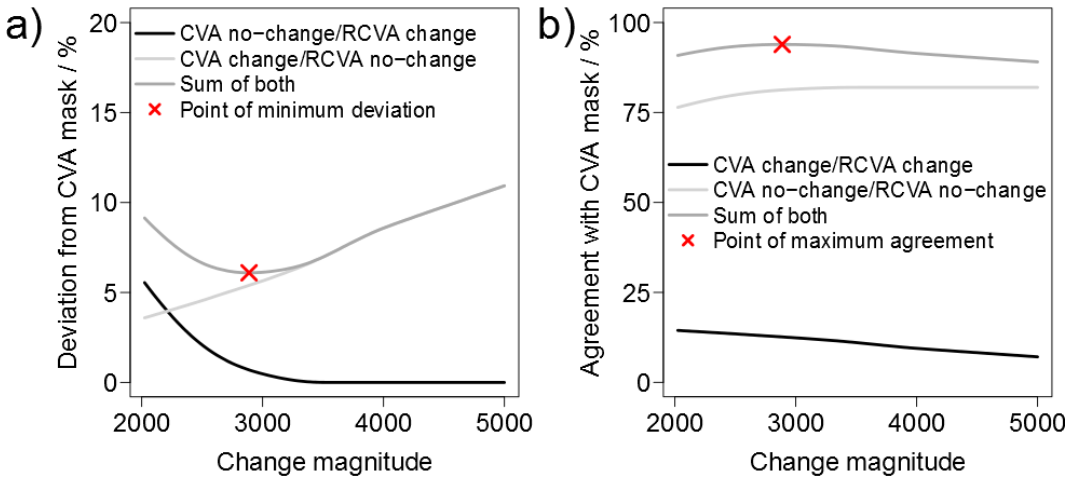


Fig. 2.4.5: Change magnitude histograms - threshold calculated for CVA as benchmark, RCVA threshold stepwise adjusted. a) False positives and false negatives as a function of threshold. b) True positives and true negatives as a function of threshold. **X** in each plot indicates the threshold value where the mask with least deviation to the benchmark is created.

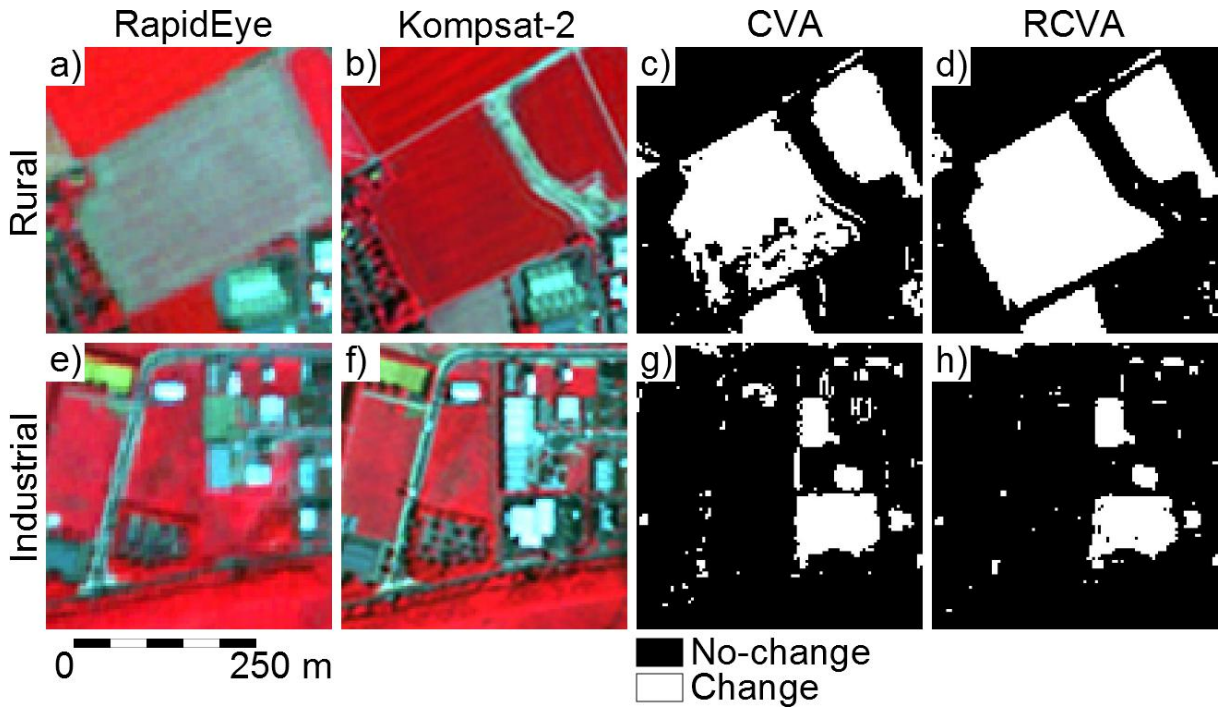


Fig. 2.4.6: CVA and RCVA results after adjusting CVA threshold to RCVA result. Input images from RapidEye (a, e) and Kompsat-2 (b, f). All subscenes displayed as RGB = NIR-red-green. CVA mask (c, g); RCVA mask (d, h). Masks are binary with white colors indicating change features; black denotes no-change areas. In contrast to CVA, RCVA more completely captures the changed agricultural field and reduces spurious changes in the industrial example.

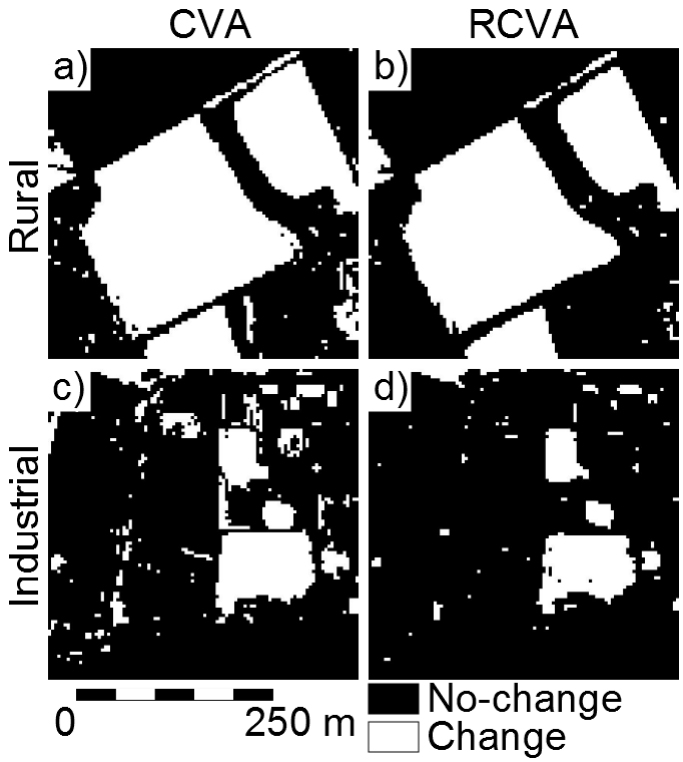


Fig. 2.4.7: Comparison of CVA and RCVA results (binary masks) after adjusting RCVA threshold to CVA result. Subscene examples are the same as those in Fig. 2.4.6.

### 2.4.3 Test of Spatial Robustness

Fig. 2.4.8 displays histograms of CVA and RCVA change magnitude along with thresholds for each of the dislocated images. The CVA mask of the original Kompsat-2/RapidEye image pair was used as benchmark. In Fig. 2.4.8, frame pairs a/b and c/d present differences between the CVA and RCVA change magnitude histograms. Histogram frame pairs a/c and b/d show the effects of image dislocation before and after radiometric normalization. It can be clearly seen that differences between CVA and RCVA are much more significant than the differences that result from image dislocation before or after normalization.

CVA and RCVA change magnitude histograms generally differ in shape. RCVA thresholds are also lower than those of CVA. Highest and lowest RCVA threshold values are similar; CVA thresholds show a wider distribution. Similar conclusions may be drawn from the results obtained using the RCVA mask as benchmark (Fig. 2.4.9). RCVA thresholds are similar, CVA thresholds are more varied. Overall, no significant effects of applying radiometric normalization after dislocation can be observed.

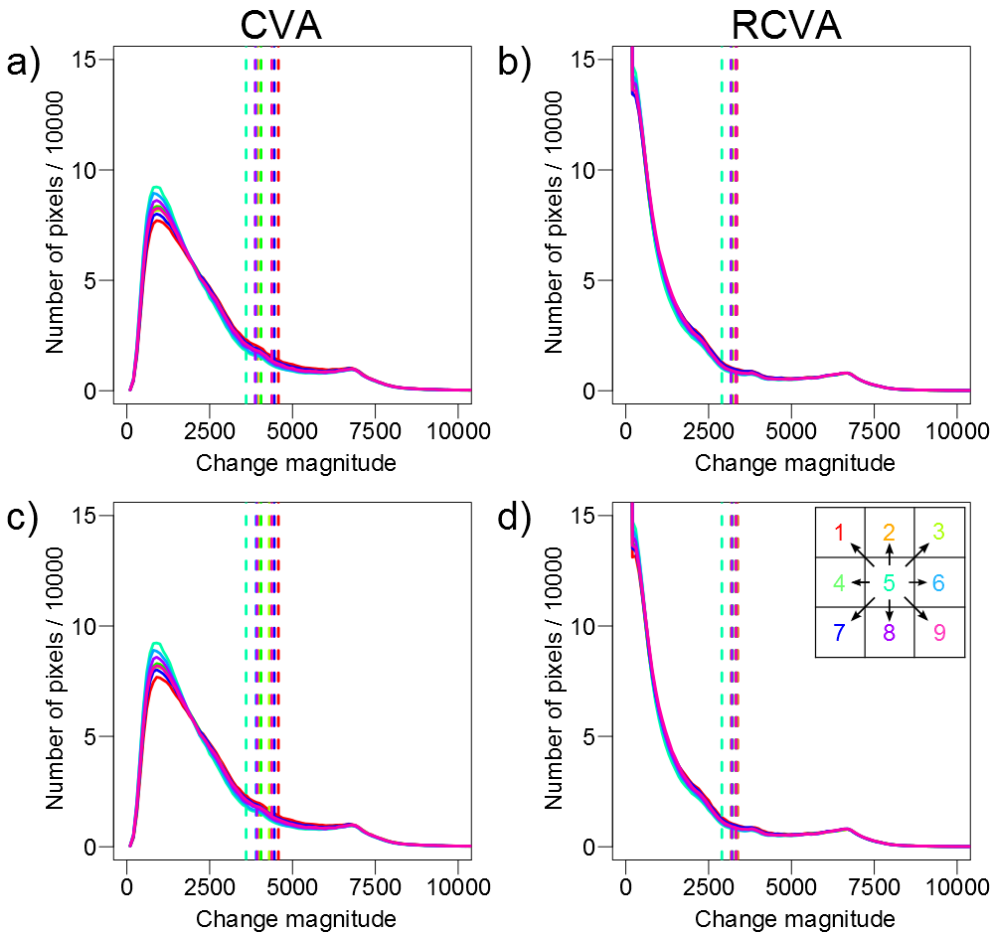


Fig. 2.4.8: Change magnitude histograms for each dislocated image. Frames a and b show CVA and RCVA results when the Kompsat-2 image is first radiometrically normalized to the RapidEye image and subsequently dislocated one pixel in each direction. Frames c and d show CVA and RCVA results when all images are radiometrically normalized after dislocation. Thresholds are adjusted to the CVA mask of the central pixel. The small diagram in upper right of d refers to the coherent pixel dislocation scheme described in Fig. 2.2.5.

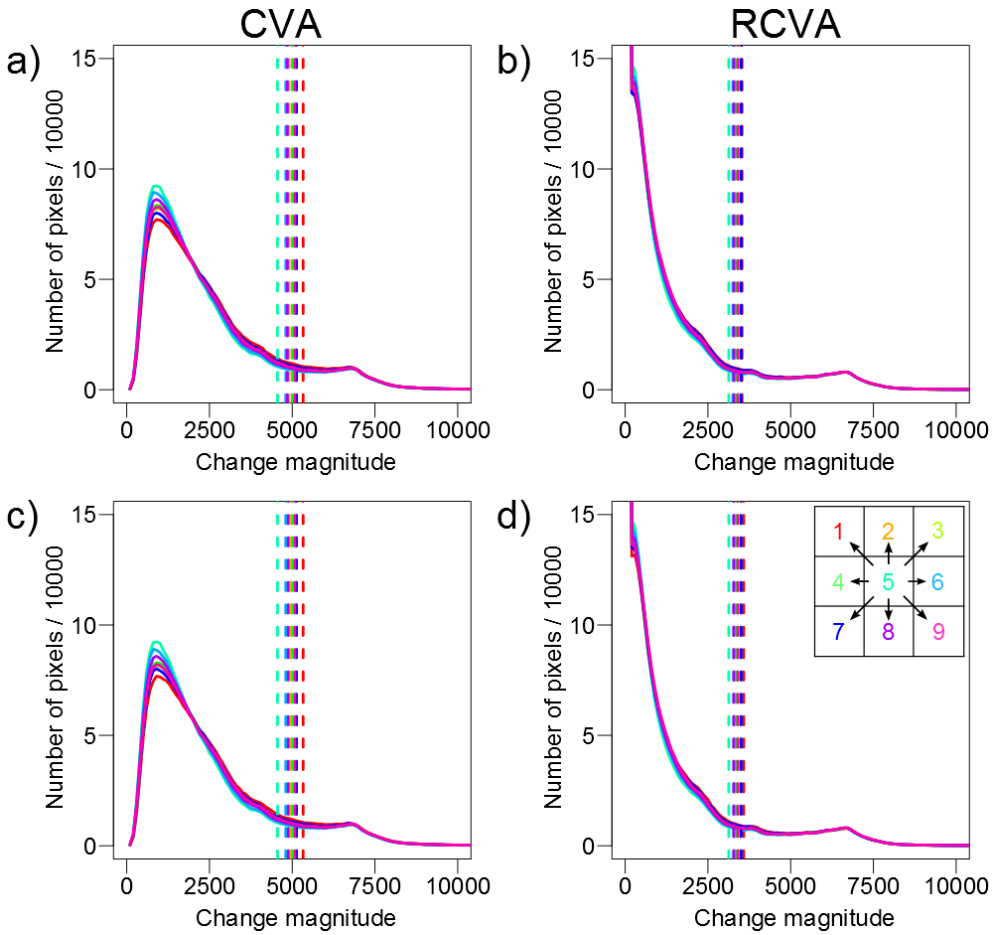


Fig. 2.4.9: Change magnitude histograms for each dislocated image. Frames a and b show CVA and RCVA results when the Kompsat-2 image is first radiometrically normalized to the RapidEye image and subsequently dislocated one pixel in each direction. Frames c and d show CVA and RCVA results when all images are radiometrically normalized after dislocation. Thresholds are adjusted to the RCVA mask of the central pixel. The small diagram in upper right of d refers to the coherent pixel dislocation scheme described in Fig. 2.2.5.

Fig. 2.4.10 presents the change area detected by CVA and RCVA for all dislocated images as well as for radiometric normalization both before and after dislocation. Again, it is clear that radiometric normalization after image dislocation leads to nearly identical results to those yielded by normalization before dislocation. The results adjusted to RCVA show uniformly lower change area percentages than the results adjusted to CVA. As shown by the black and gray bars of Fig. 2.4.10a and b, RCVA results adjusted to RCVA are only slightly lower than the RCVA results adjusted to the central CVA result (mean values = 12.18% and 12.67% respectively). The dark red and red bars of both frames indicate that CVA results adjusted to RCVA are considerably lower (mean value = 11.24%) than those adjusted to the central CVA result (mean = 15.91%). In addition, CVA results show considerably higher standard deviations in all cases than RCVA. This indicates that image dislocation affects RCVA results less than CVA results. The amount of change identified in each dislocated image is equal to or less than in the central image for both RCVA and CVA.

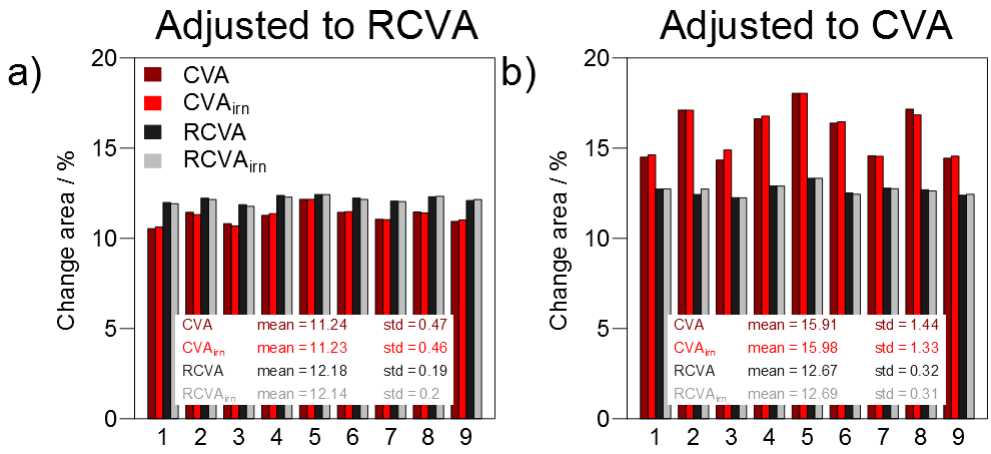


Fig. 2.4.10: Change detection results for each of the images. All thresholds were adjusted to that calculated for Number 5 image of expected best geometric fit. a) RCVA as benchmark; b) CVA as benchmark. Results for both evaluated scenarios are shown: radiometric normalization to RapidEye image performed prior to image dislocation and following dislocation. Subscript "irn" in legend (coded to red and gray bars) denotes individual radiometric normalization of each dislocated image. dark red and black bars not coded with the "irn" subscript indicate radiometric normalization applied only to the center image before dislocation.

Fig. 2.4.11 graphs the performance of CVA and RCVA for the dislocated images by error type. False positives (no-change seen as change), false negatives (change seen as no-change), and overall error (the sum of false positives and false negatives) are all shown. RCVA results are uniformly superior in avoiding false positives over CVA results. RCVA results adjusted to the RCVA benchmark show slightly more false positives than RCVA results adjusted to the CVA benchmark. For CVA, this effect is inverse (Fig. 2.4.11a and b). Analysis of false negative errors reveals that both CVA and RCVA show increased false negative errors when adjusted to the CVA benchmark than when adjusted to the RCVA benchmark (Fig. 2.4.11c and d). Regarding spatial robustness, Fig. 2.4.11e and f show that RCVA features less variation among the dislocated images than CVA. Overall errors are greater for both RCVA and CVA when adjusted to the CVA benchmark. As shown in Fig. 2.4.11a-d, performing radiometric normalization after dislocation rather than before has only minor effects on RCVA results. In some cases the results are slightly weaker than in the test with the radiometric normalization applied prior to dislocation. These differences are slightly more pronounced for CVA. In this case, $CVA_{irn}$ has a higher rate of false positive error. This increase is offset somewhat by fewer false negative errors when evaluated against the CVA with radiometric normalization prior to dislocation. The summary overall error rate is similar for both strategies, in which radiometric normalization is performed either before or after image dislocation (Fig. 2.4.11 e, f).

The overall agreement between the results of the change detection procedure is shown in Fig. 2.4.12. When RCVA is used as benchmark, RCVA yields higher agreement values than CVA. RCVA values range from 95.9% to 97.3% among the nine dislocated images. In comparison, CVA values are between 93.5% and 94.2%. Agreement values for the central images in the RCVA and CVA tests show an overall agreement of 100% for RCVA and 95.6% for CVA.

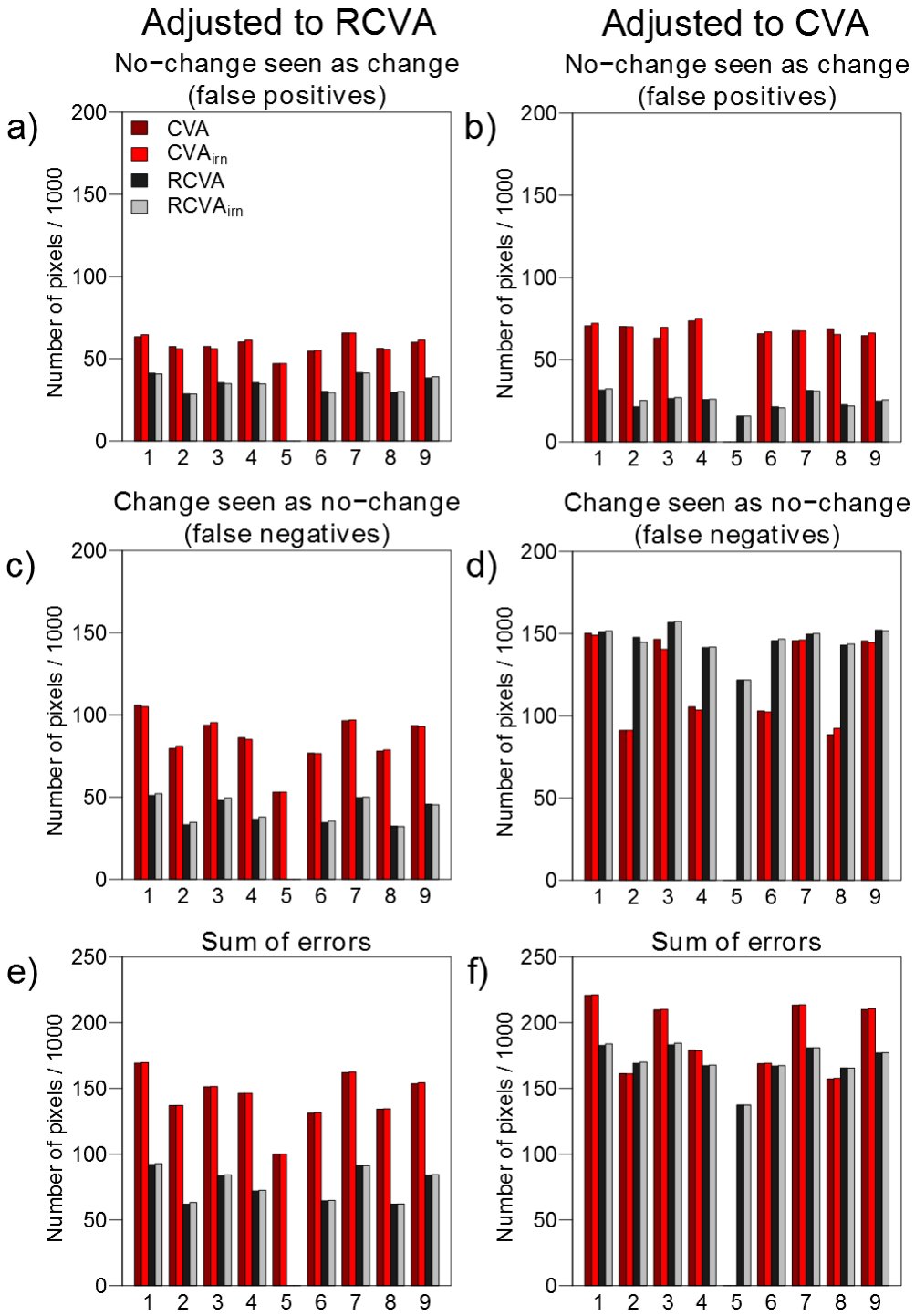


Fig. 2.4.11: Change seen as no-change, no-change seen as change, and sum of both errors in relation to the centered image. Frames a, c and e display results with RCVA as benchmark; frames b, d and f with CVA as benchmark.

The results of the test with CVA as benchmark are closer. RCVA overall agreement among the dislocated images ranges from 91.9% to 92.6% (with a value of 93.9% for the central image). CVA overall agreement ranges from 90.2% to 93.0% for the dislocated images (100% for the central image). Differences in the results of radiometric normalization before and after dislocation are not significant.

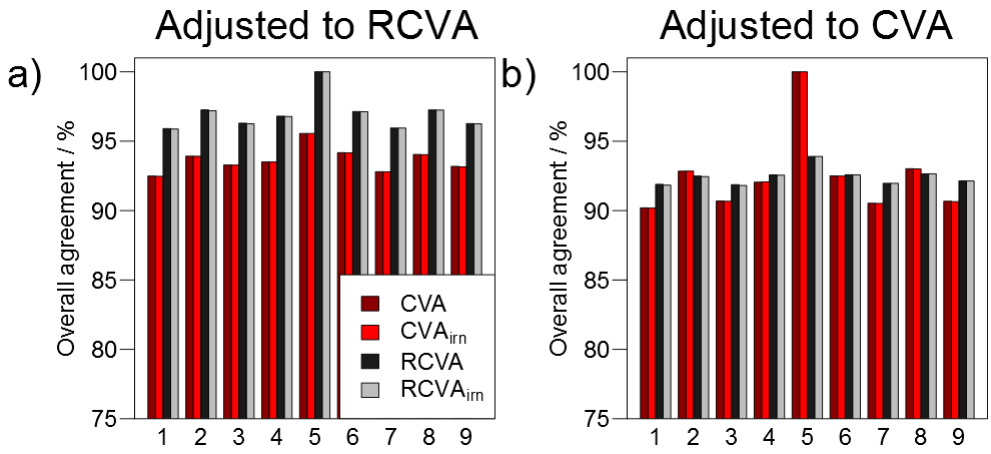


Fig. 2.4.12: Overall agreement between the results of change detection performed on image Number 5 (expected best geometric fit image) and the dislocated images. a) Images adjusted to RCVA mask; b) Images adjusted to CVA mask.

RCVA results reveal less sensitivity of the approach against dislocation than CVA. The error rate is reduced considerably in RCVA compared to CVA, and the variance is much lower among individual RCVA results. Analysis of Fig. 2.4.10 - Fig. 2.4.12 shows that the process of image dislocation introduces additional changes in the detection procedure, and also reveals that the RCVA approach yields less variation resulting from dislocation than CVA.

## 2.5 Discussion

### 2.5.1 Discussion of Methods

It is well known that CVA (and RCVA) is susceptible to radiometric and geometric preprocessing (Bovolo and Bruzzone, 2007; Coppin et al., 2004; Johnson and Kasischke, 1998). By using RCVA we addressed inaccuracies in geometric preprocessing accompanied by the effects described in Section 2.2.1. For the purpose of change detection, absolute radiometric preprocessing methods are not strictly required and were not implemented here. Prerequisite of most methods, including CVA and RCVA, is the "common radiometric scale" suggested by Song et al. (2001).

A common radiometric scale can be obtained using the fully automated IR-MAD procedure and this procedure was implemented here. Statistical analysis of the IR-MAD normalization procedure indicated a suitable result. Marpu et al. (2011) presented a method to eliminate very distinct changes prior to radiometric normalization and this method may be utilized when the typical IR-MAD procedure fails to produce reasonable results.

Absolute atmospheric correction methods produce results scaled to reflectance values with a data range between 0% and 100%. Use of these methods would prevent the magnitude histograms from plotting larger values. This issue may be adequately addressed by choosing a thresholding procedure which is not sensitive to large magnitude values. In this study we normalized the Kompsat-2 image to RapidEye. Performing this normalization in reverse would produce similar results, since IR-MAD is a linear method.

Since the aim of the study is to provide an automatic change detection method, the thresholding procedure is also automatic. Results of the thresholding procedures are different for RCVA and

CVA because the Otsu thresholding method is based on the statistics of the change magnitude histograms. As shown in Fig. 2.2.4, the CVA and RCVA histograms have different distributions and the thresholds cannot be directly compared.
The stepwise threshold adjustments were applied to assure results that show highest possible agreement. Fig. 2.4.4 and Fig. 2.4.5 show the effect of increasing thresholds on the change detection result. We used both RCVA and CVA as benchmarks to prevent bias caused by optimal thresholds for only one method. The thresholding itself is a crucial step in change detection (Bruzzone and Prieto, 2000) and, of the numerous thresholding methods that have been developed, we evaluated four for the use in this study. These were: the EM algorithm (Bazi et al., 2007), the T-point method (Coudray et al., 2010), the Rosin method (Rosin, 2001), and the Otsu method (Otsu, 1979). The Otsu method was selected, principally due to its stability and insensitivity to large magnitude values. Large magnitude values often occur when using image data with a large data range (such as the 16-bit data used here), and they often lead to the failure of thresholding methods (Coudray et al., 2010). Alternate thresholding methods may perform with equal reliability when applied to different datasets with smaller data ranges.

### 2.5.2 Discussion of Results

Another goal of the RCVA approach was to generate magnitude and direction components comparable to CVA, accompanied by a reduction in spurious changes. The visual impression of the results presented in Fig. 2.4.1 reveals that RCVA produces more credible results than CVA by reducing spurious changes. Fig. 2.4.2 indicates that magnitude and direction of CVA and RCVA are largely similar. A closer look at the difference of CVA and RCVA magnitude reveals that the greatest differences occur at the margins of larger homogeneous objects. This is expected since RCVA is supposed to eliminate spurious changes along edges of homogeneous objects. In the difference image profile all values are positive; pixels masked as no-change are zero. This also can be expected, since RCVA values tend to be lower due to the calculation of least differences in a moving window.
In some cases the effect along feature edges leads to the reduction of the size of a changed object. Thus, a minimum size of the real changed object is required in order to be detected by RCVA. This minimum size cannot be quantified from this study. But it is clear that an area at least equal in size to the window used for the difference calculation (3x3 pixels in this study) must be affected by real change on the ground in order to accurately be depicted as such through the detection process. Ground change areas smaller in size than the moving window used to calculate differences within the imagery will be integrated with non-affected pixels in the search window.
RCVA will occasionally fail to detect small change areas that are narrow or linear in shape. This effect is intended, however, in the case of spurious changes along buildings or trees. This edge effect also includes a directional component (Fig. 2.4.2e-h). The general appearance of magnitude and directional components of RCVA and CVA is virtually identical; the tendency of RCVA to suppress changes along object/feature edges is the significant difference. As demonstrated in Section 2.2.2 geometric and associated effects can only be resolved when high spatial resolution data are used. Many nadir operating satellite systems (Landsat is an example) have only moderate

spatial resolution, especially when compared to features and objects commonly found in human environments. Thus, the effects discussed in Section 2.2.1 may not be adequately addressed by considering pixel neighborhood when using data of moderate or coarse spatial resolution. Effects of ground object geometry will result in mixed pixels of varying composition. It was beyond the scope of this study to determine if there exists a threshold pixel size where the RCVA approach is no longer superior to CVA.

Significantly, the results of the CVA and RCVA performance tests reveal figures relative between the two approaches. Since our hypothesis states that RCVA reduces spurious changes this method is assumed to yield very few false positives when adjusted to the CVA mask. This is notable because the RCVA threshold has to be lowered in order to achieve optimal adjustment to the CVA mask. Lowering the threshold leads to an increase in the identification of areas as changed. When CVA is adjusted to RCVA, the CVA mask threshold has to be increased. This threshold increase leads to a reduced number of false positives at the expense of an increase in false negatives. In our study, we found an increase, rather than a reduction, in the percentage of false positives when CVA threshold is adjusted.

The effect of RCVA compared to CVA is largely dependent upon three factors: 1) the spatial resolution of the data; 2) the extent of distortions between the images; and, 3) the window size used for the difference calculation. It is not possible to completely quantify the effects introduced by ground feature/object geometry. The impact of subpixel location errors, for example, remains unknown. Even known effects such as horizontal layover can only be quantified adequately when very high resolution DSMs are available for both image acquisition dates. It is therefore both appropriate and practical to choose the window size based on the spatial resolution of the data.

At times, the accuracy required of a change detection methodology is dependent on the user's perspective. Depending upon the aim of an individual study, quality evaluation may be subjective (Hecheltjen et al., 2014). Fundamentally, however, performance metrics should be based on the detection of real ground changes and the simultaneous suppression of spurious changes. As can be seen from Fig. 2.4.6 and Fig. 2.4.7, RCVA produces more credible change/no-change masks that better support visual interpretation than those of CVA, especially when homogeneous objects are of interest.

The shape of the RCVA magnitude histogram indicates that its change and no-change marginal distributions are more distinct than those of CVA. The Fig. 2.4.3 scattergrams confirm that the no-change pixels of RCVA are more aggregated at the origin of the polar plots, while CVA no-change pixels are more widely distributed. The overlap of the change and no-change marginal distributions is also reduced with RCVA. This in turn increases their separability and makes the RCVA magnitude histogram less sensitive to thresholding. This is confirmed by Fig. 2.4.6 and Fig. 2.4.7, where RCVA results may be seen to be similar for the two tests that separately compared the use of RCVA and CVA as benchmark. In contrast, CVA results differ considerably, thus indicating more susceptibility to thresholding.

The labeling of from/to classes is an additional step in the change detection process. From/to labeling requires accurate information regarding the identification of the relevant classes during at least one point in time. However, the change result in the polar domain can be aggregated into a number of change clusters. Each of these clusters indicates a different type of change, with

specific identification being optional. Bovolo et al. (2010) presented an automated method to label changes based on CVA. This method takes advantage of the EM algorithm, which operates under the assumption that different changes are represented by different clusters in the masked directional component. Since the masked CVA and RCVA results are assumed to be similar in direction (Fig. 2.4.2), the labeling of both results using this technique should lead to similar labeling results.

Final CVA and RCVA performance may be seen in Fig. 2.4.11 and Fig. 2.4.12. RCVA results in fewer errors and better agreement with the benchmark in all plots except Fig. 2.4.11d. Fig. 2.4.10d displays false negatives -- changes in the CVA benchmark result that were identified as no-change. This outcome must be evaluated carefully, because RCVA is intended to reduce spurious changes which are components of the CVA benchmark mask.

Spatial robustness is an important performance measure since we assume geometric effects between the two images used for bi-temporal change detection. The dislocation experiment used here also accounted for radiometric normalization. We conducted a twofold experiment, first dislocating the normalized image, thereby assuming best common radiometric scale. Second, we normalized each of the nine images after dislocation. The central image is radiometrically equal to the ones used in the first experiment. All the others are normalized as if the dislocated image would have best geometric fit. This results in small differences of the DNs of corresponding pixels in the dislocated images. However, the results shown in Fig. 2.4.10 - Fig. 2.4.12 reveal no noticeable differences between the two experimental approaches. This confirms the assumption that the pixels used for radiometric normalization are part of larger homogeneous objects whose dislocation has only minor influence on the normalization procedure. Differences between the resulting magnitude histograms and corresponding thresholds are insignificant and cannot be readily identified on Fig. 2.4.8 and Fig. 2.4.9.

The spatial robustness and the dislocation effect can be quantified from Fig. 2.4.10 - Fig. 2.4.12. If pixel dislocation had no effect on the change detection process, the bars in each plot would be identical among the nine results of each method. Instead, the graphics show considerable differences among the plots, and these differences are more pronounced for the CVA results. These findings confirm higher spatial robustness of RCVA compared to CVA. The particular "zigzag" pattern of the results (best seen in Fig. 2.4.11e) is of special interest. Pixels 1, 3, 7, and 9, oriented diagonally from the centroid Pixel 5, show the largest errors. This may result from the fact that the dislocation of the diagonal image pixels corresponds to a larger ground distance than that of the perpendicular pixels. As the moving window centeroid, Pixel 5 is assumed to have least positional errors and is expected to present smallest positional errors. This is confirmed for both RCVA and CVA in all test runs.

## 2.6 Conclusions

RCVA is an innovative change detection method that can reduce the false detection of spurious changes in imagery acquired under differing sun-target-sensor constellations. The RCVA approach described and tested here shows clear advantages when used with high spatial resolution data or data acquired by sensors with different spatial resolution. From theoretical

considerations alone it is assumed that change detection algorithms which account for pixel neighborhood effects are better suited to manage all error sources than those that do not. This assumption was confirmed by several tests. The RCVA method is focused on high spatial resolution data acquired under substantially varying conditions. RCVA can be applied to any multi-channel optical image data, including data with particular differences in spatial resolution characteristics. Further improvements to the RCVA approach may be considered. These include the precise quantification of surface heights before RCVA, as well as optimizing the selection of the spectral difference windowing function. Adaptive windowing size or spatial weighting may further reduce errors in heterogeneous areas with exceptionally dynamic surface profiles. Exploring issues of spatial resolution to develop information on where RCVA performance converges to that of CVA would also be an important topic for future research.
This study confirms the effective performance of RCVA. From the findings it can be concluded that the RCVA approach has several advantages. Specifically, RCVA:

- is superior to standard CVA in terms of the detection of real changes on the ground and the elimination of spurious changes,
- is robust against varying change thresholds,
- is robust against positional errors,
- reliably produces credible results that satisfy the user's perception.

RCVA can be useful in a number of change detection applications, including urban analyses, forestry, agriculture, and other general environmental studies that can utilize high spatial resolution imagery.

## Acknowledgments

This study was conducted within the ENVILAND2 research project. ENVILAND2 was sponsored by the Space Agency of the German Aerospace Center (DLR) with federal funds of the German Federal Ministry of Economics and Technology on the basis of legislation by the German Parliament grant no. 50 EE 0844 - 50 EE 0847. RapidEye data were provided by the RapidEye Science Archive RESA within the AO RESA-ENVILAND2, project ID 272. Kompsat-2 data were provided by the European Space Agency (ESA) within the AO DESC3295. Preprocessing was performed to large extends with the EnvilandVision software that was developed within the ENVILAND2 consortium (Jena-Optronik GmbH, Jena, Germany, Friedrich-Schiller University, Jena, Germany, and Zentrum für Bild- und Signalverarbeitung e.V., Ilmenau, Germany).

# 3 Change Detection of Forest Cover using the Earth Explorer Landsat Archive

## 3.1 Study Site and Data

### 3.1.1 Study Site

The studies conducted within this section of the present PhD thesis were undertaken on a test site on Vancouver Island, British Columbia, Canada. Most of the area is composed of forested land with some areas of old-growth forest that have been entitled National Parks or Provincial Parks due to their unique value as temperate rain forests. Most parts of the island, however, are not protected. The Vancouver Island forests are a major resource for the Canadian timber and paper industry. Thus, there is a long history of forest use and management making the area an interesting study site. Vancouver Island is entirely located within the Level I Ecoregion of North America "Marine West Coast Forests" (CEC, 1997). At Level II Vancouver Island refers to the same class "Marine West Coast Forests". The western part of the island covers Level III ecoregion "7.1.5 Coastal Western Hemlock-Sitka Spruce Forests" whereas the eastern part of the island covers Level III ecoregion "7.1.7 Strait of Georgia/Puget Lowland" (CEC, 1997). The ecosystems levels are hierarchical organized with Level I having the smallest scale and Level III showing the most details. Vancouver Island exhibits a unique temperate rain forest. Hamann et al. (2005) used botanical sample data to model tree species distribution in British Columbia. Their results confirm the dominance of western hemlock (*Tsuga heterophylla*), western redcedar (*Thuja plicata*), Amabilis fir (*Abies amabilis*), Douglas-fir (*Pseudotsuga menziesii*), yellow-cedar (*Chamaecyparis nootkatensis*), lodgepole pine (*Pinus contorta*), grand fir (*Abies grandis*), and Sitka spruce (*Picea sitchensis*) in the southern part of Vancouver Island (Hamann et al., 2005; Pojar et al., 1991). Red alder (*Alnus rubra*) is a widespread species on logged or otherwise disturbed sites (Pojar et al., 1991). Western white pine (*Pinus monticola*), bigleaf maple (*Acer macrophyllum*), mountain hemlock (*Tsuga mertensiana*), pacific yew (*Taxus brevifolia*), Sitka willow (*Salix sitchensis*), Scouler's willow (*Salix scouleriana*), and Shining willow (*Salix lucida*) are widespread tree species on southern Vancouver Island with less importance (Hamann et al., 2005).

From a remote sensing perspective the area has some characteristics that make it a perfect research object. These characteristics include, for example, pronounced topography, a strong climatic gradient, and complex ecosystem dynamics that will be described subsequently. Since the opening of the archive in 2008, all Landsat images ever taken have been thoroughly integrated in catalogues such as the USGS Global Visualization Viewer (http://glovis.usgs.gov/) and Earth Explorer (http://earthexplorer.usgs.gov/). At the time of beginning of this research the integration process was not yet completed except for Northern America. Due to the consistent pre-processing of the data in the catalogs, the exploration of large datasets is facilitated.

The study site (Fig. 3.1.1) was chosen in the overlapping region of two World Reference System WRS-2 tiles with path/row indices p048r026 and p047r026 for the following reasons: The achievement of the objectives of this section requires temporal coverage of more than one decade and spatial coverage of two neighboring WRS-2 tiles to increase the density of the time

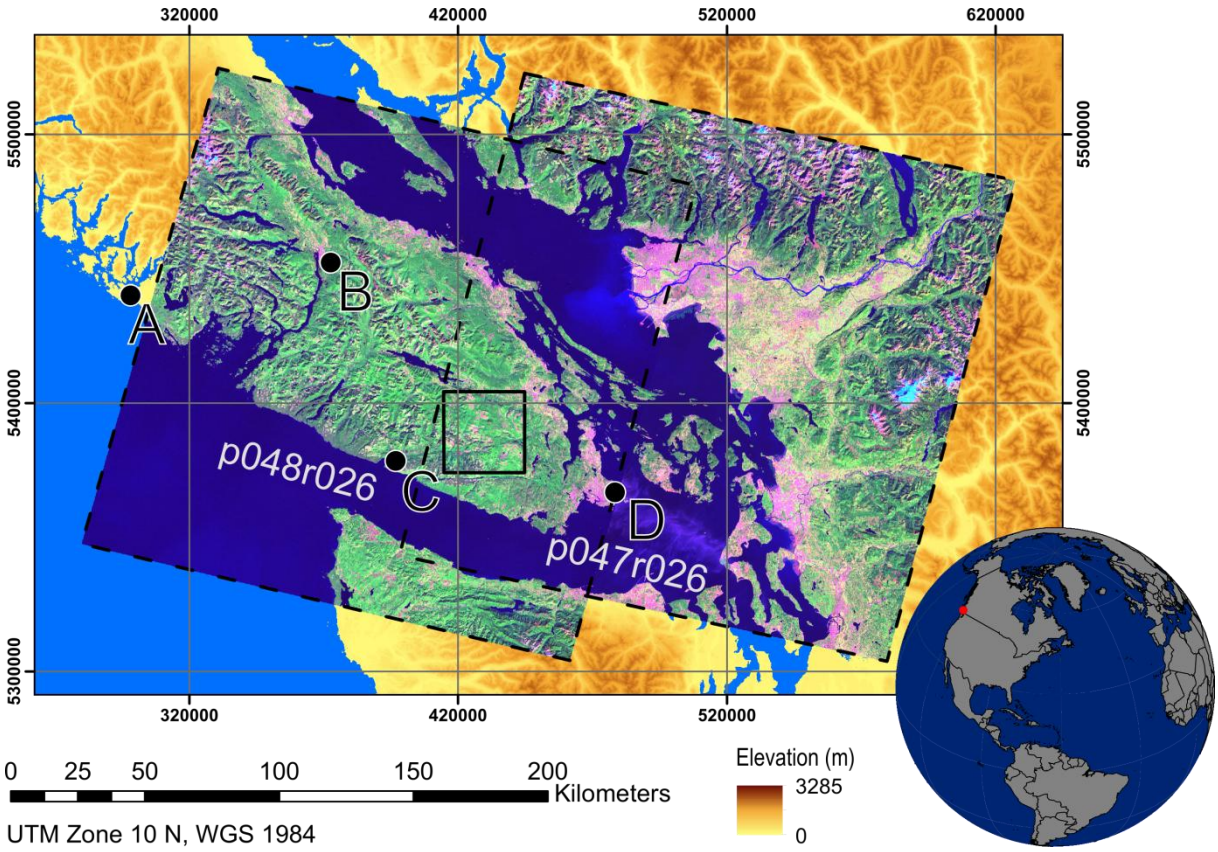


Fig. 3.1.1: Study site (black solid quadrangle) in the overlapping part of two neighboring WRS-2 tiles (p048r026 & p047r026, black dashed line). The Landsat image is displayed in RGB 7-4-2. The image background shows the SRTM DEM with 90 m resolution. A, B, C, and D refer to the climate stations of Tofino Airport, Port Alberni/Cox Lake, Port Renfrew, and Victoria/Phyllis Street.

series. This region in the south-eastern part of the island is also covered by the Shuttle Radar Topography Mission (SRTM) X-band acquisitions which were used to generate a digital elevation model (DEM) with 30 m spatial resolution. The study site has an area of 1000 x 1000 pixels (i.e. 30 x 30 km²) with elevation ranging from sea level to heights of about 1135 m. The area shows a

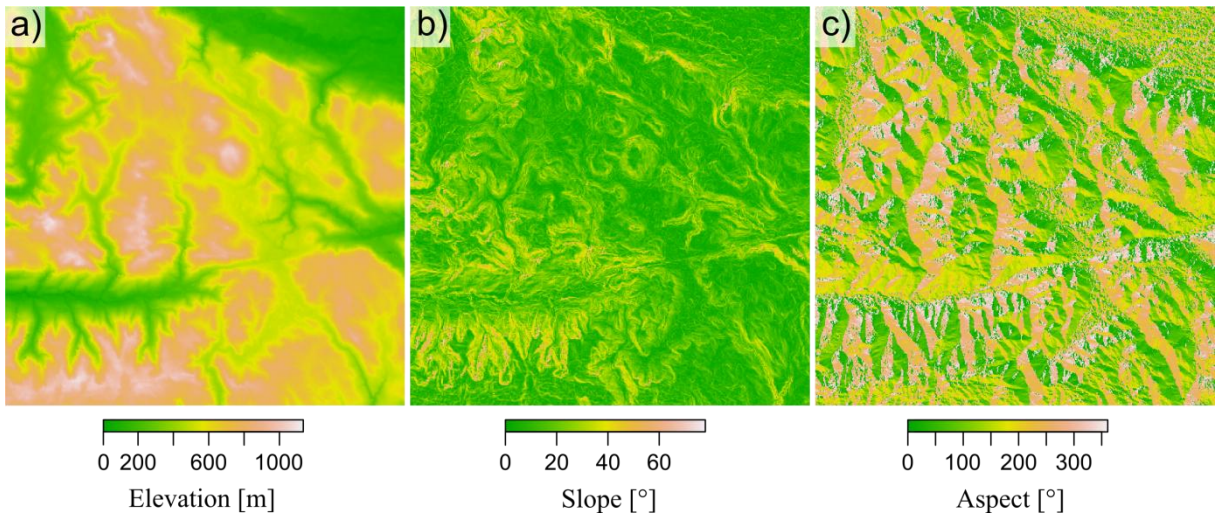


Fig. 3.1.2: DEM (a), slope (b) and aspect map (c) of the study site.

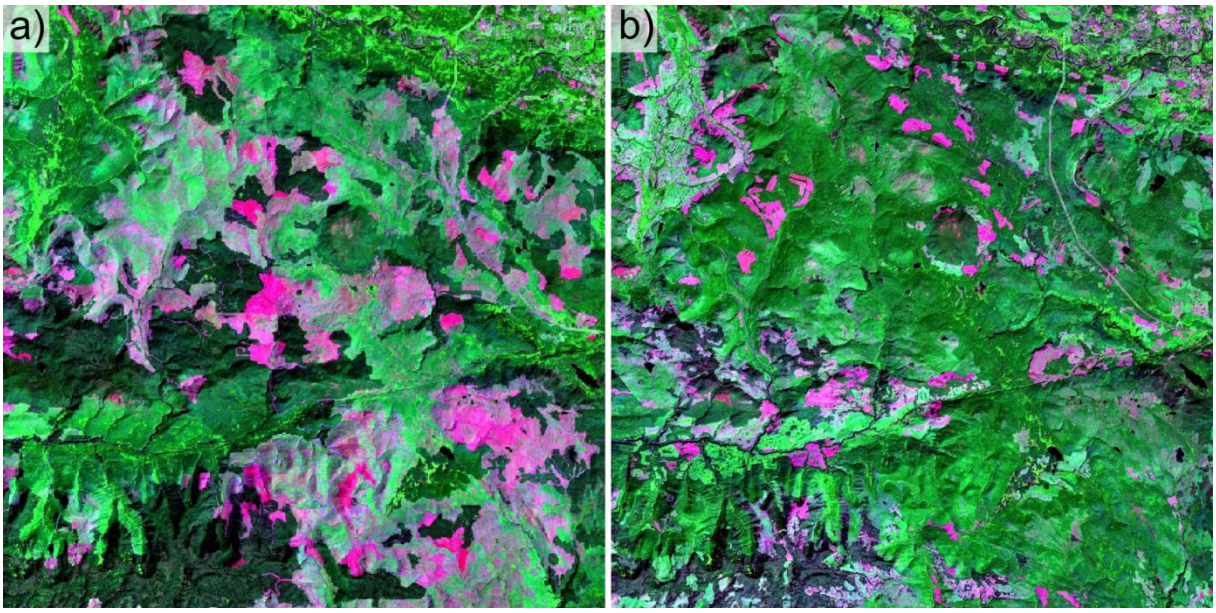


Fig. 3.1.3: Study site (30x30 km²) at the beginning (1984-07-17) and at the end (2013-07-26) of the observation period seen by Landsat 5 TM and Landsat 8 OLI, respectively. RGB = 7-4-2.

hilly, mountainous terrain with steep slopes, large height differences within short distances, and frequent changes of valleys and summits. The diversified terrain is displayed in the DEM (a), slope (b), and aspect (c) maps of the study site (Fig. 3.1.2). Slope varies between 0° and 79°, aspect ranges between 0° and 360°.

Fig. 3.1.3 shows the study site at the beginning, 17th July 1984, and at the end, 26th July 2013, of the observation period. It can be seen that the area has changed dramatically although forest is still the major land cover. In some areas the forests have been cleared and recovered quickly between the two dates. Old forests appear dark green whereas younger forest stands have luscious green tones. Pioneer vegetation, shrubs, and grass appear in light green colors. Bare soil and clearcuts with woody debris appear in magenta tones, water bodies are black. From Fig. 3.1.3 it is obvious that huge forest clearings appeared already before the observation period, indicated by large portions of magenta colors in (a). The area of clearcuts is considerably smaller in (b), but of course, the harvesting activities shifted to other places since the forest needs time to recover. A comparison with Fig. 3.1.2 reveals that the old forests are mainly restricted to higher altitude, hilly terrain with steep slopes and which are difficult to access.

### 3.1.2 Climate

Vancouver Island is amongst the warmest places of Canada with a typical oceanic climate characterized by relatively high winter temperatures and mild summers. Rainfall varies even at short distances and is strongly influenced by topography. The rain shadow effects of the Vancouver Island mountain ranges cause large local variations of precipitation. Precipitation has a pronounced peak during autumn and winter. The summers are relatively dry. The climate of Vancouver Island is strongly influenced by the moist western winds from the Pacific Ocean. The southernmost part of Vancouver Island receives least precipitation due to the additional protecting effect of the Olympic Peninsula. Vancouver Island's west coast is considerably wetter

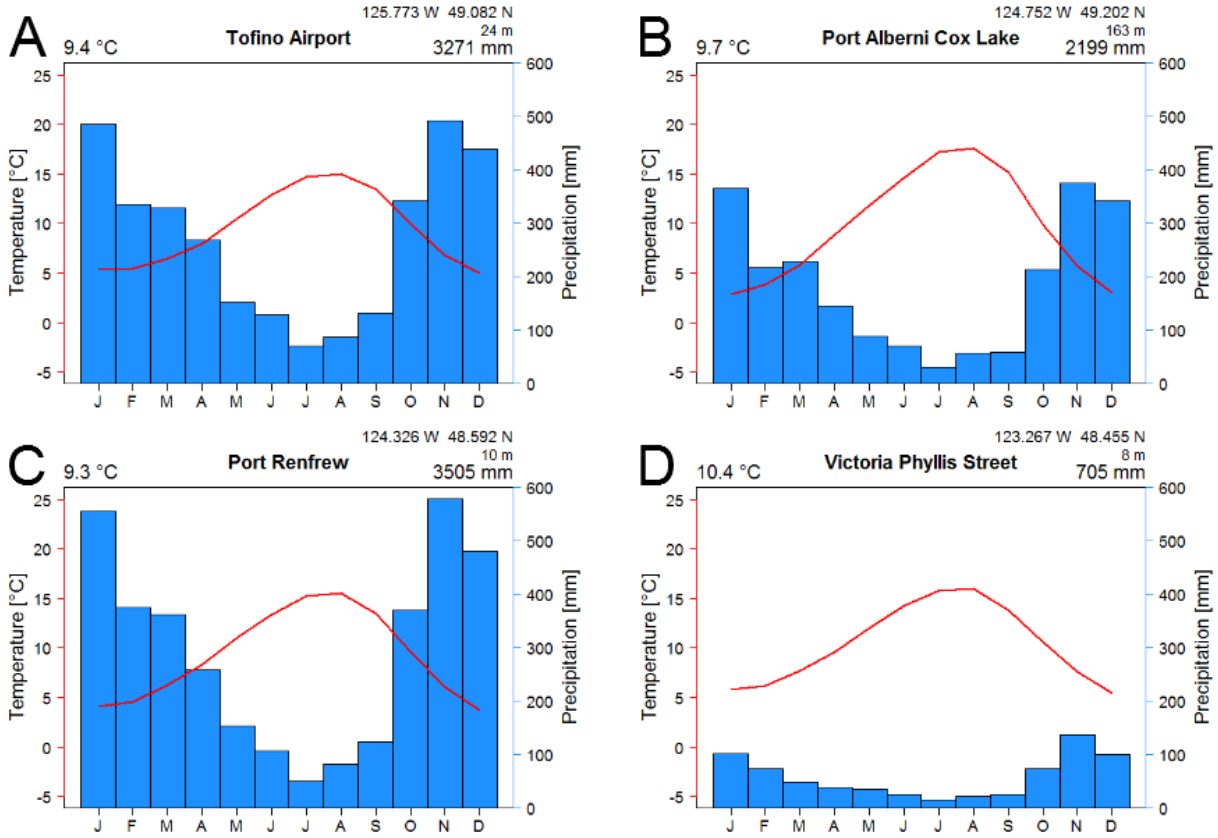


Fig. 3.1.4: Climate charts of four climate stations on Vancouver Island: A) Tofino, B) Port Alberni/Cox Lake, C) Port Renfrew, and D) Victoria/Phyllis Street. The locations refer to Fig. 3.1.1. Climate data are 1981 to 2010 Canadian climate normals (Government of Canada, 2011).

than the east coast. The climate charts presented in Fig. 3.1.4 refer to locations A, B, C, and D in Fig. 3.1.1. From Fig. 3.1.4 it can be seen that the west coast climate stations at Tofino Airport and in Port Renfrew show large average rainfall amounts above 3000 mm/a. The weather station of Port Alberni/Cox Lake, located more in the central part of the island, has less average precipitation. Victoria, British Columbia's provincial capital, receives about 700 mm precipitation in average which equals about one fifth of the amount of Port Renfrew. Only little precipitation falls as snow (Pojar et al., 1991). The average temperature is 9.4 °C in Tofino, 9.3 °C in Port Renfrew, 9.7 °C in Port Alberni/Cox Lake and 10.4 °C in Victoria/Phyllis Street. Although being influenced by the compensational effects of the Pacific Ocean, the climate station of Port Alberni/Cox Lake reveals continental effects, too: the winter temperatures are lower and summer temperatures are higher than those of the Tofino Airport climate station which is located at similar latitude. This effect cannot be observed when comparing the climate stations of Port Renfrew and Victoria/Phyllis Street. The temperatures of the latter station show less difference between summer and winter. Maximum temperatures, however, are at a similar level. The difference arises from higher winter temperatures at Victoria/Phyllis Street.

### 3.1.3 Data

In the past, observation interval was often determined by the availability of satellite data (Coppin and Bauer, 1996). Even today, more than five years after the opening of the Landsat archive,

most studies pay a lot attention on the selection of anniversary, cloud free images. In case of excessive cloud cover, off-year acquisitions are preferred over off-seasonal images (Wulder et al., 2004b). With upcoming satellites with wide footprints such as Sentinel-2 (Drusch et al., 2012) the probability of totally cloud free acquisitions will be reduced compared to sensors with small footprints and off-nadir capabilities (which allow for more flexible acquisition strategies). Thus, seeking cloud free images is challenging if not misleading.

Many studies are published that make use of long Landsat time series including the Multi-Spectral Scanner (MSS) data taken from Landsat 1 to 5 (e.g.; Pflugmacher et al., 2012; Gómez et al., 2011). Landsat 4 was the first satellite of the Landsat program that carried the Thematic Mapper (TM). All successors had similar instruments with almost identical band definitions and spatial resolution. Even the latest satellite of the Landsat program, Landsat 8 – Landsat Data Continuity Mission (LDCM), has comparable bands, supplemented by additional bands for coastal applications and the characterization of atmospheric properties (Irons et al., 2012). Spatial resolution of MSS and TM/ETM+/OLI are different as are the spectral properties. Landsat MSS data are not included in this study since MSS acquisitions are taken less frequent resulting in longer data gaps. Furthermore, Landsat MSS pre-processing requires huge efforts to achieve consistent datasets. The main reason not to consider these data here, however, is their spectral resolution that would limit the studies on spectral indices.

In the present study, all available Landsat images between 1984 and end of 2012 were used that are available from the USGS Global Visualization Viewer (http://glovis.usgs.gov/) or Earth Explorer (http://earthexplorer.usgs.gov/) likewise. The Scan Line Corrector (SLC) of Landsat 7 ETM+ failed in May 2003 resulting in data gaps whose extent increases from zero at nadir to 14 pixels at the far edges of each scan (Markham et al., 2004). Consequently, about 22% per scene are lost whilst the precise location of the missing scan lines varies from scene to scene (J. Chen et al., 2011). From late 2011, no Landsat 5 TM data are available for the study area. Thus, only Landsat 7 ETM+ SLC-off images are available for 2012. The overall number of images amounts

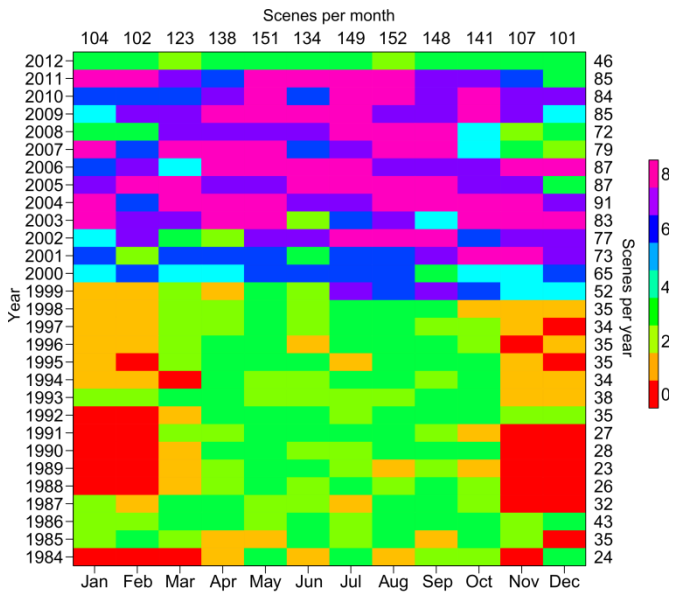


Fig. 3.1.5: Overview of data distribution during the observation period. Note: only the overlapping part of WRS-2 tiles p047r026 and p048r026 can be covered by all scenes.

in 1550 scenes including cloudy images as well as Landsat ETM+ SLC-off data. Fig. 3.1.5 shows the distribution of acquisitions during the observation period. It can be clearly seen that in the eighties and nineties winter acquisitions were rarely taken. Up to four images per month are available for this period during summer. With the start of Landsat 7 in 1999 and Landsat 5 working simultaneously, the number of acquisitions was increased up to eight per month. Winter acquisitions are less available but all seasons are covered from 1998 on.

### 3.1.4 Cloud Detection

The general concept of this research is to use all clear land pixels. All pixels that are not contaminated by clouds, cloud shadows or snow are referred to as "clear". Clear land pixels are clear pixels that do not show water bodies. Thus, masking of clouds, cloud shadow, snow and water is essential.

Several cloud detection methods have been published, e.g., the Automated Cloud Cover Assessment (ACCA) (Irish, 2000; Irish et al., 2006) and the method by (Huang et al., 2010b). A sophisticated method was presented by (Zhu and Woodcock, 2012) with the object-based Function of Mask (Fmask) algorithm. It provides masks for clouds, cloud shadows, snow, and water. The algorithm is also used for the generation of the Landsat Climate Data Record (CDR) products provided by the USGS Earth Explorer (http://earthexplorer.usgs.gov/), e.g., surface reflectance (USGS, 2013a) and spectral indices (USGS, 2013b). Fmask makes use of the clouds' and cloud shadows' physical properties to extract potential cloud and cloud shadow layers. Several combination sets of spectral bands from the Landsat Ecosystem Disturbance Adaptive Processing System (LEDAPS) Top of Atmosphere (TOA) reflectance output as well as TOA-derived spectral indices are used in this step. The two segmented cloud and cloud shadow layers and their geometric relationships are used to create the final cloud and cloud shadow mask. Clearland pixels, water masks and snow masks are also derived from spectral indices, brightness temperature and spectral bands (Zhu and Woodcock, 2012). From Fig. 3.1.6 it can be seen that the Fmask results is relatively accurate, yet not perfect. Recent advances extended the Fmask algorithm to reduce errors based on multi-temporal analysis of Landsat data (Zhu and

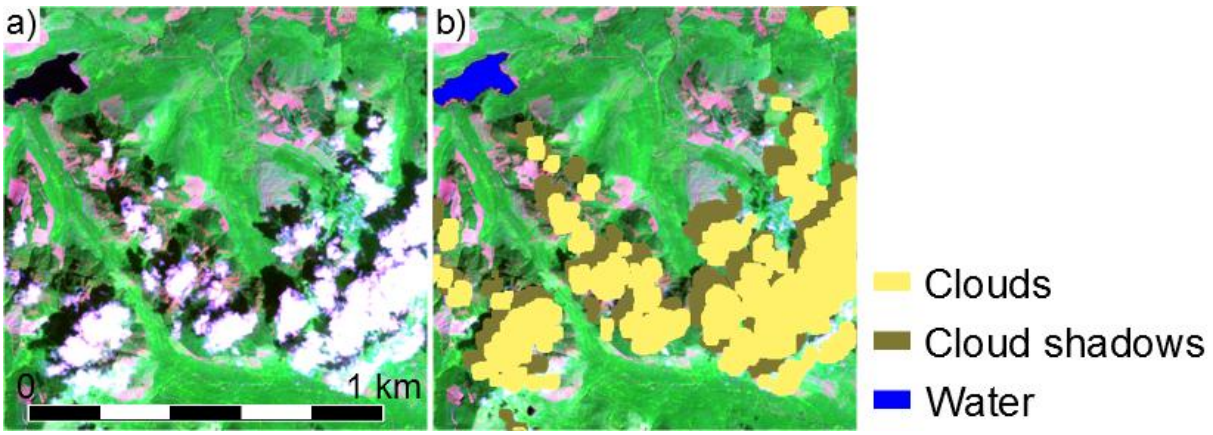


Fig. 3.1.6: Fmask result for a subset of a Landsat 7 ETM+ scene taken on 6th August, 2000: a) RGB-composite displaying bands 7-4-2, b) same subscene example superimposed with water, cloud and cloud shadow masks.

Woodcock, 2014; Zhu et al., 2012). The Windows stand-alone Fmask software (version 2.1, https://code.google.com/p/fmask/) was used with standard configuration to derive cloud, cloud shadow, snow, water, and clear land masks as well as a gap mask.

### 3.1.5 Cloud/Cloud Shadow Statistics

Since the opening of the Landsat archive many studies have been published that use time series (e.g., Cohen et al., 2010; Griffiths et al., 2012; Meigs et al., 2011). Usually the analyses are based on annual or bi-annual data. Fig. 3.1.7 shows the seasonal and annual distribution of Landsat images with less than 5% cloud/cloud shadow cover according to the results of Fmask. It can be seen that although the sample size amounts to the relatively high number of 113 scenes, it is not possible to construct a time series of images taken at the same time of a year. An option would be to partition the image to smaller subsets thereby increasing the number of cloud/cloud shadow free subscenes. Recent advances can be reported from compositing techniques that aim at constructing harmonized and radiometrically consistent images by selecting suitable pixels from a bulk of images (Griffiths et al., 2013). Compositing is somewhat antipodal to our approach since it discards most observations. Compositing as a means to create regular Landsat time series products such as the MODIS 16day composites is on its way (Hansen et al., 2014; Roy et al., 2010) but has not yet been fully implemented. However, compositing requires reliable cloud masking, too. The climate charts presented in Fig. 3.1.4 pretend high probabilities of cloud free images during summer. For that period it can be assumed that little rainfall is associated with little cloud coverage. However, from the Pacific west coast of Vancouver Island it is well known that the lower parts are frequently foggy in August and September. As reported earlier, the area is also known for its spatially highly variable rainfall distribution. Thus, cloud distribution cannot be estimated from climate charts alone. The best figure about cloud coverage during image acquisition can be derived directly from the image itself. Hence, cloud statistics were calculated from the Fmask output. There is some bias in the cloud statistics because the footprints of the different Landsat sensors explored here are variable over time. Besides that, there is no

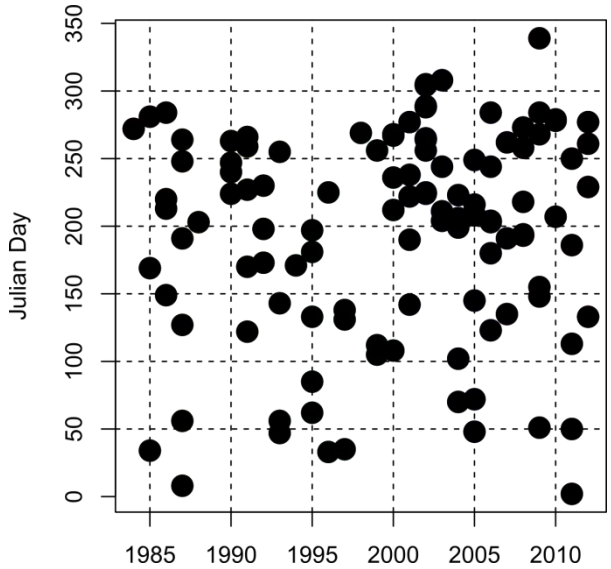


Fig. 3.1.7: Images with less than 5% cloud/cloud shadow coverage over the observation period.

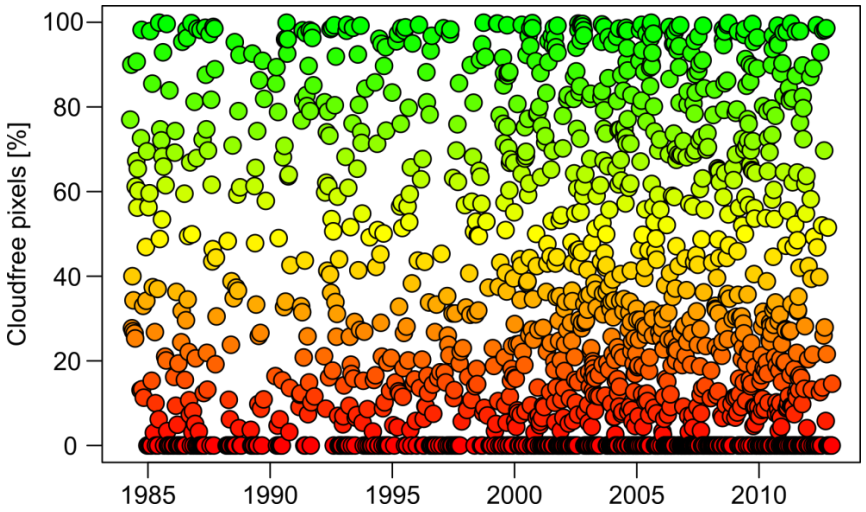


Fig. 3.1.8: Distribution of cloud free pixels as percentage of all pixels of an image that contain information over time.

information for the gaps of Landsat 7 ETM+ SLC-off, which are also variable from scene to scene. Consequently, the figures shown here represent cloud and cloud shadow coverage in terms of percentage of pixels that contain data (i.e., either clear land, clear water, cloud, cloud shadow, or snow). From Fig. 3.1.8 it can be seen that although a lot of images show excessive non-usable data (i.e., low percentage of cloud free pixels) there are numerous images that have high percentage of usable data (i.e., cloud free pixels). These usable data are not necessarily entirely cloud free. Fig. 3.1.9 shows that about 25% of all images are totally cloud covered and may be skipped for further processing since they do not contain any information about land.

The Landsat Level 1 Product Generation System (LPGS) is an automated processing system to produce terrain-corrected Landsat level 1T images. It may only be applied if sufficient ground control points (GCPs) are available. Images with more than 80% cloud and cloud shadow coverage were considered too inaccurately registered and error-prone and consequently not considered for further processing. This arbitrary threshold is also recommended by other users (C. Woodcock, personal communication). As a result the amount of data to be analyzed was

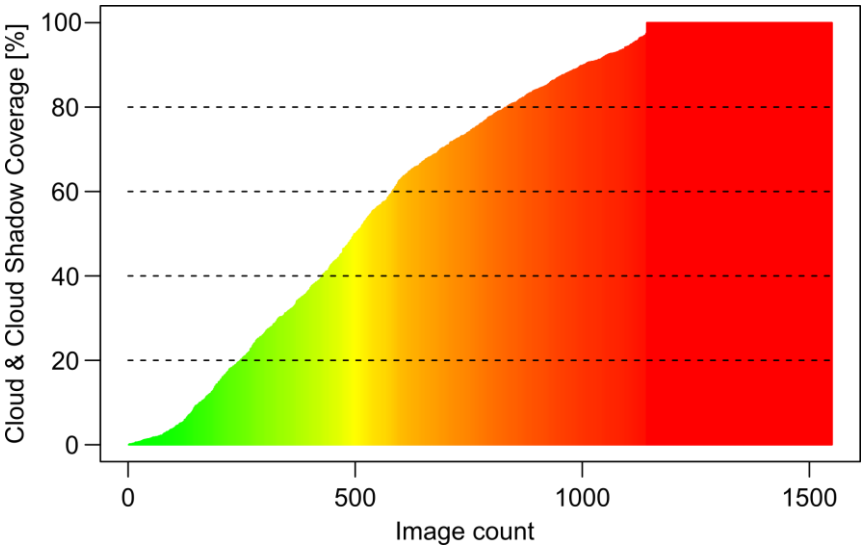


Fig. 3.1.9: Cloud and cloud shadow distribution over the complete time series in increasing order.

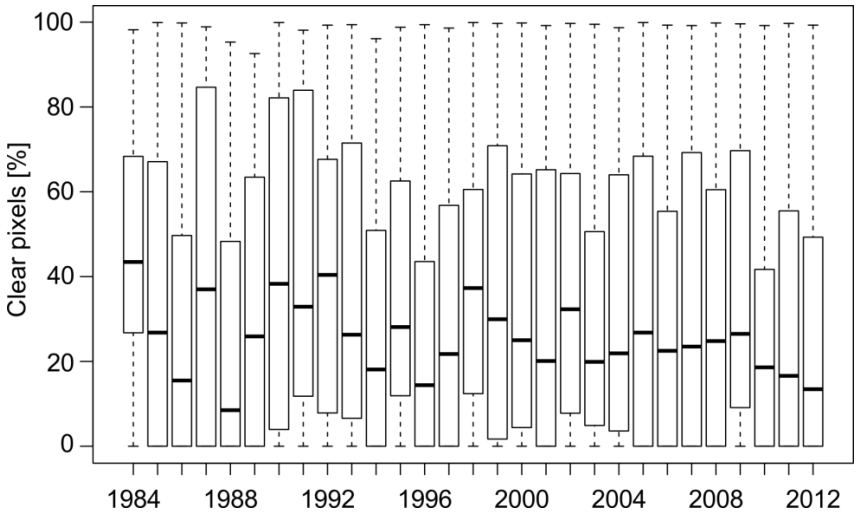


Fig. 3.1.10: Box-whisker plots showing median, upper/lower quartiles, and extreme values of clear pixel percentages for each year (note: until the 1990s winter acquisitions were avoided).

reduced to 778 images (which is about the half of all images). Along with the temporal distribution of clear pixels (Fig. 3.1.8), the yearly statistics offer additional information (Fig. 3.1.10). One might tend to read trends from this statistics. This should be strictly avoided since there were no winter acquisitions during the early 1980s. A somewhat clearer picture may be derived from Fig. 3.1.11 where results of averages by month were calculated (e.g., all January data from 29 years). Average percentages of clear pixels are highest for July, August, and September. These findings correspond largely to the temporal rainfall pattern displayed in the climate charts of the study region (Fig. 3.1.4). Depending on the weather conditions it may happen that clouds (and cloud shadows) are limited to the sea which wouldn't affect land applications in any way. In these cases, even high cloud coverage results in large cloud free areas. Fig. 3.1.12 shows different Landsat scenes with 46% (a), 71% (b), and 41% (c) cloud cover, respectively. Large portions of the land are cloud free, however. From this example it is clear that the temporal statistics of clouds is of limited use to characterize data availability.

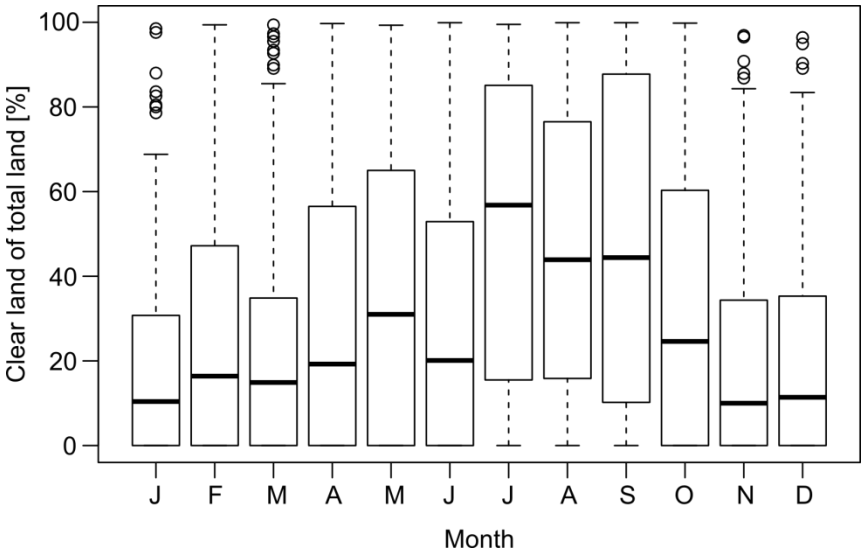


Fig. 3.1.11: Box-whisker plots of clear pixel percentages for each month.

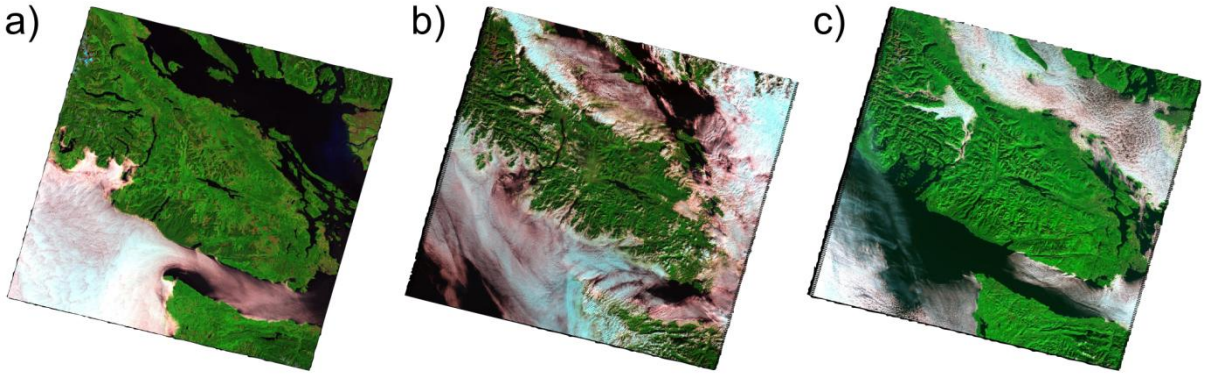


Fig. 3.1.12: Landsat data (full WRS2 tile 048/026) from 1985/07/20, 2002/10/07, and 2002/10/23 with 46%, 71%, and 41% cloud and cloud shadow coverage, respectively.

What is more important for studies like the present (with large parts of coastal water and open sea) is the spatio-temporal distribution of clouds, cloud shadows, snow and other obstacles. Since Fmask does not apply any haze correction, effects associated with haze may be a source of error

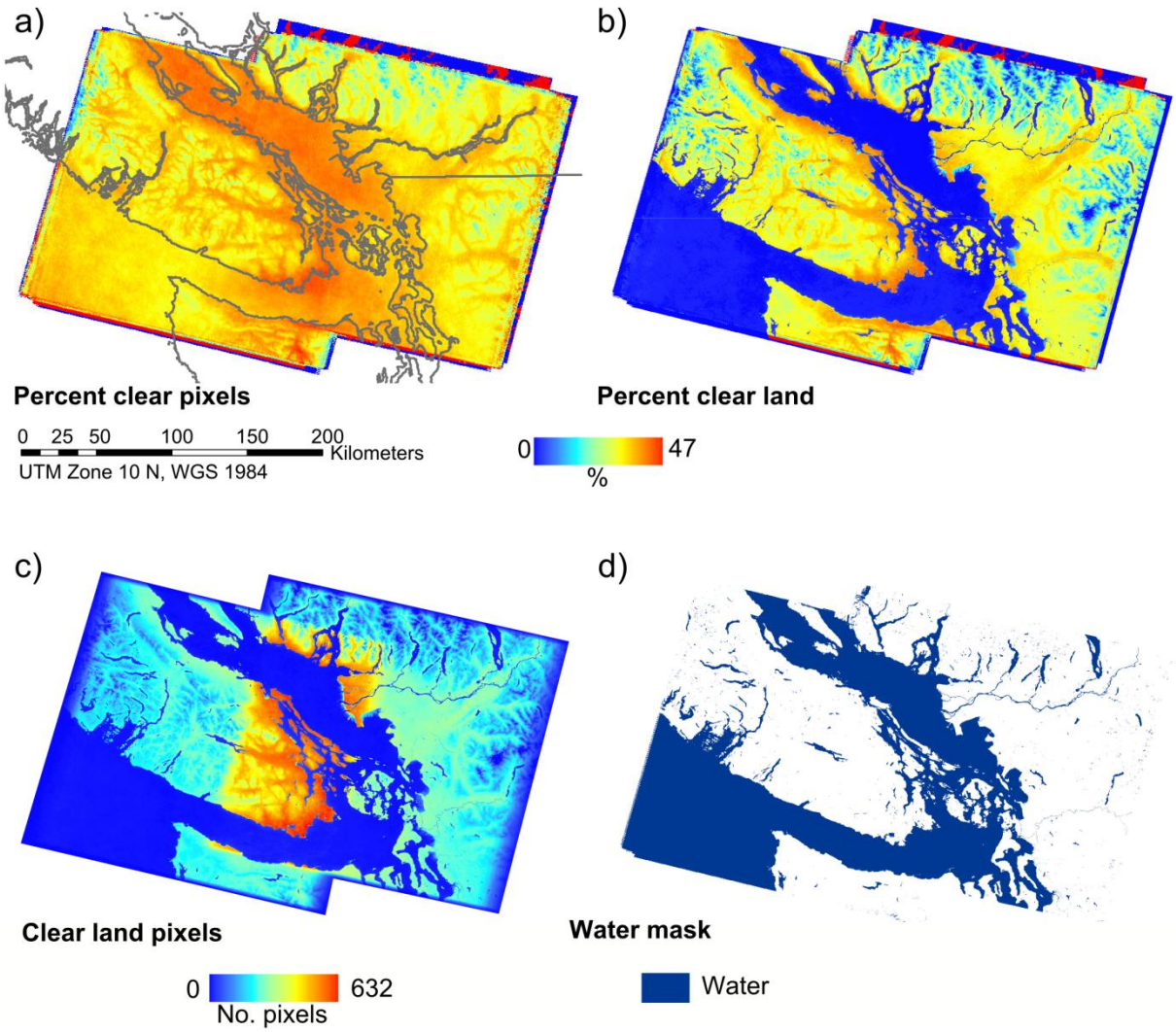


Fig. 3.1.13: Spatio-temporal cloud and cloud shadow distribution derived from all Landsat images between 1984 and 2012: a) percent clear pixels (land and water), b) percent clear land pixels (color legends are identical), c) number of clear land pixels, and d) water mask.

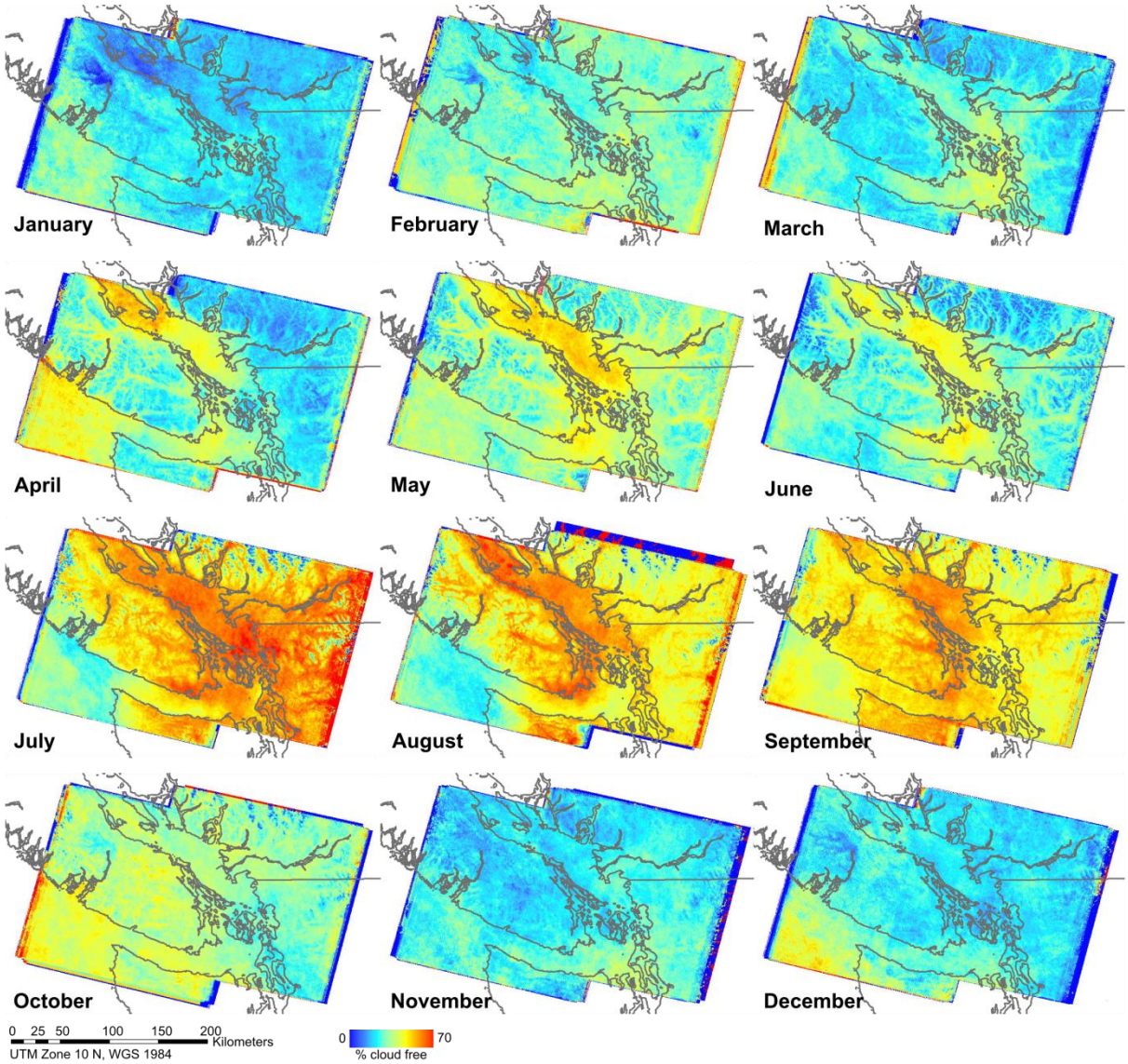


Fig. 3.1.14: Percent clear pixels (water and land) derived from all Landsat images between 1984 and 2012.

that cannot be reflected by the Fmask cloud statistics. The spatio-temporal statistics are presented in Fig. 3.1.13. From Fig. 3.1.13a it can be seen that the water bodies in the rain shadow of Vancouver Island (Strait of Georgia, Juan de Fuca Strait) experience least cloud cover. Up to 47% of all pixels are cloud free in the area around Victoria at the southernmost tip of Vancouver Island and the adjacent sea. Cloud/cloud shadow coverage are highest in the mountains of Vancouver Island as well as along the western coast. Glaciated areas on the mainland show no clear land observation and appear in blue colors (Fig. 3.1.13b). It can be seen that the eastern and southern parts of Vancouver Island have highest percentage of clear land observations. The west coast areas as well as mountainous areas have considerably fewer clear land pixels. The urban area of the city of Vancouver in the rain shadow of Vancouver Island is also a place that is frequently free of cloud and cloud shadows. In terms of methodology the number of cloud free observations is more significant than the percentage. The number of cloud free observations per pixel is shown in Fig. 3.1.13c. The real number of available scenes and cloud free Landsat observations is higher in those parts of the image where neighboring image tiles overlap

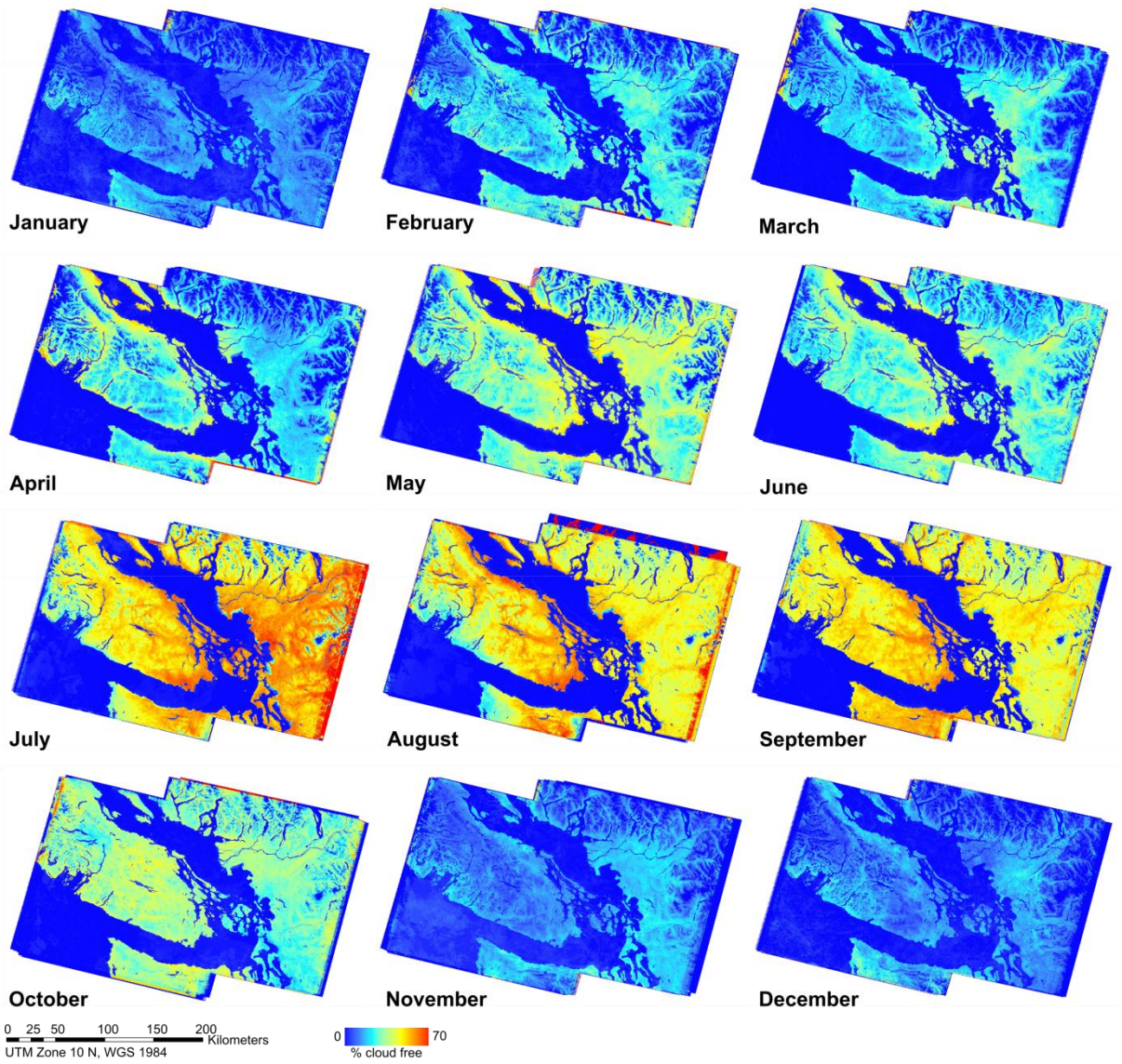


Fig. 3.1.15: Percent clear land pixels derived from all Landsat images between 1984 and 2012.

(westernmost and easternmost image margins). A side effect of the Fmask statistics is the generation of a water mask for the region (Fig. 3.1.13d).

Fig. 3.1.14, Fig. 3.1.15 and Fig. 3.1.16 show the same spatio-temporal information on a monthly basis. From these figures, the spatio-temporal cloud/cloud shadow distribution over a year is visible. It is evident that July, August, and September have least cloud contamination. It is worth noting that the open seas have more cloud free pixels during winter (December, January) than Vancouver Island or the Strait of Georgia. During the rest of the year, the open sea has much more cloud coverage than Vancouver Island, the Strait of Georgia or the mainland (Fig. 3.1.14). The distribution of the percentage of cloud free land pixels is strongly related to the topography (Fig. 3.1.15). Mountain ranges can be identified as hot spots of cloud contamination all over the year. October is an exception, most likely due to inversion in autumn. Differences between mountain tops and valleys are less pronounced at that time. Good chances for cloud free observations and hence high number of cloud free land pixels during the observation period can be reported for summer and autumn (May to October) (Fig. 3.1.16). It is worth noting that there

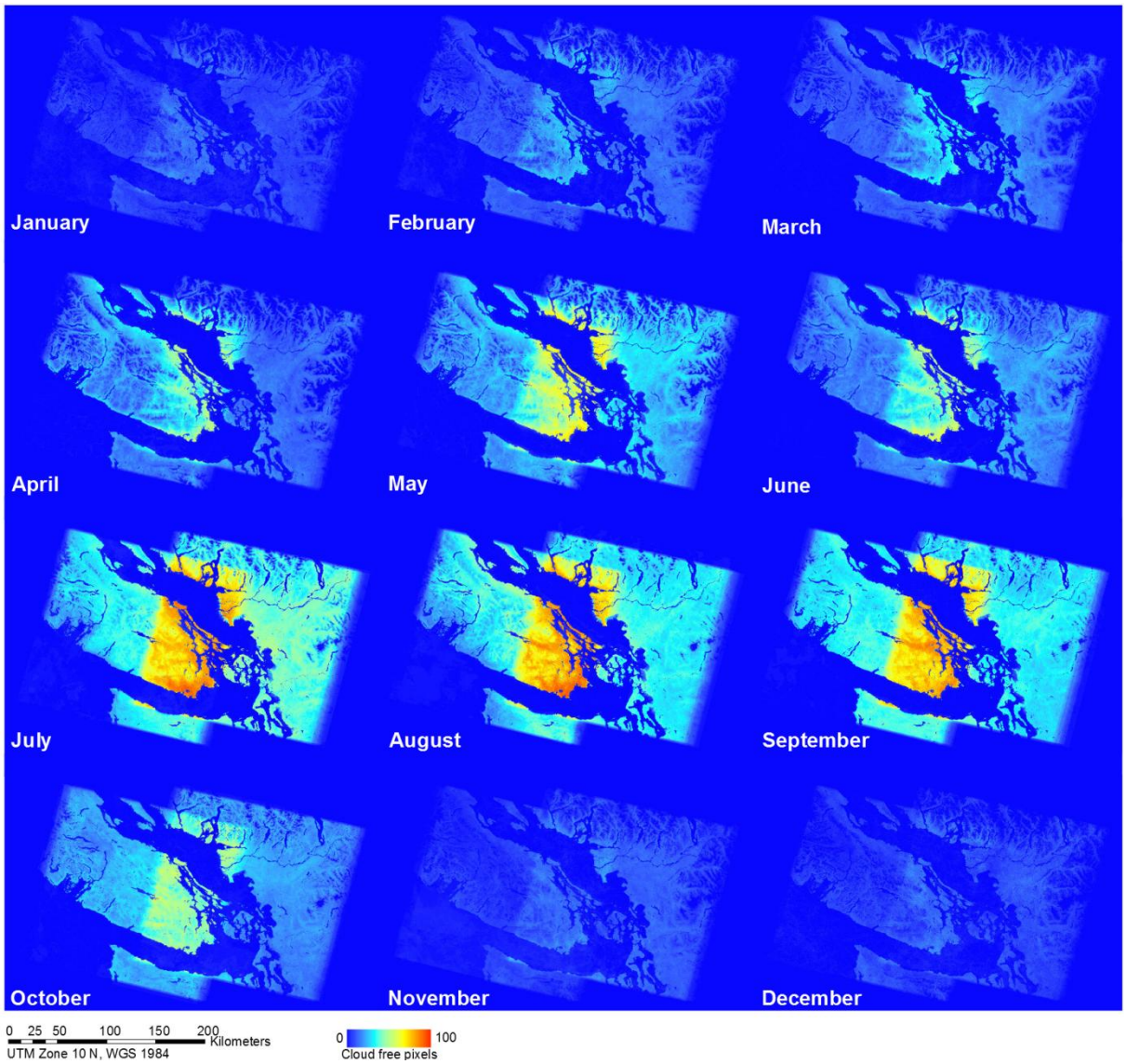


Fig. 3.1.16: Number of clear land pixels derived from all Landsat images between 1984 and 2012.

are a considerable number of non-contaminated winter observations. The Fmask results presented above are likely not to be perfect. However, they display general cloud and cloud shadow distribution patterns that correspond well to the local climate records (e.g., in terms of intra-annual distribution). A climate gradient from west to east is obviously largely associated with spatio-temporal cloud patterns.

### 3.2 Forest Dynamics

Forests are dynamic systems (Franklin et al., 2002). Closed canopy conifer forests evolve from young to old-growth when they mature. During this development a large number of structural and compositional attributes of the canopy change, including tree size, variation in tree size, tree density, tree species, crown vigour, and cover of canopy lichen (Spies and Franklin, 1991).
As mature canopies develop into old-growth, the proportion of shadow in the stands increases due to increasing area, depth, and size of gaps (Cohen et al., 1995). The study by Spies and Franklin (1991) indicates that the variation in old-growth-forest structure is largely driven by low

to moderate disturbance during the life of the stands. Disturbance in this context means the death of trees that leaves space for other plants to grow. According to Oliver and Larson (1996) and Linke et al. (2007) autogenic and allogenic processes of disturbance may be distinguished. Autogenic processes refer to the death of individual trees whose drivers are particular to the tree or ecosystem. Allogenic disturbances have their drivers outside the affected tree or ecosystem. Although forest development is continuous several classifications to forest stand structural stages have been published (e.g., Oliver and Larson, 1996; Franklin et al., 2002). These classifications are arbitrary but assist in characterizing periods where specific stand structural conditions and related processes dominate. Some of the development processes take place continuously across each stage of the lifetime of a stand. Some development stages may not occur in individual stands.

Franklin et al. (2002) distinguish eight stand structural development stages: 1) disturbance and legacy creation, 2) cohort establishment, 3) canopy closure, 4) biomass accumulation/competitive exclusion, 5) maturation, 6) vertical diversification, 7) horizontal diversification, and 8) pioneer cohort loss. The most common classification schemes for stand structural development stages are shown in Tab. 3.2.1. The first stage of the classification by Franklin et al. (2002) is characterized by the disturbance and its legacy. Natural disturbances usually leave structural elements such as living trees. Dead trees remain in the ecosystem after natural disturbances in most instances. Biological legacy is defined by persisting living and dead structures (Franklin et al., 2002).

The major disturbance occurring in the study site is clearcut harvest. Timber companies claim to manage forests in a sustainable way, creating patterns that are comparable to natural disturbances

Tab. 3.2.1: Comparison of stand development stages classification schemes.

| Typical stand age (years) | Classification | | |
|---|---|---|---|
| | Franklin et al. (2002) | Oliver & Larson (1996) | Carey & Curtis (1996) |
| 0 | Disturbance and legacy creation | | |
| 20 | Cohort establishment | Stand initiation | Ecosystem initiative |
| 30 | Canopy closure | Stem exclusion | Competitive exclusion |
| 80 | Biomass accumulation/ competitive exclusion | Understory re-initiation | Understory re-initiation |
| 150 | Maturation | Old-growth | Botanically diverse |
| 250 | Vertical diversification | | Niche diversification<br>Fully functional<br>Old-growth |
| 800 | Horizontal diversification | | |
| | Pioneer cohort loss | | |

Modified after Franklin et al. (2002).

such as those caused by fire or insects (West Fraser, 2014). Unfortunately, traditional clearcutting techniques leave little or no biomass in contrast to most natural disturbances (Franklin et al., 2002; Spies et al., 1988). Hence, the structural legacy of clearcuts is distinct from that originating from natural disturbances. Practice in the field, however, also includes trees left standing either in small patches or as individual trees, and leaving large woody debris on the forest floor (Fig. 3.2.1). The second stage, the cohort establishment, describes the phase of establishing a new generation of trees. According to the timber industry, forests are replanted with the same species composition that have been harvested with similar proportions as were found before harvest in the study site (West Fraser, 2014). Regeneration of forests is achieved by both planting trees and natural seedling from cones left in the harvesting area. The overarching goal is the replication of the harvested forest (West Fraser, 2014). Old growth forests, however, have stand ages of several hundred years which is much more than the current average 80 years harvest rate. The cohort establishment stage varies widely in duration and stocking level according to the type of disturbance and the ecosystem properties.

The canopy closure stage is described as "the most dramatic developmental episode in rate and degree of change in stand conditions" (Franklin et al., 2002). This stage is characterized by canopy closure achieved by the overlap among individual tree canopies. Light reduction in the understory, increased relative humidity and wind reduction greatly affect the forest interior conditions. Major changes occur in both the composition and function of the forest ecosystem (Franklin et al., 2002). Canopy closure may take several decades when productivity is low. The biomass accumulation/competitive exclusion stage is characterized by rapid growth and biomass accumulation. Competitive exclusion of organisms and intense competition among the tree cohort dominate the site together with density-dependent tree mortality or self-thinning (Franklin et al., 2002).

Fig. 3.2.1: Groups of tree left standing, woody debris and slash within clearcut patches (Photo: F. Thonfeld, southern Vancouver Island, 2013).

The pioneer cohort of trees attains maximum height and crown spread during the maturation stage (Franklin et al., 2002). Overstory tree mortality is density-independent rather than density-dependent during the maturation stage. According to Franklin et al. (2002) the maturation stage typically begins at 80 – 100 years and may persist for 100 – 150 years in naturally-regenerated Douglas-fir stands. Individual trees may continue growing in size and accumulating biomass. Shade-tolerant tree species may re-establish during this stage. The vertical diversification stage is characterized by the development of late-successional forest attributes. The late-successional phase is synonymous to the old-growth phase. In particular the re-establishment of canopy continuity between the forest floor and upper tree crowns occurs during this stage that may occur at 200 – 350 years (Franklin et al., 2002). Horizontal diversification is largely driven by gap creation and development. These processes are typical for this stage although being active throughout the forest development. Horizontal diversification leads to patchy forest patterns. The last stage described by Franklin et al. (2002) is the pioneer cohort loss stage that occurs when shade-intolerant species are present but the gaps present in older stands are too small for their successful regeneration.

The classification of forest stand stages by (Carey and Curtis, 1996) will not be described here. From Tab. 3.2.1 it can be seen that their scheme is also rather detailed but differs somewhat from the scheme by Franklin et al. (2002). The scheme by Oliver and Larson (1996, Fig. 3.2.2) has only four stages: 1) stand initiation, 2) stem exclusion, 3) understory re-initiation, and 4) old-growth. The first stage is characterized by the establishment of a cohort of vegetation. This period lasts until the community of trees fully occupies the available growing space (Linke et al., 2007). The dominant process during stem exclusion stage is competition among established trees. Competition (i.e., density-dependent mortality) affects ecosystem development and structure leaving hardly any space for new trees.

The understory re-initiation stage begins when diseases and insects lead to the death of individual trees in the stands leaving space for the establishment of some new tree species. During this stage, there is not enough space available to generate a lower canopy layer – the pioneer cohort is still dominating the ecosystem although stand structure becomes increasingly complex (Linke et al., 2007). The last stage in this scheme is the old-growth stage. It is rarely achieved in natural ecosystems because disturbances return the ecosystem to the stand initiation stage (Linke et al., 2007). The old-growth stage is characterized by the release of growing space to allow some patches for the establishment of a stand initiation stage. New cohorts of trees become established and replace the original cohort. The species shown in Fig. 3.2.2 are red alder (*Alnus rubra*) which dominates the stand initiation stage as pioneer species, Douglas-fir (*Pseudotsuga menziesii*) which is the dominant species during the stem exclusion and the understory reinitiation stages, western hemlock (*Tsuga heterophylla*), and western redcedar (*Thuja plicata*). Western hemlock and western redcedar are shade tolerant and coexist with the dominant Douglas-fir. During the old-growth stage Douglas-fir, western hemlock, and western redcedar dominate together the forest stand exemplified in Fig. 3.2.2.

As mentioned earlier, the harvesting practices in the study area include replantation of harvested species with proportions found before harvest. Since species composition and spatial arrangement of individual trees is a result of distinct processes operating for a particular time

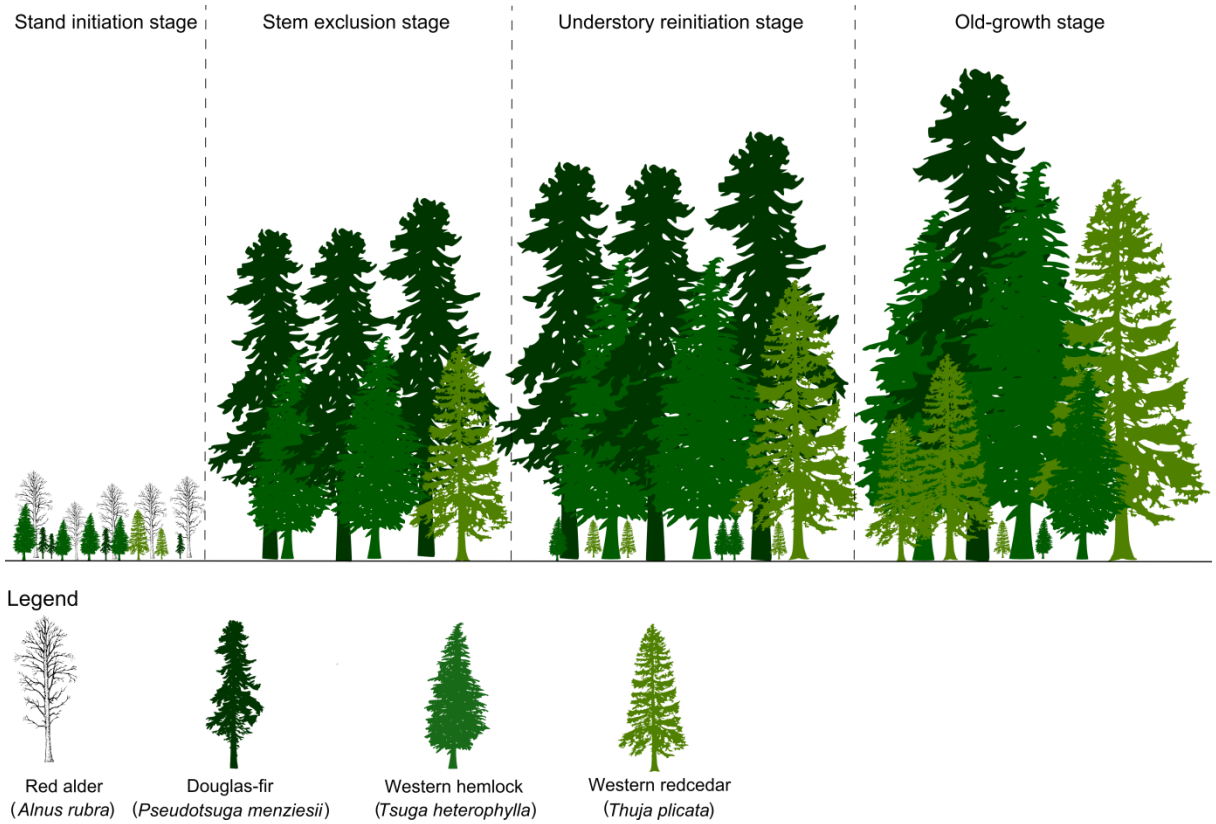


Fig. 3.2.2: Schematic stages of stand development after a stand replacing disturbance. All trees forming the forest start growing soon after the disturbance. The dominant tree type changes with progressing vertical stratification of species (modified after Oliver and Larsen, 1996; Linke et al., 2007; silhouettes from Government of Canada, 2013).

these practices may affect the processes. Oliver and Larson (1996) showed that it is common for several tree species including pioneers and long-living, shade-tolerant species to be established in the stand initiation stage. Usually, fast-growing species dominate the overstory in the years after the disturbance. Since they have relatively short life times they once leave space for the slowly-growing species dominating the lower strata. Global change scenarios reveal long term turns in tree species distribution in British Columbia (Hamann and Wang, 2006) and in whole North America (Hansen et al., 2001). Thus, monitoring programs accounting for the complexity of forest environments and the manifold human-ecosystem interactions are required. Forest stand development has several implications for remote sensing. Whereas single remote sensing images are valuable in describing forest stand structures, time series of satellite data allow for the description of processes.

The spectral response of each single spectral band over time is a function of the forest stand development. Some of the major spectral classes occurring in the managed forest ecosystems of the study site are shown exemplary in Fig. 3.2.3. It can be seen that a stand replacing disturbance means reduced reflectance in the NIR domain (band 4 in Fig. 3.2.3) and strongly increased reflectance in the SWIR (bands 5 and 7 in Fig. 3.2.3). In the visible domain (bands 1, 2, and 3 in Fig. 3.2.3) reflectance increases considerably when all debris and litter are removed from the site. If wood slash, branches and other debris remain in the site, the reflectance increases in the blue (1) and red (3) bands and is only little changed in the green (2) band.

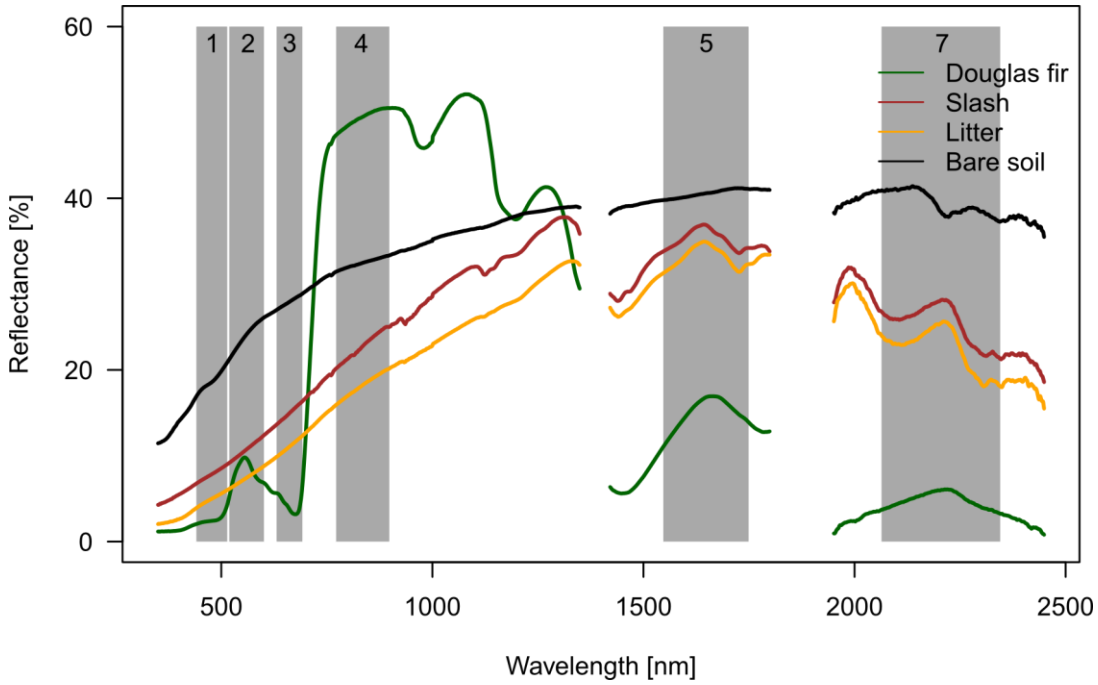


Fig. 3.2.3: Spectral signatures of Douglas fir, slash, litter and bare soil (available at FRAMES, 2014) with Landsat 7 ETM+ bands.

The spectral response, however, is not only changed when a disturbance occurs. It is also influenced by the changes inside a stand. Most dramatic changes are visible until crown closure is reached. This is due to the rapid growth of the young trees, usually deciduous trees, rapid biomass accumulation and excessive space to grow. Ecosystem properties such as climate, altitude, and nutrient availability control the speed of growth. During the stages that are characterized by competition, the structural changes inside the stand hardly display in the spectral signatures. The stands are dense, and emerging gaps are soon closed by other trees. The spatial and spectral resolutions of Landsat are not sufficient to adequately detect these intra-stand dynamics. Understory re-initiation is also obscured by the larger trees in the stand. Multispectral data are inappropriate to estimate biomass of high-biomass forest stands (Duncanson et al., 2010). Hence, structural developments are hardly reflected in spectral reflectance. Thinning and consequently increasing shadow proportions inside the stand in late development stages are predominantly reflected by the NIR and SWIR bands. These findings lead to the generalized graphs of Fig. 3.2.4. Three phases may be detected: 1) forest establishment until crown closure is achieved, 2) competition during stem exclusion and understory reinitiation stages, and 3) occurrence of shadow in a old-growth stand as horizontal and vertical structure change considerably. These phases are strongly related to the forest stand stages although a spectral differentiation between stem exclusion and understory reinitiation stage is hardly possible. Phase 1, however, is characterized by the most dramatic changes – reflectance in the VIS and SWIR domain decreases whereas it increases in NIR. During phase 2 which is characterized by competition, the spectral response hardly changes over time in VIS and SWIR. However, reflectance of band 4 decreases slightly with the replacement of pioneer species by coniferous trees and levels off over time. In the old-growth stage gaps may be released in the forest giving space for the occurrence of shadow. Shadow affects the overall reflectance.

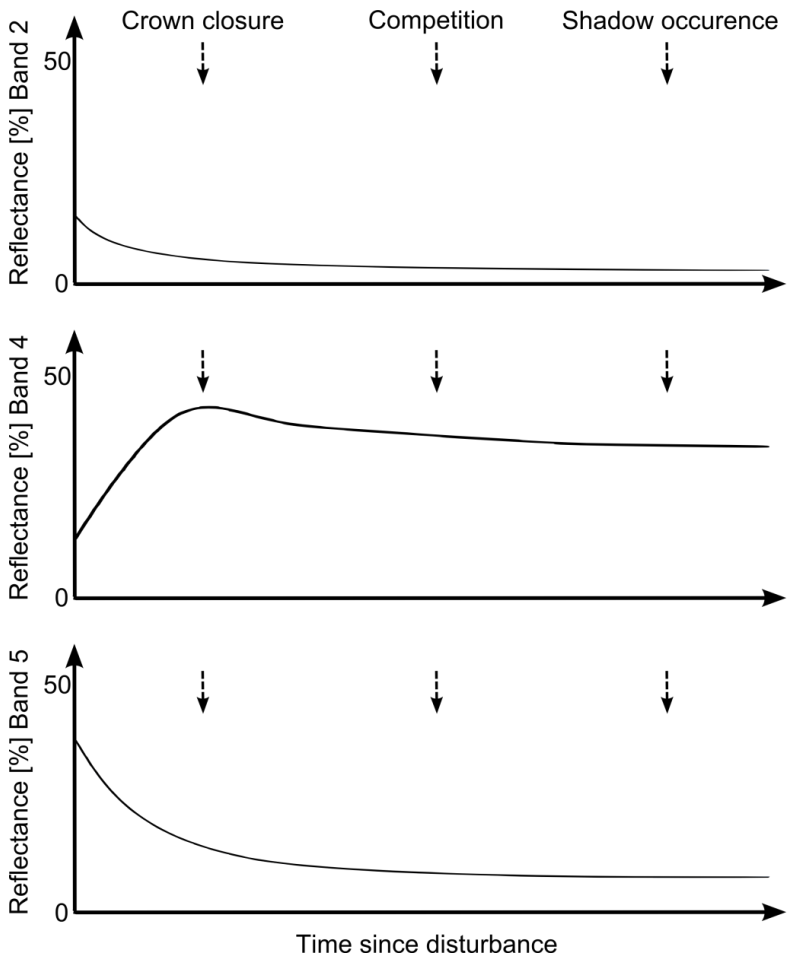


Fig. 3.2.4: Schematic spectral response of Landsat 7 bands 2, 4 and 5 over time after a major disturbance event.

### 3.3 Spectral Indices and their Applicability to Forest Monitoring

Numerous spectral indices have been published (an overview is given in Henrich et al., 2009), many of them aiming at vegetation applications. There may have been two primary drivers to develop indices: 1) enhancement of features that are specific for certain land cover types and particular properties of them, and 2) data reduction to enhance computation time. Both reasons are valid still today. Due to sophisticated hardware and software, data reduction played a minor role in the past decades. As the size of received and stored data increases drastically, efficient computing becomes more important than ever despite the development of large computing clusters. We understand data reduction in a way that useless data might be disregarded. Spectral indices allow emphasizing phenomena that are of particular interest and omitting those that are redundant. Here, we discuss a selection of spectral indices and their suitability for forest monitoring, notably conifer forests.

From Fig. 3.3.1 it can be seen that the reflection of the visible spectral bands is mainly affected by leaf pigments and chlorophyll absorption. Near infrared spectral response is driven by cell structure whereas shortwave infrared bands reflect leaf water content. Fig. 3.3.1 also shows the effect of atmospheric water absorption. The position of Landsat 7 ETM+ spectral bands is shown as well. Landsat 5 spectral bands are similarly designed. It is obvious that VIS bands and

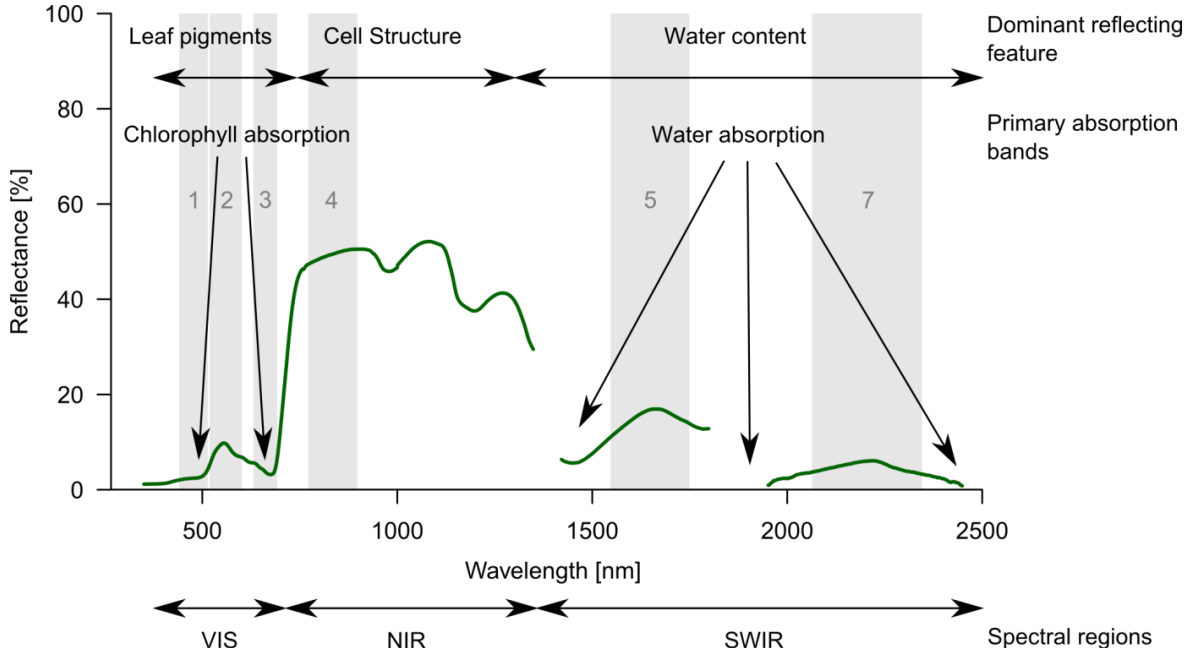


Fig. 3.3.1: Douglas-fir spectrum (available at FRAMES, 2014) and features that impact reflection (modified after from Sieber, 1986). Landsat 7 ETM+ bands and spectral regions are shown in relation to dominant reflecting features.

hence the indices that include VIS are dominated by the internal leaf structure. Indices that are based on shortwave-infrared (SWIR) and near-infrared (NIR) regions are more related to leaf water content and canopy structure.

### 3.3.1 Normalized Difference Vegetation Index (NDVI)

The index reported to be the most widely used in remote sensing is the Normalized Difference Vegetation Index (NDVI) (Tucker, 1979). It is calculated as:

$$NDVI = \frac{NIR\ (4) - red\ (3)}{NIR\ (4) + red\ (3)} \quad (9).$$

Vogelmann (1990) examined the effectiveness of NDVI and short-wave infrared/near infrared index (SWIR/NIR) for measuring different types of damage in distinct forest communities in the eastern United States. Results of the study indicate that both indices may be successfully applied on broadleaf forests. However, NDVI was less appropriate for monitoring conifer forests. The study by Townsend et al. (2012) reports better results for indices considering SWIR bands than NDVI for predicting defoliation in broadleaf forests. Only few Landsat based forest change studies are reported in literature that utilize NDVI (e.g., Borrelli et al., 2014; Lee, 2008).

### 3.3.2 Enhanced Vegetation Index (EVI)

Another index similar to the NDVI is the Enhanced Vegetation Index (EVI). It was extended to reduce atmospheric influences and to optimize the vegetation signal. EVI is calculated as follows (Huete et al., 2002):

$$\text{EVI}=G*\frac{\text{NIR (4)} - \text{red (3)}}{\text{NIR (4)} + C_1 * \text{red (3)} - C_2 * \text{blue (1)} + L} \quad (10).$$

where NIR, *red* and *blue* are the atmospherically corrected surface reflectances of the respective bands, $G$ is the gain factor that scales the index, $L$ is a factor adjusting the canopy background (addressing the different radiant transfer of NIR and red trough the canopy), and $C_1$ and $C_2$ are coefficients of the aerosol resistance term, which take the blue band to correct for aerosol scattering in the red band (Huete et al., 2002). The coefficients were adopted from the original EVI algorithm implementation and were not adjusted to the dense forest canopies in the study area. They are defined as $L$=1, $C_1$=6, $C_2$=7.5, and $G$=2.5 (Huete et al., 2002). The advantage of EVI over NDVI is that it does not saturate even over dense forests (Saleska et al., 2007). Thus, it has improved sensitivity in high biomass regions. Because EVI is less sensitive for the soil background and stronger related to biophysical parameters such as Fraction of Absorbed Photosynthetically Active Radiation (FAPAR) it is often used in drylands (Cabello et al., 2012; Fang et al., 2005; Sjöström et al., 2011). Wardlow et al. (2007) used MODIS EVI time series to differentiate Crops in the U.S. Central Great Plains. Their results show similar performance for NDVI and EVI. Generally, NDVI and EVI show similar temporal behavior with EVI being less affected by soil properties, especially important outside the growing season (Lhermitte et al., 2011). Large scale classification is a common application of the MODIS EVI (Bagan et al., 2005; Boles et al., 2004). Several studies applied the EVI in tropical forests (Galvão et al., 2011). The use of EVI for forest change studies is debatable: Jin and Sader (2005a) report MODIS EVI to be inferior compared to NDVI. Melaas et al. (2013) successfully applied EVI to study long-term phenological variation of a deciduous broadleaf forest. A disadvantage of EVI may be that the soil adjustment factor $L$ in the EVI formulation (10) makes it more sensitive to topographic conditions than is the NDVI (Matsushita et al., 2007). The author is not aware of forest change studies exploring the Landsat based EVI.

### 3.3.3 Tasseled Cap (TC) Components Brightness, Greenness, and Wetness

Although being one of the older remote sensing concepts, the Tasseled Cap (TC) transformation (Kauth and Thomas, 1976) obtains vast attention in forest applications (Cohen and Spies, 1992; Cohen et al., 1995; Collins and Woodcock, 1996; Czerwinski et al., 2014; Dymond et al., 2002; Han et al., 2007; Meddens et al., 2013; Rogan et al., 2002; Skakun et al., 2003). A physically-based transformation of Landsat Thematic Mapper (TM) data is presented in Crist and Cicone (1984). The transformation was adapted to reflectance data by Crist (1985). As the present study is based on surface reflectance data, the transformation matrix by Crist (1985, Tab. 3.3.1) was used. The first three components of the TC transformation may be physically interpreted.

The first feature, brightness, is a weighted sum of all six reflective bands with the thermal band being omitted due to its different nature. Brightness is susceptible for those physical processes that affect total reflectance. This feature is sensitive for changes in soil properties such as particle size because all spectral bands react on changes in particle size distribution similarly. Brightness is less sensitive for changes in vegetation density. Increasing vegetation density would increase near-

Tab. 3.3.1: Tasseled Cap transformation matrix for Landsat TM reflectance data.

| Feature | Band 1 | Band 2 | Band 3 | Band 4 | Band 5 | Band 7 |
|---|---|---|---|---|---|---|
| Brightness | 0,2043 | 0,4158 | 0,5524 | 0,5741 | 0,3124 | 0,2303 |
| Greenness | -0,1603 | -0,2819 | -0,4934 | 0,7940 | -0,0002 | -0,1446 |
| Wetness | 0,0315 | 0,2021 | 0,3102 | 0,1594 | -0,6806 | -0,6109 |
| Fourth | -0,2117 | -0,0284 | 0,1302 | -0,1007 | 0,6529 | -0,7078 |
| Fivth | -0,8669 | -0,1835 | 0,3856 | 0,0408 | 0,1132 | 0,2272 |
| Sixth | 0,3677 | -0,8200 | 0,4354 | 0,0518 | 0,0066 | -0,0104 |

Source: Crist (1985)

infrared reflectance while decreasing visible response. Both contrasting effects would be leveled in the brightness feature (Crist and Cicone, 1984). The second feature, greenness, reflects the contrast between the sum of the visible bands and the near-infrared bands (Crist and Cicone, 1984). The third feature, wetness, contrasts the sum of the visible and near-infrared bands with the sum of the long wavelength-infrared bands. Wetness is sensitive for soil moisture and to a smaller extent for plant moisture because of the susceptibility of the long wavelength-infrared bands to moisture (Crist and Cicone, 1984). As the SWIR bands are known to be sensitive to shadowing and leaf water content, the wetness feature is also seen as sensitive not only to moisture but also to shadowing and structure of the target (Cohen et al., 1995; Horler and Ahern, 1986). Brightness, greenness and wetness can be combined to explore distinct image properties. Greenness and brightness form the plane of vegetation, wetness and brightness form the plane of soils, and greenness and wetness built up the transition zone. Each of those views allows for a better characterization of the classes contained in an image. A more detailed explanation can be found in Crist and Cicone (1984).

It was shown that TC components are susceptible to forest change caused by insects (Price and Jakubauskas, 1998; Skakun et al., 2003). TC features and TC based indices are also successfully used to detect stand replacing disturbances, e.g., harvest (Cohen et al., 2010, 2002). Of the three TC features that can be physically interpreted (i.e. brightness, greenness, and wetness), wetness has been probably most widely used. The TC wetness was used to develop the Enhanced Wetness Difference Index (EWDI) (Skakun et al., 2003) which is the difference of two TC wetness features from two images taken at different dates. The effects of the acquisition interval were explored by Franklin et al. (2005). They found that year-to-year change detection leads to overestimation of change whereas intervals of several years lead to underestimation of change. Lunetta et al. (2004) reported a minimum of 3-4 year acquisition frequency to monitor forest change in North Carolina. Their findings reveal that a higher frequency (1-2 years) could reduce omission errors.

Of the TC features wetness was used in many studies (Cohen et al., 1995; Collins and Woodcock, 1996; Jin and Sader, 2005b). Cohen et al. (1995) found that TC wetness is not only sensitive to moisture but also to structure. Their work revealed that TC wetness is a good indicator of maturity and structure and hence an important spectral variable for classifying closed canopy conifer forests. Although there is no common physical interpretation of TC wetness (Cohen et

al., 1995; Horler and Ahern, 1986), it is considered useful in forest change detection (Collins and Woodcock, 1996; Fiorella and Ripple, 1993).

### 3.3.4 Tasseled Cap Angle index (TCA)

Early studies, based on Landsat MSS, explored brightness and greenness since the third TC feature of MSS data cannot be interpreted (Kauth and Thomas, 1976); e.g., Li and Strahler (1985) developed a conifer forest canopy model and explored the response of the reflective bands as well as brightness and greenness of Landsat MSS data.
The brightness and greenness features were further investigated to develop the Tasseled Cap Angle (TCA) index (Powell et al., 2010) which is calculated as follows:

$$\text{TCA}=\arctan(\text{TC greenness}/\text{TC brightness}) \quad (11).$$

It was developed as predictor variable for aboveground biomass modeling for study regions in Arizona and Minnesota (Powell et al., 2010). A similar measure was developed by Duane et al. (2010). The so-called Tasseled Cap Distance (TCD) was used to map forest ages which were then translated to forest carbon stocks. TCD is calculated as follows:

$$\text{TCD}=\sqrt{\text{TC brightness}^2+\text{TC greenness}^2} \quad (12).$$

Both features – TCA and TCD – allow for the implementation of Landsat MSS data because TC brightness and greenness may be interpreted similarly for MSS and TM (Crist and Cicone, 1984). The work of Huang et al. (2002) demonstrated similar properties of the TC transformation for ETM+ data, although their transformation was adapted to at-satellite reflectance.

### 3.3.5 Disturbance Index (DI)

#### 3.3.5.1 Calculation and Interpretation

Another feature based on TC indices that allows for the characterization of forests and forest disturbances is the Landsat Disturbance Index (DI) (Healey et al., 2005). On the one hand it is a method of feature reduction since the three TC bands explaining the vast majority of variation in a scene are combined to one single feature. On the other hand the outcome is a single feature that differentiates between forest and disturbed (non-forested) areas. In its original definition the features are re-scaled to its standard deviation above or below the scene's mean forest value:

$$B_r=(B-B_\mu)/B_\sigma$$

$$G_r=(G-G_\mu)/G_\sigma$$

$$W_r=(W-W_\mu)/W_\sigma \quad (13).$$

where $B_r$, $G_r$ and $W_r$ are rescaled brightness, greenness and wetness, $B_\mu$, $G_\mu$ and $W_\mu$ are the mean forest brightness, greenness and wetness, and $B_\sigma$, $G_\sigma$ and $W_\sigma$ are the standard deviation of forest brightness, greenness and wetness. Mean and standard deviation are derived from a reference population that should be representative of the forest pixels in the scene (Healey et al., 2005).

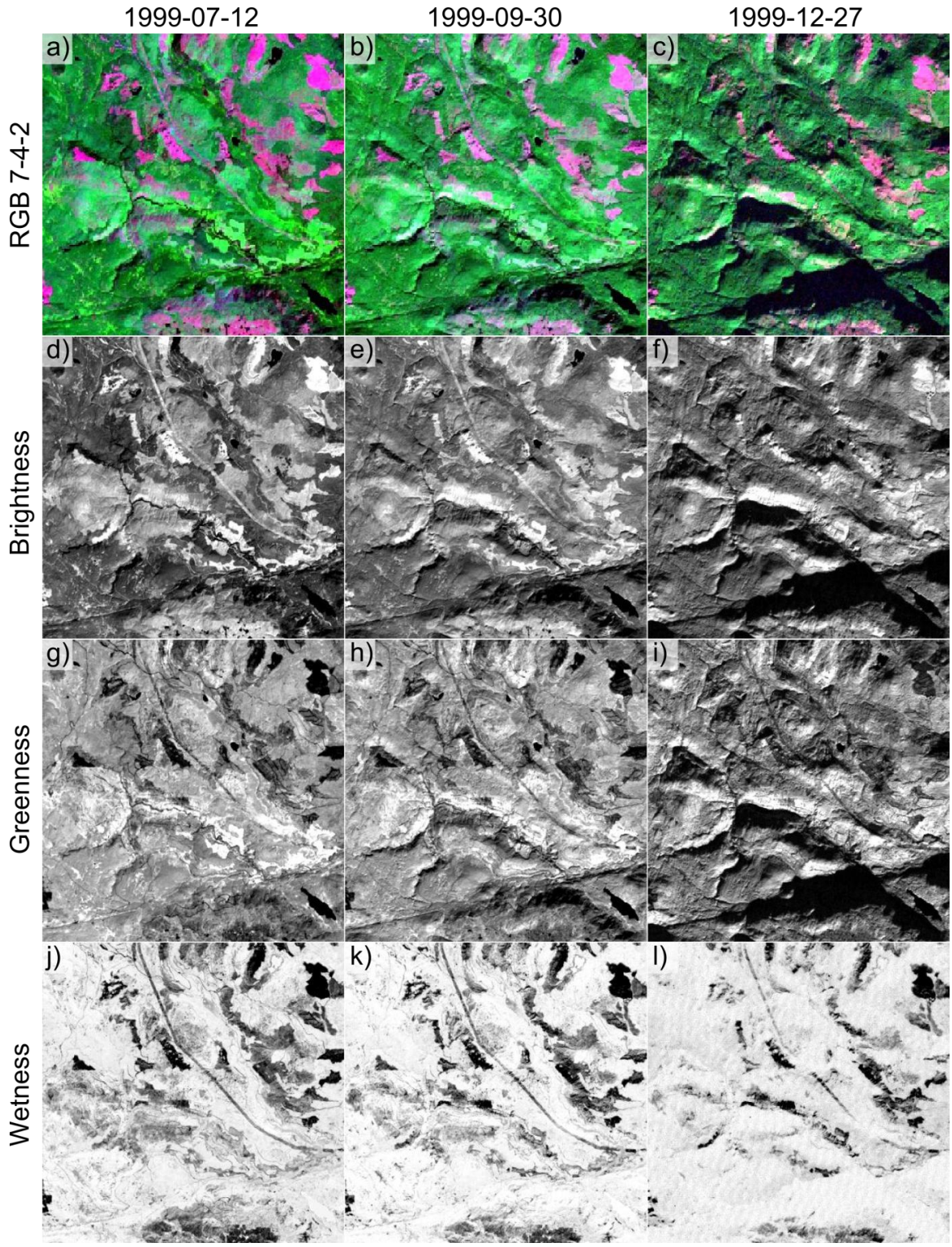


Fig. 3.3.2: TC components at different times of a year, July, September, and December images shown in left, center, and right column. a-c) Subset of Landsat scenes (RGB = 7-4-2), d-f) TC brightness, g-i) TC greenness, j-l) TC wetness.

However, this statement implies knowledge of the study area or at least availability of up-to-date forest maps. The DI is finally derived by combining the rescaled TC features:

$$DI = B_r - (G_r + W_r) \quad (14).$$

From the physical interpretation given in Crist and Cicone (1984) it is assumed that disturbances will decrease greenness and wetness, and increase brightness, and hence lead to high DI values. Undisturbed forests will have values around zero resulting from low brightness, high greenness and high wetness (Healey et al., 2005). Fig. 3.3.2 and Fig. 3.3.3 show that the DI is insensitive to within-scene illumination effects and separates very well disturbed from undisturbed forest areas. At the same time the figures confirm that the TC components are much more sensitive to illumination. Clearcuts appear red in the RGB representation (Fig. 3.3.3a-c) due to high brightness and low greenness and wetness values. Blue colors show strong response in wetness

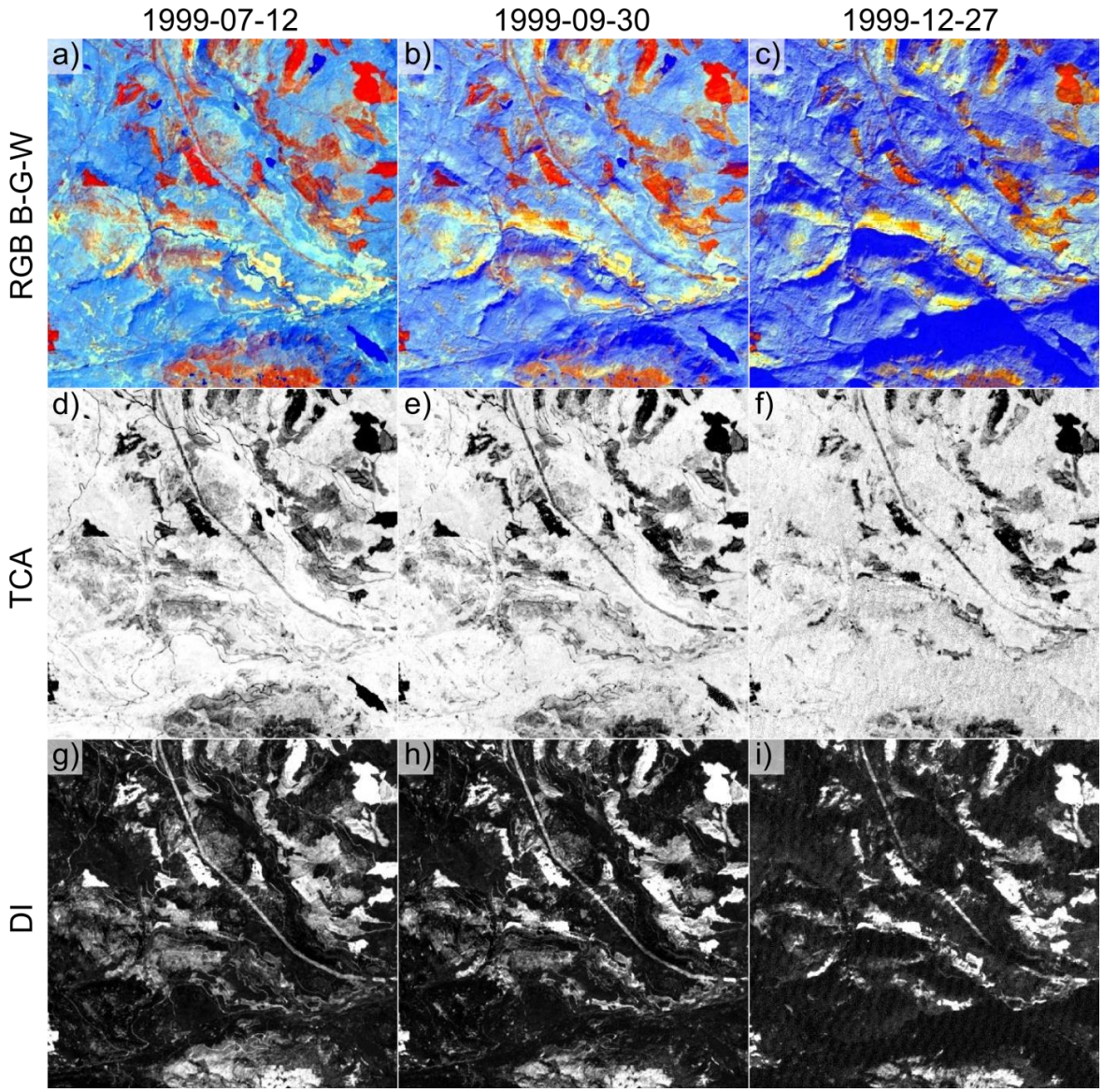


Fig. 3.3.3: RGB composite of TC components (a-c), TCA (d-f), and DI (g-i) at different times of a year, July, September, and December images shown in left, center, and right column.

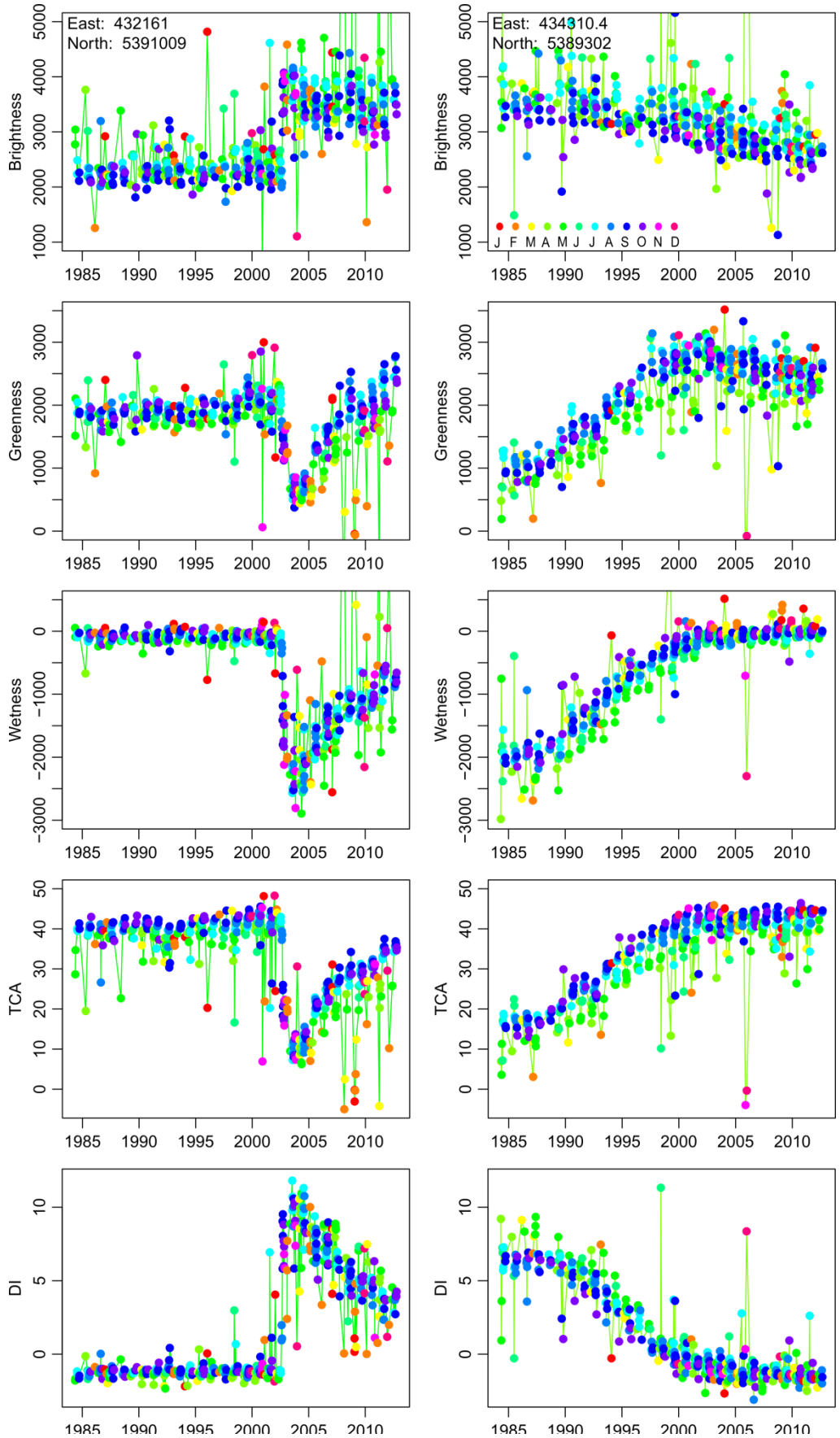


Fig. 3.3.4: Time series of TC brightness, greenness and wetness, TCA, and DI from two different locations (left column break approximately 2002, right column recovery after disturbance. Colors refer to the month of observation.

and lower brightness values whereas light blue and yellow areas have higher greenness values and are associated with young forests. TCA is also successful in separating disturbed from undisturbed areas (Fig. 3.3.3e-f). However, it is also visible that all indices are affected by changing illumination during the course of a year.

The relationship between season and TC components (and related indices) is shown in Fig. 3.3.4. The left column shows a time series that experienced a disturbance during the observation period, visible as strong increase in brightness and DI, and decrease in greenness, wetness and TCA. The right column shows a time series during the recovery phase following a disturbance that took place before the observation period started. Brightness and DI decrease as new forests establish whereas greenness, wetness and TCA increase smoothly. Fig. 3.3.4 indicates that brightness, greenness and wetness and related indices (i.e., TCA and DI) are sensitive for disturbances. Wetness, however, seems most susceptible to changes whereas greenness seems very sensitive to structural changes: the curve increases strongly during establishment of new vegetation and decreases slightly when new species start dominating. DI seems not to react on subtle changes in a mature forest but is very sensitive to disturbance. The figure also reveals a seasonal dependence of all TC components, particularly immediately after a strong disturbance. This might be due to the fact that pioneer species are deciduous trees that show more pronounced phenological patterns than coniferous trees. DI is only little affected by seasonal variation compared to the other TC related indices.

The disturbance index was presented as a tool to detect forest harvest. It was also used to distinguish between two types of disturbances (bark-beetle outbreak and clear-cutting) and to assess the associated disturbance dynamics (Hais et al., 2009). These authors also presented a alternate DI version that does not account for the greenness component (Hais et al., 2009):

$$DI' = W_r - B_r \quad (15).$$

The study by DeRose et al. (2011) took advantage of DI to assess spruce mortality caused by spruce beetle outbreak. The DI is promising for forest change assessment as it is highly associated with forest structure (Healey et al., 2006). The DI index was evaluated for its application in North America by Masek et al. (2008). Baumann et al. (2014) used the DI to detect windfall disturbance in the U.S. and in European Russia.

#### 3.3.5.2 DI Time Series Generation

The examples reviewed above use either bi-temporal datasets or annual (cloud free) datasets. Since DI is based upon a normalization of healthy forest mean and standard deviation its application to time series using all cloud free observations is challenging. The subset of forest pixels changes over time twofold: 1) previously disturbed areas become forest as a result of growth and forest development, 2) clouds, cloud shadows, and snow as well as data gaps (e.g., Landsat 7 ETM+ SLC-off) affect the subset of appropriate pixels. These two phenomena produce forest samples that change with each time step in size and location. Consequently, forest mean and standard deviation differ with each image. In the original article by Healey et al. (2005)

neither an indication is given how to deal with this situation nor is there detailed information about what is included in forested pixels that are representative for the scene. For example, it has not yet been explored if deciduous and coniferous should be analyzed separately. There is also no study that explored the influence of the forest mask or if disturbed forest patches (not necessarily cleared) may be included in the forest mask. Furthermore, the forest mask depends on the definition of forests.

For the usability of DI in time series analysis it is important to have more comprehensive understanding of the index and the influence of varying forest sample sizes used for its calculation. The study site used here has pronounced topography and heterogeneous forest structures with different ages and different species compositions. However, coniferous trees are dominating, and forests are the major land cover type. We explored four different ways to calculate DI based on equations (13) and (14):

1) The sample of forest pixels was taken from all cloud free observations that intersect with the annual MODIS Vegetation Continuous Filed (VCF) tree mask provided by DiMiceli et al. (2011). All pixels with more than 70% tree cover are labeled forest as recommended by Healey et al. (2005). The MODIS VCF product dates back until 2000. For the years before the product of 2000 was used. It can be assumed that for these years some areas are included that have less than 70% tree cover. But since recovery is rather slow in the region these areas are likely to be forested to a certain extent. Some mature and old-growth forests that have been cleared after 2000 may be excluded from the mask. Nonetheless, as there is pronounced topographic variability (resulting in relatively high standard deviation even for small sample sizes) in the region we assume that the resulting forests masks before 2000 are representative. The resulting forest mask is closest to the one proposed by Healey et al. (2005). This mask is hereafter called yearly forest mask.

2) The sample of forest pixels was taken from a relatively small region that was unchanged forest over the whole observation period. Unchanged areas were calculated by means of bi-temporal change detection between the first cloud free image in 1984 and a cloud free Landsat 8 OLI image taken in 2013 (Fig. 3.1.3). The final unchanged forest area was derived by intersecting the 2010 forest mask (>70% tree cover) with the unchanged portion the change detection result. The resulting mask is hereafter called constant forest mask.

3) The sample of pixels used to normalize the data does not include a forest mask. This method does not apply scaling using representative forest pixels, it rather considers all cloud free observations. It translates the resultant DI to a comparable data range of the "original" DI.

4) No scaling is applied. Equation (13) is omitted and the TC components are directly combined as in equation (14). Consequently the data range is different from the one of the previous DI representations.

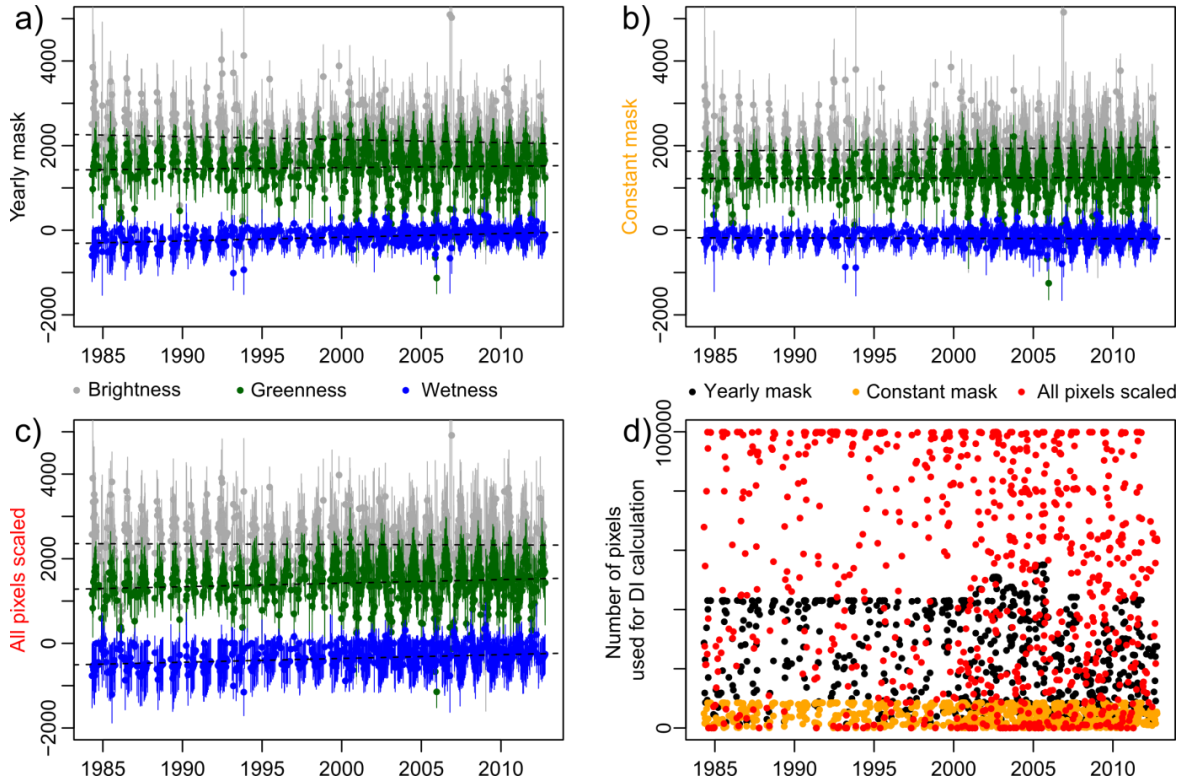


Fig. 3.3.5: TC brightness, greenness and wetness mean values of the three different masks used for DI scaling: a) yearly forest mask, b) constant forest mask, c) all pixels used for scaling. Standard deviation is indicated by vertical bars. The number of pixels per date used for the scaling is shown in d).

The four different DI representations were calculated. Results are shown for the same pixels as in Fig. 3.3.4. The mean values of TC brightness, greenness and wetness, and their standard deviation are shown in Fig. 3.3.5. In Fig. 3.3.5d) it can be seen that the number of pixels of the forest masks varies over time and also between the three approaches (note: the fourth approach omits scaling). Fig. 3.3.5 shows the TC features for the approaches with the yearly forest mask (a), the constant mask (b), and the use of all pixels for scaling (c). The three TC features are stable under the constant mask (b). Seasonal variation, however, is pronounced. The stability here is caused by the stable forest structure. Only old forests are included. The yearly mask also accounts for changes of the forest mask including new ones when a tree cover of 70% is reached and disregarding pixels when they were cleared. Vast areas have been cleared before the observation period. This causes increasing greenness, slightly decreasing brightness (when deciduous trees are replaced by coniferous trees) and increasing wetness (a). If all pixels are used for scaling the resultant sample is much larger and contains more seasonal variation (c).
Fig. 3.3.6 and Fig. 3.3.7 show how the resulting time series of the several DI approaches coincide. There is a slight increase of the reference DI (i.e., the one calculated with the yearly forest mask) during the stable forest period (Fig. 3.3.6a). This might be caused by pre-2000 forest mask which were not derived from the data itself. From Fig. 3.3.7a it is indicated that DI is stable during the stable forest period after 2000. More important is the difference to the other approaches. The plots show the respective DI time series; the difference plot refer to *Z*-transformed values. Those are calculated as:

$$Z = \frac{X - \mu}{\sigma} \quad (16),$$

where $X$ is the value to be transformed, $Z$ is the transformed value of $X$, and $\mu$ and $\sigma$ are mean and standard deviation of $X$. The difference plots are on top of each DI plot. It can be seen that there are differences between all approaches. Under the constant mask DI is stable during the stable forest period, i.e, there is neither increase nor decrease (Fig. 3.3.6b, Fig. 3.3.7b). The profiles of the DI approach using all pixels for scaling coincide with the shape of the time series based on the yearly mask. The data range is lower, impeding the detection of changes (Fig. 3.3.6c, Fig. 3.3.7c). If no scaling is applied at all, then the data range within a time series largely depends on the relative magnitude of brightness, greenness and wetness. The resultant non-scaled DI would be rather low when small values are used and rather high when the TC components are high. Spatial comparison would be impeded in this case. If no scaling is applied, unwanted seasonal patterns appear. All DI approaches are rather insensitive to seasonality except the one that omits scaling – there is only little seasonal variation in plots a, b, and c of Fig. 3.3.6 and Fig. 3.3.7 but considerable seasonal variation in plot d.

The time series using the yearly forest mask (and to a certain extent also the constant mask approach) is consistent over time. There are only few outliers – variation during stable stages is very low indicating that varying sample sizes only little affect DI calculation in our study site. Transferability has to be confirmed. Scaling the TC components based on a constant mask is probably the most reliable way to achieve consistent time series since the mask is most reliable.

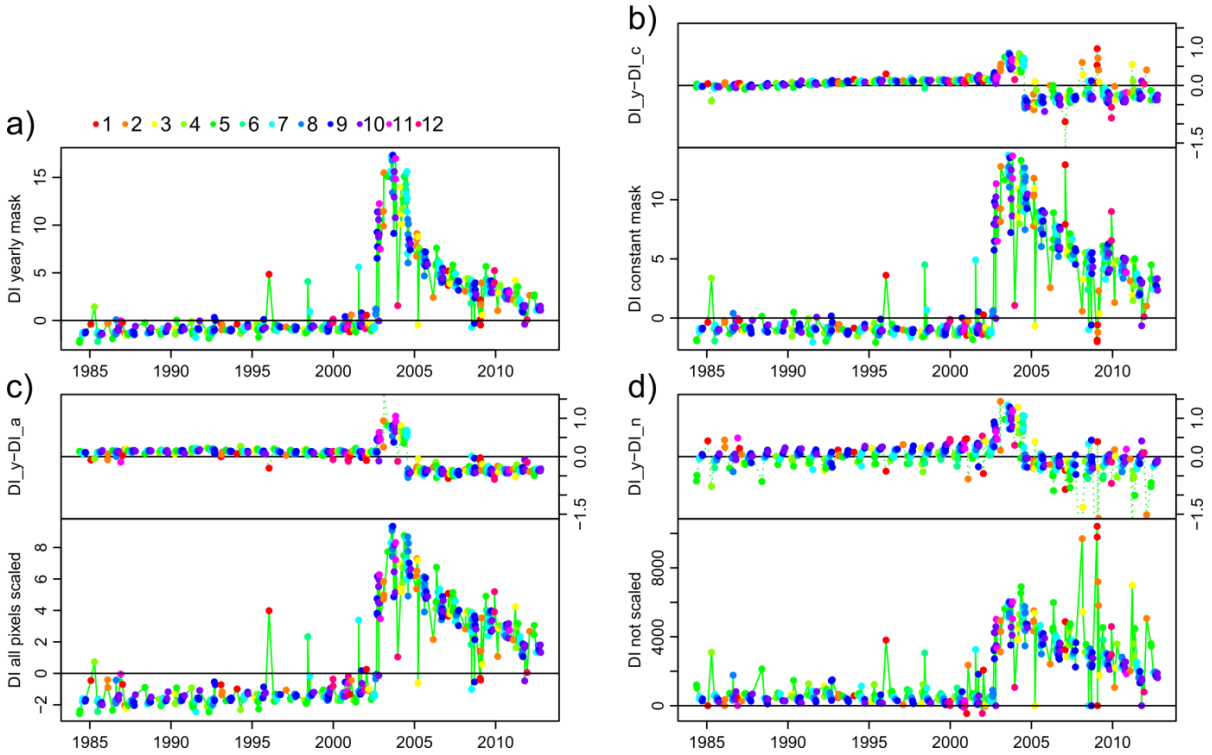


Fig. 3.3.6: Standardized DI time series of a pixel with a clearcut in late 2002 for a) yearly forest mask, b) constant forest mask, c) all cloud free pixels used for scaling, and d) no scaling applied. The upper parts of the plots show the difference to the yearly forest mask approach. Colors refer to months of the year.

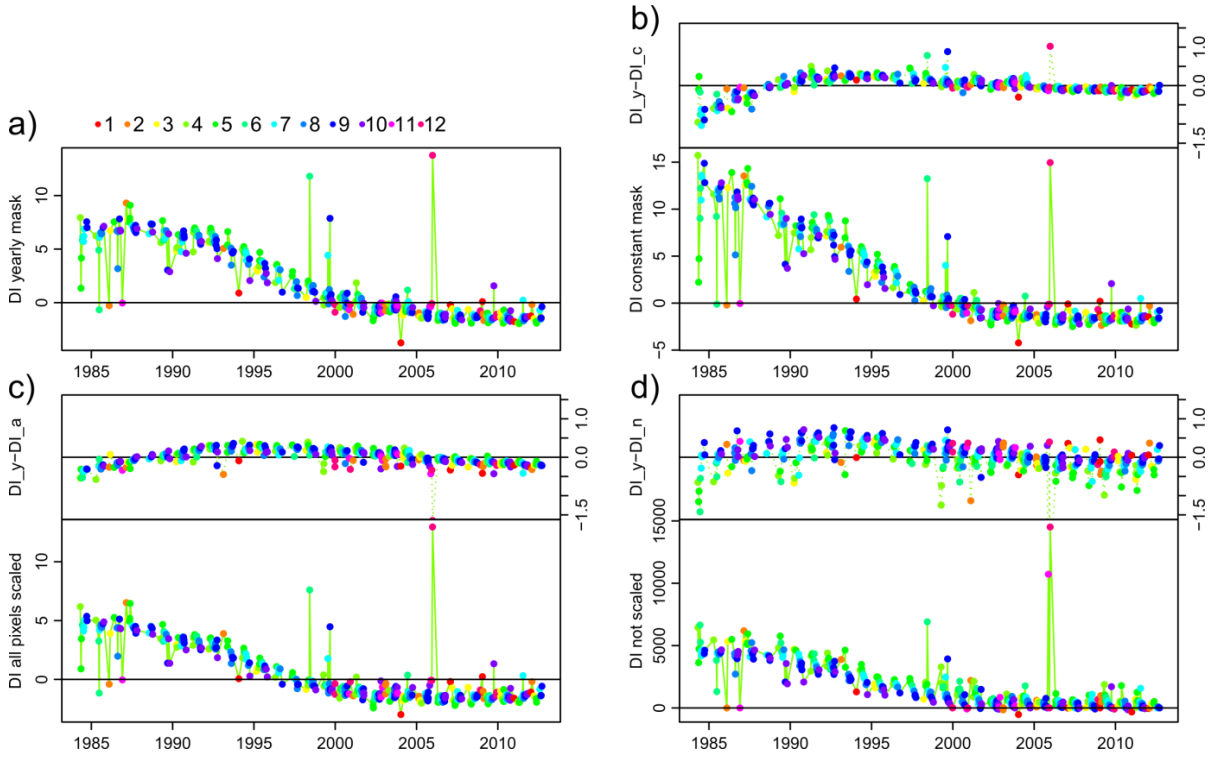


Fig. 3.3.7: Same as Fig. 3.3.6 for a pixel showing forest recovery.

This approach, however, may be limited by the availability of sufficient forest pixels that are unchanged over the whole period and that are representative for the scene's forests. As there is huge variation in managed forests, old forest stands are most likely not representative. Due to high variation even within the old forests caused by topography the constant mask approach may be adequate. In our case the number of pixels of the constant forest mask is small although almost the whole study region consists of forests and clearcuts. When clouds occur it is likely that there are not sufficient pixels available for scaling. Hence, the yearly forest mask approach is based on more representative samples but requires reliable forest masks for each year. Applying scaling with the statistics of all pixels of a scene works comparably well in the present study due to the huge forest coverage. If forests were only a minor class the resultant DI would be more affected. We thus do not suggest to use this approach. Omitting scaling is not considered an adequate solution since the resultant DI signal is blurred and undesired seasonal effects occur.
From these findings we can conclude that the calculation of DI with varying representative forest samples is adequate to generate consistent time series. In the following we use the DI based on the yearly forest mask.

### 3.3.6 Normalized Difference Moisture Index (NDMI)

An index based on the NIR and SWIR bands of Landat is the Normalized Difference Moisture Index (NDMI) (Hardisky et al., 1983; Wilson and Sader, 2002), sometimes also referred to as Normalized Difference Infrared Index (NDII):

$$\mathrm{NDMI}=\frac{\mathrm{NIR}\ (4)-\mathrm{SWIR}\ (5)}{\mathrm{NIR}\ (4)+\mathrm{SWIR}\ (5)} \qquad (17).$$

The SWIR region was identified as most closely associated with forest removal (Healey et al., 2006). Hence, SWIR bands and variables that are strongly influenced by the SWIR bands (e.g., TC wetness) are valuable for the detection of forest removal. As TC wetness and NDMI both reflect water absorption in the SWIR region, they are supposed to be similarly sensitive to forest change (Wilson and Sader, 2002). Although NDVI is widely used, the less frequently used NDMI may produce higher accuracies for detecting forest harvest (Wilson and Sader, 2002). (Jin and Sader, 2005b) reported high correlation between NDMI and TC wetness resulting in similar change detection accuracies. An advantage of the NDMI over TC wetness may be its simplicity. The NIR and SWIR image bands are sensitive to foliage water content and fraction of dead leaf material (Hunt et al., 1987). Hence, Coops et al. (2010) utilized NDMI to assess changes in forest fragmentation following infestation based on a Landsat time series. Goodwin et al. (2010, 2008) assessed infestation dynamics in conifer forests based on NDMI. Superiority of NDMI (and SWIR/NIR ratio) over NDVI is also reported for defoliation prediction modeling in broadleaf forests (Townsend et al., 2012). Meddens et al. (2013) compared several spectral indices (red/green ratio, NDVI, SWIR/NIR ratio, NDMI, and TC features brightness, greenness and wetness) to detect bark beetle-caused tree mortality. They report highest accuracies for the TC features and the SWIR/NIR ratio.

### 3.3.7 Normalized Burn Ratio (NBR)

Another spectral index accounting for the SWIR information was developed by Hunt and Rock (1989). This index is sensitive to fire activity. Hence, it was used to detect fire-caused disturbances with Landsat data and termed Normalized Burn Ratio (NBR) (Key and Benson, 1999). It is calculated like the NDVI except using Landsat TM/ETM+ band 7 instead of the red band as follows:

$$\mathrm{NBR}=\frac{\mathrm{NIR}\ (4)\text{-}\mathrm{SWIR}\ (7)}{\mathrm{NIR}\ (4)+\mathrm{SWIR}\ (7)} \qquad (18).$$

The index is similar to NDMI but uses Landsat band 7 instead of band 5. The SWIR spectral information is considered useful in the detection of fire-caused disturbances (Miller and Yool, 2002). The NBR is often used to compare before and after-event images (X. Chen et al., 2011b). (X. Chen et al., 2011b) used one pre-fire image as baseline and calculated the difference of several post-fire images to this baseline image. They took images acquired with different time spans after a fire and compared the sensitivity of several indices to the burn severity and the recovery after the fire. They found high correlations of NDVI and EVI with the burn severity. Long-term recovery was better captured by NBR and a measure called the Integrated Forest Index (IFI) (X. Chen et al., 2011b). In a different study, (X. Chen et al., 2011a) estimated aboveground forest biomass with different spectral indices. Studies like these are important to estimate carbon release caused by fire. A good understanding of post-fire recovery processes may be achieved by time series analysis of the NBR (Huang et al., 2010a). Fire does not play a significant role on Vancouver Island. However, NBR was considered here for comparison purposes.

### 3.3.8 Normalized Difference Built-up Index (NDBI)

An index once developed to distinguish built-up areas from other land-use classes is the Normalized Difference Built-up Index (NDBI) (Zha et al., 2003). The index is calculated as follows:

$$NDBI = \frac{SWIR\ (5) - NIR\ (4)}{SWIR\ (5) + NIR\ (4)} \quad (19).$$

In fact, it is the inverse of the NDMI. Whereas the NDMI emphasizes plant water content and soil moisture, NDBI is supposed to highlight artificial surfaces with high index values. Other studies show that NDBI is only little correlated with impervious surfaces (Deng and Wu, 2012). Consequently, it is not appropriate to term the index "built-up index". (Zhang et al., 2009) found high correlation between NDBI and Land Surface Temperature (LST). This is not surprising since NDMI (and consequently its inverse NDBI) is sensitive to plant water and soil moisture both of which are reflected by their thermal response.

From the literature reviewed above it can be concluded that SWIR bands are highest correlated to forest removal and insect defoliation. Several studies report that the relationship between NIR bands (and related indices) and forest structure is less consistent (Healey et al., 2006). The relationship between NIR and forest structure can be influenced by several factors including understory conditions (Danson and Curran, 1993; Spanner et al., 1990), species composition (Olsson, 1994), and thinning grade and coverage of cutting waste on the ground (Nilson et al., 2001). Furthermore, the SWIR information is most effective in separating fires from clearcut harvest (Schroeder et al., 2011).

### 3.3.9 Spatio-Temporal Variation of Spectral Indices

#### 3.3.9.1 Methods

Wulder et al. (2004b) explored the reflectance of a dense conifer forest in British Columbia, Canada, with a set of within-year images and a set of near-anniversary images. They could show that that reflectance varies strongly over the course of one year whereas the near-anniversary signal is in agreement.

Although there are few studies that explored the illumination and viewing geometry effects on the TC (e.g., Dave, 1981) there is no comprehensive spatio-temporal evaluation of different TC features and spectral indices for forest applications. However, Song and Woodcock (2003) identified atmosphere, topography, phenology, and sun and viewing angles as major uncertainty factors in using multi-temporal Landsat images for subtle change detection. Their analysis evaluated NDVI and the TC features brightness, greenness and wetness. The study revealed that atmospheric effects reduce NDVI and greenness, and increase brightness and wetness. Topography has strong effects on brightness and greenness, but has minimal effects on NDVI and wetness.

In this section, the spatio-temporal variability of the ten indices NDVI, EVI, TC brightness, TC greenness, TC wetness, TCA, DI, NDMI, NDBI, and NBR is demonstrated. To explore the spatio-temporal behavior of the indices the cloud statistics were screened and those years identified that have most cloud free images covering most parts of a year. All cloud free images of the selected years were visually checked. Images recorded as cloud free by Fmask with portions of clouds or cloud shadows that have not been captured were removed. The best series of images was found for 2002 where snow cover disappeared earlier than in other years (e.g., 1995 and 1999). The 2002 images cover the course of a year (Tab. 3.3.2). Hence, illumination conditions vary considerably. The main purpose, however, is to show the spatio-temporal variation of indices over forests and fresh clear cut areas. It is broadly accepted that vegetation and its spectral response are dynamic, showing long-term and seasonal changes. In the present study, the absolute magnitude of spectral variability of a single pixel is a minor effect. Instead of studying intra-annual variability of a single pixel we aim at showing the differences in this intra-annual variability of different indices amongst pixels at different locations caused by terrain and illumination.

To ensure that no land cover changes took place during the time observed we applied bi-temporal change detection on two images taken under identical acquisition conditions. These images are two summer images from 2001 and 2003 (i.e, the years before and after the observation period). A change/no-change mask was derived by applying RCVA. The resultant mask was further overlain with a forest mask derived from the vegetation continuous field (VCF) product (DiMiceli et al., 2011; Hansen et al., 2003). As proposed by (Healey et al., 2005) a threshold of 70% tree cover was chosen to separate forest. Only those pixels identified as forest and being unchanged between 2001 and 2003 were selected as forest pixels for further analysis. As no detailed forest species map is available for the study site, the whole sample was treated as one forest class. Similarly, all fresh clear cuts have been treated as one class although there may be differences amongst them regarding left debris etc. Fresh clear cut pixels are those that have been identified as change with the bi-temporal change detection procedure. The integration of all

Tab. 3.3.2: Scenes used for spatio-temporal index evaluation.

| Date | Sensor | Path/Row |
|---|---|---|
| 2002/02/26 | Landsat 7 ETM+ | 047/026 |
| 2002/06/09 | Landsat 7 ETM+ | 048/026 |
| 2002/06/26 | Landsat 5 TM | 047/026 |
| 2002/07/11 | Landsat 7 ETM+ | 048/026 |
| 2002/07/12 | Landsat 5 TM | 047/026 |
| 2002/08/12 | Landsat 7 ETM+ | 048/026 |
| 2002/08/13 | Landsat 5 TM | 047/026 |
| 2002/08/28 | Landsat 7 ETM+ | 048/026 |
| 2002/09/13 | Landsat 7 ETM+ | 048/026 |
| 2002/09/21 | Landsat 5 TM | 048/026 |
| 2002/09/22 | Landsat 7 ETM+ | 047/026 |
| 2002/10/15 | Landsat 7 ETM+ | 048/026 |
| 2002/10/16 | Landsat 5 TM | 047/026 |
| 2002/10/23 | Landsat 5 TM | 048/026 |
| 2002/10/31 | Landsat 7 ETM+ | 048/026 |
| 2002/11/01 | Landsat 5 TM | 047/026 |

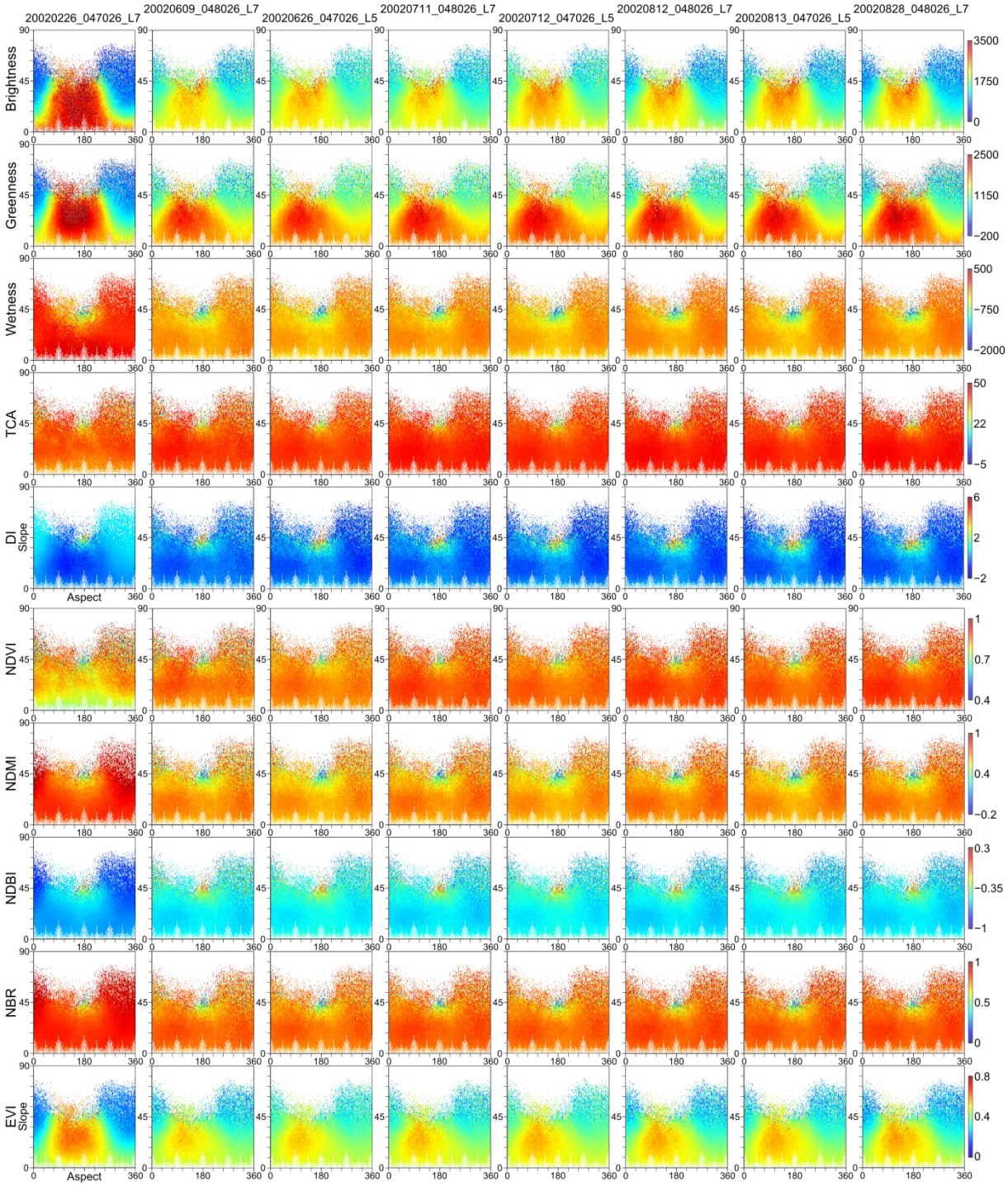


Fig. 3.3.8: Spatio-temporal behavior of the selected indices for unchanged forest pixels.

forest types into one forest class does not allow for species specific analysis. As the subset used in the study is identical for all images we assume that spatio-temporal variation can be comparable between the different indices.

The spatial stability of indices is important for any classification purpose where little intra-class variation is appreciated by most state-of-the-art classifiers. It is less affecting methods working on a temporal sequence of single pixels (as do most time series methods). Temporal variability, however, is affecting classification as most natural classes show seasonal patterns along with long-term variation, but also time series methods. Irregular shifts of these patterns, e.g., offsets in

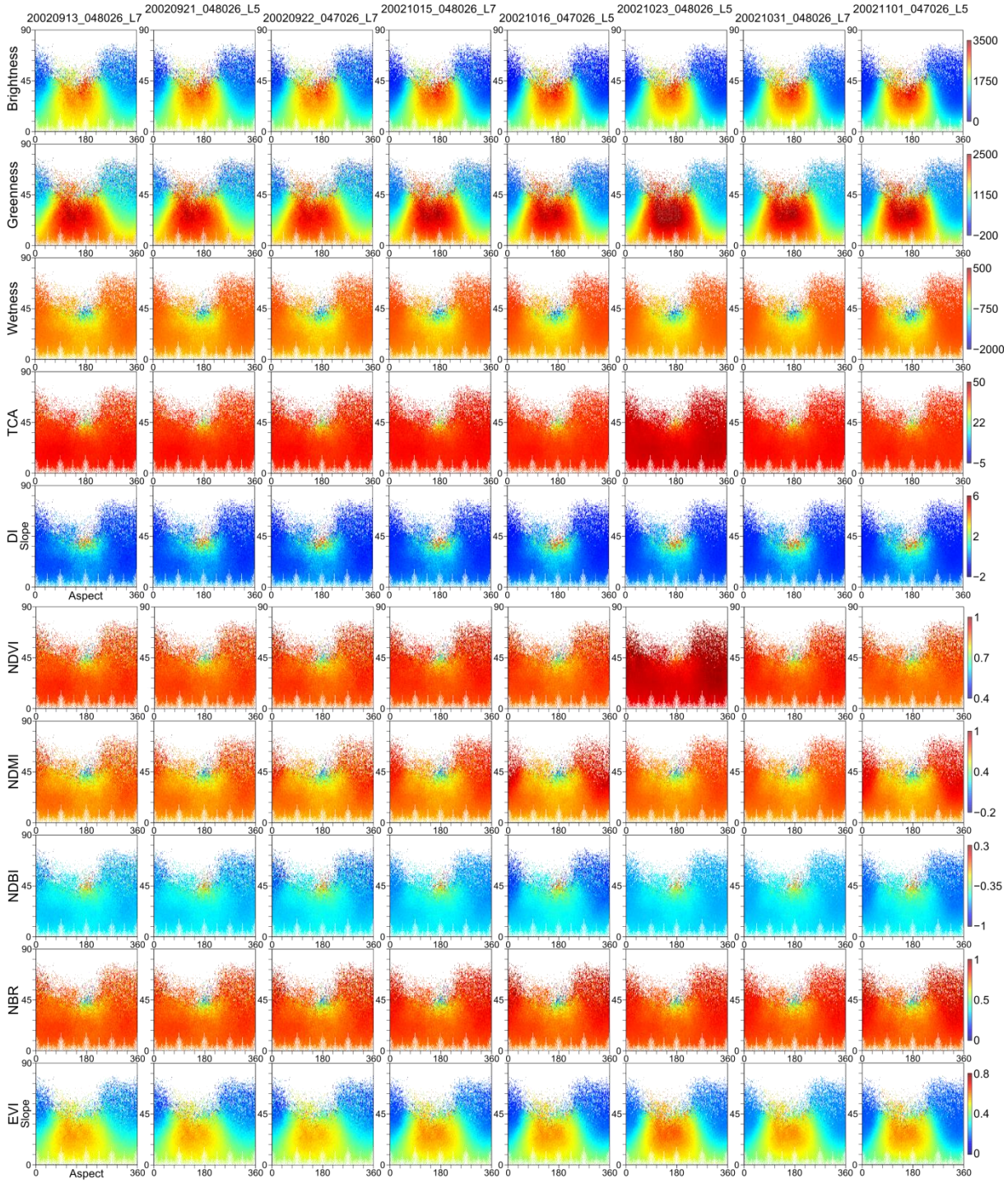


Fig. 3.3.8 (continued).

greening, impede analysis. Ideally, spectral indices vary only according to the condition and state of the observed class. Due to illumination, topography, and BRDF effects the spectral response varies spatially and temporally.

### 3.3.9.2 Results

The data range of the indices differs considerably. Furthermore, the way they are responding to abrupt changes on the ground differs as well. Some indices such as DI, TC brightness, and NDBI

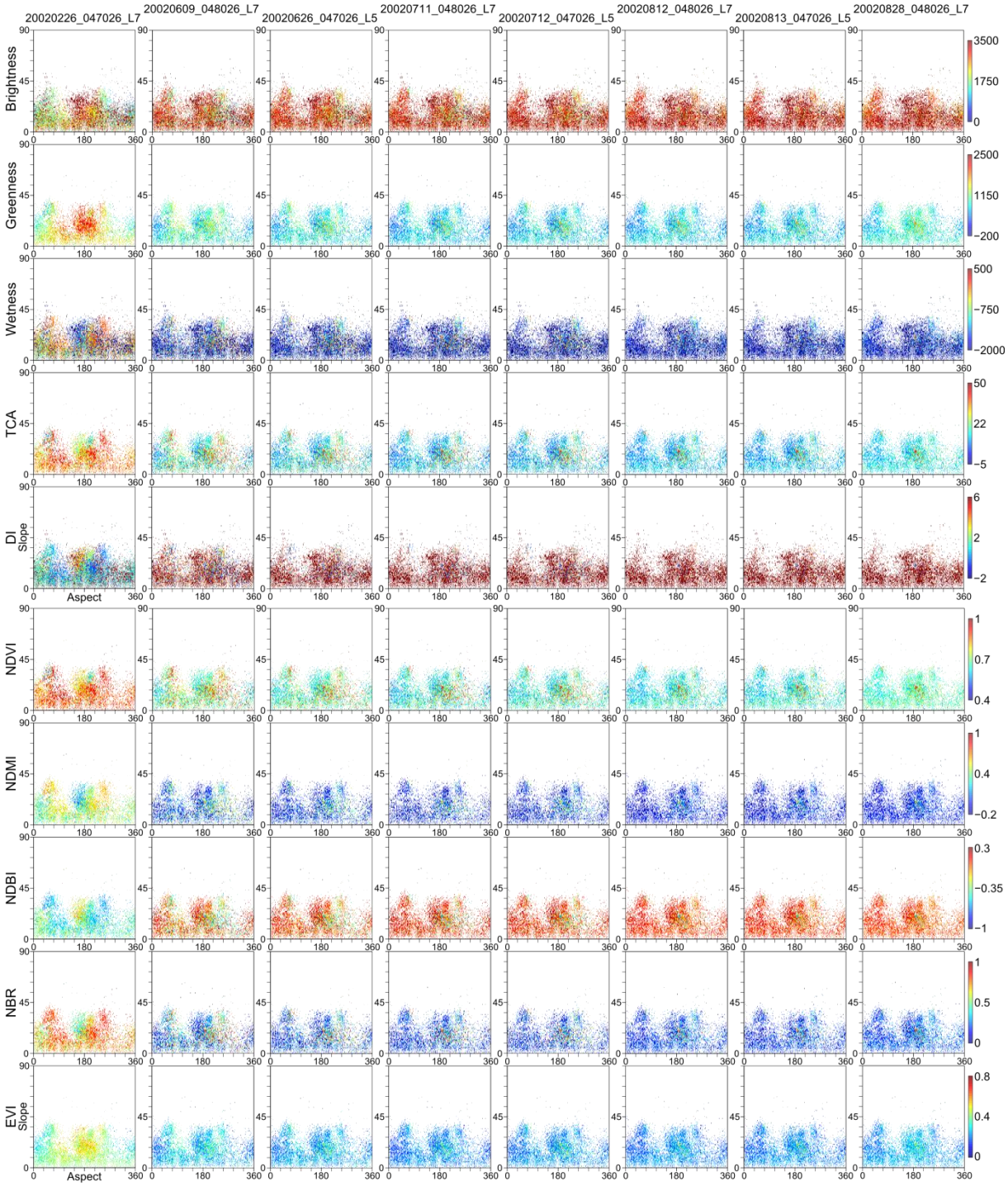


Fig. 3.3.9: Spatio-temporal behavior of the selected indices for fresh clear cuts.

increase whereas the other indices considered here decrease abruptly when a change event occurs. Consequently, direct comparison of the indices is not possible.

The mean values for each slope/aspect configuration of forests and fresh clear cuts in the study site are plotted in Fig. 3.3.8 and Fig. 3.3.9, respectively. The scene from 2002/02/26 is affected by snow cover; the scene from 2002/10/23 has partial haze contamination. It can be seen that clear cuts did not appear in extreme slopes (Fig. 3.3.9). The sample size of fresh clear cuts is much smaller than that of forests. Nonetheless, some general patterns are revealed by the plots. Most indices show higher variation with respect to slope than with varying aspect angles. TC

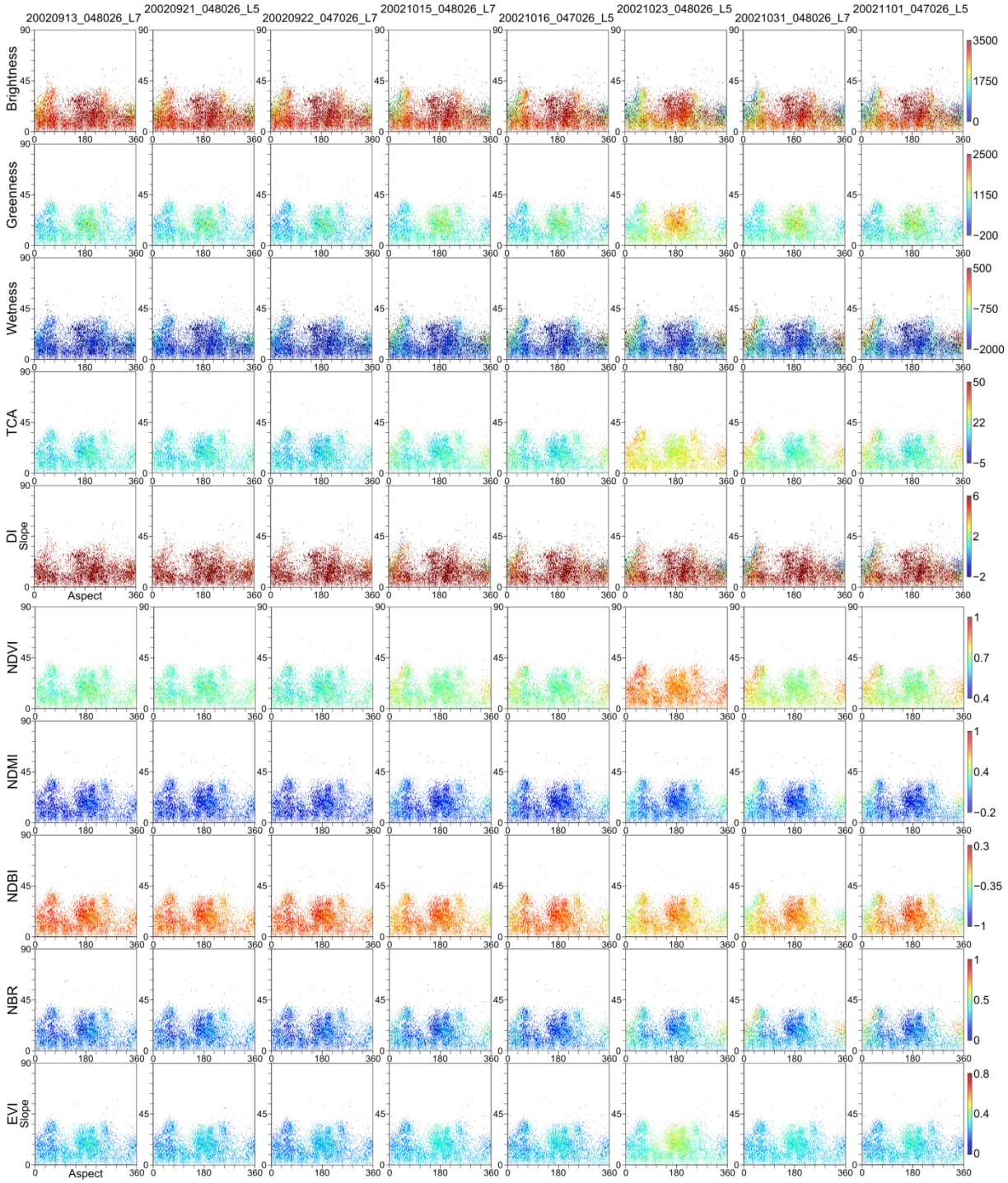


Fig. 3.3.9 (continued).

brightness and greenness as well as EVI show huge variation in both dimensions. From the indices explored here, NDMI is probably least affected by seasonal changes. Most pronounced seasonal variation occurs in TC brightness, TC greenness and EVI. Our results show that all indices are affected by illumination (Fig. 3.3.8, Fig. 3.3.9). However, DI and TCA are less sensitive to illumination than Tasseled Cap features alone. The spectral indices that include SWIR (NDMI, NDBI, NBR) are generally less sensitive to changing illumination conditions and topography than those that include visible bands (NDVI, EVI). Brightness is the most responsive TC index to incidence angle whereas wetness is least correlated to sun illumination (Cohen and

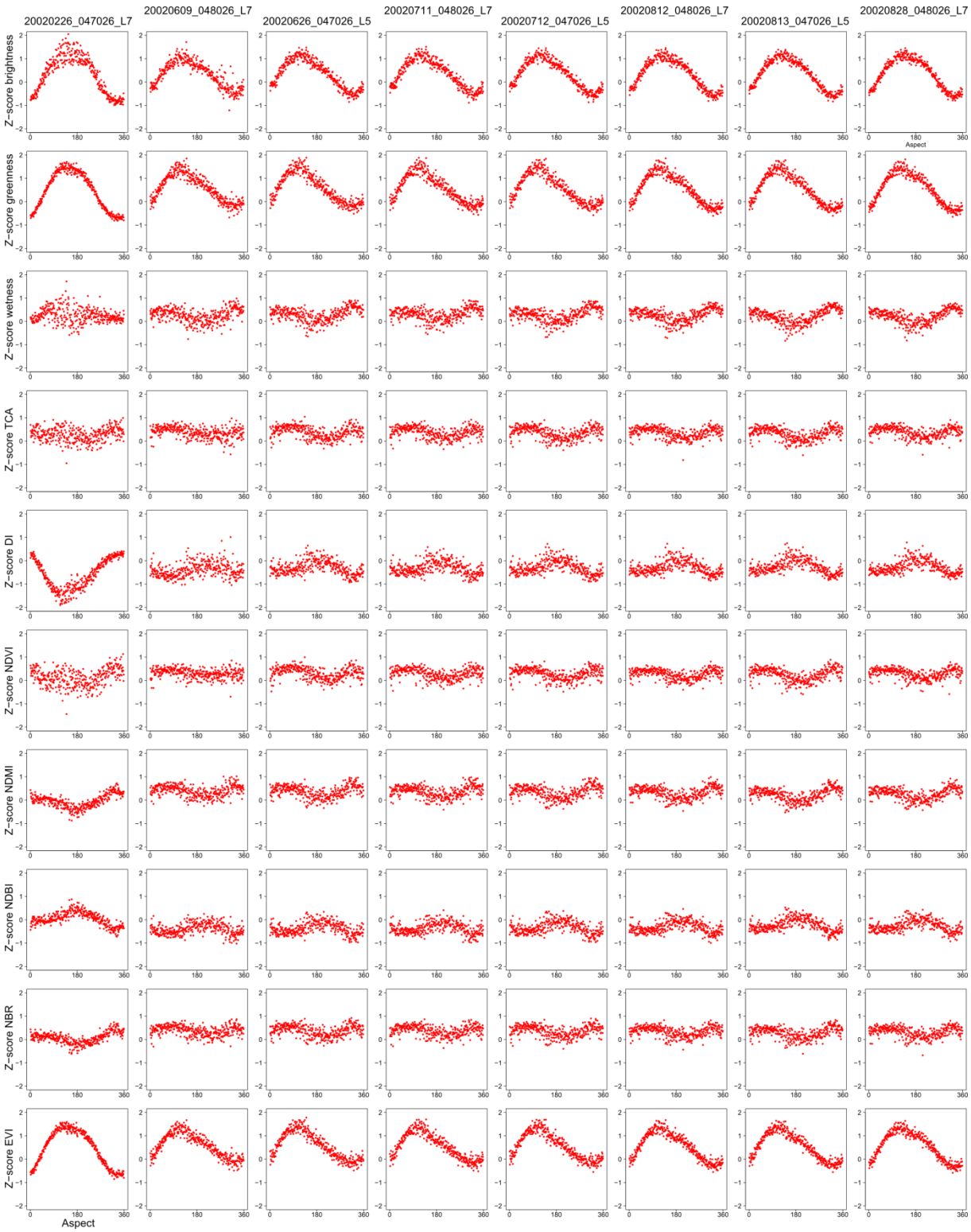


Fig. 3.3.10: Mean of *Z*-transformed index values of all forest pixels at 20° slope (2002/02/26 – 2002/08/28).

Spies, 1992; Cohen et al., 1995). The decreased sensitivity of wetness to shadowing compared to the other TC features make it suitable to differentiate between old-growth and mature forest types (Fiorella and Ripple, 1993). As wetness is relatively insensitive to sun illumination angle, it is advantageous over other indices or original TM bands for some applications (Cohen and Spies, 1992; Cohen et al., 1995). The first statement is confirmed by our findings. Other indices show

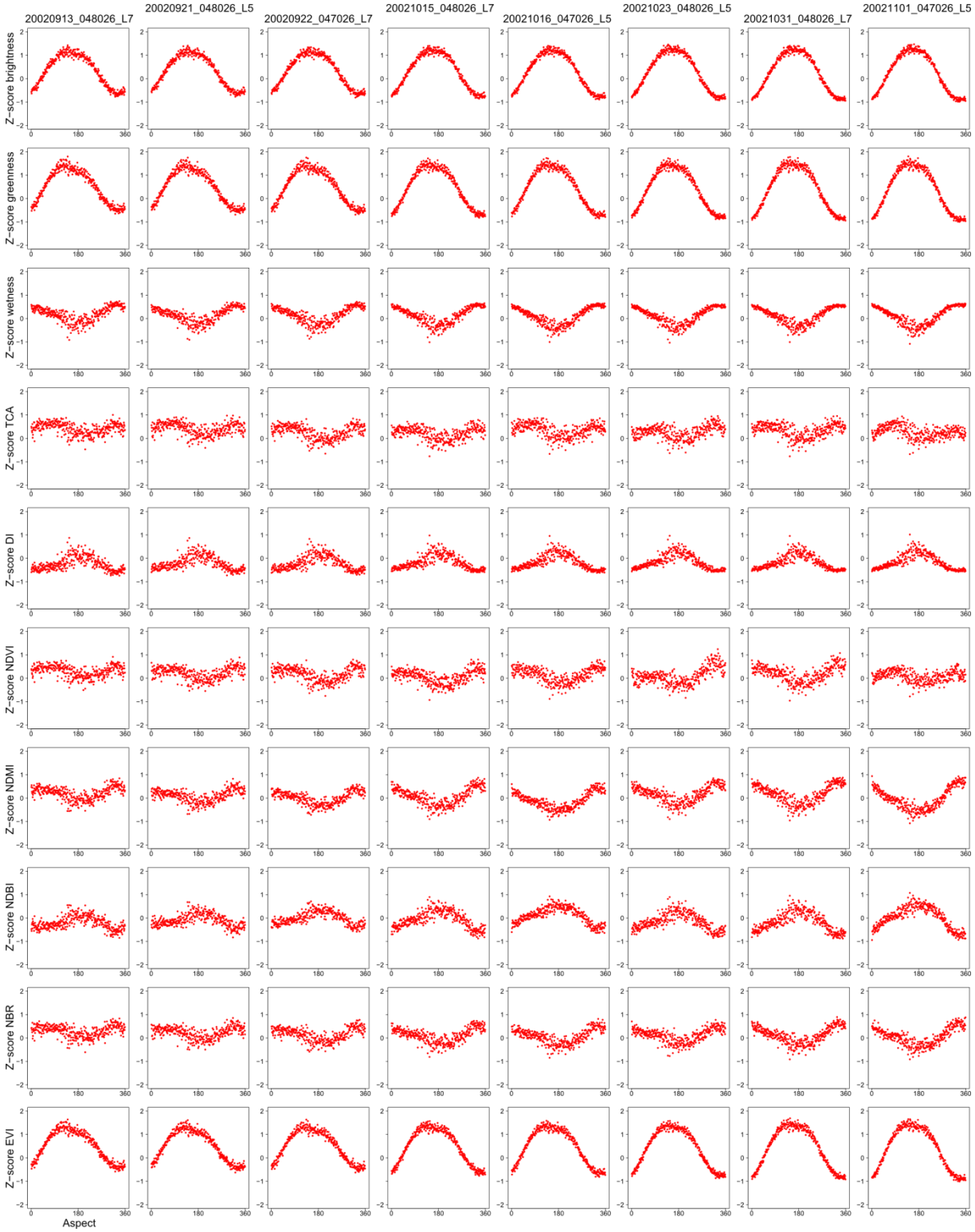


Fig. 3.3.10 (continued; 2002/09/13 – 2002/11/01).

similar temporal behavior to wetness, e.g., NBR, NDMI, and NDBI. The reason is most likely that they are also strongly influenced by SWIR. The DI is strongly affected by wetness and hence the SWIR bands. Consequently, DI is stable over time. The temporal changes in each index can be explained with the interaction of topography with sun angle. Sun angle effects are furthermore confounded with phenology (Song and Woodcock, 2003). Another representation of the spatio-temporal index behavior is given in Fig. 3.3.10 and Fig. 3.3.11 where the mean and standard

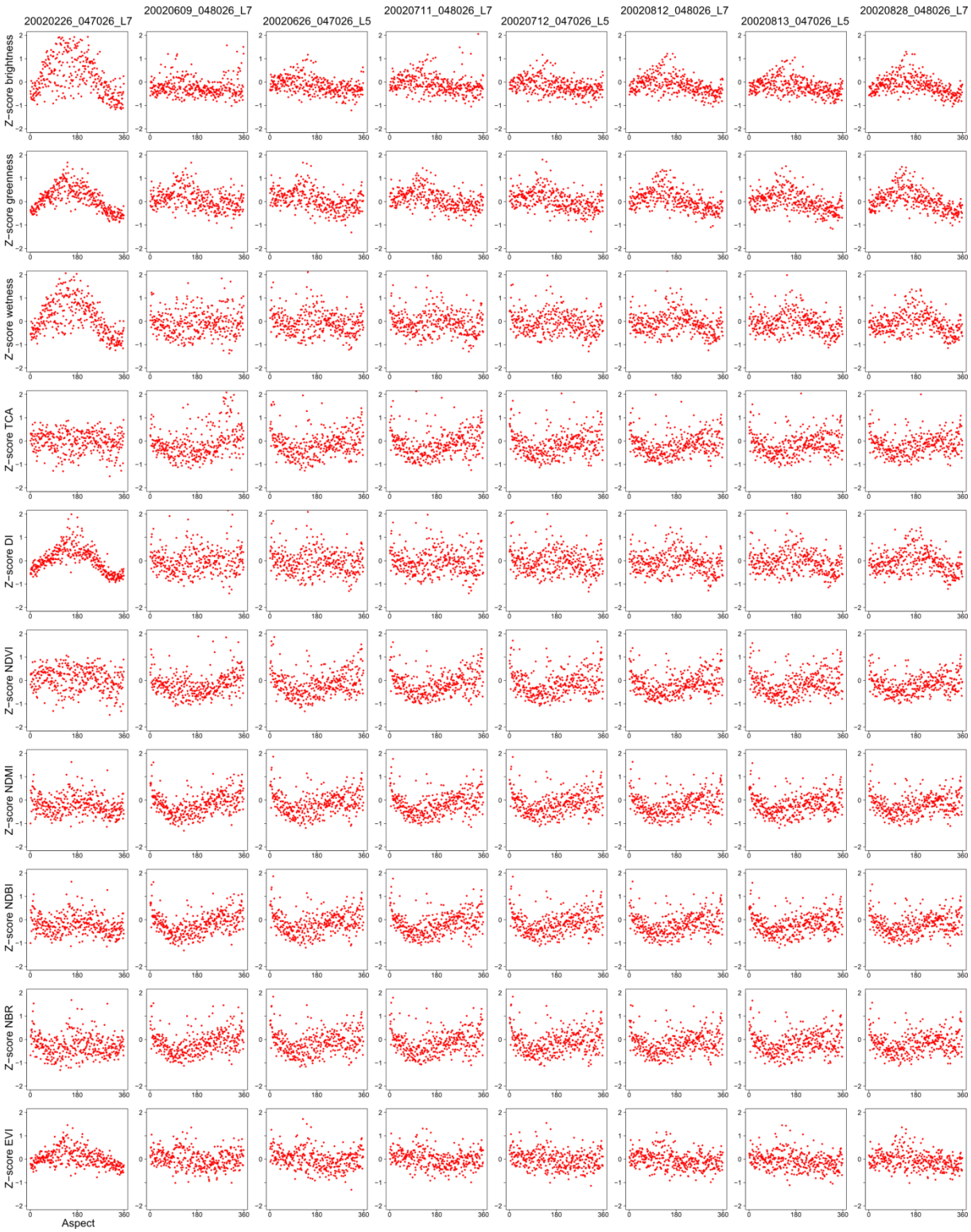


Fig. 3.3.11: Standard deviation of *Z*-transformed index values of all forest pixels at 20° slope (2002/02/26 – 2002/08/28).

deviation are shown for all forest pixels at 20° slope. Hence, only aspect angles vary. For comparison reasons the plots of Fig. 3.3.10 and Fig. 3.3.11 have been *Z*-transformed. It can be seen that brightness, greenness and EVI have strongest spatial variation caused by illumination (i.e., changing aspect angles) and also most pronounced seasonal variation. As an effect of phenology and changing illumination conditions, standard deviation becomes less scattered in

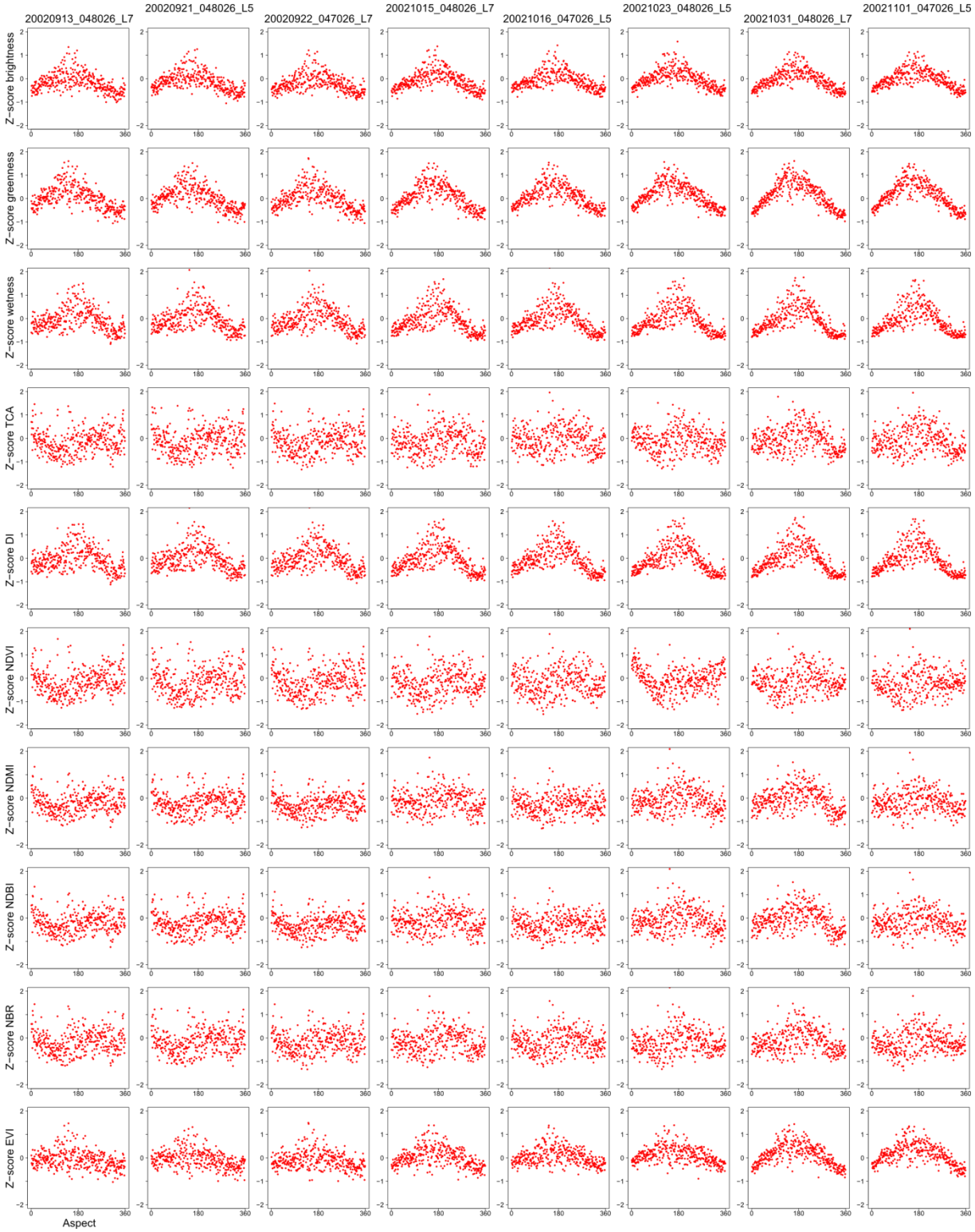


Fig. 3.3.11 (continued; 2002/09/13 – 2002/11/01).

late season. The first column (as of 2002/02/26) differs due to snow patches. For all other plot some clear patterns can be derived for mean values: scattering at sun averted areas becomes smaller during the course of a year. Brightness, greenness, and EVI develop a bell-shaped curve that is more distinct in fall scenes. Note, disregarding the left most column, the time series starts in early June and ends up in November. Indices like TC wetness, DI, NDMI, NDBI, and NBR have little variation until August and then start forming bowl- or bell-shaped curves – much less

pronounced than brightness, greenness, and EVI. NDVI and TCA become more scattered during the year but they do not develop bowl- or bell-shaped curves (Fig. 3.3.10). The standard deviation plot of the indices at 20° slope reveal interesting index properties as well (Fig. 3.3.11): brightness, wetness, TCA, DI, and EVI do not show significant variation with changing aspect angles in June. NDVI, NDMI, NDBI, and NBR show very weak bowl-shaped curves; greenness a weak bell-shaped curve. From August on these shapes become more pronounced for brightness, greenness, wetness, and DI; from September for EVI. Standard deviation becomes small at sun averted areas during late seasons indicating that there is only little radiation left in the shadows – values are generally low and variation within the shadows as well. TCA is rather scattered all over the year. But as for NDVI, NDMI, NDBI, and NBR, its standard deviation of all aspect angles increases slightly in late seasons (Fig. 3.3.11). This might be caused by increasing within-stand shadow effects caused by lower illumination angles.

#### 3.3.9.3 Implications

The limited number of scenes during winter plus lower probabilities of cloud free acquisitions due to increased cloud cover in that period are not favoring time series analysis in the study region. There are, however, numerous "off-perfect" cloud free observations during spring, and winter. Our findings confirm that their usage is challenging when illumination-sensitive features are explored. To be able to identify changes in time series of an index, the intra-annual variation of that index must be lower than differences caused by land cover changes. Little intra-annual variation of an index with comparable clear signal variation in case of a change event is helpful for the detection of clear cuts. An example that fulfills these requirements is the DI although it is affected by illumination. TC brightness and greenness, and EVI have strongest spatial variation and also pronounced seasonal variation. The latter is indicated by the changes of standard deviation over a year. Ratios show generally higher spatio-temporal stability. Wetness is an example as it is stable, too. For the understanding of environmental processes, however, indices that are sensitive to phenology are well suited, e.g., NDVI. As NDMI is both sensitive to vegetation response and abrupt changes, and spatio-temporally stable, this index may be preferred over others.
Furthermore, our results confirm previous suggestions (Wulder et al., 2004b) to prefer anniversary data over off-seasonal if bi-temporal change detection is applied or annual time steps are explored. As shown here, some indices are less sensitive for illumination conditions than others. Since our approach uses all observations we can rely on the temporal context of each observation making the whole strategy less sensitive for timing of the data.

## 3.4 Time Series Processing

### 3.4.1 Common Pre-Processing Steps

The processing of large amounts of data must be automated to a high degree. Otherwise, it is not feasible to use them. The most critical issues in pre-processing are geometric and radiometric consistency. Usability of Landsat data is enormously facilitated by the consistent processing with

the Landsat Product Generation System (LPGS) which processes all Landsat scenes to Standard Terrain Correction Level 1T if the required ground control and elevation data are available. Geometric accuracy of Level 1T images was randomly checked by visual inspection. As all evaluated images showed high agreement no further geometric pre-processing was applied. However, radiometric pre-processing including cloud and cloud shadow detection requires more efforts to create a consistent time series. At the time of start of this research no surface reflectance product was available for the study area. We performed atmospheric correction using the LEDAPS atmospheric correction tool (Masek et al., 2006; Vermote et al., 1997). It converts the raw DN values into surface reflectance and brightness temperature based on the MODIS/6S code presented by (Vermote et al., 1997). Aerosols are obtained from the images themselves using dark dense vegetation methodology (Kaufman et al., 1997). Unfortunately, the algorithm does not provide haze correction. All processing steps are conducted automatically once the LEDAPS code is run. We used the Linux based LEDAPS software provided by Jeff Masek (http://ledapsweb.nascom.nasa.gov/index.html) to process all Landsat images. Recently, all data acquired by Landsat 4-7 can be downloaded as surface reflectance products with supplementary layers such as cloud and cloud shadow masks, snow mask, water mask, and quality flags from the USGS Earth Explorer (http://earthexplorer.usgs.gov/). Random comparison confirmed that our results are identical to those provided by USGS.

Masking of clouds, cloud shadow, snow and water is essential when using all data. As described above, we used the Fmask algorithm with standard configuration to generate the respective masks individually for each image.

### 3.4.2 The Usefulness of Radiometric Normalization in Time Series

Remote sensing is an efficient means to detect land cover and land use changes over large areas. Time series of satellite data allow for the monitoring of environmental processes and the assessment of dynamics. In non-urban environments these may be seasonal patterns, long-term changes caused by the maturation of forests or abrupt changes due to management practices such as harvest. Several studies pointed out the importance of consistent datasets for the application of satellite time series and related products (Dardel et al., 2014; Latifovic et al., 2012; Verger et al., 2011).

Several studies explored the effect of atmospheric correction on change detection and image classification (e.g., Collins and Woodcock, 1996; Schroeder et al., 2006; Song et al., 2001). While all of them recommend applying radiometric correction they also conclude that relative atmospheric correction performs as well as absolute correction and is usually easier to implement. Many change detection and classification approaches do not require absolute atmospheric correction (Song et al., 2001). For time series analysis, it is important to have consistent measurements (Schroeder et al., 2006). This consistency is referred to as "common radiometric scale" (Song et al., 2001) which can be achieved by either absolute or relative atmospheric correction or a combination of both. Absolute atmospheric correction is recommended for the calculation of spectral indices because index values calculated from satellite data without adequate atmospheric correction differ substantially from the values that would be measured at ground

(Jones and Vaughan, 2010). Vegetation indices calculated from at-sensor reflectance or from radiance may lead to different relationships between vegetation indices and biophysical parameters such as Leaf Area Index (LAI). Vicente-Serrano et al. (2008) assessed different preprocessing methods for land cover change detection and suggested the implementation of a processing sequence including cross-sensor calibration, absolute radiometric correction, topographic correction and automatic relative radiometric normalization when vegetation trends are analyzed. They concluded that for the analysis of abrupt vegetation changes the use of Top of Atmosphere (TOA) reflectances and accurate relative radiometric normalization are sufficient to achieve useful results (Vicente-Serrano et al., 2008). However, these researchers did not include the fully automated Iteratively Re-weighted Multivariate Alteration Detection (IR-MAD) (Canty and Nielsen, 2008) in their study. Since IR-MAD is based on linear regression, cross-sensor calibration using empirically derived slope and intercept parameters is redundant and may be omitted (Vogelmann et al., 2001). In recent change detection studies based on multiple images, one image is atmospherically corrected using an absolute procedure and all the other images are subsequently normalized to that master image using a relative method (Coops et al., 2010; Griffiths et al., 2012; Powell et al., 2008). The majority of Landsat time series studies published in the last years explored annual time series (Cohen et al., 2010; Griffiths et al., 2012; Meigs et al., 2011). Recent trends direct towards the exploration of the full archive (Zhu and Woodcock, 2014; Zhu et al., 2012). Although there is common agreement that a radiometrically consistent dataset is required for change detection studies there is no research published about the effects of relative radiometric normalization in time series that covers images from all seasons.

#### 3.4.2.1 Radiometric Normalization using the Iteratively Re-weighted Multivariate Alteration Detection (IR-MAD)

Subsequent to absolute atmospheric correction we applied IR-MAD on all images. The IR-MAD procedure is an enhancement of the Multivariate Alteration Detection (MAD) introduced by (Nielsen et al., 1998). MAD has been used to correct AVHRR time series for sensor degradation (Schmidt et al., 2008). More common is the application of MAD or IR-MAD and their modified versions on image pairs to identify bi-temporal changes (Canty and Nielsen, 2012; Nielsen et al., 1998). The basic concept of IR-MAD is to detect unchanged pixels. Radiometric normalization is achieved by orthogonal linear regression. The formula is calculated from a subset of the unchanged pixels. Relative radiometric normalization, i.e., adjusting a target image to a reference image, is supposed to level non-surface related noise such as sun angle effects (e.g., differing shadow lengths and incident illumination characteristics) and sensor degradation effects. Early relative atmospheric correction methods made use of Pseudo-Invariant Features (PIF) identified in both images (Schott et al., 1988) or Temporally Invariant Clusters (TIC) (Chen et al., 2005). State-of-the-art algorithms such as IR-MAD function completely automatically and do not require any knowledge of the acquisition conditions or of the study area. MAD is frequently used for radiometric normalization (e.g., Canty and Nielsen, 2008; Canty et al., 2004; Nielsen, 2007; Xu et al., 2012).

Cloud cover is a severe problem when using optical data. This becomes even more evident when using time series of all images.

Since water bodies may affect the IR-MAD normalization, the clear land mask created during the Fmask process was applied to each image before radiometric normalization. In the present study, the master image was chosen from 2000, in the middle of the time series. As two WRS-2 tiles are used, two neighboring scenes had to be combined to one image. We used one master scene from 23 September 2000 (path/row 048/026) and the adjacent scene from 24 September 2000 which was radiometrically normalized to the former using IR-MAD. This decision was made to ensure a medium level of divergence for all scenes since it is well known that the area experiences extensive changes. An image pair from the middle of the observation period seemed appropriate. Furthermore, the adjacent images were required to be cloud free and with little temporal mismatch. One day difference was seen as optimal although the data comes from different sensors (Landsat TM & ETM+).

The IR-MAD procedure may be applied on subsets that are representative for the whole scene (Canty and Nielsen, 2008). Most of the images of the time series contain clouds. Cloud coverage and spatial distribution of the clouds vary considerably over time. Hence, the cloud free subset available for IR-MAD and further analysis changes as well. We defined an arbitrary minimum subset size of three million pixels in order to achieve reliable results. Images with smaller subsets were excluded from further analysis. The number of pixels finally used for the normalization is refined by the IR-MAD procedure. The IR-MAD code allows for the inspection of the statistics of the normalization. Random tests revealed good statistics even for large cloud coverage. The IR-MAD procedure (available as ENVI/IDL implementation free of charge from Mort Canty's personal webpage http://ms-image-analysis.appspot.com/static/homepage/software.html, Canty, 2014) was automatized and run on all images. The subset was individual for each scene. The study site comprises mainly coniferous forests, thereby reducing the variability of land cover types in the scene. Consequently, it is likely to have representative subsets even with the automated procedure.

#### 3.4.2.2 Assessment of Radiometric Normalization Impacts on Time Series

The creation of a single mosaic image which can be used as master scene for the radiometric normalization follows the procedure presented in Canty and Nielsen (2008). In our case, the Landsat ETM+ scene of 23 September 2000 is the master image and the Landsat TM scene from one day later is used as slave image that is normalized to the former. To justify the radiometric normalization as additional step after atmospheric correction we created three mosaics consisting a) of the raw data, b) the LEDAPS atmospheric corrected images, and c) the radiometric adjusted LEDAPS images after applying IR-MAD.

From Fig. 3.4.1 it can be seen that atmospheric correction is essential to create the "common radiometric scale" as proposed by (Song et al., 2001). The images differ substantially without any atmospheric correction (Fig. 3.4.1a). After applying LEDAPS, both images appear harmonized (Fig. 3.4.1b). Differences can only be seen in the detailed image of Fig. 3.4.1h in the water body. These differences are likely to be caused by BRDF effects and/or different water turbidity.

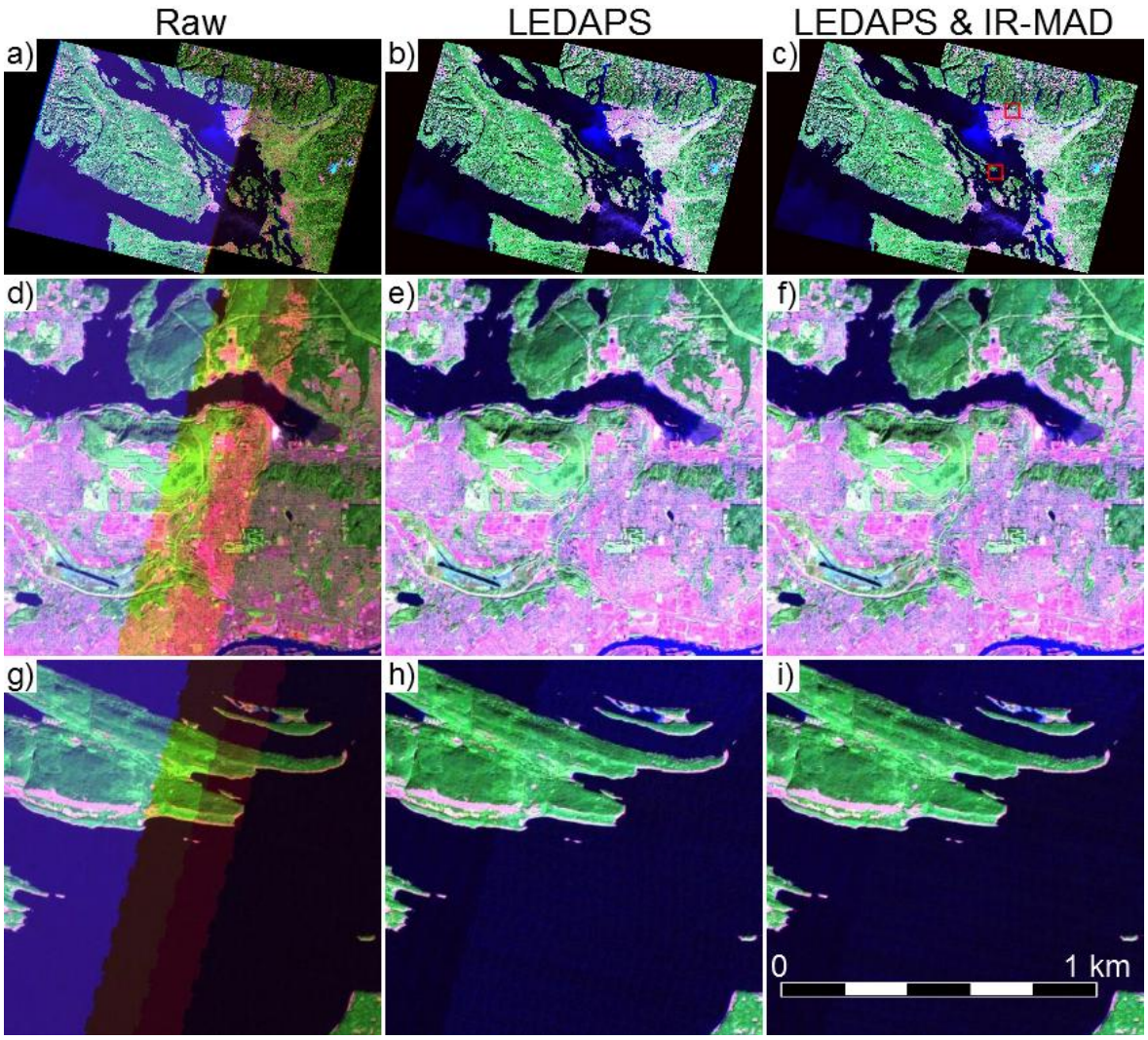


Fig. 3.4.1: Visual evaluation of atmospheric correction effects shown with an example of two Landsat images taken only one day apart (Landsat 7 ETM+ from September 23, 2000 and Landsat 5 TM from September 24, 2000; RGB = 7-4-2).

However, after applying IR-MAD subsequently to LEDAPS even those fine scale differences are further reduced (Fig. 3.4.1c, f, i). Hence, radiometric normalization as a relative correction method is well suited to level even small radiometric differences between images. Both images are cloud-free and show no evidence of haze. They are only one day apart. Subtle changes on the ground such as phenology are unlikely to affect spectral reflectance within such short time periods. Consequently, the IR-MAD effect can be attributed to noise-leveling.
For the assessment of the radiometric normalization impacts on time series two datasets were generated. One includes the images after applying LEDAPS, the other includes the images after the additional IR-MAD processing step. Profiles of selected locations of the two datasets were compared. We compared spectral bands as well as spectral indices generated from both datasets.

### 3.4.3 The Effect of Radiometric Normalization on Time Series of Spectral Bands

The time series plots of the selected locations are shown exemplary for three pixels in Fig. 3.4.2 - Fig. 3.4.4. For comparison reasons time series of both datasets (with and without radiometric

normalization) were plotted. Furthermore, the difference between the two is plotted allowing for the analysis of leveling effects as well as long-term trends in the normalization. Color coding of the time series difference refers to the month of acquisition. This allows for the identification of seasonal effects of the normalization. The displayed examples show forested pixels where a clear cut occurred in 2011, 1986, and 2002, respectively. Consequently, pixel A (Fig. 3.4.2) shows stable forest conditions for most of the observation period, pixel B (Fig. 3.4.3) displays forest recovery after a disturbance very early in the observation period, and pixel C (Fig. 3.4.4) includes both, stable forest and recovery.

It can be seen that the reflectance of the spectral bands 1, 2, 3, 5 and 7 abruptly increases when the forest is cleared whereas the reflectance of band 4 decreases slightly. During the recovery phase all spectral bands tend to resume to their previous reflectance level. Band 4 is an exception since its reflectance excels the previous level. On a long run the reflectance of all spectral bands

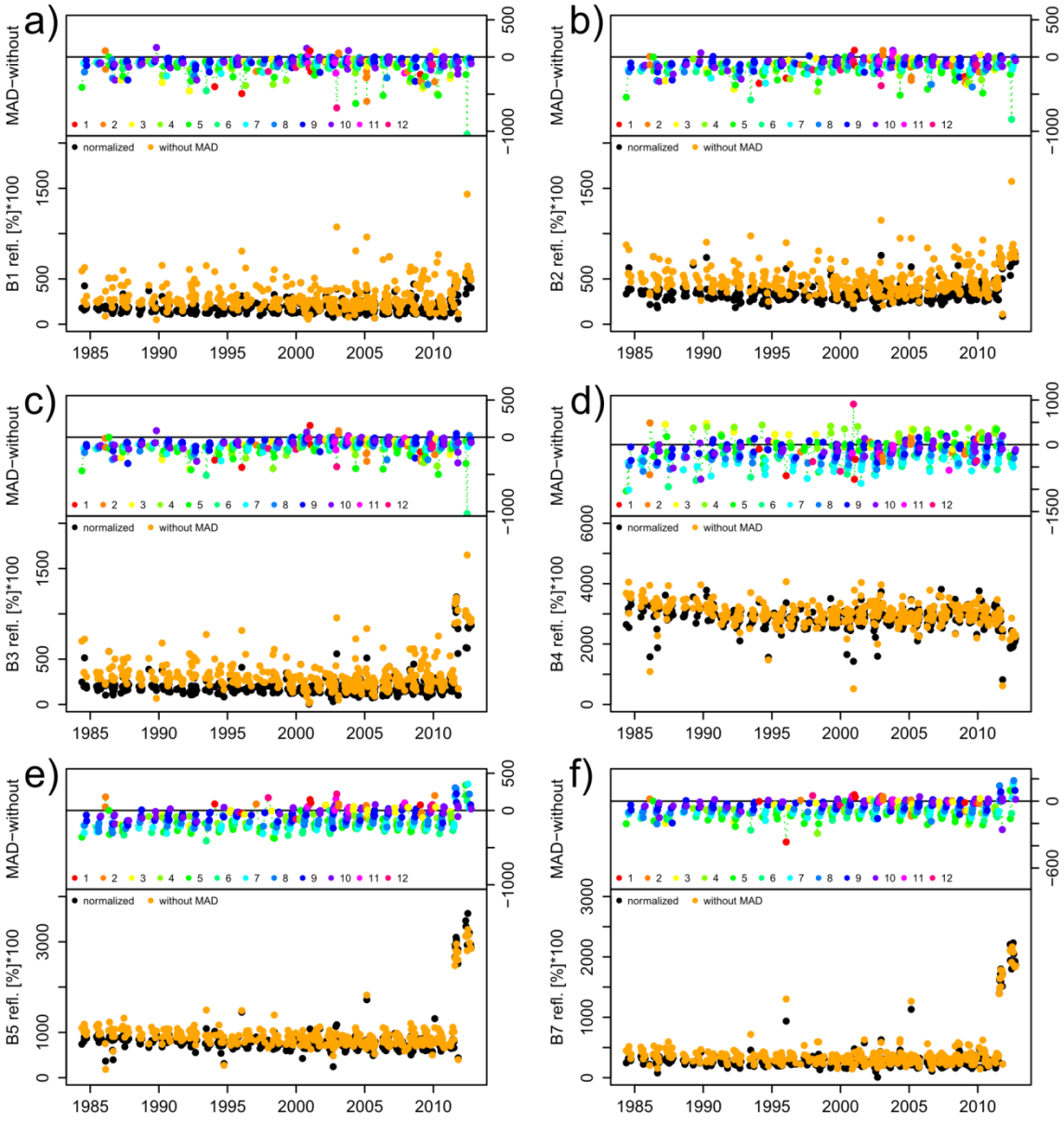


Fig. 3.4.2: Comparison of normalized and non-normalized time series of spectral bands of one single pixel and their difference, case A – late change.

converges to the typical reflectance level of each individual pixel once crown closure is achieved and a new forest stand has established. This could also be observed for all the other randomly selected pixels that are not shown here. The observed temporal pattern is irrespective of radiometric normalization.

The difference between the LEDAPS based surface reflectance time series and the normalized time series reveals that the former has generally slightly higher values in bands 1, 2, 3, 5, 7 as long as no clear-cut event occurs. The observations taken earlier than the master image have been leveled down in the time series of normalized images. It can also been seen from Fig. 3.4.2 - Fig. 3.4.4 that this effect increases with increasing temporal distance from the master image, i.e., the observations at the beginning of the time series show largest difference from the respective non-normalized observation. Band 4 is an exception since the difference values of this band also show positive values (predominantly in March, April and May). The difference plots also show an slight

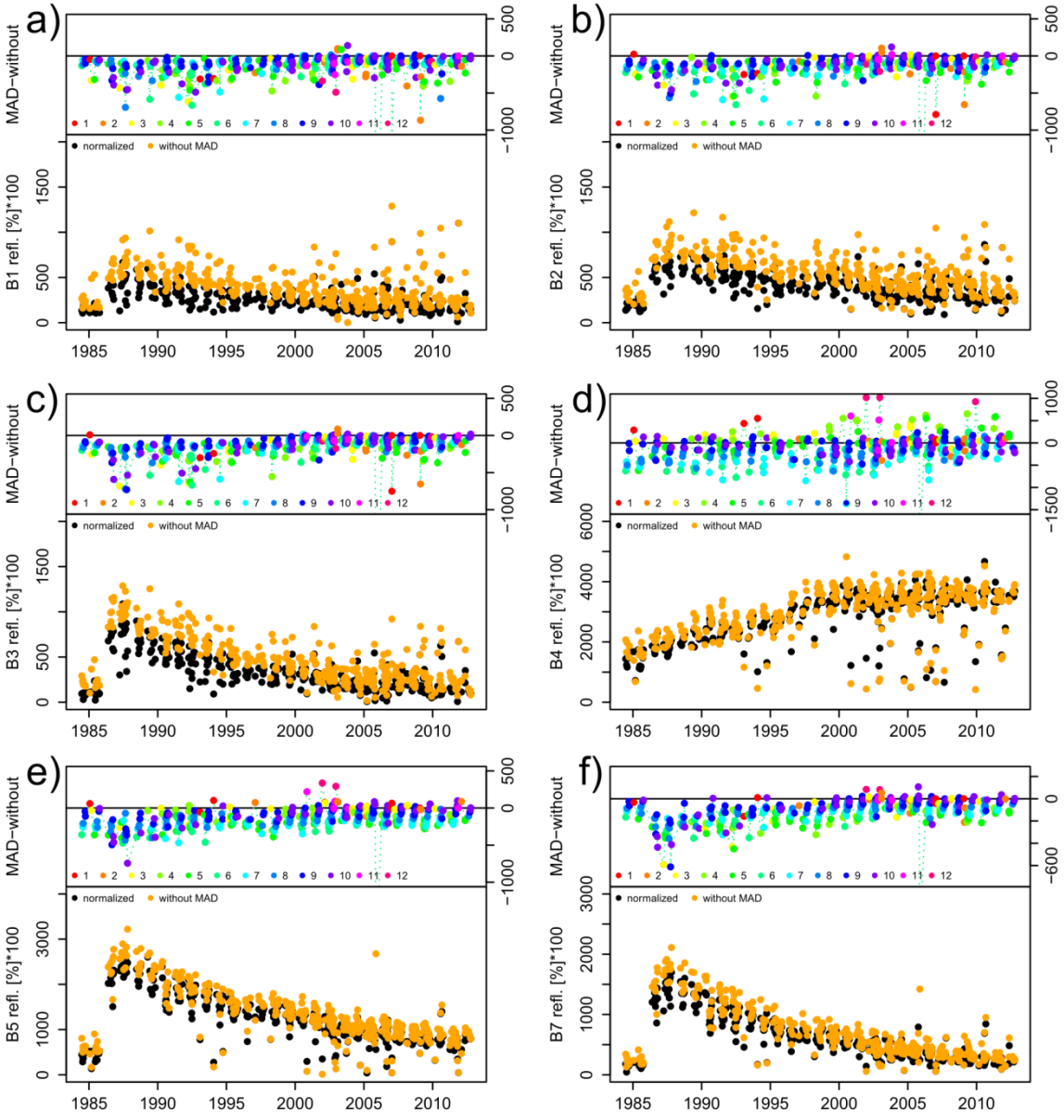


Fig. 3.4.3: Comparison of normalized and non-normalized time series of spectral bands of one single pixel and their difference, case B – early change.

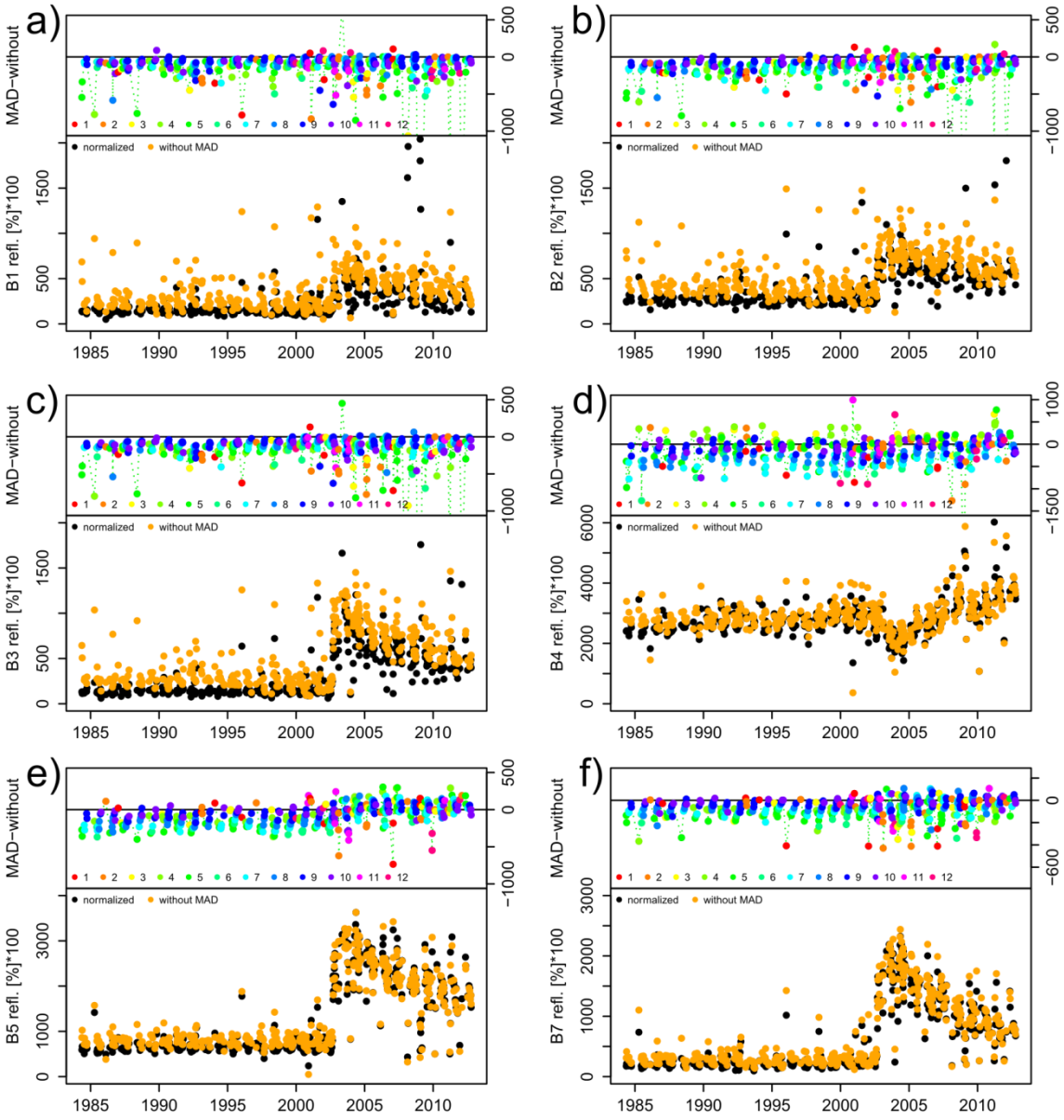


Fig. 3.4.4: Comparison of normalized and non-normalized time series of spectral bands of one single pixel and their difference, case C – change in the middle of the time series.

increase in all bands converging towards zero. When forests grow, they mature, change species composition as well as structure. Although forest growth cannot be fully displayed by spectral reflectance (forest may continue maturation but spectral indices saturate), a continuous change of reflectance can be observed over several years or even decades. The increase of the difference in all spectral bands indicates that these long-term changes are leveled by the radiometric normalization. Furthermore, it can be observed that the difference becomes more scattered and more pronounced after forest harvest, i.e., an abrupt change event. This can be attributed to the forest succession after the clear-cut. Small deciduous trees such as red alder (*Alnus rubra*) are a widespread species on logged or otherwise disturbed sites (Pojar et al., 1991) and start settling. Over time they are replaced by other species until conifers are dominating. Frequently, conifer seedlings are planted by the forest companies directing the future species composition. Deciduous trees have a much more pronounced seasonal pattern. The increased difference after a

clear-cut event may be interpreted as a consequence of the increased seasonal dynamics in fresh deciduous forest stands with vast areas of bare soil and dead biomass. The difference becomes less again after a couple of years when conifers start dominating.

### 3.4.4 Effect of Radiometric Normalization on Time Series of Spectral Indices

The plots of the indices show some similarities to the temporal pattern of the spectral bands. However, there are also some major differences. The NDVI curves show high values for the normalized time series, even after a clear-cut event (>0.2; Fig. 3.4.5 - Fig. 3.4.7). The non-normalized values are generally lower. Most of the indices reveal subtle changes contrasting the maturation process of a forest (Fig. 3.4.5 - Fig. 3.4.7). These are completely leveled in the normalized time series. In general, the difference plots of NDVI, EVI, NDMI, NBR and TCA show long-term negative trends, supporting the previous interpretation that IR-MAD levels long-term trends of spectral reflectance bands and also indices. The only exception is TC brightness which shows long-term increases in the difference plot. The increased differences after a clear-cut event are less pronounced for the indices than for the spectral bands, however, they are well discernible in the NDMI, NDVI and wetness plots. The tasseled cap components are somewhat different from the other indices. The difference plot of the wetness component shows a very clear seasonal pattern, indicating that IR-MAD levels seasonal fluctuations. Abrupt changes are clearly visible in the wetness component. They are displayed in a different way in the greenness component where the drop in greenness is rapidly balanced by a subtle increase when fresh vegetation starts growing. Similar to the NIR band, greenness is reduced immediately after a clear-cut, but increases rapidly after short time, excelling the initial level. This may be due to the occurrence of deciduous tree species after the clear cut. EVI shows similar behavior. Brightness slightly decreases with the maturation of forests and increases very fast after a clear-cut event since bare soil has higher brightness values than conifer forests. DI is an exception from all indices. It shows virtually no difference between the LEDAPS based time series and the normalized time series during stable forest periods (Fig. 3.4.5i and early period of Fig. 3.4.7i). Small differences are apparent immediately after disturbance, particularly from observations in early season.

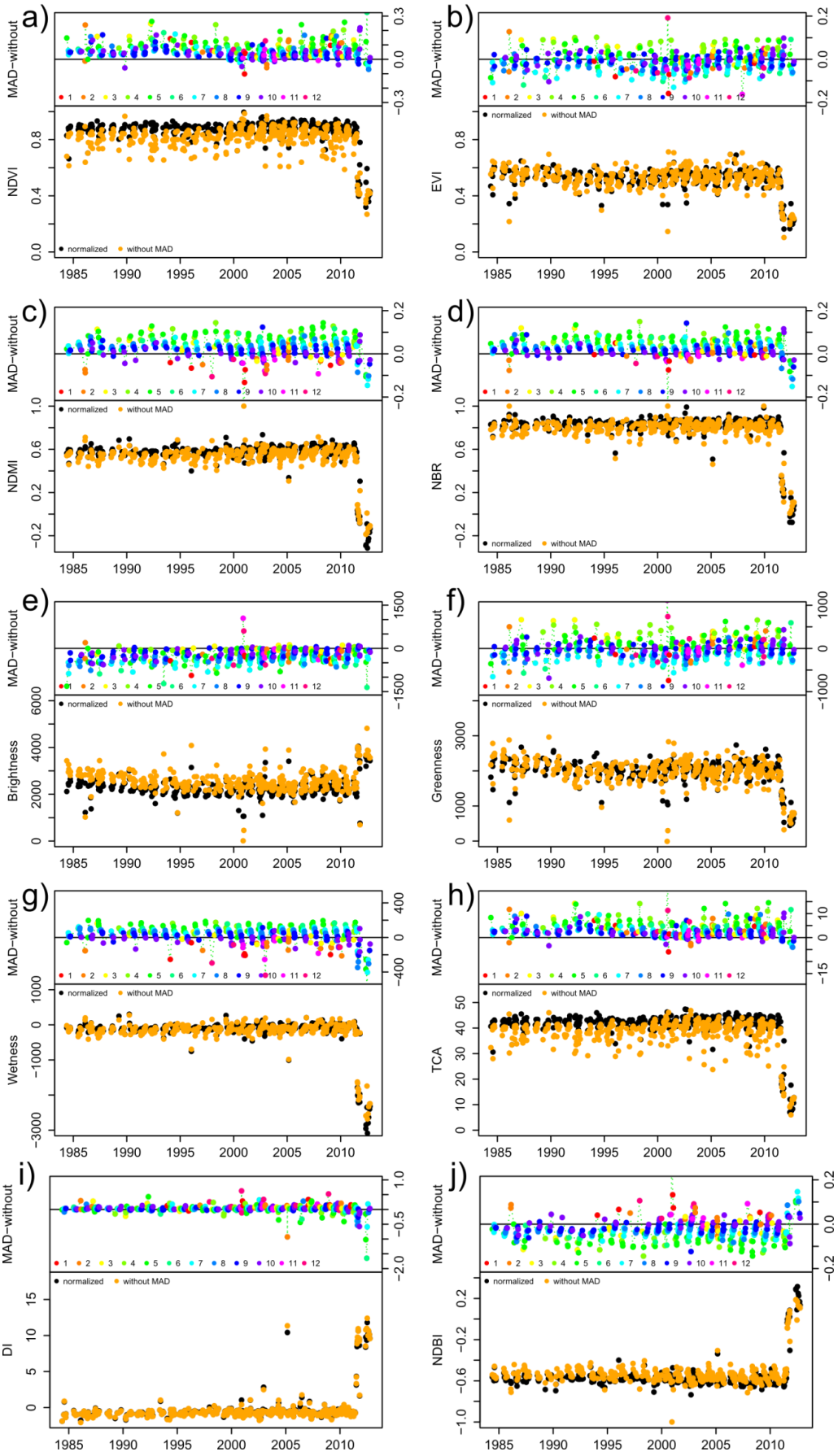


Fig. 3.4.5: Comparison of normalized and non-normalized time series of selected indices of one single pixel and their difference, case A – late change.

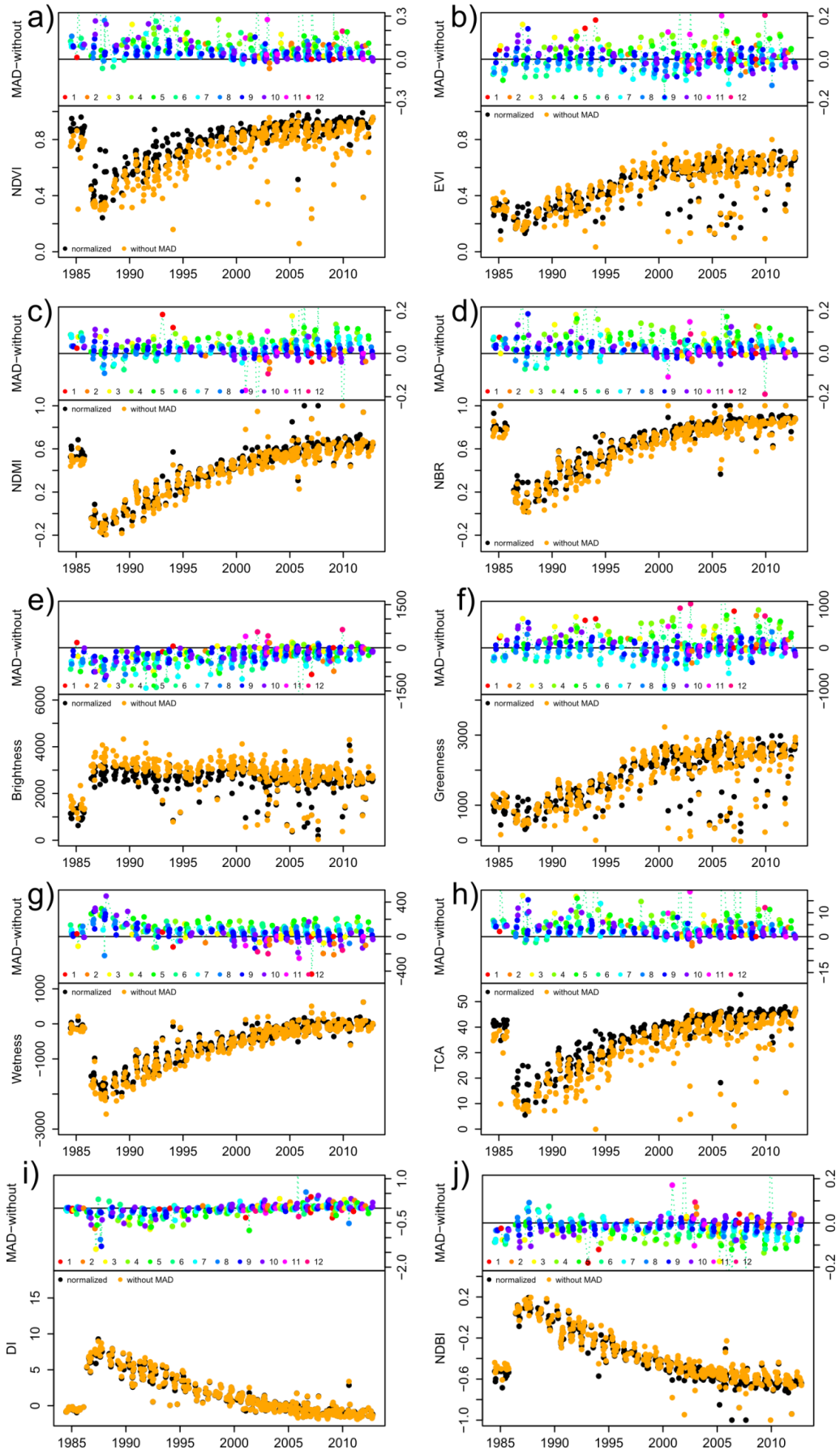


Fig. 3.4.6: Comparison of normalized and non-normalized time series of selected indices of one single pixel and their difference, case B – early change.

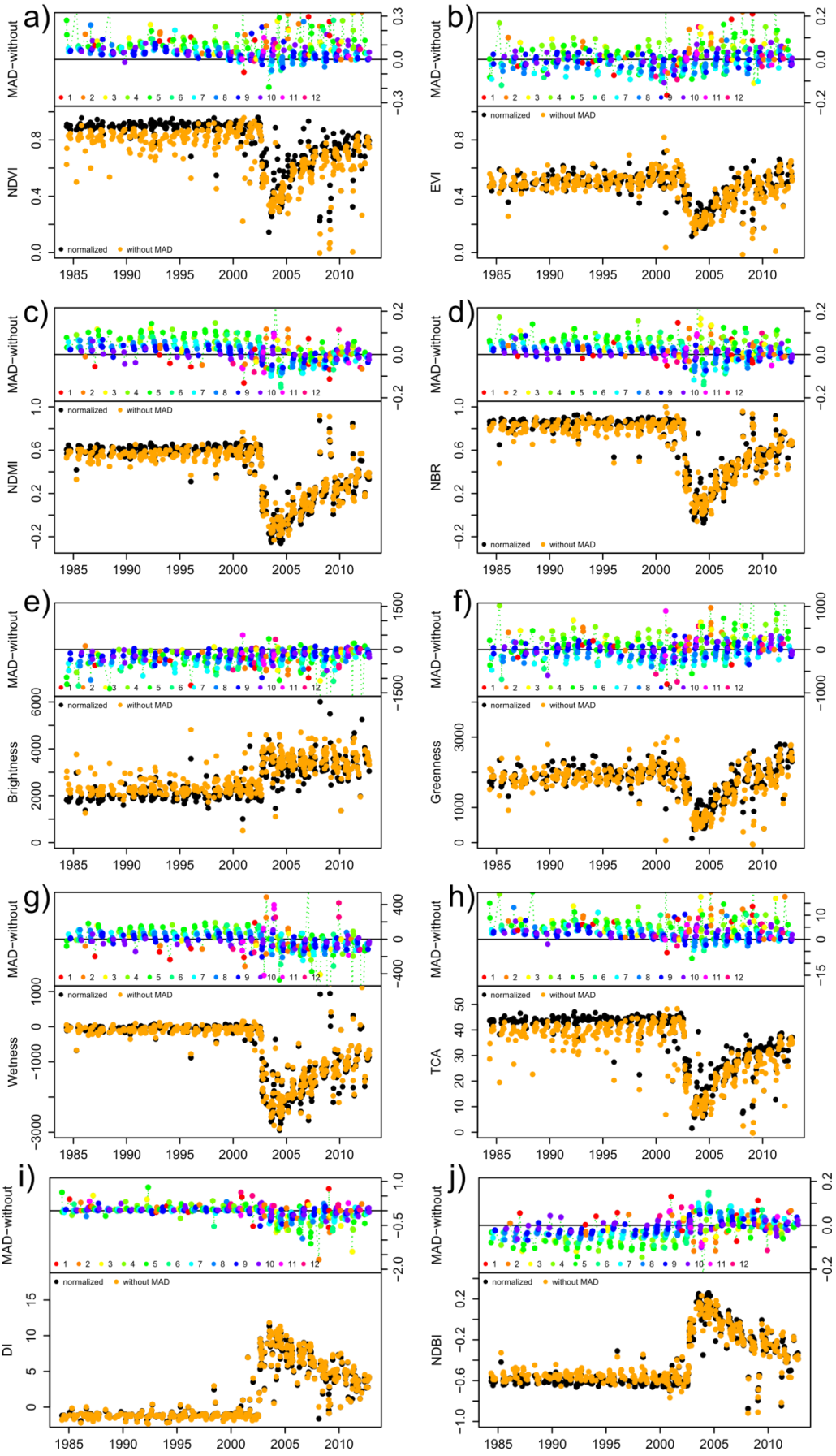


Fig. 3.4.7: Comparison of normalized and non-normalized time series of selected indices of one single pixel and their difference, case C – change in the middle of the time series.

### 3.4.5 Assessment of Seasonal Effects

Another temporal pattern can be observed in the difference plots. All bands reveal a seasonal dependence of the difference magnitude. Fig. 3.4.8 and Fig. 3.4.9 show the differences of spectral reflectance and index values of normalized and non-normalized time series as a function of Day Of Year (DOY). It can be seen that each spectral band and hence also each index shows an individual temporal pattern. Forest condition, state, and age affect the magnitude of deviation. The individual seasonal pattern, however, is the same over time. Band 1 shows a more or less constant difference with slightly larger differences when sun is close to its highest elevation in June. The pattern is similar for bands 2 and 3. The difference curves of bands 5 and 7 show a similar shape but with less variation and a more pronounced negative difference around DOY 150. During the peak of growing season the non-normalized reflectance of all bands is higher than the normalized. Very early and very late observations of bands 5 and 7 show positive differences indicating that the non-normalized reflectances are smaller than the normalized ones. This is most likely caused by poor illumination conditions. Band 4 has a somewhat unique pattern compared to other spectral bands. It shows a positive difference during spring and a negative difference after the peak of the growing season (DOY 180). For all spectral bands the differences are smallest when images of the same DOY are compared.
The indices also show individual seasonal patterns. EVI and TC greenness have a similar pattern to band 4. NDVI which is supposed to be more affected by NIR than other indices does not show a clear seasonal difference pattern. The NDVI of the non-normalized time series is generally smaller. The largest difference to the normalized data occurs in spring (DOY 100). NDMI, NBR, and TC wetness show a simple pattern. The difference from the normalized time series is least in autumn, the acquisitions date of the master image. The difference decreases over winter when illumination conditions become worse and increases sharply in spring. The maximum deviation is around DOY 120 where the normalized time series has much higher values than the non-normalized. The TCA has a similarly shaped curve. But it also contains more noise. DI is again an exception. There is no seasonal variation of the difference of normalized time series and LEDAPS time series (Fig. 3.4.9).
Generally, the differences are most pronounced in April and May (and July for band 4). The non-normalized observations show higher reflectances during most time of the year and smaller values when acquired at the same time of a year as the master image. Sometimes positive differences occur (negative ones for band 4) in winter scenes when light conditions are worse. These observations indicate that IR-MAD also levels seasonal patterns.
One might assume that the observed seasonal pattern is mainly driven by bad cloud situations and hence the limited number of available invariant features. In Fig. 3.4.10 and Fig. 3.4.11 the relationship of the differences between normalized and non-normalized time series and cloud/cloud shadow coverage is plotted. Although the differences are more pronounced when cloud/cloud shadow coverage is high, there is no statistical relationship. The observed seasonal pattern can be found for any cloud/cloud shadow percentage and for all three stable forest/recovery scenarios (A, B, C).

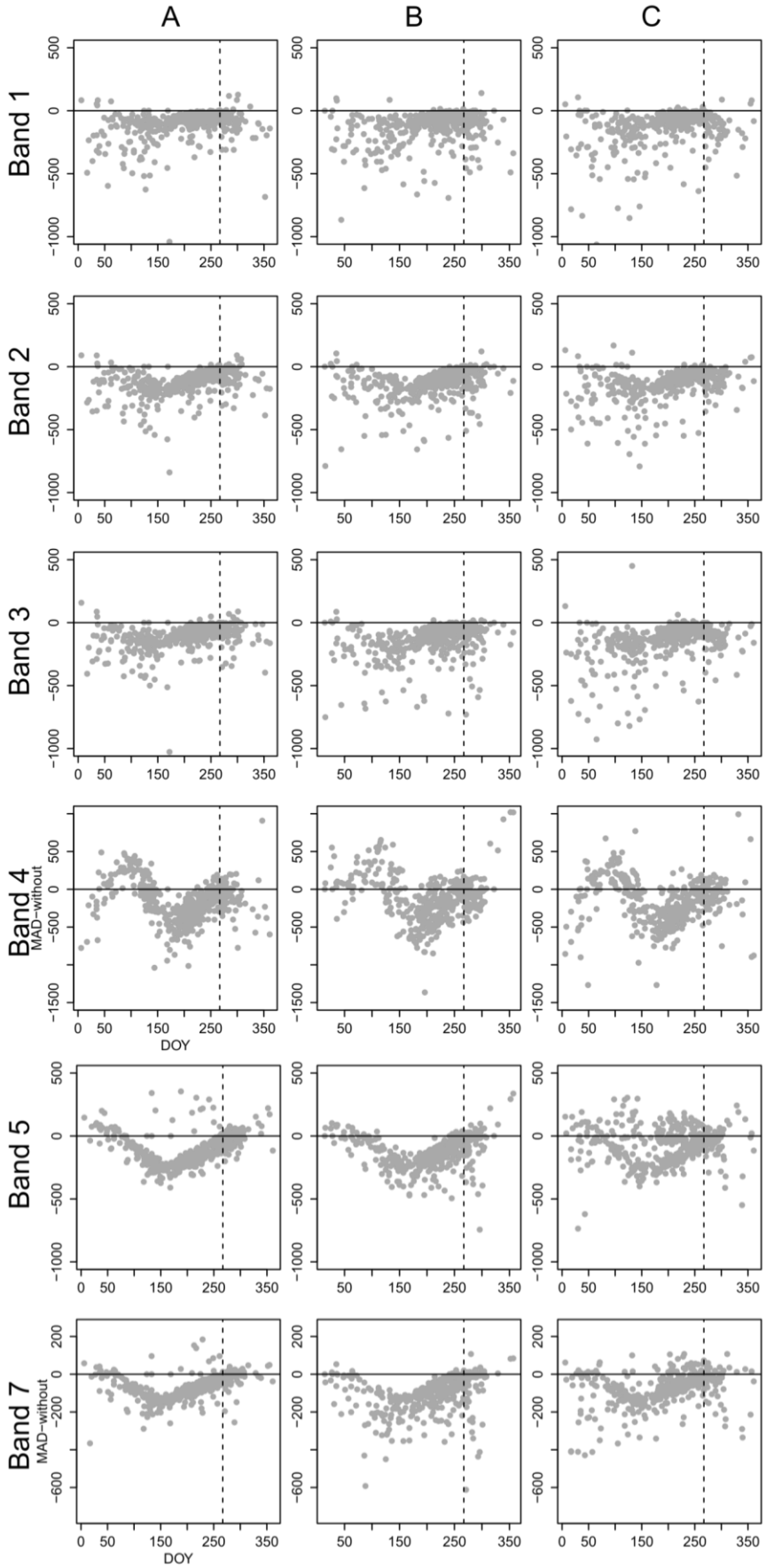


Fig. 3.4.8: Difference between normalized and non-normalized reflectance as a function of day of year. Dashed line shows date of master scene. The locations A, B, and C refer to the time series of Fig. 3.4.2, Fig. 3.4.3, and Fig. 3.4.4.

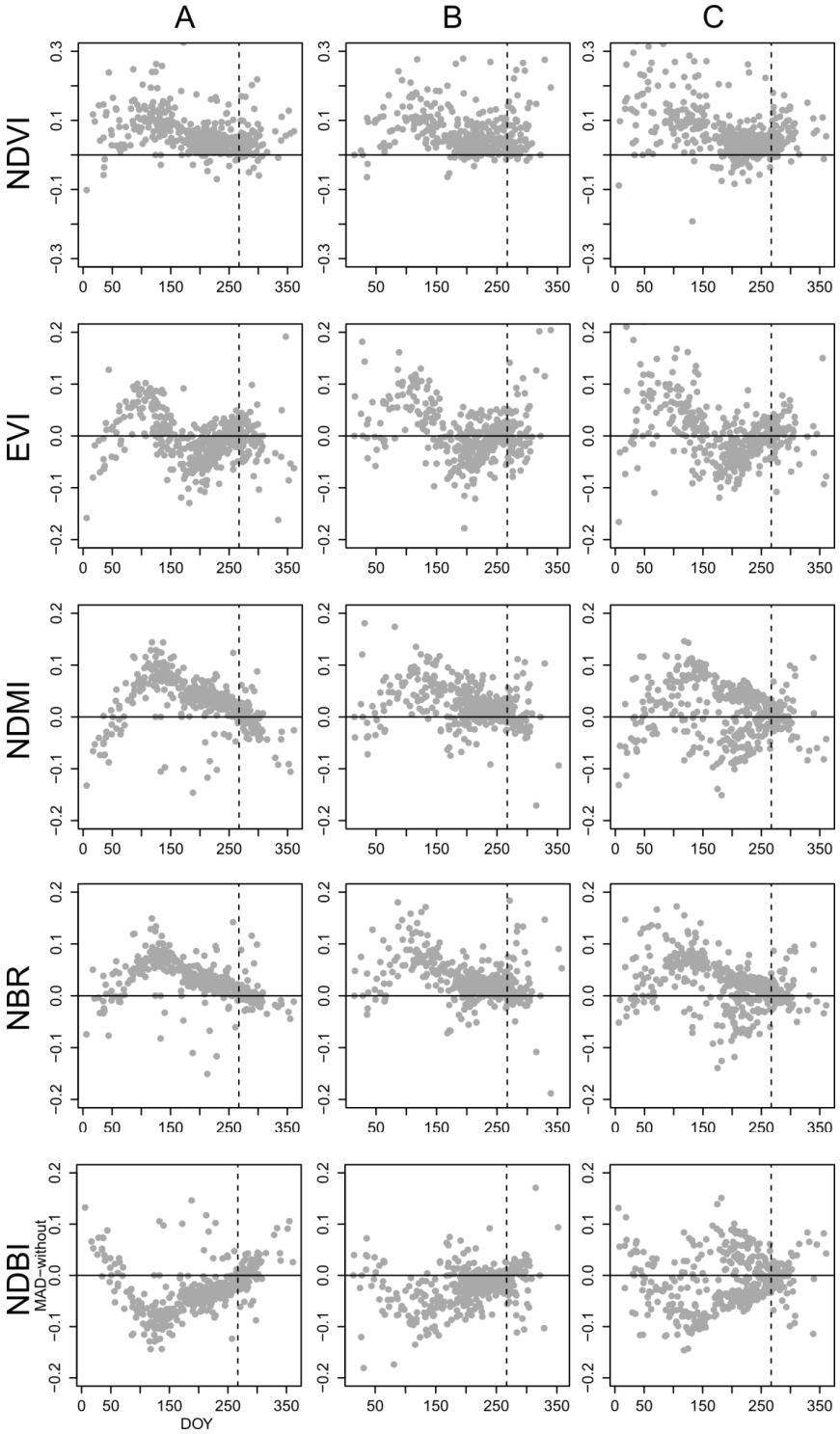


Fig. 3.4.9: Difference between normalized and non-normalized index time series as a function of day of year. Dashed line shows date of master scene. The locations A, B, and C refer to the time series of Fig. 3.4.5, Fig. 3.4.6, and Fig. 3.4.7.

### 3.4.6 Findings and Implications

Several issues have to be considered when normalizing data of long time series. The first is that the approach used here considers all Landsat data irrespective of percentage of cloud cover. That means that the cloud free subset used for the normalization procedure changes between every

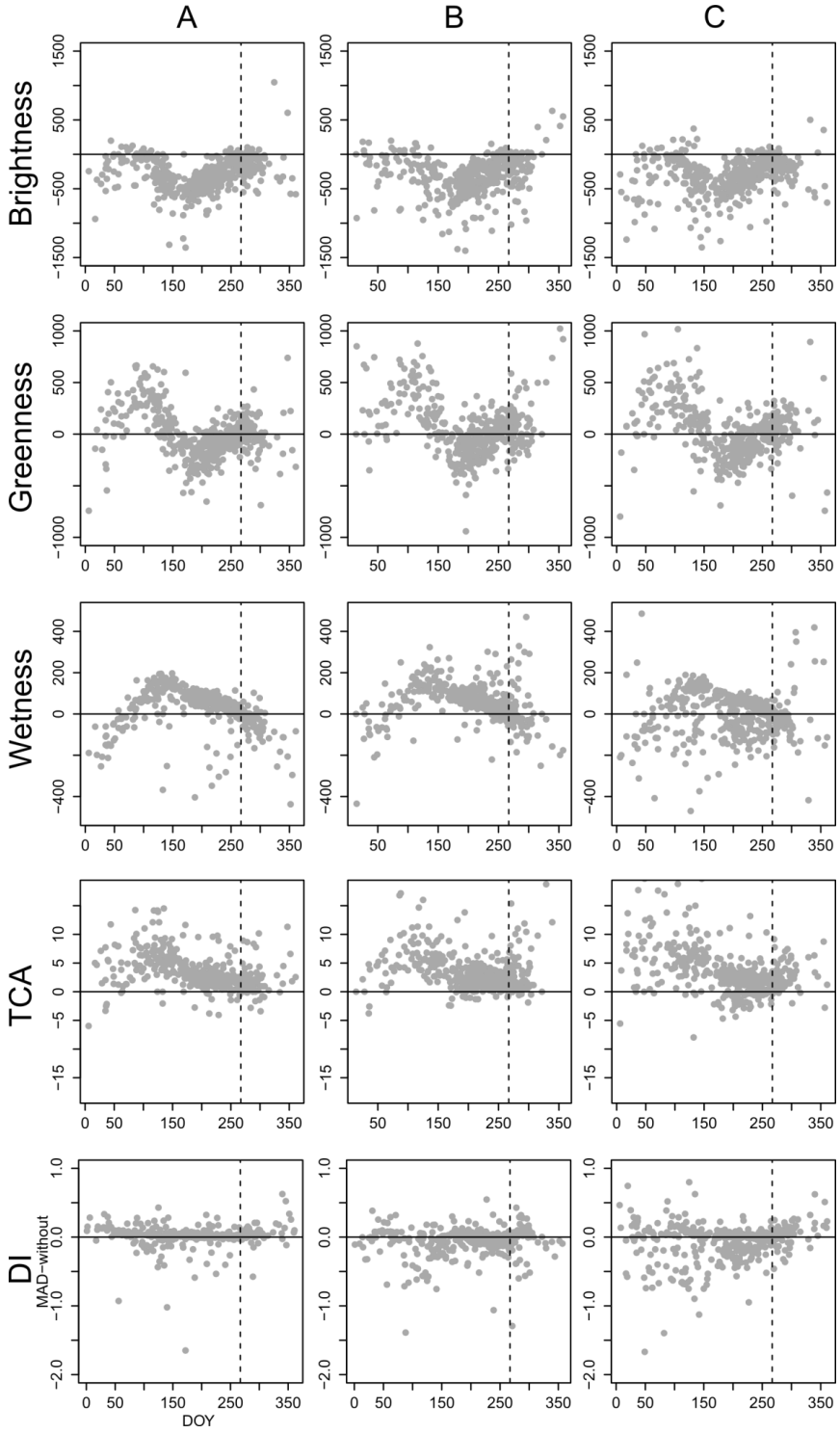


Fig. 3.4.9 (continued)

image pair. The quality of the cloud mask is of little importance since the IR-MAD procedure is able to detect missed clouds as change and disregards them for the normalization process. The spatial distribution of the cloud free pixels, their respective land cover, and their abundance, however, may affect the normalization results when the subset is selected without user interaction. Automated processing is inevitable with big datasets. The subsets selected for the normalization process have to be representative for the study region in order to ascertain a satisfactory regression for the normalization (Schroeder et al., 2006). This can only be ensured

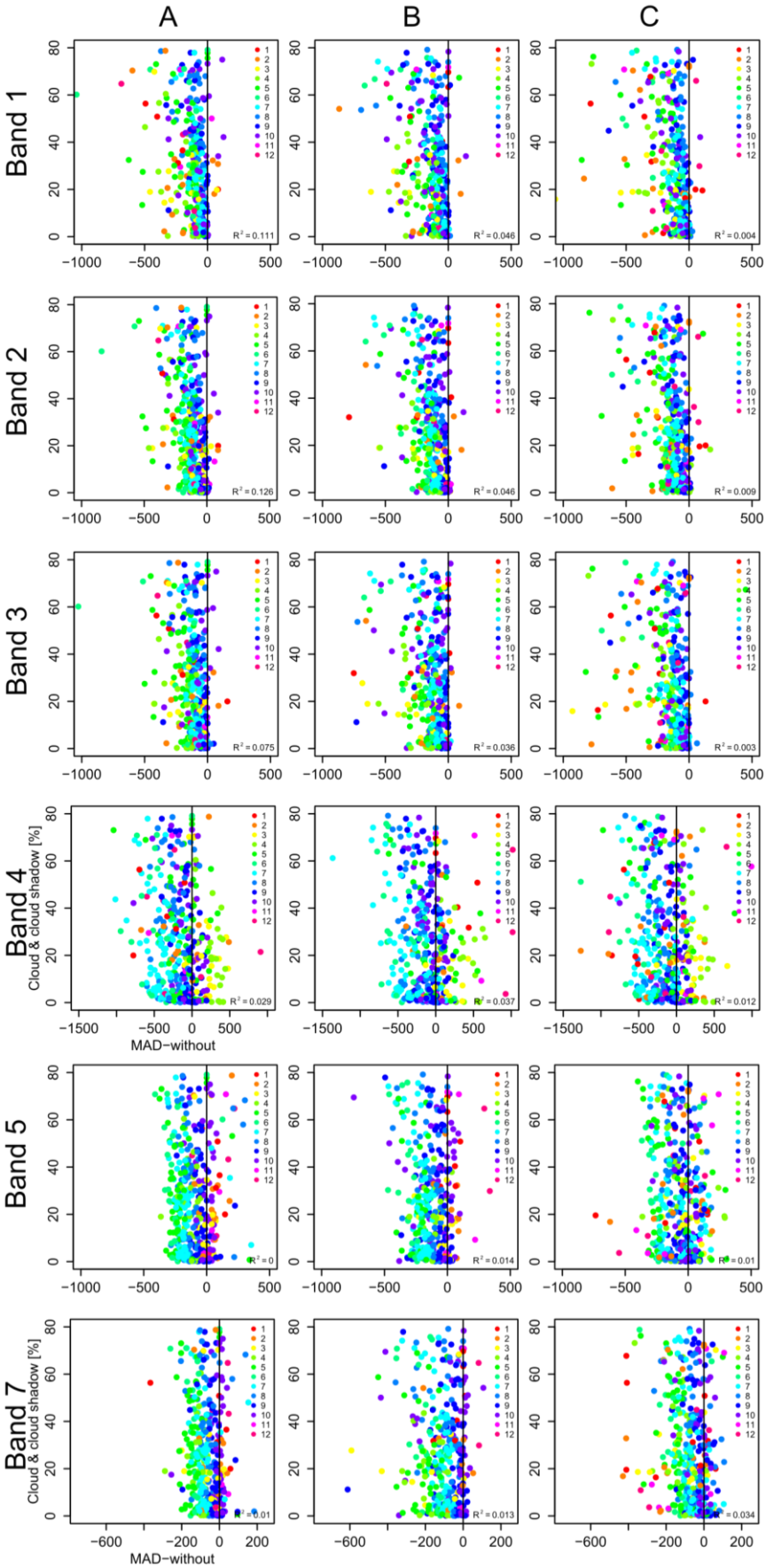


Fig. 3.4.10: Relationship between difference of normalized and non-normalized reflective bands and cloud/cloud shadow cover. The locations A, B, and C refer to the time series of Fig. 3.4.2, Fig. 3.4.3, and Fig. 3.4.4.

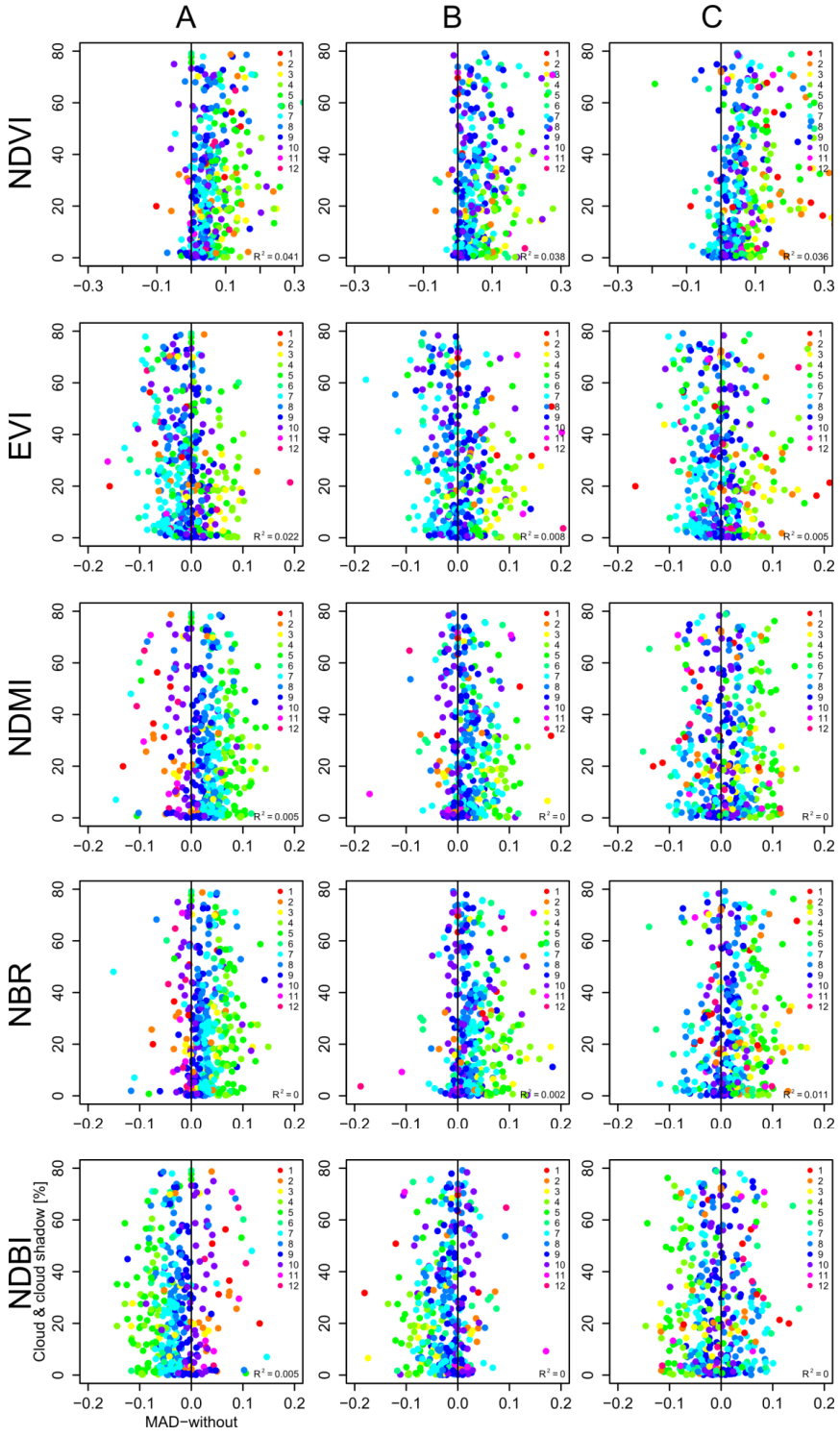


Fig. 3.4.11: Relationship between difference of normalized and non-normalized index bands and cloud/cloud shadow cover. The locations A, B, and C refer to the time series of Fig. 3.4.5, Fig. 3.4.6, and Fig. 3.4.7.

under controlled processing conditions, i.e., manual subset selection. In an environment like the present study site it is difficult to identify invariant features that do not change even over decades. We did not explore the effects of different subset definitions on the success of the radiometric normalization. The study area explored here is rather homogenous in terms of land cover (i.e., almost the total study area is forested). Species distribution and forest growth stages

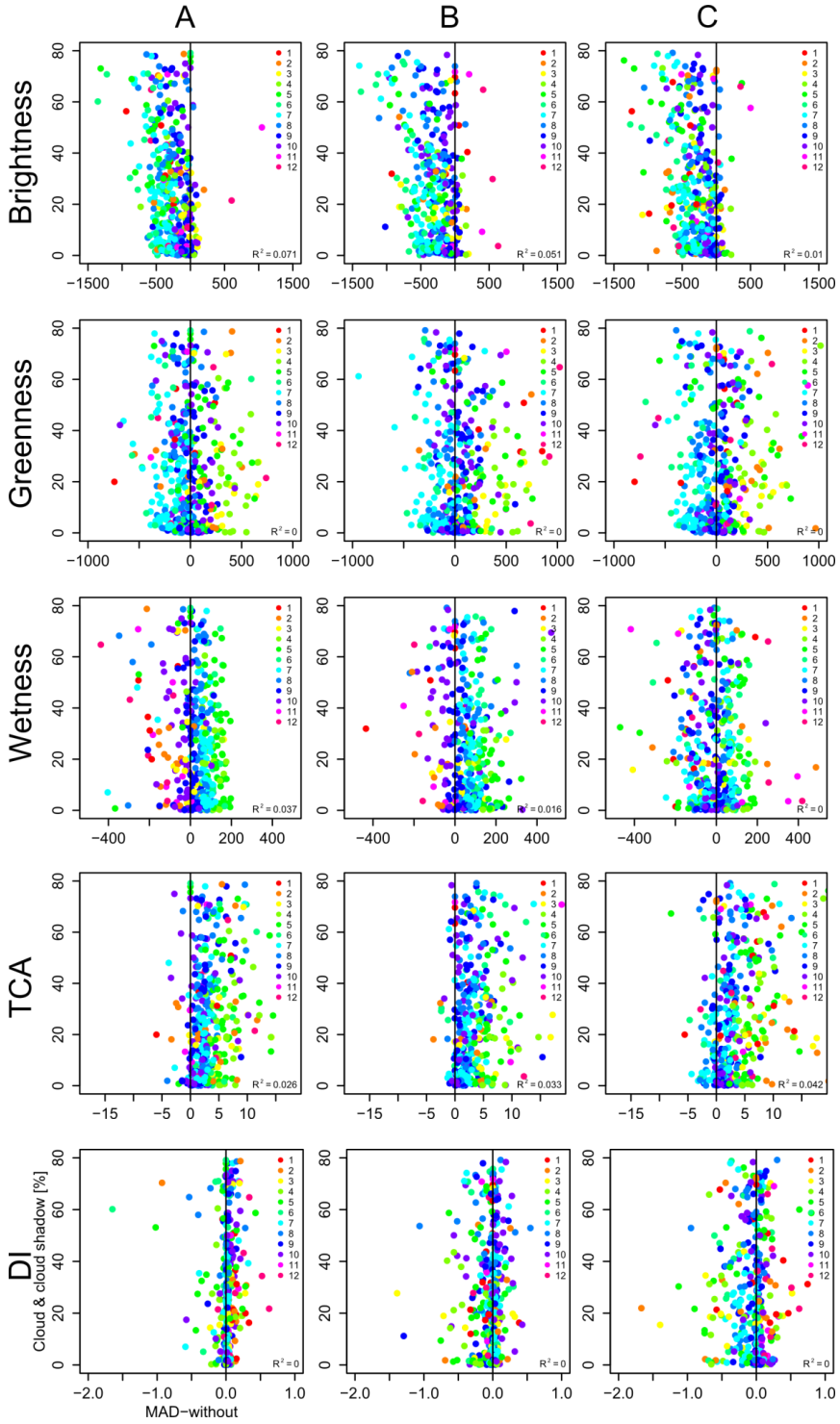


Fig. 3.4.11 (continued).

are not homogeneously distributed. Thus, at least a small effect of subset size and location is assumed.

The second and third issues that have to be considered are related to time. The former deals with seasonal changes and phenology, the latter with long-term changes. Seasonal changes within each land cover type may cause differences between the unchanged pixels of the master and slave scenes. Those may be leveled by the normalization. In addition, illumination conditions changing over the year cause different shadow proportions and distributions in hilly terrain and also inside

forest stands. Bidirectional reflectance effects may affect the choice of no-change pixels for the radiometric normalization using IR-MAD and are more pronounced in hilly terrain (Canty and Nielsen, 2008). Consequently, seasonal changes of illumination conditions have an impact on the normalization as can be seen from Fig. 3.4.2 - Fig. 3.4.7. All plots reveal largest differences between normalized and non-normalized images for off-season images. The reasons are varying illumination conditions and shadow proportions on the one hand and phenological changes on the other hand. To minimize the effect of seasonality-leveling an optional strategy would be to use different master images for each season or month, i.e., instead of normalizing all images to one master images the images are normalized to a master image of the same season or month, e.g., a image from April is normalized to a master image from April.

Long-term changes refer to the growth and development of forests. With maturation forests change their spectral behavior. Pixels located in forests are likely to be determined unchanged by the IR-MAD procedure. The associated forests experience subtle changes due to maturation and forest structure changes. Hence, the long-term change of these pixels is leveled to a certain degree by the regression. Long-term leveling is less pronounced in indices that make use of SWIR bands (e.g., TC wetness, NDMI, NBR). It is more evident in indices that are based on visible and NIR bands (e.g., NDVI, EVI, TC brightness, TC greenness, TCA). However, only minor effects of radiometric normalization can be identified for DI.

Several conclusions can be drawn from this study which affect the application of radiometric normalization on time series. Generally, radiometric normalization blurs seasonal patterns of reflective bands and vegetation indices. The deviation from the non-normalized signals is least when data from the same season are used. Hence, it is important for mosaicing and compositing techniques to consider data from about the same date. If seasonal phenomena such as phenology are to be studied radiometric normalization should not be applied. Trend estimation and exploration of subtle changes are also hampered by radiometric normalization because of its leveling effect. Since reflectance and index values are modified by normalization procedures their physical interpretability cannot sustained. The strength of radiometric normalization lies in bi-temporal applications where small radiometric changes due to phenological differences, long-term trends, and changing illumination conditions are considered noise and strong changes are to be studied. The efficiency of IR-MAD for bi-temporal change detection is proven in many studies (Nielsen et al., 2010).

## 3.5 Forest Harvest Detection and Characterization of Forest Changes with Dense Satellite Time Series

### 3.5.1 Detection of Abrupt Changes

From the many change detection methods that exists (Coppin et al., 2004; Hecheltjen et al., 2014) only few were developed to separate long-term processes from abrupt changes (Cohen et al., 2010; Verbesselt et al., 2010a, 2010b). Instead, many methods exist that either use bi-temporal datasets or time series. Before the Landsat archive was opened, time series analysis was associated with coarse resolution imagery such as MODIS (Dubovyk et al., 2013a), MERIS (O'Connor et

al., 2012) or NOAA AHVRR (Fontana et al., 2012). Time series analysis is often related to trend detection (e.g., Dardel et al., 2014; Jeganathan et al., 2014; Lhermitte et al., 2011). This makes sense in many environments where abrupt changes and conversion of land uses play a minor role. However, in many ecosystems such as managed forests long-term trends cover only parts of the various processes that take place. Exploring processes with different temporal characteristics is crucial for comprehensive understanding of complex processes. Goodwin et al. (2010, 2008) estimated insect infestation dynamics of mountain pine beetle attacks in British Columbia using a sequence of annual and bi-annual Landsat data. They report potential for deriving estimates of the year of stand death but also conclude that a higher temporal frequency is required for more accurate timing of the infestation. Only few methods account for long-term trends, seasonal variation, and abrupt changes. One recent method that became popular is the Breaks For Additive Season and Trend (BFAST) (Verbesselt et al., 2010a, 2010b). Time series decomposition into trend, seasonal and remainder (noise) components is a common technique to characterize time series and describe their temporal behavior. An example is the Seasonal-Trend decomposition procedure (STL) based on a LOcally wEighted regreSsion Smoother (LOESS) (Cleveland et al., 1990). This method, however, is not designed to detect abrupt changes since it assumes slow changes which are then characterized by the trend component. BFAST is also an additive model. It iteratively fits piecewise linear trend and seasonal models (Verbesselt et al., 2010a). The general form of the model is

$$Y_t = T_t + S_t + e_t \; (t = 1, \dots, n), \tag{20}$$

where $Y_t$ is the observed data at time $t$, $T_t$ is the trend component and time $t$, $S_t$ is the seasonal component at time $t$, and $e_t$ is the remainder component at time $t$. In the piecewise linear model the trend and the seasonal components are composed of one or more segments. Each segment has individual slopes and intercepts. In BFAST the seasonal component is fixed between breakpoints, but can vary between segments. The breakpoints of the trend component may be different from that of the seasonal component. Hence, breakpoints (i.e., abrupt changes) can be detected in the seasonal behavior of a time series as well as in long-term trends (Verbesselt et al., 2010b).

The critical part of the method is the estimation whether breakpoints occur in the time series. The BFAST implementation in the R statistical environment (R Core Team, 2014) makes use of the ordinary least squares residuals-based MOving SUM (MOSUM) test to determine the occurrence and the number of breakpoints (Zeileis, 2005). The optimal position of these breaks is determined by minimizing the residual sum of squares using the method of Bai and Perron (2003). The optimal number of breaks is calculated by minimizing the Bayesian Information Criterion (BIC) (Zeileis et al., 2002). All breakpoints are estimated with a confidence interval of 95% thereby indicating the reliability of the estimated dates (Verbesselt et al., 2010b). However, the BFAST implementation requires regular time series such as the MODIS 16-days NDVI product. The BFAST method was modified to be applicable to irregular time series and to detect abrupt changes in near-real time (Verbesselt et al., 2012). The focus of this approach, available as *bfastmonitor()* function within the *bfast* package for R (R Core Team, 2014), is on the detection of

changes at the end of time series. For that purpose, the method derives a stable history period which is compared to the entries at the end of the time series, a so-called monitoring period.

The approach presented here is oriented on the idea of detecting irregularities in time series. The method is largely driven by the fact that compositing techniques (e.g., Griffiths et al., 2013) are not entirely promising in areas with frequent and steady cloud cover. Usually, compositing produces harmonized datasets at the expense of temporal resolution. The benefit of Landsat time series in contrast to composites is its high spatial resolution compared to MODIS or MERIS and its dense, yet irregular, observation frequency. To date, comparable revisiting intervals at same spatial resolution can only be achieved with costly commercial satellite systems. These lack historical records, however. Compositing means data reduction which in turn means loss of information. Forest harvesting happens very quickly in the study area. Figures of harvesting rates are coarse and lack of temporal precision. Analysis of annual data would neither allow to detect preferred harvesting months nor to properly identify the year of harvest. When using annual data from summer or fall, it is only possible to discover the time period of change. The change itself may start in late fall of one year or in early spring of the year after.

The primary goal of the presented method is to detect abrupt changes in time series which are associated with harvesting and precisely determine location and timing of the harvest events. Since we make use of all images a more precise timing of the change event is ought to be possible compared to existing reporting practices. Abrupt changes are assumed to be displayed as most pronounced slope of a time series. Hence, the extreme values of the first derivative are a good means to detect abrupt changes. From several tests we found that harvesting although being an abrupt change may occur as a process that takes several months resulting in a slope that is less steep than expected. Rather than finding extremes of changes in a time series it is more appropriate to determine discontinuities. Another measure that produces more reliable results than the first derivative is the discontinuity detection method proposed by Webster (1973). It was once developed to detect borders of geological formations. It is based on a moving window run over each single time series (in Webster, 1973, it was a spatial profile). The moving window is divided into two parts. For each part the mean is calculated; the difference of the left hand and right hand means is plotted. The principle of the method is that the difference is large at points where the values of the two window halves are considerably distinct (Legendre and Legendre, 2012). The timing of change is assumed at the point with the biggest difference. In case that the abrupt change is associated with a decrease in a spectral index time series this point is indicated by the minimum value of the Webster measure. In case the change event causes an increase in the spectral index the maximum value of the Webster measure indicates the change event. The method does not work properly for irregularly spaced time series. Thus we linearly interpolated the time series and subsequently applied a Savitzky-Golay filter (Savitzky and Golay, 1964) to minimize remaining noise. The Savitzky-Golay filter is well established in time series processing (Chen et al., 2004; Jönsson and Eklundh, 2004, 2002; Ren et al., 2008). Interpolation of time series is critical when the gaps become too long and blur seasonal pattern (e.g., phenology). In the present dataset the minimum time gap of consecutive observations is one day since we are using data from different Landsat sensors and adjacent orbits. Using all available Landsat data allows constructing dense time series.

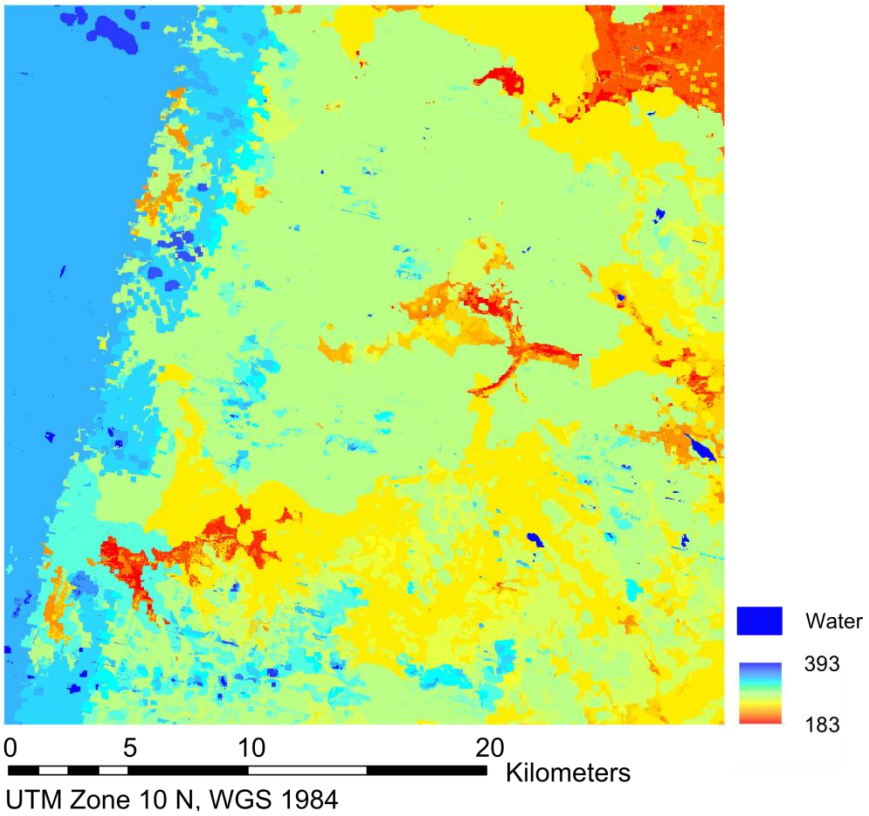


Fig. 3.5.1: Maximum gap length in the time series.

The average gap length in our dataset is less than 20 days in the favored areas and up to 70 days in less favored areas that are covered by only one Landsat tile. As can be seen from the cloud statistics, gaps between consecutive clear land observations vary considerably in time and space. However, maximum length of data gaps is less than one year for most parts of our study site (Fig. 3.5.1). Hence, interpolation as a means to fill data gaps (Verbesselt et al., 2006), construct regularly spaced time series, and consistently process Landsat data is meaningful. Filtering of the time series is not mandatory but produces clearer curves which can then be further processed. Filter length is set to one year, i.e., 365 days. This value is arbitrary. But it was chosen under the assumption that a one-year filter would account for all within-year variability. Tests revealed that it gives consistent results. For the change detection with the Webster method we define a window width of 365 days. Hence, the time period considered is always one full year, ensuring that seasonality is leveled out. This means that in a time series without change the Webster measure will be zero. None-zero values indicate temporal shifts in the seasonal signal or changes in the annual amplitudes. Abrupt changes that result in a different level of an index value will be displayed as pronounced deviation from zero. Since clear cut events cannot occur in two successive years due to the recovery time which is much longer, abrupt changes caused by harvesting cannot be leveled out. Compared to the first derivative, the Webster method better captures the timing of changes and it is less sensitive to outliers. The principle of the proposed method is shown in Fig. 3.5.2.

The proposed method accounts for the extreme values of the Webster measure. Hence, breakpoints can be detected in each individual time series. To assure that the detected breaks are associated with true changes on the ground, we perform a two-sided two-sample Kolmogorov-

Smirnov test (K-S test) of the detected breakpoints considering thirty observations before and after the break event. The K-S test is a nonparametric test for the equality of one-dimensional probability distributions that can be used to compare two samples. In the two-sample case, the K-S test tests if the empirical distributions functions of two samples differ. For a level of significance *a* equality of the distributions is rejected when *D* exceeds the critical value given for a known size of each sample. Critical values of the K-S test statistic *D* are provided as table (e.g. http://www.soest.hawaii.edu/wessel/courses/gg313/Critical_KS.pdf). For sample sizes larger than 12 the approximate critical value $D_a$ is given by the equation:

$$D_\alpha = c(\alpha)\sqrt{\frac{n_1 + n_2}{n_1 n_2}} \quad (21).$$

where the coefficient $c(a)$ for a significance level of 0,01 equals 1,63.

In the present application we use the K-S test to compare the last part of a time series before a detected break and the part of the time series directly after the detected break. In case there are less than thirty observations on one of either side (e.g., breaks at the very beginning or at the very end of a time series), a smaller number of observations is used for the respective side. However, for a *a* of 0,01 the K-S statistic cannot be calculated if one sample is smaller than three. Since in the given application one sample is always as large as thirty we can assume that the critical value of *D* will not be higher than 0,92. We set the critical value to 0,95. Sample sizes of three and smaller are considered too small and detected breaks are rejected. If the K-S statistics is smaller than the critical value then the other extreme values of the Webster measure are tested repeatedly with the K-S test according to decreasing magnitude until a significant value of *D* is achieved. More than one occurrence of abrupt changes per year is unlikely. Consequently, the number of iterations is set to the number of years in the time series.

Trends are calculated for the time before and after the break using a linear regression. In case there is no break detected, trends are calculated for the beginning of the time series and for the end of the time series to account for the decelerated index increase. A time span of three years is used. A trend over the complete time series is calculated as well. To assess the presence of trends we performed a Mann-Kendall trend analysis (Kendall, 1938; Mann, 1945). It is a non-parametric trend test which estimates the presence of monotonic trends. The Kendall's rank correlation coefficient *Tau* ranges between -1 and 1, indicating negative and positive trends, respectively. Values of 0 indicate no trend. The Mann-Kendall trend test is frequently used in vegetation and degradation studies (Tüshaus et al., 2014; Wessels et al., 2012).

The proposed method has several advantages over bi-temporal change detection. Besides its ability to display comprehensive temporal profiles of indices the method does not require thresholding or user adjustment. This is important when considering the spatio-temporal variability of most spectral indices as shown above. Application of thresholds on either the Webster measure or the change magnitude (index difference caused by abrupt change) or one of the other features that describe the temporal profile (Fig. 3.5.3) can be done as additional post-processing step.

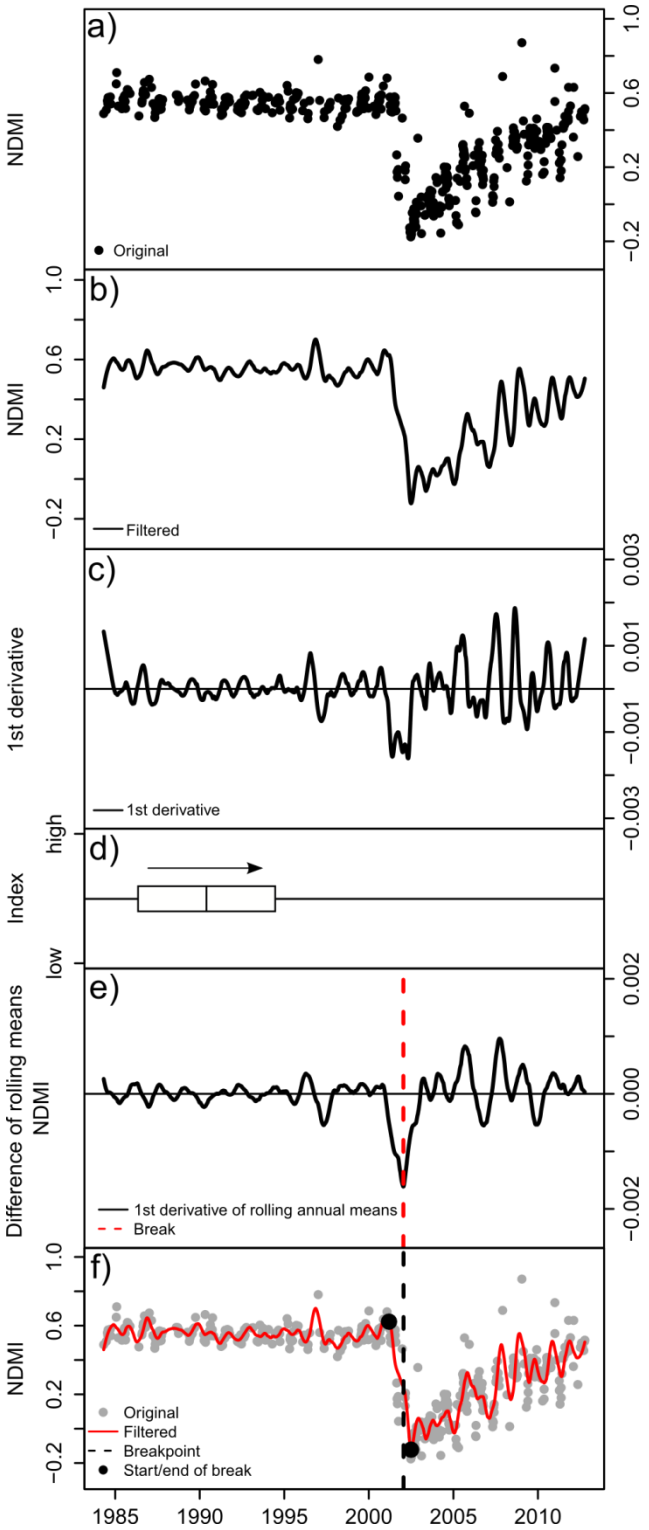


Fig. 3.5.2: Scheme of processing steps for break detection: a) cleaning time series from invalid observations (data gaps, clouds, cloud shadow), b) filtering, c) first derivative as a measure of dynamics in the time series, d) the moving window principle of the Webster method that is applied on the time series, e) resulting curve, and f) time series of original observations, filtered time series, break detected with the Webster approach, and start and end of break.

### 3.5.2 Time Series Properties

A collection of properties that can be derived from annual vegetation index cycles (usually NDVI) have been presented by (Hill and Donald, 2003; Jönsson and Eklundh, 2004; Reed et al., 1994). These properties, sometime referred to as phenometrics, are well suited to describe phenology of photosynthetic active vegetation and comprise among others start of season, end of season, peak, amplitude, length of season, and time-integrated vegetation index. Comparison over several years allows for the identification of shifts of some features. Examples can be found in Fisher et al. (2006), Melaas et al. (2013), and Zhang et al. (2003).

Since conifer forests show only little seasonal variation those properties are not of particular interest in the present study. Here, seasonality can be seen as a proxy for the occurrence of broad-leaf tree species since those show more pronounced response to phenology than coniferous trees. Trends are also of particular interest rather than phenology. If additional data is available (e.g., Light Detection and Ranging (LiDAR)) then index values can be related to forest growth rates and biomass accumulation which is important for carbon budget estimation (Duncanson et al., 2010). Calculations of trends before a harvest event are of limited value since their interpretation is complex. The main reason is that vegetation indices saturate more or less as a function of crown closure. Biomass accumulation or forest maturation can hardly be displayed by trends of vegetation indices. That means that index values saturate after few years of undisturbed growth although forest development, change of species composition, and change of forest structure continue. The physical interpretation of trends of index time series from forests can be very complex. However, the slope of the early recovery stage may be an important measure for regrowth rates under consideration of local and regional climate and ecological conditions.

Once the break point is detected several properties of the time series may be analyzed, e.g., magnitude of index change. Since the timing of forest clearing cannot be attributed to a single day, it is useful to indicate the starting and ending date of the change. A good approximation can be derived from the extreme values directly before and after the change event. In case these are

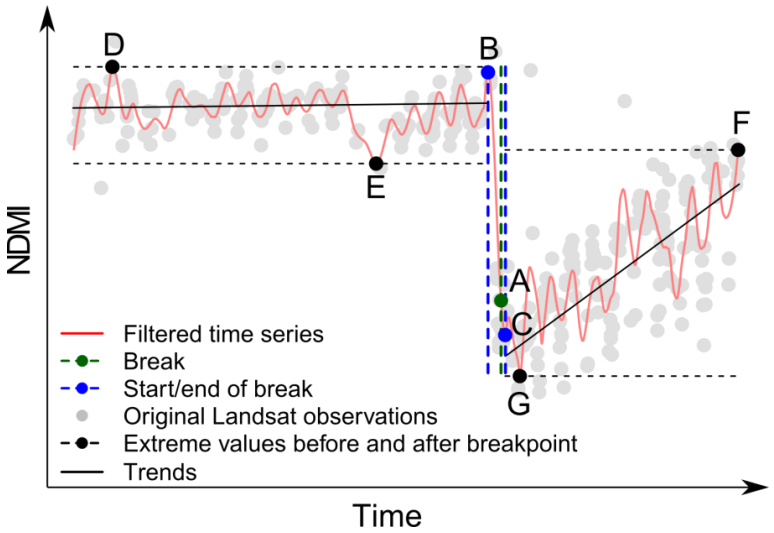


Fig. 3.5.3: Descriptors of time series that characterize the change event exemplified in a NDMI time series (see text for explanation).

similar, the detected change is most likely a outlier. Otherwise, they depict the duration of the change and its intensity. Several descriptors of breaks and trends in time series may be extracted that characterize the change event. These are shown in Fig. 3.5.3. The descriptors are: A) break (time & index value), B) start of break (time & index value), C) end of break (time & index value), D) maximum index value before break & its time, E) minimum index value before break & its time, F) maximum index value after break & its time, and G) minimum index value after break & its time. A good characterization can also be derived from: the difference B-C (the time difference indicating the duration of the break event; the index value difference indicating the magnitude of change), the difference D-E (indicating stability in both the time and index domain), and the difference F-G (indicating recovery and its strength). Under the assumption of linearity the interpretation of trends becomes ambiguous, however, the longer the time series are (Fig. 3.5.5). Nonetheless, we calculated the trends before and after a break, and over the complete time series for a more comprehensive understanding of the underlying processes, particularly during the regrowth phase.

### 3.5.3 Results

#### 3.5.3.1 Landsat Time Series of Selected Spectral Indices

As it is well known, spectral indices are not a mere measure to distinguish vegetation from bare ground. Instead, each spectral band used for the index calculation displays distinct properties of the target class. Ideally, these properties are unique and allow to distinguishing the target class or its condition from other classes or other conditions. In the present case the target class is (coniferous) forest. The selected spectral indices are known to highlight different phases of the forest life cycle in different ways. The most dramatic change occurs if clearcut harvesting takes place. Fig. 3.5.4 shows one single pixel over time captured by the indices. From Fig. 3.5.4 it can be seen that the Webster measure is a good indicator for abrupt changes in all indices. It is also an indicator for seasonal shifts in the index values. As the time window used for the calculation is one year seasonality is leveled out (Fig. 3.5.4, right column). The first derivative has more periodic patterns (Fig. 3.5.4, center column). Although not well suited for the break detection, it provides valuable information about the intensity of within-year dynamics before and after the change event. There are, however, huge differences between the first derivatives of all indices. DI is very stable during the time of stable forest. As the new forest develops there is pronounced variability in the first derivative and also in the Webster measure. Other indices such as greenness or EVI are dynamic during all growing stages captured by the pixel of Fig. 3.5.4. The detected date of change varies slightly among the indices. Duration of the change event varies also. One of the prerequisites that variation of the index value must be smaller than the abrupt change intensity is best captured by the indices that include SWIR bands (TC wetness, TCA, DI, NBR, NDBI, NDMI).

In Fig. 3.5.5 a set of time series with different temporal evolution and from different randomly selected locations is exemplified with the NDMI. The locations differ in altitude, slope and aspect. Hence, the impact of illumination and shadow is distinct in each time series.

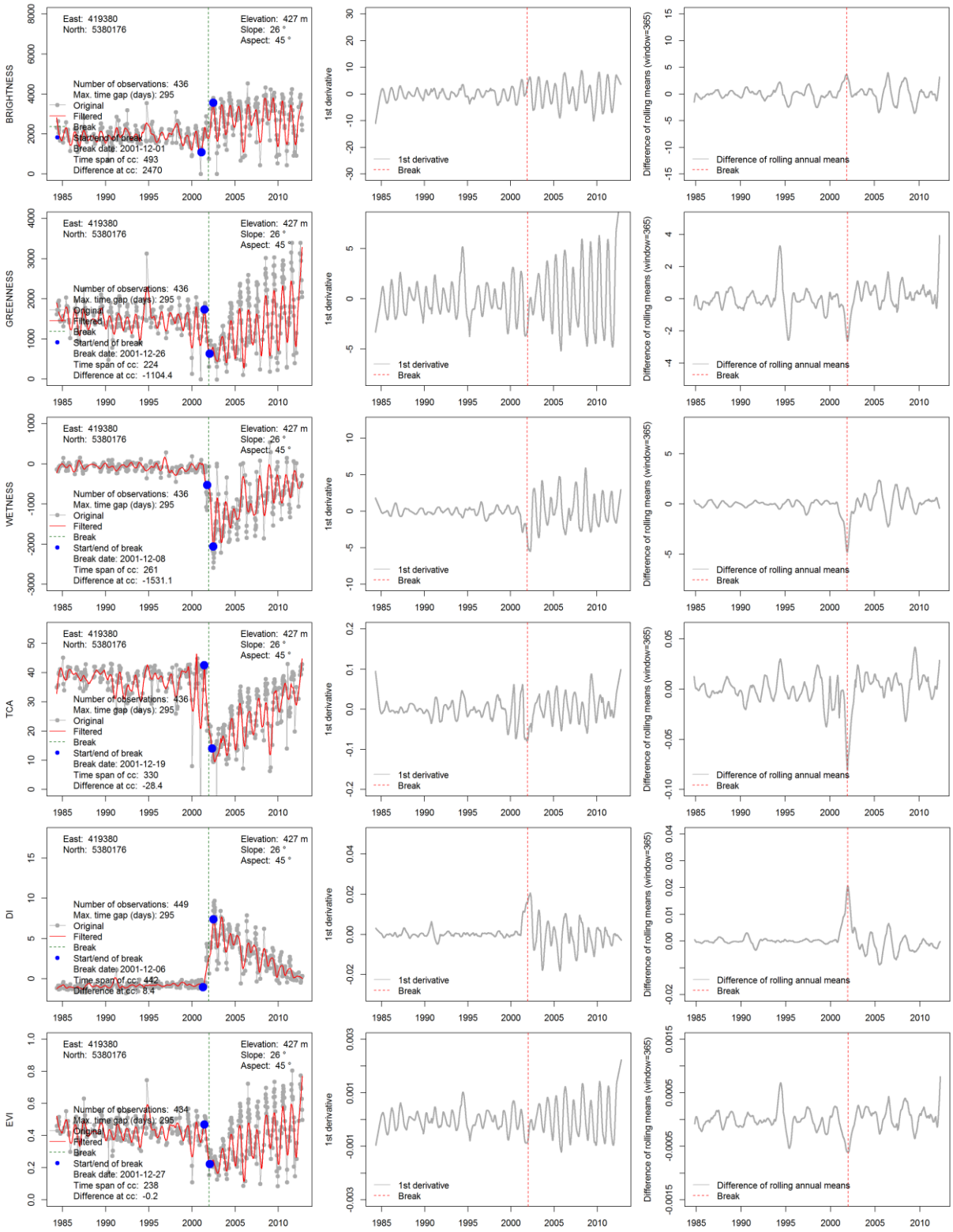


Fig. 3.5.4: Time series for ten indices of one single pixel and detected breaks, time span, and magnitude of change; left column shows the index time series, centre column shows first derivative, and right column shows Webster measure from which the break is calculated.

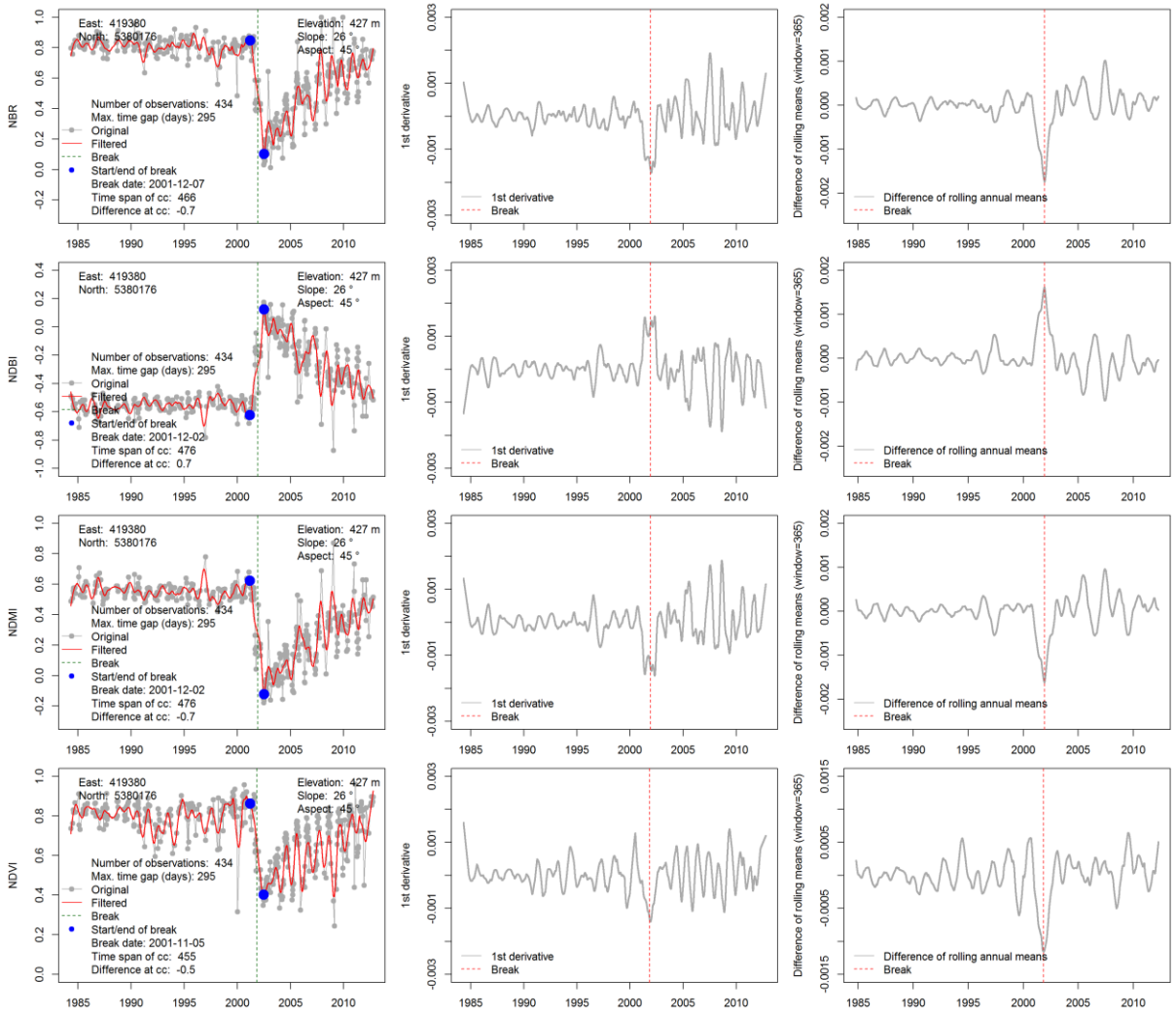


Fig. 3.5.4 (continued).

Furthermore, the number of clear observations and their timing differs between the selected points. The previously described break detection method was applied on each pixel. The number of clear observations and the length of the largest time gap are plotted for each pixel. In case a break was detected, time of break, duration of the break, and magnitude of break are plotted as well (Fig. 3.5.5, left column).

The plots of Fig. 3.5.5 confirm the efficiency of the proposed method. All breaks of the pixel time series are well detected. Pixels without abrupt changes are seen as no-change pixels. Again, the first derivative and the Webster measure are plotted, too.

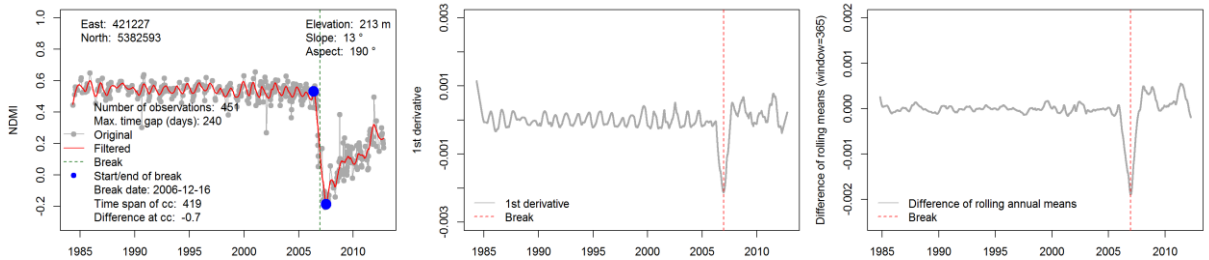


Fig. 3.5.5: Break detection in NDMI time series for randomly selected pixels. For each pixel (left column) the first derivative (centre column) and the Webster measures (right column) are plotted.

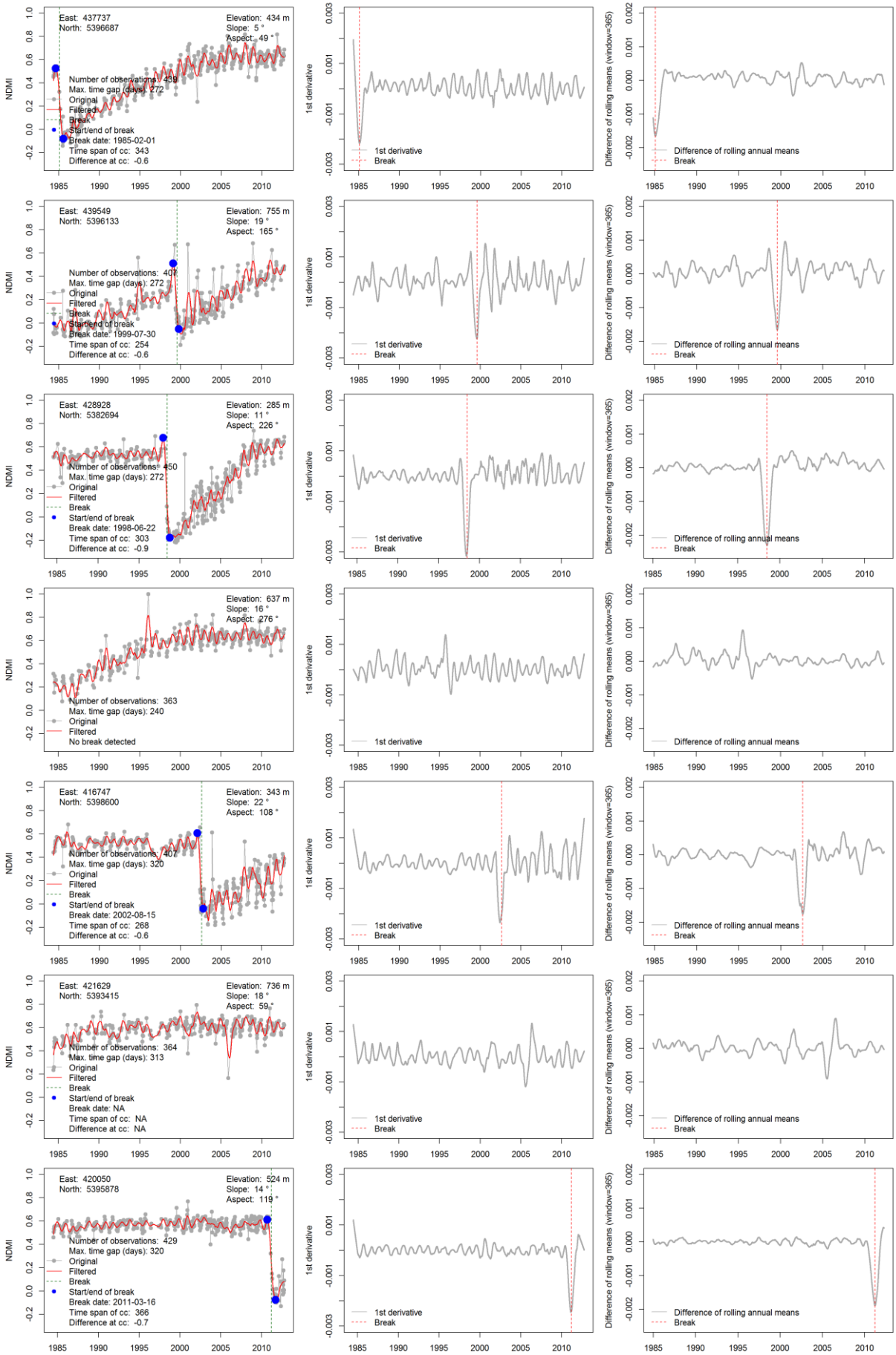


Fig. 3.5.5 (continued).

### 3.5.3.2 Clearcut and Recovery Patterns 1984-2012

Southern Vancouver Island experiences vast changes for decades. As a result of intense forest management practices large parts of the study site have been harvested during the observation period. The overall clearcut area between 1984 and 2012 is about 26153 ha. This area corresponds to 29% of the area. Almost the same area (26167 ha) shows significant positive trends indicating forest regrowth. It is very likely that this area has been cleared before the observation period started and has not reached the crown closure stage at the start of the time series in 1984. Whereas it is well known that the area is heavily used (e.g, Hansen et al., 2013, http://earthenginepartners.appspot.com/science-2013-global-forest) our results show unprecedented temporal details. Annual forest loss or forest harvest maps are a valuable result of many recent studies (e.g., Griffiths et al., 2012; Hansen et al., 2013). An equivalent map is presented in Fig. 3.5.6a showing the timing (as year) and spatial patterns of clearcut disturbances. The method presented here allows deriving exact clearcut dates and patterns according to clearcut month (Fig. 3.5.6b). The strength of the disturbance is a good indicator to separate stand replacing disturbances from subtle changes such as insect defoliation. Major disturbances, mainly forest harvest patterns, are shown in Fig. 3.5.6c as disturbance magnitude. As forest harvest takes several days up to months, it is challenging and debatable to define such an event as a single date. It is appropriate, however, to provide the duration of the disturbance as time between disturbance onset and start of regrowth. As shown in Fig. 3.5.6d, break duration is usually less than one year. Few patches have remarkably longer break duration. It is not clear if this extended duration is caused by the management practice (e.g., wood debris left in the field) or if it is a phenomenon originating from the remote sensing data. Time series can be described by several parameters (Fig. 3.5.3). An indication whether a pixel's history is stable is given by its extreme values. Although they have to be interpreted with caution since they largely depend on the quality of the clear land mask, the extreme values (i.e, maximum and minimum) and their difference accentuate time series long-term stability. From the maximum (Fig. 3.5.6e) all areas that have been forest at least for a short term of the observation period are recognizable. Shades of orange and red in Fig. 3.5.6e indicate forest cover whereas yellow and bluish colors indicate non-forest. As this is the maximum of the whole time series it is obvious that the latter areas are non-forest areas (mainly in the north-eastern part of the study site). Healthy forest areas in the study site have NDMI values around 0,5 or higher. The minimum plot (Fig. 3.5.6f) reveals the areas that have high NDMI values during the whole observation period, indicated by values larger than about 0,3. Areas with high minimum values and hence high NDMI values over the whole period can be attributed to forests. The minimum plot also shows those areas that have been unforested for at least parts of the observations period. This picture is complemented by the difference of maximum and minimum (Fig. 3.5.6g). Only small areas of the study site show little change during the observation period (indicated by blue colors). It must be noted that even difference values of 0.2 can indicate stable forest conditions (e.g., mature or old-growth forests) – the differences may be attributed to strong seasonal illumination changes. As shown in Fig. 3.5.6g, the difference is not necessarily huge in clearcut areas – depending on the management practice, topography, forest stage and rotation time. Consequently, using fixed thresholds may introduce mapping

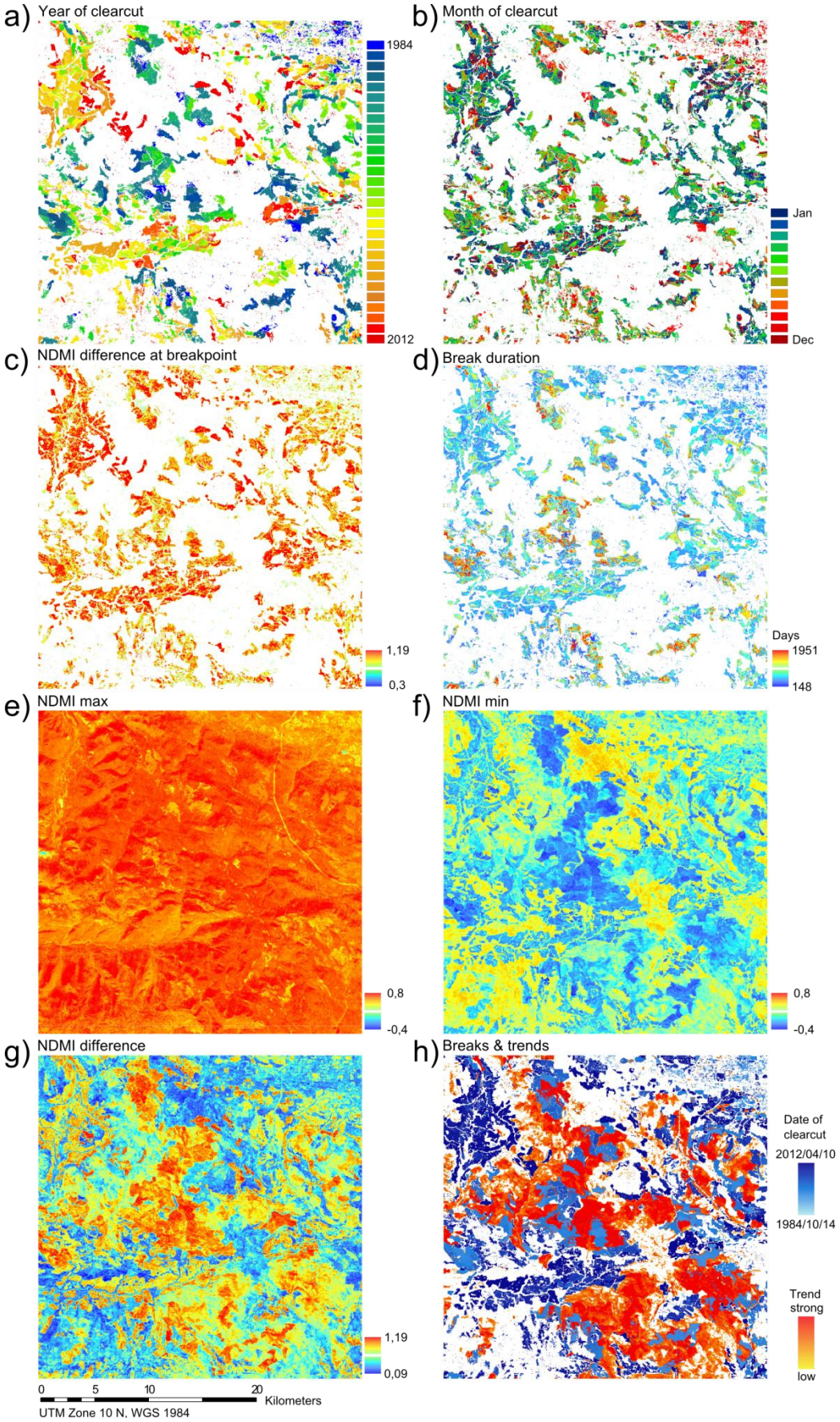


Fig. 3.5.6: a) Annual disturbance map, b) monthly disturbance map, c) disturbance magnitude, d) break duration, e) NDMI maximum, f) NDMI minimum, g) NDMI difference, h) final map with detected disturbance dates and strength of detected significant trends.

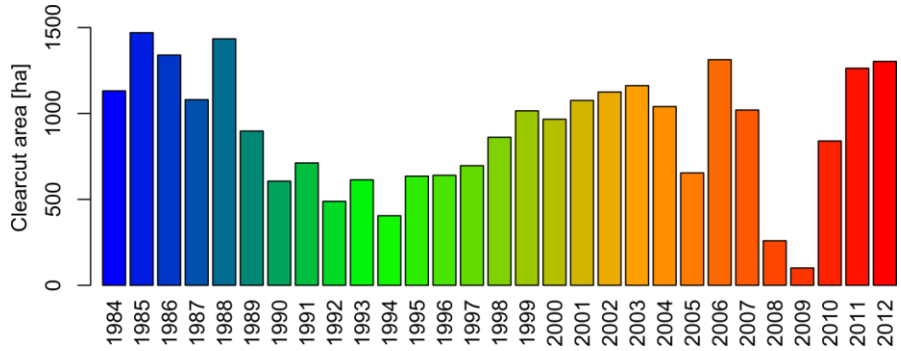


Fig. 3.5.7: Area of clearcut harvest per year in hectares (colors refer to Fig. 3.5.6a).

errors. On the other hand, strong differences occur in areas where no clearcut was detected. As a consequence of forest regrowth the spectral index steadily increases. A change event (e.g., a clearcut) is likely to have happened before the start of the observation period. A final change detection map is presented in Fig. 3.5.6h. Here, clearcut events are shown as continuous dates in shades of blue. Recovery trends are shown in shades of red.

Although the study site does not represent an administrative entity Fig. 3.5.7 to Fig. 3.5.9 demonstrate how the results may be used. Fig. 3.5.7 provides statistics of the annual clearcut area in the study site. Underlying reasons and causal agents are not explored here and cannot be derived from the figures alone. The temporal variation in Fig. 3.5.7 may have several reasons. The pattern may be caused by the fact that the forest companies change their harvesting locations randomly or even in an organized way. That means they simply harvested in different locations when a decline is observable in the study site. Another reason may be that the harvesting rate decreased due to economic or other factors. The abrupt decrease of harvested area in 2008 and 2009 is very likely to be driven by the worldwide economic crisis (The Vancouver Sun, 2008). The area harvested within a spatial entity also depends on the size of the forest area that is ready to be harvested. The annual average harvested area during the 29 years observation period is 900 ha/a. Given a full forest coverage (which is not entirely true as there are waterways, unvegetated high altitude rocky areas, and small settlements) this would mean 100 years to once clear the whole area. At a rotation time of about 80 years the forest could recover. However, it must be noted that a 100 year forest is far away from the mature and old-growth forest stages and also provides only limited biological variety.

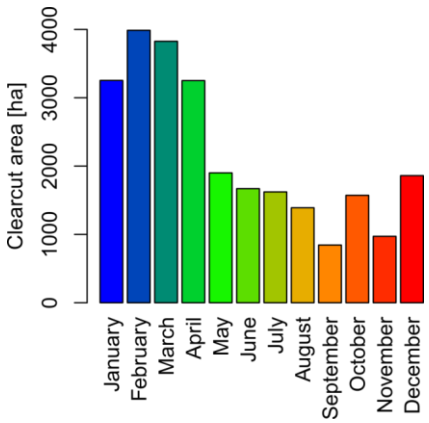


Fig. 3.5.8: Area of clearcuts per month in hectares (colors refer to Fig. 3.5.6b).

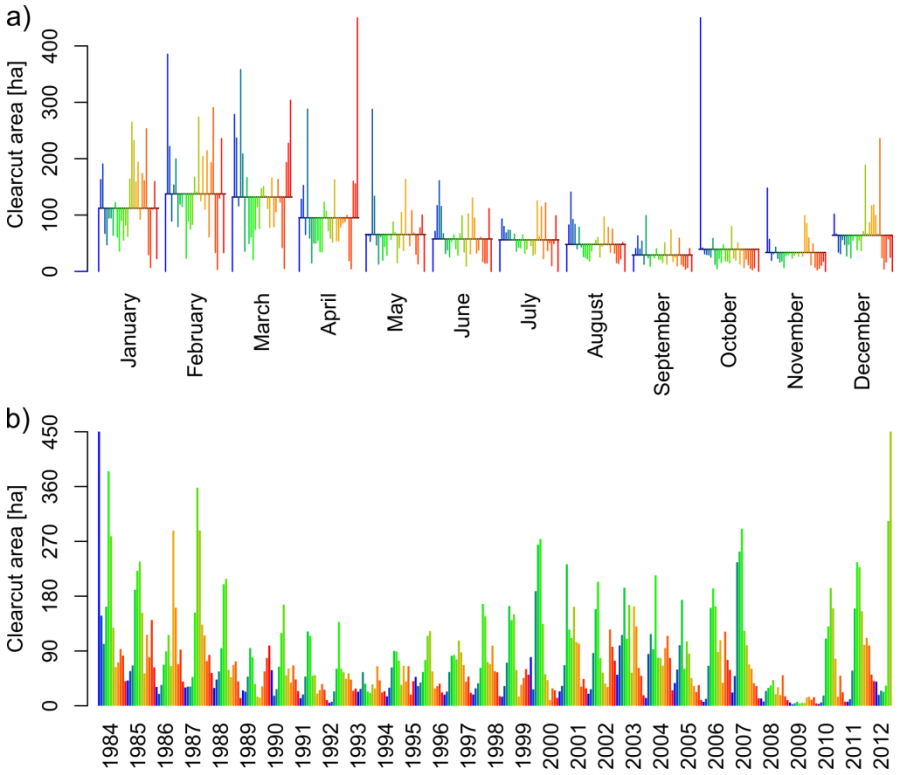


Fig. 3.5.9: a) Clearcut areas per month and year (colors refer to Fig. 3.5.6a), b) Clearcut area statistics for the study site as monthly time series (colors refer to Fig. 3.5.6b).

Fig. 3.5.8 contains a lot of uncertainty. Nonetheless, it shows a temporal regularity. We assume that the presented method works fairly accurate and the temporal pattern is not random. The date of strongest change derived with the Webster measure is relatively close to the onset of the disturbance. We assume that a clearcut results in a change of the spectral index value. Hence, the date of disturbance extracted with the Webster method cannot be shifted to too early dates. A slight shift to later dates is possible. Consequently, it is possible that the pattern of Fig. 3.5.8 is slightly shifted as well and the true peak lays in the winter months. The temporal pattern could also be a consequence of missing winter observations. The combination of linear interpolation and filtering, however, make the proposed method rather robust against these effects.
Fig. 3.5.9a displays the harvest statistics as month plots, e.g., January values are listed by year. The clearcut areas are plotted as deviation from averages by month. Figures like that reveal differences annual differences per month. Very striking are the huge bars of October 1984 and April 2012. These are earliest and latest clearcut periods of the presented observation period, indicating that there is uncertainty of our results in the very beginning and the very end of the time series. A different way of representing is shown in Fig. 3.5.9b. The time series has not been further explored. But there is a lot of temporal dynamics that is undiscovered or blurred in annual time series alone.

### 3.5.4 Validation of Time Series Analysis Results

Validation of change detection results is often challenging even with bi-temporal datasets. It becomes more complicated when using time series. Timely reference data is hardly available and

often biased. Studies exploring annual Landsat time series refer on the year of disturbance onset or the first year with detected disturbance (Griffiths et al., 2012). If there are missing observations due to clouds or other obstacles there is tremendous time lag and uncertainty in the results. As our approach provides more comprehensive and more detailed information on the change process (Fig. 3.5.3) we can perform more accurate accuracy assessment. Reference data is taken from the Landsat time series itself since this dataset provides most comprehensive temporal information. The reference dataset was generated as follows. We performed bi-temporal change detection on annual cloud free images using RCVA. The resultant 29 magnitude images were subjected to automated thresholding. The results were manually corrected by comparing the both input datasets and the binary change detection mask. As there are only Landsat 7 ETM+ SLC-off images for 2012, we used a Landsat 8 OLI image from 2013/07/26 as second image for 2012. Some changes occurring in the resulting mask are not covered by our time series which ends by end of 2012. As mentioned previously, these bi-temporal datasets (as well as annual time series) allow to indicate a period of change rather than an exact year. The 29 yearly masks were combined to one single reference image. From that reference image we selected 30 pixels per disturbance year plus 30 pixels from the undisturbed pixels based on stratified random sampling. For each of the resulting 900 locations we extracted the NDMI time series and plotted them. Each individual plot was manually checked. For some of the reference points the labels had to be revised. This was mainly because the changes happened in late fall of the previous year rather than in spring of the next year. Some pixels had to be relabeled because they experienced change in early 2013 – after the end of the observation period. In some instances, the location did not include a change although it was supposed to. This happened when small patches of trees were left inside a clearcut or in isolated pixels. The corrected reference dataset contains samples of slightly different size. About 13% of the reference data had to be revised confirming that imperfect ground or reference data are a major error source (Foody, 2010). For each of the 900 locations we checked 1) if change and no-change pixels were detected, 2) if the specified time span covers the most pronounced change, and 3) if the year of change was specified correctly. A simple change/no-change accuracy was calculated from Tab. 3.5.1. It can be seen that the accuracy is quite good although some of the changes were not detected. In fact, most of these changes were not detected because the curve immediately after the change event was heavily disturbed. A more comprehensive accuracy assessment is presented in Tab. 3.5.2. It reveals that most errors occur for the changes in the very first year of the time series. This result confirms that the presented method is not optimally setup to detect very early and very late changes. The method may be adjusted by setting the number of samples used for the KS-test higher. As described earlier, it uses 30 points from either side of the detected change.

Tab. 3.5.1: Confusion matrix of change and no-change.

| | Reference change | Reference no-change | Sum | User Accuracy |
|---|---|---|---|---|
| Detected change | 805 | 3 | 808 | 99,63 |
| Detected no-change | 38 | 54 | 92 | 58,70 |
| Sum | 843 | 57 | 900 | |
| Producer Accuracy | 95,49 | 94,74 | | 95,44 |

Tab. 3.5.2: Confusion matrix of change detection results with respect to year of change (NC = No Change, UA = User Accuracy, PA = Producer Accuracy).

| | | Reference | | | | | | | | | | | | | | | | | | | | | | | | | | | | | | |
|---|---|---|---|---|---|---|---|---|---|---|---|---|---|---|---|---|---|---|---|---|---|---|---|---|---|---|---|---|---|---|---|---|
| | | NC | 1984 | 1985 | 1986 | 1987 | 1988 | 1989 | 1990 | 1991 | 1992 | 1993 | 1994 | 1995 | 1996 | 1997 | 1998 | 1999 | 2000 | 2001 | 2002 | 2003 | 2004 | 2005 | 2006 | 2007 | 2008 | 2009 | 2010 | 2011 | 2012 | Sum | UA |
| Detected | NC | 54 | 12 | 1 | 1 | 1 | 0 | 0 | 0 | 0 | 1 | 0 | 0 | 5 | 2 | 2 | 2 | 0 | 1 | 2 | 0 | 1 | 1 | 1 | 1 | 1 | 0 | 0 | 1 | 0 | 0 | 90 | 60,0 |
| | 1984 | 0 | 14 | 1 | 0 | 0 | 0 | 1 | 0 | 0 | 0 | 0 | 0 | 0 | 0 | 0 | 0 | 0 | 0 | 0 | 0 | 0 | 0 | 0 | 0 | 0 | 0 | 0 | 0 | 0 | 0 | 16 | 87,5 |
| | 1985 | 1 | 0 | 28 | 2 | 1 | 0 | 0 | 0 | 0 | 0 | 0 | 0 | 0 | 0 | 0 | 0 | 0 | 0 | 0 | 0 | 0 | 0 | 0 | 0 | 0 | 0 | 0 | 0 | 0 | 0 | 32 | 87,5 |
| | 1986 | 0 | 0 | 0 | 24 | 1 | 0 | 0 | 0 | 0 | 0 | 0 | 0 | 0 | 0 | 0 | 0 | 0 | 0 | 0 | 0 | 0 | 0 | 0 | 0 | 0 | 0 | 0 | 0 | 0 | 0 | 25 | 96,0 |
| | 1987 | 0 | 0 | 0 | 0 | 21 | 1 | 0 | 0 | 0 | 0 | 0 | 0 | 0 | 0 | 0 | 0 | 0 | 0 | 0 | 0 | 0 | 0 | 0 | 0 | 0 | 0 | 0 | 0 | 0 | 0 | 22 | 95,5 |
| | 1988 | 1 | 0 | 0 | 0 | 0 | 27 | 2 | 0 | 0 | 0 | 0 | 0 | 0 | 0 | 0 | 0 | 0 | 0 | 0 | 0 | 0 | 0 | 0 | 0 | 0 | 0 | 0 | 0 | 0 | 0 | 30 | 90,0 |
| | 1989 | 0 | 0 | 0 | 0 | 0 | 0 | 30 | 0 | 0 | 0 | 0 | 0 | 0 | 0 | 0 | 0 | 0 | 0 | 0 | 0 | 0 | 0 | 0 | 0 | 0 | 0 | 0 | 0 | 0 | 0 | 30 | 100,0 |
| | 1990 | 0 | 0 | 0 | 0 | 0 | 0 | 0 | 29 | 1 | 0 | 0 | 0 | 0 | 0 | 0 | 0 | 0 | 0 | 0 | 0 | 0 | 0 | 0 | 0 | 0 | 0 | 0 | 0 | 0 | 0 | 30 | 96,7 |
| | 1991 | 0 | 0 | 0 | 0 | 0 | 0 | 0 | 1 | 29 | 2 | 0 | 0 | 0 | 0 | 0 | 0 | 0 | 0 | 0 | 0 | 0 | 0 | 0 | 0 | 0 | 0 | 0 | 0 | 0 | 0 | 32 | 90,6 |
| | 1992 | 0 | 0 | 0 | 0 | 0 | 0 | 0 | 0 | 0 | 24 | 0 | 1 | 0 | 0 | 0 | 0 | 0 | 0 | 0 | 0 | 0 | 0 | 0 | 0 | 0 | 0 | 0 | 0 | 0 | 0 | 25 | 96,0 |
| | 1993 | 0 | 0 | 0 | 0 | 0 | 0 | 0 | 0 | 0 | 0 | 28 | 3 | 0 | 0 | 0 | 0 | 0 | 0 | 0 | 0 | 0 | 0 | 0 | 0 | 0 | 0 | 0 | 0 | 0 | 0 | 31 | 90,3 |
| | 1994 | 0 | 0 | 0 | 0 | 0 | 0 | 0 | 0 | 0 | 0 | 0 | 27 | 0 | 0 | 0 | 0 | 0 | 0 | 0 | 0 | 0 | 0 | 0 | 0 | 0 | 0 | 0 | 0 | 0 | 0 | 27 | 100,0 |
| | 1995 | 0 | 0 | 0 | 0 | 0 | 0 | 0 | 0 | 0 | 0 | 0 | 0 | 24 | 1 | 0 | 0 | 0 | 0 | 0 | 0 | 0 | 0 | 0 | 0 | 0 | 0 | 0 | 0 | 0 | 0 | 25 | 96,0 |
| | 1996 | 0 | 0 | 0 | 0 | 0 | 0 | 0 | 0 | 0 | 0 | 0 | 0 | 0 | 32 | 0 | 0 | 0 | 0 | 0 | 0 | 0 | 0 | 0 | 0 | 0 | 0 | 0 | 0 | 0 | 0 | 32 | 100,0 |
| | 1997 | 0 | 0 | 0 | 0 | 0 | 0 | 0 | 0 | 0 | 0 | 0 | 0 | 0 | 0 | 18 | 0 | 0 | 0 | 0 | 0 | 0 | 0 | 0 | 0 | 0 | 0 | 0 | 0 | 0 | 0 | 18 | 100,0 |
| | 1998 | 0 | 0 | 0 | 0 | 0 | 0 | 0 | 0 | 0 | 1 | 0 | 0 | 0 | 0 | 0 | 33 | 0 | 0 | 0 | 0 | 0 | 0 | 0 | 0 | 0 | 0 | 0 | 0 | 0 | 0 | 34 | 97,1 |
| | 1999 | 1 | 0 | 0 | 0 | 0 | 0 | 0 | 0 | 0 | 0 | 0 | 0 | 0 | 0 | 0 | 0 | 30 | 0 | 0 | 0 | 0 | 0 | 0 | 0 | 0 | 0 | 0 | 0 | 0 | 0 | 31 | 96,8 |
| | 2000 | 0 | 0 | 0 | 0 | 0 | 0 | 0 | 0 | 0 | 0 | 0 | 0 | 0 | 0 | 0 | 0 | 0 | 24 | 0 | 0 | 0 | 0 | 0 | 0 | 0 | 0 | 0 | 0 | 0 | 0 | 24 | 100,0 |
| | 2001 | 0 | 0 | 0 | 0 | 0 | 0 | 0 | 0 | 0 | 0 | 0 | 0 | 0 | 0 | 0 | 0 | 0 | 0 | 32 | 0 | 0 | 0 | 0 | 0 | 0 | 0 | 0 | 0 | 0 | 0 | 32 | 100,0 |
| | 2002 | 0 | 0 | 0 | 0 | 0 | 0 | 0 | 0 | 0 | 0 | 0 | 0 | 0 | 0 | 0 | 0 | 0 | 0 | 0 | 32 | 0 | 0 | 0 | 0 | 0 | 0 | 0 | 0 | 0 | 0 | 32 | 100,0 |
| | 2003 | 0 | 0 | 0 | 0 | 0 | 0 | 0 | 0 | 0 | 0 | 0 | 0 | 0 | 0 | 0 | 0 | 0 | 0 | 0 | 0 | 34 | 1 | 0 | 0 | 0 | 1 | 0 | 0 | 0 | 0 | 36 | 94,4 |
| | 2004 | 0 | 0 | 0 | 0 | 0 | 0 | 0 | 0 | 0 | 0 | 0 | 0 | 0 | 0 | 0 | 0 | 0 | 0 | 0 | 0 | 0 | 30 | 0 | 0 | 0 | 0 | 1 | 0 | 0 | 0 | 31 | 96,8 |
| | 2005 | 0 | 0 | 0 | 0 | 0 | 0 | 0 | 0 | 0 | 0 | 0 | 0 | 0 | 0 | 0 | 0 | 0 | 0 | 0 | 0 | 0 | 0 | 24 | 0 | 0 | 0 | 0 | 0 | 0 | 0 | 24 | 100,0 |
| | 2006 | 0 | 0 | 0 | 0 | 0 | 0 | 0 | 0 | 0 | 0 | 0 | 0 | 0 | 0 | 0 | 0 | 0 | 0 | 0 | 0 | 0 | 0 | 0 | 31 | 0 | 0 | 0 | 0 | 0 | 0 | 31 | 100,0 |
| | 2007 | 0 | 0 | 0 | 0 | 0 | 0 | 0 | 0 | 0 | 0 | 0 | 0 | 0 | 0 | 0 | 0 | 0 | 0 | 0 | 0 | 0 | 0 | 0 | 0 | 31 | 0 | 0 | 0 | 0 | 0 | 31 | 100,0 |
| | 2008 | 0 | 0 | 0 | 0 | 0 | 0 | 0 | 0 | 0 | 0 | 0 | 0 | 0 | 0 | 0 | 0 | 0 | 0 | 0 | 0 | 0 | 0 | 0 | 0 | 0 | 25 | 0 | 0 | 0 | 0 | 25 | 100,0 |
| | 2009 | 0 | 0 | 0 | 0 | 0 | 0 | 0 | 0 | 0 | 0 | 0 | 0 | 0 | 0 | 0 | 0 | 0 | 0 | 0 | 0 | 0 | 0 | 0 | 0 | 0 | 0 | 27 | 0 | 0 | 0 | 27 | 100,0 |
| | 2010 | 0 | 0 | 0 | 0 | 0 | 0 | 0 | 0 | 0 | 0 | 0 | 0 | 0 | 0 | 0 | 0 | 0 | 0 | 0 | 0 | 0 | 0 | 0 | 0 | 0 | 0 | 0 | 28 | 0 | 0 | 28 | 100,0 |
| | 2011 | 0 | 0 | 0 | 0 | 0 | 0 | 0 | 0 | 0 | 0 | 0 | 0 | 0 | 0 | 0 | 0 | 0 | 0 | 0 | 0 | 0 | 0 | 0 | 0 | 0 | 0 | 0 | 0 | 30 | 0 | 30 | 100,0 |
| | 2012 | 0 | 1 | 0 | 0 | 0 | 0 | 0 | 0 | 0 | 0 | 0 | 0 | 0 | 0 | 0 | 0 | 0 | 0 | 0 | 0 | 0 | 0 | 0 | 0 | 0 | 0 | 0 | 0 | 0 | 18 | 19 | 94,7 |
| | Sum | 57 | 27 | 30 | 27 | 24 | 28 | 33 | 30 | 30 | 28 | 28 | 31 | 29 | 35 | 20 | 35 | 30 | 25 | 34 | 32 | 35 | 32 | 25 | 32 | 32 | 26 | 28 | 29 | 30 | 18 | 900 | |
| | PA | 94,7 | 51,9 | 93,3 | 88,9 | 87,5 | 96,4 | 90,9 | 96,7 | 96,7 | 85,7 | 100,0 | 87,1 | 82,8 | 91,4 | 90,0 | 94,3 | 100,0 | 96,0 | 94,1 | 100,0 | 97,1 | 93,8 | 96,0 | 96,9 | 96,9 | 96,2 | 96,4 | 96,6 | 100,0 | 100,0 | | 93,1 |

In case there are less observations available a smaller number is used in order to allow to detect changes at the ends of the time series. The requirement here was not to miss any change at the expense of including false changes. Post-processing such as thresholding of change magnitude or spatial filtering is a suitable processing step to improve results. Very good performances are achieved for all other years. A considerable number of changes has been missed – mostly due to noisy time series, sometimes with huge gaps. User accuracy, however, is still 60% for the unchanged class.
In about 94,3% of all samples with changes the time span of change has been detected correctly. The year of change was correctly assigned for 93,4% of all samples containing changes.

## 3.6 Conclusions

The analyses showed that cloud cover is a serious issue affecting remote sensing studies of southern Vancouver Island. Particularly the spatio-temporal cloud statistics confirm that the potential of getting cloud free imagery is rather good during July, August, and September. Although least cloud coverage was found for the summer months there is a considerable number of datasets from other seasons in the archive that is at least partially cloud free. The analysis of this thesis considers all temporal scales (i.e., abrupt changes, and intra-annual, inter-annual, long-term dynamic) and benefits from every cloud free observation of any season since all non-contaminated observations are used. The use of all observations allows to rely on the temporal context of each observation making the whole strategy less sensitive for timing of the data. The challenges caused by unfavorable illumination conditions during winter and different phenological conditions of the observed forests were addressed by exploring the spatio-temporal variation of the selected spectral indices. It was shown that some indices are less sensitive for illumination conditions than others. Ratio-based indices are generally more spatio-temporally stable than those that use only sums and differences. Indices based on SWIR bands tend to be less variable than those that are based on VIS and NIR bands.
The analysis of several approaches for time series generation of the DI included four different options. From the findings presented here it can be concluded that the calculation of DI with varying representative forest samples is adequate to generate consistent time series. A yearly forest mask is suggested to scale the TC features used for the DI calculation. The forest masks can be derived from products such as the MODIS VCF. Backdating to pre-MODIS times is challenging but is likely not to affect the general temporal behavior of the DI.
To be able to identify changes in time series of an index that are distinct from seasonal variation, the intra-annual variation of that index must be lower than the differences caused by land cover changes. Consequently, little intra-annual variation of an index accompanied by clear signal variation in case of a change event is mandatory for the detection of clear cuts. An example that fulfills these requirements is the DI although it is affected by illumination. Its strong response to forest structure make the DI a good measure for abrupt changes like clearcuts. The NDMI is both sensitive to vegetation response and abrupt changes. Because of its spatio-temporal stability this index may be preferred over others. Another advantage of the NDMI is that it can be calculated for sensors for which no TC formulation is developed (e.g., Sentinel-2).

The study of time series pre-processing revealed that radiometric normalization of all scenes to one master image levels long-term trends and reduces the seasonal signal variation, thereby blurring phenological patterns. As a consequence, radiometric normalization cannot be recommended for time series analysis. Reflectance and index values are modified by relative radiometric normalization procedures leading to restricted physical interpretability. The strength of radiometric normalization lies in bi-temporal applications where small radiometric changes are considered noise and strong changes are to be studied.

The key feature of this Section is the introduction of a new method to detect abrupt changes at high spatial and temporal resolution. It requires good cloud detection results to exclude contaminated observations from further analysis. Missed clouds can be compensated to a certain degree by interpolation and filtering. In the proposed approach the cloud detection accuracy was not quantified. Instead, the study relies on existing processing routines and the results available as ready-to-use product from USGS (i.e., LEDAPS and Fmask products on Earth Explorer). Better cloud detection accuracies can be achieved by considering the temporal domain (Zhu et al., 2012). A promising approach would also be to apply weights on each observation during interpolation or filtering according to cloud coverage or cloud coverage in a selected neighborhood. Weighted interpolation and filtering is supposed to eliminate noise more efficiently. Although promising it is challenging to integrate spatial information in the proposed method. Only little improvements, however, are expected from such enhancements since the presented results are spatially very homogeneous.

One of the benefits of the presented method is its ability to detect year as well as month of abrupt changes (i.e., clearcuts). Spatio-temporal pattern are detected that have been unknown previously. The results presented here show only clearcut detection results and long-term recovery trends. It is, however, possible to detect subtle changes as well. The limiting factor of the presented approach is its sensitivity to contaminated observations. Single outliers hardly affect change detection performance. But a series of outliers may blur the Webster feature and bypass the KS-test. Although only NDMI results are shown here, the presented method can be applied to any spectral index that is sensitive to forest structure and condition. The accuracy assessment confirms excellent clearcut detection performance of our approach with a change detection accuracy of 93%. Further improvements can be achieved by appropriate post-processing, e.g., segment-based calculation of clearcut patch size, application of minimum mapping units, and/or clustering of changes.

# 4 Summary and Outlook

This thesis has demonstrated how particular sensor characteristics and data availability influence remote sensing based change detection. Remote sensing based land cover and land use change detection offer the unique opportunity to uncover a variety of changes taking into account the different dimensions and properties of change. The first section of this thesis demonstrated that there are different dimensions and different properties of change that we can use to characterize change by means of remote sensing, e.g., temporal, spatial, and spectral change properties. The most important properties of the remote sensing system that may affect detectability of change are reviewed in the first section. These are – widely corresponding to the change attributes – temporal, spatial, and spectral resolution plus radiometric resolution, off-nadir capability, data availability and other factors. External acquisition conditions such as atmospheric conditions is a third component that affects remote sensing based change detection.

Availability of suitable data is often regarded as the major constraint of remote sensing studies. The remote sensing research community and users tend to expect that upcoming sensors will provide an easy solution to improve the existing analysis and the understanding of the system under investigation. Simultaneously, some fields of remote sensing research focus on exploring non-optimal datasets. There is, for example, a tendency of developing classification algorithms capable of using small training datasets (Foody and Mathur, 2006; Mountrakis et al., 2011) and validation methods capable of using imperfect datasets (Foody, 2010). In change detection studies, however, the tedious task of seeking "perfect" datasets still dominates over resourceful methods able to compensate "imperfectness". It has been shown in this thesis that "imperfectness" often results from unfavorable viewing geometries and/or from restricted data availability. From the various sensor characteristics that influence change detection, off-nadir capabilities and temporal aspects – both related to availability of suitable data – have been identified as most relevant field of research in this thesis.

In Section 2, four sun-target-sensor scenarios were identified that are fundamental for understanding geometry effects of remote sensing based change detection (research question 1a). The scenarios are exemplified for bi-temporal change detection. In fact, they apply to time series as well. The scenarios result from variable sun illumination and variable viewing capabilities of most modern satellite sensors. There is only one scenario where sun-target-sensor geometries are identical and consequently do not introduce false changes. This scenario occurs when annual acquisitions are taken under identical viewing angles. All the other scenarios lead to distortions that may be detected as spurious changes if non-adequate methods are used. In Section 2, the false changes resulting from varying viewing geometries are quantified. These are considerable when using off-nadir images.

To eliminate these distortions and reduce spurious changes, this thesis developed a new method that accounts for pixel neighborhood (research question 1b). This method represents an enhancement of the well-established CVA method and was named Robust Change Vector Analysis (RCVA) since it is robust against geometric distortions resulting from different sun-target-sensor constellations and against thresholding. The robustness against thresholding is of great advantage since many other methods are sensitive to thresholding, particularly when the

data range is huge. RCVA calculates the strength of change as Euclidean distance in the multi-dimensional change space, and the direction as multi-dimensional angle. This direction angle indicates the nature of change and facilitates interpretation of changes. Urban change detection was the field of application for which RCVA was developed in Section 2. The images used for this purpose are from different satellites with different spatial and spectral resolution. Nonetheless, the results achieved with RCVA are sound. A dislocation experiment showed that RCVA is superior to CVA because it emphasizes true changes and reduces the amount of false changes resulting from geometrical distortions and erroneous geolocation. With the development of the RCVA it was demonstrated that the consideration of the pixel neighborhood is valuable when performing change detection of high spatial resolution images taken under different sun-target-sensor constellations. Cross-sensor change detection of sensors with different spatial resolutions becomes feasible with RCVA. Prerequisite of RCVA is the availability of similar spectral bands.

As shown in Section 1, different change categories such as flooding, urban expansion or forest growth are characterized by different temporal behavior. Using bi-temporal datasets may be insufficient to separate *seasonal variation* from *abrupt changes* or *subtle long-term trends*. A bi-temporal change detection result is very likely to be imperfect even under ideal sun-target-sensor constellations. Consequently, the time domain and the availability of suitable date are crucial for comprehensive process recognition and accurate change detection. Landsat time series processing is an emerging research topic with operational implementation (e.g., Cohen et al., 2010; Hansen et al., 2013; Kennedy et al., 2010; Zald et al., 2014). An increase in the number of Landsat related publications over the last years re-emphasizes the merit of the now freely accessible Landsat data (Wulder et al., 2012). However, only a fraction of the data has been explored. Recent trends favor compositing techniques (Griffiths et al., 2013; Hansen et al., 2014; Roy et al., 2014, 2010). These disregard the majority of (usable) observations to generate harmonized composites for a predefined period. Some of the advantages and disadvantages have been discussed in Section 3. They work reasonable in favored areas but less reliable in unfavored areas. Lower probabilities of cloud free acquisitions during winter and extreme observation conditions may be the reasons why most scientists are reluctant in using full Landsat time series. It may be naïve to believe that simply using all cloud free observations from the Landsat archive is the Holy Grail for environmental monitoring and change detection. The subject is challenging since several issues have not yet been entirely discussed, amongst others pre-processing requirements, spatio-temporal index variability, and appropriate methods. Section 3 of this thesis addresses some of the challenges related to the processing of dense (Landsat) time series. Southern Vancouver Island, British Columbia, Canada, was chosen as study site. It was chosen mainly because of its pronounced topography, strong climatic gradient, intense changes and comfortable Landsat coverage.

Ten different spectral indices were reviewed with respect to forest monitoring (research question 2a). The major finding of this investigation was that indices including SWIR bands are strongly related to (conifer) forest structure. Amongst the reviewed indices the TC features are frequently used as they allow for the integration of Landsat MSS data. TC wetness is particularly valuable for

forest monitoring. TC greenness and brightness, NDVI, and EVI show strong seasonal variation and are reported to be of limited use in forest studies.

The effect of changing illumination on canopy reflectance is well known. Generally, it is challenging to quantify these effects due to lack of appropriate datasets. The spatio-temporal variation of the selected spectral indices was assessed to address their suitability for dense time series generation (research question 2b). Most of the indices under consideration have been used for time series analysis previously, but none of them for dense Landsat time series. The study was based on a time series of 16 images that cover one growing season. Rather than testing capabilities of capturing phenology it was explored how stable the derived patterns are over one year. As a result it was shown that differences between different topographic situations vary over time. This in turn means that unfavorable acquisition conditions (e.g., poor illumination in winter) lead to huge differences between index values of the same land cover at different topographic locations. Under favorable conditions (e.g., more homogeneous illumination during summer) these differences are considerably reduced. Change detection in general and time series analysis in particular require spectral features or indices that are sensitive to the subject under consideration but are as much as possible invariant in space and time. From the indices used here those that make use of SWIR bands meet best the abovementioned requirements (e.g., TC wetness, DI, NDMI, NDBI, NBR). They vary only little under changing illumination conditions and heterogeneous topography. Furthermore, they depict well the forest growth stages. Other indices such as EVI, TC greenness or brightness vary considerably. Even strong changes are occasionally within the range of seasonal variation of these indices, thus hampering the detection of abrupt changes. NDVI is rarely used in conifer forest applications as it is less related to forest structure. It is, however, rather invariant towards changing illumination. TCA is a good trade-off as it is capable of integrating Landsat MSS data. It is, however, worse for dense time series than NDMI or DI. Ratio-based indices are generally less variable than indices based on sums and differences. From the stable indices that reflect forest structure reasonably, NDMI and DI were identified as best-suited for forest time series analysis. DI is closely related to forest structure; NDMI is both sensitive to vegetation response and abrupt changes. NDMI is hence well related to forest condition, making it sensitive to subtle changes as well. The findings of the spatio-temporal stability assessment confirmed the suggestions from the literature that were reviewed to answer research question 2a. DI time series generation of partially clouded images was not addressed in any previous publication. It is a challenging task since a representative sample of forest pixels is needed to scale the TC components that are used to calculate the DI. Several approaches were tested: scaling with a sample of pixels from a old-growth forest area that have not changed over the whole observation period, scaling using all pixels irrespective of their classification, scaling using a sample of forest pixels that were derived from the annual MODIS VCF product for each year, and no scaling at all. The findings indicate that for the study site of this thesis the DI can be calculated from a varying sample of forest pixels that were derived from the annual MODIS VCF product. It was shown that DI calculation is only little affected by seasonally changing illumination conditions or spatially and numerically varying samples due to cloud cover, data gaps and other obstacles. The findings of this thesis enable better understanding of the index.

Time series pre-processing requirements were addressed in Section 3, too. These requirements refer mainly to cloud and cloud shadow detection, and to radiometric processing. Tools that are operationally implemented to date were used in this study to process the data (at the time of processing for this thesis the Landsat CDR dataset was not yet released and processing had to be carried out on a desktop machine). Geometric accuracy is of high quality for the used products according to random tests. Atmospheric correction was automated with the LEDAPS software. Cloud detection was applied using the Fmask implementation with default settings. Atmospheric correction using LEDAPS is appropriate and well justified (Ju et al., 2012). Improvements of the cloud mask may be achieved by considering the temporal domain (Zhu et al., 2012), but was beyond the scope of this thesis. The usefulness of radiometric normalization as additional processing step is discussed ambivalently in the science community. Existing knowledge was restricted to annual time series for which automatic relative radiometric normalization is recommended (Schroeder et al., 2006; Vicente-Serrano et al., 2008). A comprehensive analysis was presented in Section 3 where we assessed the impact of radiometric normalization on dense Landsat time series using IR-MAD (research question 2c). The results reveal that radiometric normalization to one master image based on IR-MAD levels long-term trends and seasonal variation, and phenological properties are blurred. Consequently, radiometric normalization of time series cannot be recommended. However, alternative approaches of radiometric normalization have not been tested. It is likely that seasonality can be maintained when an image of each month or season is used as reference for all images of the same month. It is worth testing if the leveling effect of long-term trends remains with that approach.

The major findings related to research questions 2a-2c led to the development of a method capable of detecting discontinuities in time series (research question 2d). A major challenge in using all Landsat scenes is the irregular time interval of cloud free observations that is, above all, individual for each pixel. Most existing methods require regular-spaced time series. The irregular spacing of the time series was overcome by linear interpolation in the temporal domain and subsequent filtering. Noise in the time series due to missed clouds and other contaminants is the main source of errors. More sophisticated interpolation and filtering methods that weight cloud coverage in the pixel's neighborhood or account for seasonal effects should be tested in future research.

The first derivative of the interpolated and filtered time series is an adequate descriptor of time series dynamics. It is a measure that depicts changes in the dynamics of time series that occur when different processes dominate. An example is the seasonal variation of deciduous trees compared to that of conifer trees. The overarching goal of Section 3 was to present a method capable of detecting abrupt changes due to forest clearcut harvesting and subtle changes such as insect defoliation. As the latter play a minor role in the study site, no detailed study on that was performed. The first derivative was found to be closely related to major changes in the time series. The signal is sometimes ambiguous, however, making it less reliable for accurate clearcut detection and the characterization of minor changes. The Webster measure – a detector of discontinuities – was applied to the time series. It was demonstrated that it is well suited to detect clearcut events. Subtle changes are also detectable as well as secondary and minor changes. The higher the quality of the time series (in terms of noise reduction and outlier elimination) the finer

the changes that can be detected with the Webster measure. The method was demonstrated to be applicable to the ten spectral indices. It can be applied to any signal that reflects processes on the ground such as SAR backscatter.

Applying the new method to a NDMI time series revealed that 29% of the 900 km² study site have been harvested during the 29 year observation period from 1984 to 2012. Another 29% of the area show significant index increase trends indicating forest regrowth of forests that have been cleared before the observation period. Spatial as well as temporal clearcut patterns are presented in Section 3 at a unprecedented temporal resolution. Validation – a tedious process in change detection studies, particularly when using time series – revealed very good performance of the presented method using the Webster measure. An overall accuracy of 93% was achieved. False detections of changes occur particularly at the beginning and in the end of the time series where the restrictions of the KS-test are lowered to be able to apply the measure. Although the study site is only an arbitrary subscene that was chosen with respect to Landsat tile boundaries, the example demonstrates the intense use of the forests of southern Vancouver Island. Future work should consider the integration of dense SAR time series as well as combined optical-SAR products from which closer relationship to biophysical parameters can be expected. To date availability of such datasets is still limited.

The two aims of this thesis – to contribute to a more accurate estimation of land use/land cover changes by accounting for the effects of variable sun-target-sensor geometries, and to contribute to a better understanding of forest dynamics by providing a new approach of remotely sensed data exploration – were achieved with the introduction of two new methods.

It was shown that bi-temporal change detection and change detection based on multi-temporal data are fundamentally distinct. Notwithstanding the recent trend of time series related research, bi-temporal change detection methods are still important for most applications. As shown in Section 1 there is need for sophisticated methods to deal with the challenges that originate from the flexibility of modern satellite sensors and "imperfect" data. Although annual time series have not been explored in this thesis, some of its advantages and challenges have been outlined. Major findings from the reviewed literature and the research conducted here are presented in Tab. 3.6.1. The intention of this table is neither to vote for or against a particular category nor to stimulate discussions about new paradigms in remote sensing based change detection. It was rather assembled to provide information about the most important characteristics of each category. This compilation confirms the relevance of each category for different applications. A focus is on temporal aspects of changes, e.g., the ability of the categories to detect abrupt changes, long-term trends, and seasonal variation. It can be seen from Tab. 3.6.1 that the temporal properties of changes are best characterized by time series methods. Whereas bi-temporal methods are well-suited to detect the result of a change process, methods using multi-temporal data are well-suited to monitor the processes themselves (or spectral indices as indicator). As a byproduct information about state and condition of land cover and related processes can be derived from time series. It may be debatable if it makes sense to separate time series analysis from multi-temporal change detection since time series are multi-temporal datasets. As Tab. 3.6.1 confirms there are, however, differences in the way the data are analyzed and also in the diversity of the resulting products. It must be noted that a separation of the two categories is dependent on the

Tab. 3.6.1: Comparison of bi-temporal change detection, multi-temporal change detection, and time series analysis.

| | Bi-temporal change detection | Multi-temporal change detection (including trajectories of annual observations) | Time series analysis (more than one observation per year) |
|---|---|---|---|
| Suitable to detect abrupt changes? | yes | yes | yes |
| Suitable to detect long-term trends? | no, trends cannot be clearly separated from noise or phenological differences | yes; but each observation must be chosen with respect to rainfall, phenology, and sun illumination | yes |
| Suitable to detect seasonal variation (e.g. phenology)? | no | no, inter-annual changes that fall below a certain threshold are considered noise, those above are seen as abrupt change | yes |
| Date of change detectable? | no, it is only known that the change happened between two observations | a rather coarse indication of the date of abrupt changes can be estimated | changes can be detected with good temporal precision |
| Major pre-processing steps | co-registration; atmospheric correction or radiometric normalization; (manual) scene selection | geometric & radiometric processing (atmospheric correction, radiometric normalization); cloud detection; scene selection; compositing (Griffiths et al. 2013) | geometric & radiometric processing (atmospheric correction); cloud detection |
| Requirements | cloudfree scenes; ideally equal phenological conditions & equal sun position | cloudfree pixels (may be achieved by compositing techniques); ideally equal phenological conditions & equal sun position | cloudfree observations |
| Option to label changes? | yes, several methods exists (Hecheltjen et al. 2014) | yes, if multi-temporal classifications are compared; usually, the change itself can be related to a certain class | yes (Zhu & Woodcock 2014); usually, the change itself can be related to a certain class |
| Advantages | small data volume; many algorithms (Hecheltjen et al. 2014) | moderate data volume; good balance of outcome and effort; trends and abrupt changes detectable | seasonal effects, inter- & intra-annual dynamics may be detected; all observations used; no scene selection or compositing required; almost gapless characterization of processes; option for time series decomposition; no thresholding required |
| Limitations | processes and their spatio-temporal characteristics are not detectable; thresholding required to separate change from no-change | data selection and/or compositing required; (off-year data are preferred over off-seasonal data); areas of frequent cloud coverage are challenging; seasonal variation & dynamics are no detectable; assumption of linear trends is debatable; data availability in some regions | big data volume; comprehensive preprocessing requires automation; data availability in some regions |
| Application | various (Hecheltjen et al. 2014), e.g., emergency response, flood detection, urban expansion | forest cover change; mining; various possible | forest cover change; continuous map update; various possible |
| Examples of methods | RCVA, Post Classification Comparison, IR-MAD | LandTrendr | BFAST, approach presented here |

temporal scale. The distinct approaches of the categories presented in Tab. 3.6.1 lead to huge differences in prerequisites, field of application, and benefits/drawbacks.

The focus of the thesis was on methodological improvements to overcome "imperfectness" of data and acquisition conditions. These are relevant for many existing applications and become increasingly important with recently launched (e.g., Sentinel-1, first satellite launched 3rd April 2014; Landsat 8 LDCM, launched 11 February 2013) and future satellite missions (e.g., Sentinel-2, first satellite to be launched in early 2015). Particularly constellations such as Landsat 8/Sentinel-2 will provide substantial amounts of data. Compositing of regular products may be one direction of future developments, the enhancement of methods ready for dense time series may be another. Robust methods such as RCVA and the Webster time series discontinuity detection presented here improve accuracy and diversity of remote sensing based (change detection) products. Particularly dense time series provide detailed spatial and temporal information that can be related to processes on the ground. Contribution to programs such as the European Copernicus (http://www.copernicus.eu/) is appreciated with this kind of information. The promise for future is that we are not only able to detect what happened in the past but also learn to use this knowledge for respectful stewardship of environmental resources.

## References


Aguilar, M.A., Saldaña, M. del M., Aguilar, F.J., 2013. Assessing geometric accuracy of the orthorectification process from GeoEye-1 and WorldView-2 panchromatic images. International Journal of Applied Earth Observation and Geoinformation 21, 427–435. doi:10.1016/j.jag.2012.06.004

Agustan, Kimata, F., Pamitro, Y.E., Abidin, H.Z., 2012. Understanding the 2007–2008 eruption of Anak Krakatau Volcano by combining remote sensing technique and seismic data. International Journal of Applied Earth Observation and Geoinformation 14, 73–82. doi:10.1016/j.jag.2011.08.011

Allen, T.R., Kupfer, J.A., 2000. Application of Spherical Statistics to Change Vector Analysis of Landsat Data: Southern Appalachian Spruce–Fir Forests. Remote Sensing of Environment 74, 482–493. doi:10.1016/S0034-4257(00)00140-1

Arvor, D., Meirelles, M., Dubreuil, V., Bégué, A., Shimabukuro, Y.E., 2012. Analyzing the agricultural transition in Mato Grosso, Brazil, using satellite-derived indices. Applied Geography 32, 702–713. doi:10.1016/j.apgeog.2011.08.007

Bagan, H., Wang, Q., Watanabe, M., Yang, Y., Ma, J., 2005. Land cover classification from MODIS EVI times-series data using SOM neural network. International Journal of Remote Sensing 26, 4999–5012. doi:10.1080/01431160500206650

Bai, J., Perron, P., 2003. Computation and analysis of multiple structural change models. J. Appl. Econ. 18, 1–22. doi:10.1002/jae.659

Bamler, R., Hartl, P., 1998. Synthetic aperture radar interferometry. Inverse Problems 14, R1–R54. doi:10.1088/0266-5611/14/4/001

Baumann, M., Ozdogan, M., Wolter, P.T., Krylov, A., Vladimirova, N., Radeloff, V.C., 2014. Landsat remote sensing of forest windfall disturbance. Remote Sensing of Environment 143, 171–179. doi:10.1016/j.rse.2013.12.020

Bazi, Y., Bruzzone, L., Melgani, F., 2007. Image thresholding based on the EM algorithm and the generalized Gaussian distribution. Pattern Recognition 40, 619–634.

Benz, U.C., Hofmann, P., Willhauck, G., Lingenfelder, I., Heynen, M., 2004. Multi-resolution, object-oriented fuzzy analysis of remote sensing data for GIS-ready information. ISPRS Journal of Photogrammetry and Remote Sensing 58, 239–258.

Blaschke, T., 2010. Object based image analysis for remote sensing. ISPRS Journal of Photogrammetry and Remote Sensing 65, 2–16. doi:10.1016/j.isprsjprs.2009.06.004

Boles, S.H., Xiao, X., Liu, J., Zhang, Q., Munkhtuya, S., Chen, S., Ojima, D., 2004. Land cover characterization of Temperate East Asia using multi-temporal VEGETATION sensor data. Remote Sensing of Environment 90, 477–489. doi:10.1016/j.rse.2004.01.016

Borrelli, P., Modugno, S., Panagos, P., Marchetti, M., Schütt, B., Montanarella, L., 2014. Detection of harvested forest areas in Italy using Landsat imagery. Applied Geography 48, 102–111. doi:10.1016/j.apgeog.2014.01.005

Bovolo, F., Bruzzone, L., 2007. A Theoretical Framework for Unsupervised Change Detection Based on Change Vector Analysis in the Polar Domain. IEEE Transactions on Geoscience and Remote Sensing 45, 218–236. doi:10.1109/TGRS.2006.885408

Bovolo, F., Marchesi, S., Bruzzone, L., 2010. A nearly lossless 2d representation and characterization of change information in multispectral images. Presented at the IEEE International Geoscience and Remote Sensing Symposium (IGARSS), Honolulu, pp. 3074–3077.

Bruzzone, L., Cossu, R., 2003. An adaptive approach to reducing registration noise effects in unsupervised change detection. IEEE Transactions on Geoscience and Remote Sensing 41, 2455–2465. doi:10.1109/TGRS.2003.817268

Bruzzone, L., Prieto, D.F., 2000. Automatic analysis of the difference image for unsupervised change detection. IEEE Transactions on Geoscience and Remote Sensing 38, 1171–1182. doi:10.1109/36.843009

Cabello, J., Alcaraz-Segura, D., Ferrero, R., Castro, A.J., Liras, E., 2012. The role of vegetation and lithology in the spatial and inter-annual response of EVI to climate in drylands of Southeastern Spain. Journal of Arid Environments 79, 76–83. doi:10.1016/j.jaridenv.2011.12.006

Canty, M.J., 2014. Image Analysis, Classification and Change Detection in Remote Sensing: With Algorithms for ENVI/IDL and Python, 3rd ed. Crc Pr Inc, New York.

Canty, M.J., Nielsen, A.A., 2008. Automatic radiometric normalization of multitemporal satellite imagery with the iteratively re-weighted MAD transformation. Remote Sensing of Environment 112, 1025–1036. doi:10.1016/j.rse.2007.07.013

Canty, M.J., Nielsen, A.A., 2012. Linear and kernel methods for multivariate change detection. Computers & Geosciences 38, 107–114. doi:10.1016/j.cageo.2011.05.012

Canty, M.J., Nielsen, A.A., Schmidt, M., 2004. Automatic radiometric normalization of multitemporal satellite imagery. Remote Sensing of Environment 91, 441–451. doi:10.1016/j.rse.2003.10.024

Carey, A.B., Curtis, R.O., 1996. Conservation of biodiversity: a useful paradigm for forest ecosystem management. Wildlife Society Bulletin 24, 610–620.

Castilla, G., Guthrie, R.H., Hay, G.J., 2009. The land-cover change mapper (LCM) and its application to timber harvest monitoring in Western Canada. Photogrammetric Engineering & Remote Sensing 75, 941–950.

CEC, C. for E.C., 1997. Ecological regions of North America = Régions écologiques de l'Amerique du Nord = Regiones ecológicas de América del Norte; http://www.epa.gov/wed/pages/ecoregions/na_eco.htm.

Chen, G., Hay, G.J., Carvalho, L.M.T., Wulder, M.A., 2012. Object-based change detection. International Journal of Remote Sensing 33, 4434–4457. doi:10.1080/01431161.2011.648285

Chen, G., Zhao, K., Powers, R., 2014. Assessment of the image misregistration effects on object-based change detection. ISPRS Journal of Photogrammetry and Remote Sensing 87, 19–27. doi:10.1016/j.isprsjprs.2013.10.007

Chen, J., Gong, P., Chunyang, H., Pu, R., Shi, P., 2003. Land-Use/Land-Cover Change Detection Using Improved Change-Vector Analysis. Photogrammetric Engineering & Remote Sensing 69, 369–379.

Chen, J., Jönsson, P., Tamura, M., Gu, Z., Matsushita, B., Eklundh, L., 2004. A simple method for reconstructing a high-quality NDVI time-series data set based on the Savitzky–Golay filter. Remote Sensing of Environment 91, 332–344. doi:10.1016/j.rse.2004.03.014

Chen, J., Zhu, X., Vogelmann, J.E., Gao, F., Jin, S., 2011. A simple and effective method for filling gaps in Landsat ETM+ SLC-off images. Remote Sensing of Environment 115, 1053–1064. doi:10.1016/j.rse.2010.12.010

Chen, X., Liu, S., Zhu, Z., Vogelmann, J., Li, Z., Ohlen, D., 2011a. Estimating aboveground forest biomass carbon and fire consumption in the U.S. Utah High Plateaus using data from the Forest Inventory and Analysis Program, Landsat, and LANDFIRE. Ecological Indicators 11, 140–148. doi:10.1016/j.ecolind.2009.03.013

Chen, X., Vierling, L., Deering, D., 2005. A simple and effective radiometric correction method to improve landscape change detection across sensors and across time. Remote Sensing of Environment 98, 63–79. doi:10.1016/j.rse.2005.05.021

Chen, X., Vogelmann, J.E., Rollins, M., Ohlen, D., Key, C.H., Yang, L., Huang, C., Shi, H., 2011b. Detecting post-fire burn severity and vegetation recovery using multitemporal remote sensing spectral indices and field-collected composite burn index data in a ponderosa pine forest. International Journal of Remote Sensing 32, 7905–7927. doi:10.1080/01431161.2010.524678

Chen, Y., Wen, D., Jing, L., Shi, P., 2007. Shadow information recovery in urban areas from very high resolution satellite imagery. International Journal of Remote Sensing 28, 3249–3254. doi:10.1080/01431160600954621

Cleveland, R.B., Cleveland, W.S., McRae, J.E., Terpenning, I., 1990. STL: A seasonal-trend decomposition procedure based on Loess. Journal of Official Statistics 6, 3–73.

Cohen, W.B., Spies, T.A., 1992. Estimating structural attributes of Douglas-fir/western hemlock forest stands from landsat and SPOT imagery. Remote Sensing of Environment 41, 1–17. doi:10.1016/0034-4257(92)90056-P

Cohen, W.B., Spies, T.A., Alig, R.J., Oetter, D.R., Maiersperger, T.K., Fiorella, M., 2002. Characterizing 23 Years (1972–95) of Stand Replacement Disturbance in Western Oregon Forests with Landsat Imagery. Ecosystems 5, 122–137. doi:10.1007/s10021-001-0060-X

Cohen, W.B., Spies, T.A., Fiorella, M., 1995. Estimating the age and structure of forests in a multi-ownership landscape of western Oregon, U.S.A. International Journal of Remote Sensing 16, 721–746. doi:10.1080/01431169508954436

Cohen, W.B., Yang, Z., Kennedy, R., 2010. Detecting trends in forest disturbance and recovery using yearly Landsat time series: 2. TimeSync — Tools for calibration and validation. Remote Sensing of Environment 114, 2911–2924. doi:10.1016/j.rse.2010.07.010

Collins, J.B., Woodcock, C.E., 1996. An assessment of several linear change detection techniques for mapping forest mortality using multitemporal Landsat TM data. Remote Sensing of Environment 56, 66–77.

Conradsen, K., Nielsen, A.A., Schou, J., Skriver, H., 2003. A test statistic in the complex Wishart distribution and its application to change detection in polarimetric SAR data. Geoscience and Remote Sensing, IEEE Transactions on 41, 4–19.

Coops, N.C., Gillanders, S.N., Wulder, M.A., Gergel, S.E., Nelson, T., Goodwin, N.R., 2010. Assessing changes in forest fragmentation following infestation using time series Landsat imagery. Forest Ecology and Management 259, 2355–2365.

Coops, N.C., Wulder, M.A., White, J.C., 2007. Identifying and describing forest disturbance and spatial pattern: Data selection issues and methodological implications, in: Wulder, M.A., Franklin, S.E. (Eds.), Understanding Forest Disturbance and Spatial Pattern: Remote Sensing and GIS Approaches. CRC Press, Taylor & Francis, Boca Raton, London, New York, pp. 31–61.

Coppin, P., Jonckheere, I., Nackaerts, K., Muys, B., Lambin, E., 2004. Digital change detection methods in ecosystem monitoring: a review. International Journal of Remote Sensing 25, 1565–1596. doi:10.1080/0143116031000101675

Coppin, P.R., Bauer, M.E., 1996. Digital change detection in forest ecosystems with remote sensing imagery. Remote Sensing Reviews 13, 207–234. doi:10.1080/02757259609532305

Coudray, N., Buessler, J.-L., Urban, J.-P., 2010. Robust threshold estimation for images with unimodal histograms. Pattern Recognition Letters 31, 1010–1019. doi:10.1016/j.patrec.2009.12.025

Crist, E.P., 1985. A TM Tasseled Cap equivalent transformation for reflectance factor data. Remote Sensing of Environment 17, 301–306. doi:10.1016/0034-4257(85)90102-6

Crist, E.P., Cicone, R.C., 1984. A Physically-Based Transformation of Thematic Mapper Data—The TM Tasseled Cap. IEEE Transactions on Geoscience and Remote Sensing GE-22, 256 –263. doi:10.1109/TGRS.1984.350619

Czerwinski, C.J., King, D.J., Mitchell, S.W., 2014. Mapping forest growth and decline in a temperate mixed forest using temporal trend analysis of Landsat imagery, 1987–2010. Remote Sensing of Environment 141, 188–200. doi:10.1016/j.rse.2013.11.006

Dai, X., Khorram, S., 1998. The effects of image misregistration on the accuracy of remotely sensed change detection. IEEE Transactions on Geoscience and Remote Sensing 36, 1566–1577. doi:10.1109/36.718860

Danklmayer, A., Doring, B.J., Schwerdt, M., Chandra, M., 2009. Assessment of Atmospheric Propagation Effects in SAR Images. IEEE Transactions on Geoscience and Remote Sensing 47, 3507–3518. doi:10.1109/TGRS.2009.2022271

Danson, F.M., Curran, P.J., 1993. Factors affecting the remotely sensed response of coniferous forest plantations. Remote Sensing of Environment 43, 55–65. doi:10.1016/0034-

4257(93)90064-5

Dardel, C., Kergoat, L., Hiernaux, P., Mougin, E., Grippa, M., Tucker, C.J., 2014. Re-greening Sahel: 30 years of remote sensing data and field observations (Mali, Niger). Remote Sensing of Environment 140, 350–364. doi:10.1016/j.rse.2013.09.011

Dave, J.V., 1981. Influence of illumination and viewing geometry and atmospheric composition on the "tasseled cap" transformation of landsat MSS data. Remote Sensing of Environment 11, 37–55. doi:10.1016/0034-4257(81)90005-5

DeFries, R.S., Foley, J.A., Asner, G.P., 2004. Land-use choices: balancing human needs and ecosystem function. Frontiers in Ecology and the Environment 2, 249–257. doi:10.1890/1540-9295(2004)002[0249:LCBHNA]2.0.CO;2

Deng, C., Wu, C., 2012. BCI: A biophysical composition index for remote sensing of urban environments. Remote Sensing of Environment 127, 247–259. doi:10.1016/j.rse.2012.09.009

DeRose, R.J., Long, J.N., Ramsey, R.D., 2011. Combining dendrochronological data and the disturbance index to assess Engelmann spruce mortality caused by a spruce beetle outbreak in southern Utah, USA. Remote Sensing of Environment 115, 2342–2349. doi:10.1016/j.rse.2011.04.034

Desclée, B., Bogaert, P., Defourny, P., 2004. Object-based method for automatic forest change detection. Presented at the Geoscience and Remote Sensing Symposium, 2004. IGARSS '04. Proceedings. 2004 IEEE International, pp. 3383–3386 vol.5. doi:10.1109/IGARSS.2004.1370430

Dial, G., Bowen, H., Gerlach, F., Grodecki, J., Oleszczuk, R., 2003. IKONOS satellite, imagery, and products. Remote Sensing of Environment 88, 23–36. doi:10.1016/j.rse.2003.08.014

DiMiceli, C.M., Carroll, M.L., Sohlberg, R.A., Huang, C., Hansen, M.C., Townshend, J.R.G., 2011. Annual Global Automated MODIS Vegetation Continuous Fields (MOD44B) at 250 m Spatial Resolution for Data Years Beginning Day 65, 2000 - 2010, Collection 5 Percent Tree Cover.

Drusch, M., Del Bello, U., Carlier, S., Colin, O., Fernandez, V., Gascon, F., Hoersch, B., Isola, C., Laberinti, P., Martimort, P., Meygret, A., Spoto, F., Sy, O., Marchese, F., Bargellini, P., 2012. Sentinel-2: ESA's Optical High-Resolution Mission for GMES Operational Services. Remote Sensing of Environment 120, 25–36. doi:10.1016/j.rse.2011.11.026

Duane, M.V., Cohen, W.B., Campbell, J.L., Hudiburg, T., Turner, D.P., Weyermann, D.L., 2010. Implications of Alternative Field-Sampling Designs on Landsat-Based Mapping of Stand Age and Carbon Stocks in Oregon Forests. Forest Science 56, 405–416.

Dubovyk, O., Menz, G., Conrad, C., Kan, E., Machwitz, M., Khamzina, A., 2013a. Spatio-temporal analyses of cropland degradation in the irrigated lowlands of Uzbekistan using remote-sensing and logistic regression modeling. Environ Monit Assess 185, 4775–4790. doi:10.1007/s10661-012-2904-6

Dubovyk, O., Menz, G., Conrad, C., Thonfeld, F., Khamzina, A., 2013b. Object-based identification of vegetation cover decline in irrigated agro-ecosystems in Uzbekistan. Quaternary International 311, 163–174. doi:10.1016/j.quaint.2013.07.043

Duncanson, L., Niemann, K.O., Wulder, M.A., 2010. Integration of GLAS and Landsat TM data for aboveground biomass estimation. Canadian Journal of Remote Sensing 36, 129–141.

Dymond, C.C., Mladenoff, D.J., Radeloff, V.C., 2002. Phenological differences in Tasseled Cap indices improve deciduous forest classification. Remote Sensing of Environment 80, 460–472. doi:10.1016/S0034-4257(01)00324-8

Fallourd, R., Harant, O., Trouve, E., Nicolas, J.-M., Gay, M., Walpersdorf, A., Mugnier, J.-L., Serafini, J., Rosu, D., Bombrun, L., Vasile, G., Cotte, N., Vernier, F., Tupin, F., Moreau, L., Bolon, P., 2011. Monitoring Temperate Glacier Displacement by Multi-Temporal TerraSAR-X Images and Continuous GPS Measurements. IEEE Journal of Selected Topics in Applied Earth Observations and Remote Sensing 4, 372–386. doi:10.1109/JSTARS.2010.2096200

Fang, H., Liang, S., McClaran, M.P., van Leeuwen, W.J.D., Drake, S., Marsh, S.E., Thomson, A.M., Izaurralde, R.C., Rosenberg, N.J., 2005. Biophysical characterization and management effects on semiarid rangeland observed from Landsat ETM+ data. IEEE Transactions on Geoscience and Remote Sensing 43, 125 – 134. doi:10.1109/TGRS.2004.839813

Feilhauer, H., Thonfeld, F., Faude, U., He, K.S., Rocchini, D., Schmidtlein, S., 2013. Assessing floristic composition with multispectral sensors—A comparison based on monotemporal and multiseasonal field spectra. International Journal of Applied Earth Observation and Geoinformation 21, 218–229. doi:10.1016/j.jag.2012.09.002

Fensholt, R., Rasmussen, K., Nielsen, T.T., Mbow, C., 2009. Evaluation of earth observation based long term vegetation trends — Intercomparing NDVI time series trend analysis consistency of Sahel from AVHRR GIMMS, Terra MODIS and SPOT VGT data. Remote Sensing of Environment 113, 1886–1898. doi:10.1016/j.rse.2009.04.004

Fensholt, R., Sandholt, I., Stisen, S., Tucker, C., 2006. Analysing NDVI for the African continent using the geostationary meteosat second generation SEVIRI sensor. Remote Sensing of Environment 101, 212–229. doi:10.1016/j.rse.2005.11.013

Fiorella, M., Ripple, W.J., 1993. Determining Successional Stage of Temperate Coniferous Forests with Landsat Satellite Data. Photogrammetric Engineering & Remote Sensing 2, 239–246.

Fisher, J.I., Mustard, J.F., Vadeboncoeur, M.A., 2006. Green leaf phenology at Landsat resolution: Scaling from the field to the satellite. Remote Sensing of Environment 100, 265–279. doi:10.1016/j.rse.2005.10.022

Fontana, F.M.A., Coops, N.C., Khlopenkov, K.V., Trishchenko, A.P., Riffler, M., Wulder, M.A., 2012. Generation of a novel 1 km NDVI data set over Canada, the northern United States, and Greenland based on historical AVHRR data. Remote Sensing of Environment 121, 171–185. doi:10.1016/j.rse.2012.01.007

Foody, G.M., 2010. Assessing the accuracy of land cover change with imperfect ground reference data. Remote Sensing of Environment 114, 2271–2285.

Foody, G.M., Mathur, A., 2006. The use of small training sets containing mixed pixels for accurate hard image classification: Training on mixed spectral responses for classification by a SVM. Remote Sensing of Environment 103, 179–189.

FRAMES, F.R.A.M.E.S., 2014. Spectral Library: Western Montana, last accessed 25th June 2014 [WWW Document]. URL https://www.frames.gov/partner-sites/assessing-burn-severity/spectral/spectral-library-western-montana/

Franklin, J.F., Spies, T.A., Pelt, R.V., Carey, A.B., Thornburgh, D.A., Berg, D.R., Lindenmayer, D.B., Harmon, M.E., Keeton, W.S., Shaw, D.C., Bible, K., Chen, J., 2002. Disturbances and structural development of natural forest ecosystems with silvicultural implications, using Douglas-fir forests as an example. Forest Ecology and Management 155, 399–423. doi:10.1016/S0378-1127(01)00575-8

Franklin, S.E., Jagielko, C.B., Lavigne, M.B., 2005. Sensitivity of the Landsat enhanced wetness difference index (EWDI) to temporal resolution. Canadian Journal of Remote Sensing 31, 149–152. doi:10.5589/m05-005

Galvão, L.S., dos Santos, J.R., Roberts, D.A., Breunig, F.M., Toomey, M., de Moura, Y.M., 2011. On intra-annual EVI variability in the dry season of tropical forest: A case study with MODIS and hyperspectral data. Remote Sensing of Environment 115, 2350–2359. doi:10.1016/j.rse.2011.04.035

Gernhardt, S., Bamler, R., 2012. Deformation monitoring of single buildings using meter-resolution SAR data in PSI. ISPRS Journal of Photogrammetry and Remote Sensing 73, 68–79. doi:10.1016/j.isprsjprs.2012.06.009

Gianinetto, M.., Villa, P.., 2007. Rapid Response Flood Assessment Using Minimum Noise Fraction and Composed Spline Interpolation. Geoscience and Remote Sensing, IEEE Transactions on 45, 3204 –3211. doi:10.1109/TGRS.2007.895414

Gómez, C., White, J.C., Wulder, M.A., 2011. Characterizing the state and processes of change in a dynamic forest environment using hierarchical spatio-temporal segmentation. Remote Sensing of Environment 115, 1665–1679. doi:10.1016/j.rse.2011.02.025

Gong, P., Ledrew, E.F., Miller, J.R., 1992. Registration-noise reduction in difference images for change detection. International Journal of Remote Sensing 13, 773–779. doi:10.1080/01431169208904151

Goodwin, N.R., Coops, N.C., Wulder, M.A., Gillanders, S., Schroeder, T.A., Nelson, T., 2008. Estimation of insect infestation dynamics using a temporal sequence of Landsat data. Remote Sensing of Environment 112, 3680–3689. doi:10.1016/j.rse.2008.05.005

Goodwin, N.R., Magnussen, S., Coops, N.C., Wulder, M.A., 2010. Curve fitting of time-series Landsat imagery for characterizing a mountain pine beetle infestation. International Journal of Remote Sensing 31, 3263–3271. doi:10.1080/01431160903186277

Government of Canada, 2011. 1981 to 2010 Canadian Climate Normals, last accessed 28th February 2014 [WWW Document]. URL http://climate.weather.gc.ca/

Government of Canada, 2013. Trees - Trees, insects and diseases of Canada's forests, last accessed 24th June 2014 [WWW Document]. URL http://aimfc.rncan.gc.ca/en/trees/

Griffiths, P., Kuemmerle, T., Kennedy, R.E., Abrudan, I.V., Knorn, J., Hostert, P., 2012. Using annual time-series of Landsat images to assess the effects of forest restitution in post-socialist Romania. Remote Sensing of Environment 118, 199–214. doi:10.1016/j.rse.2011.11.006

Griffiths, P., van der Linden, S., Kuemmerle, T., Hostert, P., 2013. A Pixel-Based Landsat Compositing Algorithm for Large Area Land Cover Mapping. IEEE Journal of Selected Topics in Applied Earth Observations and Remote Sensing 6, 2088–2101. doi:10.1109/JSTARS.2012.2228167

Hais, M., Jonášová, M., Langhammer, J., Kučera, T., 2009. Comparison of two types of forest disturbance using multitemporal Landsat TM/ETM+ imagery and field vegetation data. Remote Sensing of Environment 113, 835–845. doi:10.1016/j.rse.2008.12.012

Hamann, A., Smets, P., Yanchuk, A.D., Aitken, S.N., 2005. An ecogeographic framework for in situ conservation of forest trees in British Columbia. Can. J. For. Res. 35, 2553–2561. doi:10.1139/x05-181

Hamann, A., Wang, T., 2006. Potential Effects of Climate Change on Ecosystem and Tree Species Distribution in British Columbia. Ecology 87, 2773–2786. doi:10.1890/0012-9658(2006)87[2773:PEOCCO]2.0.CO;2

Häme, T., 1991. Spectral interpretation of changes in forest using satellite scanner images. Acta Forestalia Fennica 222, 1–111.

Han, T., Wulder, M.A., White, J.C., Coops, N.C., Alvarez, M.F., Butson, C., 2007. An Efficient Protocol to Process Landsat Images for Change Detection With Tasselled Cap Transformation. IEEE Geoscience and Remote Sensing Letters 4, 147–151. doi:10.1109/LGRS.2006.887066

Hansen, A.J., Neilson, R.P., Dale, V.H., Flather, C.H., Iverson, L.R., Currie, D.J., Shafer, S., Cook, R., Bartlein, P.J., 2001. Global Change in Forests: Responses of Species, Communities, and Biomes Interactions between climate change and land use are projected to cause large shifts in biodiversity. BioScience 51, 765–779. doi:10.1641/0006-3568(2001)051[0765:GCIFRO]2.0.CO;2

Hansen, M.C., DeFries, R.S., Townshend, J.R.G., Carroll, M., Dimiceli, C., Sohlberg, R.A., 2003. Global Percent Tree Cover at a Spatial Resolution of 500 Meters: First Results of the MODIS Vegetation Continuous Fields Algorithm. Earth Interactions 7, 1–15. doi:10.1175/1087-3562(2003)007<0001:GPTCAA>2.0.CO;2

Hansen, M.C., Egorov, A., Potapov, P.V., Stehman, S.V., Tyukavina, A., Turubanova, S.A., Roy, D.P., Goetz, S.J., Loveland, T.R., Ju, J., Kommareddy, A., Kovalskyy, V., Forsyth, C., Bents, T., 2014. Monitoring conterminous United States (CONUS) land cover change with Web-Enabled Landsat Data (WELD). Remote Sensing of Environment 140, 466–484.

doi:10.1016/j.rse.2013.08.014

Hansen, M.C., Potapov, P.V., Moore, R., Hancher, M., Turubanova, S.A., Tyukavina, A., Thau, D., Stehman, S.V., Goetz, S.J., Loveland, T.R., Kommareddy, A., Egorov, A., Chini, L., Justice, C.O., Townshend, J.R.G., 2013. High-Resolution Global Maps of 21st-Century Forest Cover Change. Science 342, 850–853. doi:10.1126/science.1244693

Hardisky, M.A., Klemas, V., Smart, R.M., 1983. The Influence of Soil Salinity, Growth Form, and Leaf Moisture on-the Spectral Radiance of Spartina alterniflora Canopies. Photogrammetric Engineering & Remote Sensing 49, 77–83.

Healey, S.P., Cohen, W.B., Zhiqiang, Y., Krankina, O.N., 2005. Comparison of Tasseled Cap-based Landsat data structures for use in forest disturbance detection. Remote Sensing of Environment 97, 301–310.

Healey, S.P., Yang, Z., Cohen, W.B., Pierce, D.J., 2006. Application of two regression-based methods to estimate the effects of partial harvest on forest structure using Landsat data. Remote Sensing of Environment 101, 115–126. doi:10.1016/j.rse.2005.12.006

Hecheltjen, A., Thonfeld, F., Menz, G., 2014. Recent advances in remote sensing change detection – a review, in: Manakos, I., Braun, M. (Eds.), Land Use and Land Cover Mapping in Europe - Practices & Trends. Springer, Berlin Heidelberg, pp. 145–178.

Henrich, V., Götze, E., Jung, A., Sandow, C., Thürkow, D., Gläßer, C., 2009. Development of an online indices-database:Motivation, Concept and Implementation. EARSeL, Tel Aviv, p. 3 pp.

Herman, F., Anderson, B., Leprince, S., 2011. Mountain glacier velocity variation during a retreat/advance cycle quantified using sub-pixel analysis of ASTER images. Journal of Glaciology 57, 197–207. doi:10.3189/002214311796405942

Hill, M.J., Donald, G.E., 2003. Estimating spatio-temporal patterns of agricultural productivity in fragmented landscapes using AVHRR NDVI time series. Remote Sensing of Environment 84, 367–384. doi:10.1016/S0034-4257(02)00128-1

Horler, D.N.H., Ahern, F.J., 1986. Forestry information content of Thematic Mapper data. International Journal of Remote Sensing 7, 405–428. doi:10.1080/01431168608954695

Hostert, P., Kuemmerle, T., Prishchepov, A., Sieber, A., Lambin, E.F., Radeloff, V.C., 2011. Rapid land use change after socio-economic disturbances: the collapse of the Soviet Union versus Chernobyl. Environmental Research Letters 6, 045201. doi:10.1088/1748-9326/6/4/045201

Huang, C., Goward, S.N., Masek, J.G., Thomas, N., Zhu, Z., Vogelmann, J.E., 2010a. An automated approach for reconstructing recent forest disturbance history using dense Landsat time series stacks. Remote Sensing of Environment 114, 183–198. doi:10.1016/j.rse.2009.08.017

Huang, C., Thomas, N., Goward, S.N., Masek, J.G., Zhu, Z., Townshend, J.R.G., Vogelmann, J.E., 2010b. Automated masking of cloud and cloud shadow for forest change analysis using Landsat images. International Journal of Remote Sensing 31, 5449–5464. doi:10.1080/01431160903369642

Huang, C., Wylie, B., Yang, L., Homer, C., Zylstra, G., 2002. Derivation of a tasselled cap transformation based on Landsat 7 at-satellite reflectance. International Journal of Remote Sensing 23, 1741–1748. doi:10.1080/01431160110106113

Huete, A., Didan, K., Miura, T., Rodriguez, E.., Gao, X., Ferreira, L.., 2002. Overview of the radiometric and biophysical performance of the MODIS vegetation indices. Remote Sensing of Environment 83, 195–213. doi:10.1016/S0034-4257(02)00096-2

Hunt, E.R., Rock, B.N., 1989. Detection of changes in leaf water content using Near- and Middle-Infrared reflectances. Remote Sensing of Environment 30, 43–54. doi:10.1016/0034-4257(89)90046-1

Hunt, E.R., Rock, B.N., Nobel, P.S., 1987. Measurement of leaf relative water content by infrared reflectance. Remote Sensing of Environment 22, 429–435. doi:10.1016/0034-4257(87)90094-0

Hussain, M., Chen, D., Cheng, A., Wei, H., Stanley, D., 2013. Change detection from remotely sensed images: From pixel-based to object-based approaches. ISPRS Journal of Photogrammetry and Remote Sensing 80, 91–106. doi:10.1016/j.isprsjprs.2013.03.006

Im, J., Jensen, J.R., 2005. A change detection model based on neighborhood correlation image analysis and decision tree classification. Remote Sensing of Environment 99, 326–340.

Irish, R.R., 2000. Landsat 7 automatic cloud cover assessment. SPIE Proceedings 4049, pp. 348–355. doi:10.1117/12.410358

Irish, R.R., Barker, J.L., Goward, S.N., Arvidson, T., 2006. Characterization of the Landsat-7 ETM Automated Cloud-Cover Assessment (ACCA) Algorithm. Photogrammetric Engineering & Remote Sensing 72, 1179–1188.

Irons, J.R., Dwyer, J.L., Barsi, J.A., 2012. The next Landsat satellite: The Landsat Data Continuity Mission. Remote Sensing of Environment, Landsat Legacy Special Issue 122, 11–21. doi:10.1016/j.rse.2011.08.026

Jeganathan, C., Dash, J., Atkinson, P.M., 2014. Remotely sensed trends in the phenology of northern high latitude terrestrial vegetation, controlling for land cover change and vegetation type. Remote Sensing of Environment 143, 154–170. doi:10.1016/j.rse.2013.11.020

Jensen, J.R., 1996. Digital Change Detection, in: Introductory Digital Image Processing. A Remote Sensing Perspective. Prentice Hall, Upper Saddle River, New Jersey, p. 318.

Jin, S., Sader, S.A., 2005a. MODIS time-series imagery for forest disturbance detection and quantification of patch size effects. Remote Sensing of Environment 99, 462–470. doi:10.1016/j.rse.2005.09.017

Jin, S., Sader, S.A., 2005b. Comparison of time series tasseled cap wetness and the normalized difference moisture index in detecting forest disturbances. Remote Sensing of Environment 94, 364–372. doi:10.1016/j.rse.2004.10.012

Johnson, R.D., Kasischke, E.S., 1998. Change vector analysis: a technique for the multispectral monitoring of land cover and condition. International Journal of Remote Sensing 19, 411–426. doi:10.1080/014311698216062

Jones, H.G., Vaughan, R.A., 2010. Remote Sensing of Vegetation: Principles, Techniques, and Applications, Auflage: 1. ed. Oxford University Press, U.S.A., Oxford ; New York.

Jönsson, P., Eklundh, L., 2002. Seasonality extraction by function fitting to time-series of satellite sensor data. IEEE Transactions on Geoscience and Remote Sensing 40, 1824–1832. doi:10.1109/TGRS.2002.802519

Jönsson, P., Eklundh, L., 2004. TIMESAT—a program for analyzing time-series of satellite sensor data. Computers & Geosciences 30, 833–845. doi:10.1016/j.cageo.2004.05.006

Kaufman, Y.J., Wald, A.E., Remer, L.A., Gao, B.-C., Li, R.-R., Flynn, L., 1997. The MODIS 2.1-μm channel-correlation with visible reflectance for use in remote sensing of aerosol. IEEE Transactions on Geoscience and Remote Sensing 35, 1286–1298. doi:10.1109/36.628795

Kauth, R., Thomas, G., 1976. The Tasselled Cap - A Graphic Description of the Spectral-Temporal Development of Agricultural Crops as Seen by LANDSAT. Purdue.

Kendall, M.G., 1938. A New Measure of Rank Correlation. Biometrika 30, 81–93. doi:10.2307/2332226

Kennedy, R.E., Yang, Z., Cohen, W.B., 2010. Detecting trends in forest disturbance and recovery using yearly Landsat time series: 1. LandTrendr — Temporal segmentation algorithms. Remote Sensing of Environment 114, 2897–2910. doi:10.1016/j.rse.2010.07.008

Key, C.H., Benson, N.C., 1999. Measuring and remote sensing of burn severity: the CBI and NBR, in: Neuenschwander, L.F., Ryan, K.C. (Eds.), Proceedings Joint Fire Science Conference and Workshop. Boise, ID, p. 284.

Klonus, S., Tomowski, D., Ehlers, M., Reinartz, P., Michel, U., 2012. Combined Edge Segment Texture Analysis for the Detection of Damaged Buildings in Crisis Areas. IEEE Journal of Selected Topics in Applied Earth Observations and Remote Sensing 5, 1118–1128. doi:10.1109/JSTARS.2012.2205559

Lambin, E.F., Geist, H., Rindfuss, R.R., 2006. Introduction: local processes with global impacts, in: Lamin, E.F., Geist, H. (Eds.), Land-Use and Land-Cover Change - Local Processes and Global Impacts. Springer, Berlin, Heidelberg, pp. 1–8.

Lambin, E.F., Geist, H.J., Lepers, E., 2003. Dynamics of Land-Use and Land-Cover Change in Tropical Regions. Annual Review of Environment and Resources 28, 205–241. doi:10.1146/annurev.energy.28.050302.105459

Lambin, E.F., Turner, B.L., Geist, H.J., Agbola, S.B., Angelsen, A., Bruce, J.W., Coomes, O.T., Dirzo, R., Fischer, G., Folke, C., 2001. The causes of land-use and land-cover change: moving beyond the myths. Global environmental change 11, 261–269.

Landmann, T., Schramm, M., Huettich, C., Dech, S., 2013. MODIS-based change vector analysis for assessing wetland dynamics in Southern Africa. Remote Sensing Letters 4, 104–113. doi:10.1080/2150704X.2012.699201

Latifovic, R., Pouliot, D., Dillabaugh, C., 2012. Identification and correction of systematic error in NOAA AVHRR long-term satellite data record. Remote Sensing of Environment 127, 84–97. doi:10.1016/j.rse.2012.08.032

Lee, H., 2008. Mapping Deforestation and Age of Evergreen Trees by Applying a Binary Coding Method to Time-Series Landsat November Images. IEEE Transactions on Geoscience and Remote Sensing 46, 3926–3936. doi:10.1109/TGRS.2008.2001158

Legendre, P., Legendre, L., 2012. Numerical Ecology, 3rd revised edition. ed. Elsevier, Amsterdam.

Leifer, I., Lehr, W.J., Simecek-Beatty, D., Bradley, E., Clark, R., Dennison, P., Hu, Y., Matheson, S., Jones, C.E., Holt, B., Reif, M., Roberts, D.A., Svejkovsky, J., Swayze, G., Wozencraft, J., 2012. State of the art satellite and airborne marine oil spill remote sensing: Application to the BP Deepwater Horizon oil spill. Remote Sensing of Environment 124, 185–209. doi:10.1016/j.rse.2012.03.024

Lhermitte, S., Verbesselt, J., Verstraeten, W.W., Coppin, P., 2011. A comparison of time series similarity measures for classification and change detection of ecosystem dynamics. Remote Sensing of Environment 115, 3129–3152. doi:10.1016/j.rse.2011.06.020

Li, X., Strahler, A.H., 1985. Geometric-Optical Modeling of a Conifer Forest Canopy. IEEE Transactions on Geoscience and Remote Sensing GE-23, 705–721. doi:10.1109/TGRS.1985.289389

Linke, J., Betts, M.G., Lavigne, M.B., Franklin, S.E., 2007. Introduction: Structure, function, and change of forest landscapes, in: Wulder, M.A., Franklin, S.E. (Eds.), Understanding Forest Disturbance and Spatial Pattern: Remote Sensing and GIS Approaches. CRC Press, Taylor & Francis, Boca Raton, London, New York, pp. 1–29.

Lu, D., Mausel, P., Brondizio, E., Moran, E., 2004. Change detection techniques. International Journal of Remote Sensing 25, 2365–2401. doi:10.1080/0143116031000139863

Lunetta, R.S., Johnson, D.M., Lyon, J.G., Crotwell, J., 2004. Impacts of imagery temporal frequency on land-cover change detection monitoring. Remote Sensing of Environment 89, 444–454.

Madden, S., 2012. From Databases to Big Data. IEEE Internet Computing 16, 4–6.

Malila, W.A., 1980. Change vector analysis: an approach for detecting forest changes with Landsat. Proceedings of the 6th Annual Symposium on Machine Processing of Remotely Sensed Data, Purdue University, Indiana 329–335.

Mann, H.B., 1945. Nonparametric Tests Against Trend. Econometrica 13, 245–259. doi:10.2307/1907187

Markham, B.L., Helder, D.L., 2012. Forty-year calibrated record of earth-reflected radiance from Landsat: A review. Remote Sensing of Environment 122, 30–40. doi:10.1016/j.rse.2011.06.026

Markham, B.L., Storey, J.C., Williams, D.L., Irons, J.R., 2004. Landsat sensor performance: history and current status. IEEE Transactions on Geoscience and Remote Sensing 42, 2691–2694. doi:10.1109/TGRS.2004.840720

Masek, J.G., Huang, C., Wolfe, R., Cohen, W., Hall, F., Kutler, J., Nelson, P., 2008. North American forest disturbance mapped from a decadal Landsat record. Remote Sensing of Environment 112, 2914–2926. doi:10.1016/j.rse.2008.02.010

Masek, J.G., Vermote, E.F., Saleous, N.E., Wolfe, R., Hall, F.G., Huemmrich, K.F., Gao, F., Kutler, J., Lim, T.-K., 2006. A Landsat surface reflectance dataset for North America, 1990-2000. IEEE Geoscience and Remote Sensing Letters 3, 68–72. doi:10.1109/LGRS.2005.857030

Massonnet, D., Rossi, M., Carmona, C., Adragna, F., Peltzer, G., Feigl, K., Rabaute, T., 1993. The displacement field of the Landers earthquake mapped by radar interferometry. Nature 364, 138–142. doi:10.1038/364138a0

Matsushita, B., Yang, W., Chen, J., Onda, Y., Qiu, G., 2007. Sensitivity of the Enhanced Vegetation Index (EVI) and Normalized Difference Vegetation Index (NDVI) to Topographic Effects: A Case Study in High-density Cypress Forest. Sensors 7, 2636–2651. doi:10.3390/s7112636

Meddens, A.J.H., Hicke, J.A., Vierling, L.A., Hudak, A.T., 2013. Evaluating methods to detect bark beetle-caused tree mortality using single-date and multi-date Landsat imagery. Remote Sensing of Environment 132, 49–58. doi:10.1016/j.rse.2013.01.002

Meigs, G.W., Kennedy, R.E., Cohen, W.B., 2011. A Landsat time series approach to characterize bark beetle and defoliator impacts on tree mortality and surface fuels in conifer forests. Remote Sensing of Environment 115, 3707–3718. doi:10.1016/j.rse.2011.09.009

Melaas, E.K., Friedl, M.A., Zhu, Z., 2013. Detecting interannual variation in deciduous broadleaf forest phenology using Landsat TM/ETM + data. Remote Sensing of Environment 132, 176–185. doi:10.1016/j.rse.2013.01.011

Michalek, J.L., Wagner, T.W., Luczkovich, J.J., Stoffle, R.W., 1993. Multispectral Change Vector Analysis for Monitoring Coastal Marine Environments. Photogrammetric Engineering & Remote Sensing 59, 381–384.

Miller, J.D., Yool, S.R., 2002. Mapping forest post-fire canopy consumption in several overstory types using multi-temporal Landsat TM and ETM data. Remote Sensing of Environment 82, 481–496. doi:10.1016/S0034-4257(02)00071-8

Mountrakis, G., Im, J., Ogole, C., 2011. Support vector machines in remote sensing: A review. ISPRS Journal of Photogrammetry and Remote Sensing 66, 247–259. doi:10.1016/j.isprsjprs.2010.11.001

Nielsen, A.A., 2007. The regularized iteratively reweighted MAD method for change detection in multi-and hyperspectral data. IEEE Transactions on Image Processing 16, 463–478.

Nielsen, A.A., Conradsen, K., Simpson, J.J., 1998. Multivariate Alteration Detection (MAD) and MAF Postprocessing in Multispectral, Bitemporal Image Data: New Approaches to Change Detection Studies. Remote Sensing of Environment 64, 1–19. doi:10.1016/S0034-4257(97)00162-4

Nielsen, A.A., Hecheltjen, A., Thonfeld, F., Canty, M.J., 2010. Automatic change detection in RapidEye data using the combined MAD and kernel MAF methods, in: Geoscience and Remote Sensing Symposium (IGARSS), 2010 IEEE International. pp. 3078–3081. doi:10.1109/IGARSS.2010.5652663

Nilson, T., Olsson, H., Anniste, J., LÜkk, T., Praks, J., 2001. Thinning-caused change in reflectance of ground vegetation in boreal forest. International Journal of Remote Sensing 22, 2763–2776. doi:10.1080/01431160120213

O'Connor, B., Dwyer, E., Cawkwell, F., Eklundh, L., 2012. Spatio-temporal patterns in vegetation start of season across the island of Ireland using the MERIS Global Vegetation Index. ISPRS Journal of Photogrammetry and Remote Sensing 68, 79–94. doi:10.1016/j.isprsjprs.2012.01.004

Oliver, C.D., Larson, B.C., 1996. Forest Stand Dynamics, Updated Edition edition. ed. Wiley, New York.

Olsson, H., 1994. Changes in satellite-measured reflectances caused by thinning cuttings in boreal

forest. Remote Sensing of Environment 50, 221–230.
Otsu, N., 1979. A Threshold Selection Method from Gray-Level Histograms. IEEE Transactions on Systems, Man and Cybernetics 9, 62–66. doi:10.1109/TSMC.1979.4310076
Pflugmacher, D., Cohen, W.B., Kennedy, R.E., 2012. Using Landsat-derived disturbance history (1972–2010) to predict current forest structure. Remote Sensing of Environment 122, 146–165. doi:10.1016/j.rse.2011.09.025
Pojar, J., Klinka, K., Demarchi, D.A., 1991. Chapter 6: Coastal Western Hemlock Zone, in: Meidinger, D.V., Pojar, J. (Eds.), Ecosystems of British Columbia. BC Ministry of Forests, Victoria, B. C., pp. 95–112.
Pouliot, D., Latifovic, R., Zabcic, N., Guindon, L., Olthof, I., 2014. Development and assessment of a 250 m spatial resolution MODIS annual land cover time series (2000–2011) for the forest region of Canada derived from change-based updating. Remote Sensing of Environment 140, 731–743. doi:10.1016/j.rse.2013.10.004
Powell, S.L., Cohen, W.B., Healey, S.P., Kennedy, R.E., Moisen, G.G., Pierce, K.B., Ohmann, J.L., 2010. Quantification of live aboveground forest biomass dynamics with Landsat time-series and field inventory data: A comparison of empirical modeling approaches. Remote Sensing of Environment 114, 1053–1068. doi:10.1016/j.rse.2009.12.018
Powell, S.L., Cohen, W.B., Yang, Z., Pierce, J.D., Alberti, M., 2008. Quantification of impervious surface in the Snohomish Water Resources Inventory Area of Western Washington from 1972–2006. Remote Sensing of Environment 112, 1895–1908. doi:10.1016/j.rse.2007.09.010
Price, K.P., Jakubauskas, M.E., 1998. Spectral retrogression and insect damage in lodgepole pine successional forests. International Journal of Remote Sensing 19, 1627–1632. doi:10.1080/014311698215405
R Core Team, 2014. R: A Language and Environment for Statistical Computing. R Foundation for Statistical Computing,Vienna, Austria.
Radke, R.J., Andra, S., Al-Kofahi, O., Roysam, B., 2005. Image change detection algorithms: a systematic survey. IEEE Transactions on Image Processing 14, 294–307.
Reed, B.C., Brown, J.F., VanderZee, D., Loveland, T.R., Merchant, J.W., Ohlen, D.O., 1994. Measuring phenological variability from satellite imagery. Journal of Vegetation Science 5, 703–714. doi:10.2307/3235884
Ren, J., Chen, Z., Zhou, Q., Tang, H., 2008. Regional yield estimation for winter wheat with MODIS-NDVI data in Shandong, China. International Journal of Applied Earth Observation and Geoinformation, Modern Methods in Crop Yield Forecasting and Crop Area Estimation 10, 403–413. doi:10.1016/j.jag.2007.11.003
Richter, R., 1996. Atmospheric correction of satellite data with haze removal including a haze/clear transition region. Computers & Geosciences 22, 675–681. doi:10.1016/0098-3004(96)00010-6
Rindfuss, R.R., Walsh, S.J., Ii, B.L.T., Moran, E.F., Entwisle, B., 2004. Linking Pixels and People, in: Gutman, D.G., Janetos, A.C., Justice, C.O., Moran, D.E.F., Mustard, J.F., Rindfuss, R.R., Skole, D., II, B.L.T., Cochrane, M.A. (Eds.), Land Change Science. Springer Netherlands, pp. 379–394.
Rogan, J., Franklin, J., Roberts, D.A., 2002. A comparison of methods for monitoring multitemporal vegetation change using Thematic Mapper imagery. Remote Sensing of Environment 80, 143–156.
Rogerson, P.A., 2002. Change detection thresholds for remotely sensed images. Journal of Geographical Systems 4, 85–97. doi:10.1007/s101090100076
Rosen, P.A., Hensley, S., Joughin, I.R., Li, F.K., Madsen, S.N., Rodriguez, E., Goldstein, R.M., 2000. Synthetic aperture radar interferometry. Proceedings of the IEEE 88, 333 –382. doi:10.1109/5.838084
Rosin, P.L., 1998. Thresholding for change detection, in: Sixth International Conference on Computer Vision, 1998. Presented at the Sixth International Conference on Computer

Vision, 1998, pp. 274–279. doi:10.1109/ICCV.1998.710730
Rosin, P.L., 2001. Unimodal thresholding. Pattern Recognition 34, 2083–2096.
Rosin, P.L., Ioannidis, E., 2003. Evaluation of global image thresholding for change detection. Pattern Recognition Letters 24, 2345–2356.
Roy, D.P., Ju, J., Kline, K., Scaramuzza, P.L., Kovalskyy, V., Hansen, M., Loveland, T.R., Vermote, E., Zhang, C., 2010. Web-enabled Landsat Data (WELD): Landsat ETM+ composited mosaics of the conterminous United States. Remote Sensing of Environment 114, 35–49. doi:10.1016/j.rse.2009.08.011
Roy, D.P., Wulder, M.A., Loveland, T.R., C.E., W., Allen, R.G., Anderson, M.C., Helder, D., Irons, J.R., Johnson, D.M., Kennedy, R., Scambos, T.A., Schaaf, C.B., Schott, J.R., Sheng, Y., Vermote, E.F., Belward, A.S., Bindschadler, R., Cohen, W.B., Gao, F., Hipple, J.D., Hostert, P., Huntington, J., Justice, C.O., Kilic, A., Kovalskyy, V., Lee, Z.P., Lymburner, L., Masek, J.G., McCorkel, J., Shuai, Y., Trezza, R., Vogelmann, J., Wynne, R.H., Zhu, Z., 2014. Landsat-8: Science and product vision for terrestrial global change research. Remote Sensing of Environment 145, 154–172. doi:10.1016/j.rse.2014.02.001
Saleska, S.R., Didan, K., Huete, A.R., Rocha, H.R. da, 2007. Amazon Forests Green-Up During 2005 Drought. Science 318, 612–612. doi:10.1126/science.1146663
Sarabandi, P., Yamazaki, F., Matsuoka, M., Kiremidjian, A., 2004. Shadow detection and radiometric restoration in satellite high resolution images. Presented at the IEEE International Geoscience and Remote Sensing Symposium (IGARSS), pp. 3744–3747. doi:10.1109/IGARSS.2004.1369936
Savitzky, A., Golay, M.J.., 1964. Smoothing and differentiation of data by simplified least squares procedures. Analytical chemistry 36, 1627–1639.
Schmidt, M., King, E.A., McVicar, T.R., 2008. A method for operational calibration of AVHRR reflective time series data. Remote Sensing of Environment 112, 1117–1129. doi:10.1016/j.rse.2007.07.015
Schmitt, A., 2012. Änderungserkennung in multitemporalen und multipolarisierten Radaraufnahmen (thesis). Karlsruher Institut für Technologie (KIT).
Schmitt, A., Wessel, B., Roth, A., 2010. Curvelet-based Change Detection on SAR Images for Natural Disaster Mapping. PFG 2010, 463–474. doi:10.1127/1432-8364/2010/0068
Schott, J.R., Salvaggio, C., Volchok, W.J., 1988. Radiometric scene normalization using pseudoinvariant features. RSE 26, 1–16. doi:10.1016/0034-4257(88)90116-2
Schroeder, T.A., Cohen, W.B., Song, C., Canty, M.J., Yang, Z., 2006. Radiometric correction of multi-temporal Landsat data for characterization of early successional forest patterns in western Oregon. Remote Sensing of Environment 103, 16–26. doi:10.1016/j.rse.2006.03.008
Schroeder, T.A., Wulder, M.A., Healey, S.P., Moisen, G.G., 2011. Mapping wildfire and clearcut harvest disturbances in boreal forests with Landsat time series data. Remote Sensing of Environment 115, 1421–1433. doi:10.1016/j.rse.2011.01.022
Sen, S., Zipper, C.E., Wynne, R.H., Donovan, P., 2012. Identifying revegetated mines as disturbance/recovery trajectories using an interannual Landsat chronosequence. Photogrammetric Engineering & Remote Sensing 78, 223–235.
Sezgin, M., Sankur, B., 2004. Survey over image thresholding techniques and quantitative performance evaluation. Journal of Electronic Imaging 13, 146–168.
Sieber, A.J., 1986. Physikalische Grundlagen der Fernerkundung. Deutsche Forschungs- und Versuchsanstalt für Luft- und Raumfahrt e.V. (DFVLR), Institut für Hochfrequenztechnik, Oberpfaffenhofen.
Singh, A., 1989. Review Article Digital change detection techniques using remotely-sensed data. International Journal of Remote Sensing 10, 989–1003. doi:10.1080/01431168908903939
Sjöström, M., Ardö, J., Arneth, A., Boulain, N., Cappelaere, B., Eklundh, L., de Grandcourt, A., Kutsch, W.L., Merbold, L., Nouvellon, Y., Scholes, R.J., Schubert, P., Seaquist, J., Veenendaal, E.M., 2011. Exploring the potential of MODIS EVI for modeling gross

primary production across African ecosystems. Remote Sensing of Environment 115, 1081–1089. doi:10.1016/j.rse.2010.12.013

Skakun, R.S., Wulder, M.A., Franklin, S.E., 2003. Sensitivity of the thematic mapper enhanced wetness difference index to detect mountain pine beetle red-attack damage. Remote Sensing of Environment 86, 433–443. doi:10.1016/S0034-4257(03)00112-3

Song, C., Woodcock, C.E., 2003. Monitoring forest succession with multitemporal Landsat images: factors of uncertainty. IEEE Transactions on Geoscience and Remote Sensing 41, 2557– 2567. doi:10.1109/TGRS.2003.818367

Song, C., Woodcock, C.E., Seto, K.C., Lenney, M.P., Macomber, S.A., 2001. Classification and Change Detection Using Landsat TM Data: When and How to Correct Atmospheric Effects? Remote Sensing of Environment 75, 230–244. doi:10.1016/S0034-4257(00)00169-3

Spanner, M.A., Pierce, L.L., Peterson, D.L., Running, S.W., 1990. Remote sensing of temperate coniferous forest leaf area index The influence of canopy closure, understory vegetation and background reflectance. International Journal of Remote Sensing 11, 95–111. doi:10.1080/01431169008955002

Spies, T.A., Franklin, J.F., 1991. The Structure of Natural Young, Mature, and Old-Growth Douglas-Fir Forests in Oregon and Washington, in: Wildlife and Vegetation of Unmanaged Douglas-Fir Forests, USDA General Technical Report PNW-GTR-285. Portland, Oregon, pp. 90–109.

Spies, T.A., Franklin, J.F., Thomas, T.B., 1988. Coarse Woody Debris in Douglas-Fir Forests of Western Oregon and Washington. Ecology 69, 1689–1702. doi:10.2307/1941147

Stellmes, M., Röder, A., Udelhoven, T., Hill, J., 2013. Mapping syndromes of land change in Spain with remote sensing time series, demographic and climatic data. Land Use Policy 30, 685–702. doi:10.1016/j.landusepol.2012.05.007

Stocker, T.F., Qin, D., Plattner, G.-K., Alexander, L.V., Allen, S.K., Bindoff, N.L., Bréon, F.-N., Church, J.A., Cubasch, U., Emori, S., Forster, P., Friedlingstein, P., Gillett, N., Gregory, J.M., Hartmann, D.L., Jansen, E., Kirtman, B., Knutti, R., Krishna Kumar, K., Lemke, P., Marotzke, J., Masson-Delmotte, V., Meehl, G.A., Mokhov, I.I., Piao, S., Ramaswamy, V., Randall, D., Rhein, M., Rojas, M., Sabine, C., Shindell, D., Talley, L.D., Vaughan, D.G., Xie, S.-P., 2013. Technical Summary, in: Stocker, T.F., Qin, D., Plattner, G.-K., Tignor, M., Allen, S.K., Boschung, J.B., Nauels, A.N., Xia, Y., Bex, V., Midgley, P.M. (Eds.), Climate Change 2013: The Physical Science Basis. Contribution of Working Group I to the Fifth Assessment Report of the Intergovernmental Panel on Climate Change. Cambridge University Press, Cambridge, United Kingdom and New York, NY, USA.

Stow, D.A., 1999. Reducing the effects of misregistration on pixel-level change detection. International Journal of Remote Sensing 20, 2477–2483. doi:10.1080/014311699212137

Strozzi, T., Farina, P., Corsini, A., Ambrosi, C., Thüring, M., Zilger, J., Wiesmann, A., Wegmüller, U., Werner, C., 2005. Survey and monitoring of landslide displacements by means of L-band satellite SAR interferometry. Landslides 2, 193–201. doi:10.1007/s10346-005-0003-2

Strozzi, T., Wegmuller, U., Werner, C.L., Wiesmann, A., Spreckels, V., 2003. JERS SAR interferometry for land subsidence monitoring. IEEE Transactions on Geoscience and Remote Sensing 41, 1702–1708. doi:10.1109/TGRS.2003.813273

Sulla-Menashe, D., Kennedy, R.E., Yang, Z., Braaten, J., Krankina, O.N., Friedl, M.A., 2013. Detecting forest disturbance in the Pacific Northwest from MODIS time series using temporal segmentation. Remote Sensing of Environment. doi:10.1016/j.rse.2013.07.042

Teke, M., Başeski, E., Ok, A.Ö., Yüksel, B., Şenaras, Ç., 2011. Multi-spectral False Color Shadow Detection, in: Stilla, U., Rottensteiner, F., Mayer, H., Jutzi, B., Butenuth, M. (Eds.), Photogrammetric Image Analysis, Lecture Notes in Computer Science. Springer, Berlin Heidelberg, pp. 109–119.

The Vancouver Sun, 2008. Our forest industry faces dire times. Canada.com.

Thonfeld, F., Menz, G., 2011. Coherence and multitemporal intensity metrics of high resolution

SAR images for urban change detection. Presented at the 4th TerraSAR-X-Science Team Meeting, DLR, Oberpfaffenhofen, pp. 1–9.

Thonfeld, F., Nielsen, A.A., Skriver, H., Conradsen, K., Canty, M.J., 2013. Complex Wishart distribution-based change detection with polarimetric TerraSAR-X imagery. Presented at the 5th TerraSAR-X / 4th TanDEM-X Science Team Meeting, Oberpfaffenhofen, Germany.

Toutin, T., 2004. Review article: Geometric processing of remote sensing images: models, algorithms and methods. International Journal of Remote Sensing 25, 1893–1924. doi:10.1080/0143116031000101611

Townsend, P.A., Singh, A., Foster, J.R., Rehberg, N.J., Kingdon, C.C., Eshleman, K.N., Seagle, S.W., 2012. A general Landsat model to predict canopy defoliation in broadleaf deciduous forests. Remote Sensing of Environment 119, 255–265. doi:10.1016/j.rse.2011.12.023

Townshend, J.R.G., Justice, C.O., Gurney, C., McManus, J., 1992. The impact of misregistration on change detection. IEEE Transactions on Geoscience and Remote Sensing 30, 1054–1060. doi:10.1109/36.175340

Tucker, C.J., 1979. Red and photographic infrared linear combinations for monitoring vegetation. Remote Sensing of Environment 8, 127–150. doi:10.1016/0034-4257(79)90013-0

Turner, M.G., 1989. Landscape Ecology: The Effect of Pattern on Process. Annual Review of Ecology and Systematics 20, 171–197. doi:10.1146/annurev.es.20.110189.001131

Turner, M.G., O'Neill, R.V., Gardner, R.H., Milne, B.T., 1989. Effects of changing spatial scale on the analysis of landscape pattern. Landscape Ecol 3, 153–162. doi:10.1007/BF00131534

Tüshaus, J., Dubovyk, O., Khamzina, A., Menz, G., 2014. Comparison of Medium Spatial Resolution ENVISAT-MERIS and Terra-MODIS Time Series for Vegetation Decline Analysis: A Case Study in Central Asia. Remote Sensing 6, 5238–5256. doi:10.3390/rs6065238

Tyc, G., Tulip, J., Schulten, D., Krischke, M., Oxfort, M., 2005. The RapidEye mission design. Acta Astronautica 56, 213–219. doi:10.1016/j.actaastro.2004.09.029

Ulaby, F.T., Moore, R.K., Fung, A.K., 1986. Microwave Remote Sensing: Active and Passive, Volume III: Volume Scattering and Emission Theory, Advanced Systems and Applications. Artech House Publishers, Reading, Mass.

USGS, 2013a. Landsat Climate Data Record (CDR) surface reflectance. Product Guide Version 3.4.

USGS, 2013b. Landsat surface reflectance-derived spectral indices. Product Guide Version 1.1.

Uudus, B., Park, K.-A., Kim, K.-R., Kim, J., Ryu, J.-H., 2013. Diurnal variation of NDVI from an unprecedented high-resolution geostationary ocean colour satellite. Remote Sensing Letters 4, 639–647. doi:10.1080/2150704X.2013.781285

Van Leeuwen, W.J.D., Huete, A.R., Laing, T.W., 1999. MODIS Vegetation Index Compositing Approach: A Prototype with AVHRR Data. Remote Sensing of Environment 69, 264–280. doi:10.1016/S0034-4257(99)00022-X

Verbesselt, J., Hyndman, R., Newnham, G., Culvenor, D., 2010a. Detecting trend and seasonal changes in satellite image time series. Remote Sensing of Environment 114, 106–115. doi:10.1016/j.rse.2009.08.014

Verbesselt, J., Hyndman, R., Zeileis, A., Culvenor, D., 2010b. Phenological change detection while accounting for abrupt and gradual trends in satellite image time series. Remote Sensing of Environment 114, 2970–2980.

Verbesselt, J., Jonsson, P., Lhermitte, S., Van Aardt, J., Coppin, P., 2006. Evaluating satellite and climate data-derived indices as fire risk indicators in savanna ecosystems. IEEE Transactions on Geoscience and Remote Sensing 44, 1622–1632. doi:10.1109/TGRS.2005.862262

Verbesselt, J., Zeileis, A., Herold, M., 2012. Near real-time disturbance detection using satellite image time series. Remote Sensing of Environment 123, 98–108. doi:10.1016/j.rse.2012.02.022

Verger, A., Baret, F., Weiss, M., 2011. A multisensor fusion approach to improve LAI time series. Remote Sensing of Environment 115, 2460–2470. doi:10.1016/j.rse.2011.05.006

Vermote, E.F., El Saleous, N., Justice, C.O., Kaufman, Y.J., Privette, J.L., Remer, L., Roger, J.C., Tanré, D., 1997. Atmospheric correction of visible to middle-infrared EOS-MODIS data over land surfaces: Background, operational algorithm and validation. J. Geophys. Res. 102, 17131–17141. doi:10.1029/97JD00201

Vermote, E.F., Tanre, D., Deuze, J.L., Herman, M., Morcette, J.-J., 1997. Second Simulation of the Satellite Signal in the Solar Spectrum, 6S: an overview. IEEE Transactions on Geoscience and Remote Sensing 35, 675 –686. doi:10.1109/36.581987

Vicente-Serrano, S.M., Pérez-Cabello, F., Lasanta, T., 2008. Assessment of radiometric correction techniques in analyzing vegetation variability and change using time series of Landsat images. Remote Sensing of Environment 112, 3916–3934. doi:10.1016/j.rse.2008.06.011

Vogelmann, J.E., 1990. Comparison between two vegetation indices for measuring different types of forest damage in the north-eastern United States. International Journal of Remote Sensing 11, 2281–2297. doi:10.1080/01431169008955175

Vogelmann, J.E., Helder, D., Morfitt, R., Choate, M.J., Merchant, J.W., Bulley, H., 2001. Effects of Landsat 5 Thematic Mapper and Landsat 7 Enhanced Thematic Mapper Plus radiometric and geometric calibrations and corrections on landscape characterization. Remote Sensing of Environment 78, 55–70. doi:10.1016/S0034-4257(01)00249-8

Vogelmann, J.E., Kost, J.R., Tolk, B., Howard, S., Short, K., Chen, X., Huang, C., Pabst, K., Rollins, M.G., 2011. Monitoring Landscape Change for LANDFIRE Using Multi-Temporal Satellite Imagery and Ancillary Data. IEEE Journal of Selected Topics in Applied Earth Observations and Remote Sensing 4, 252–264. doi:10.1109/JSTARS.2010.2044478

Wardlow, B.D., Egbert, S.L., Kastens, J.H., 2007. Analysis of time-series MODIS 250 m vegetation index data for crop classification in the U.S. Central Great Plains. Remote Sensing of Environment 108, 290–310. doi:10.1016/j.rse.2006.11.021

Webster, R., 1973. Automatic soil-boundary location from transect data. Mathematical Geology 5, 27–37. doi:10.1007/BF02114085

Wegmüller, U., Walter, D., Spreckels, V., Werner, C.L., 2010. Nonuniform Ground Motion Monitoring With TerraSAR-X Persistent Scatterer Interferometry. IEEE Transactions on Geoscience and Remote Sensing 48, 895–904. doi:10.1109/TGRS.2009.2030792

Wessels, K.J., van den Bergh, F., Scholes, R.J., 2012. Limits to detectability of land degradation by trend analysis of vegetation index data. Remote Sensing of Environment 125, 10–22. doi:10.1016/j.rse.2012.06.022

West Fraser, 2014. Silviculture and Reforestation, last accessed 13th June 2014 [WWW Document]. URL http://www.westfraser.com/responsibility/forest-management/forest-management-planning/silviculture-and-reforestation

Wilson, E.H., Sader, S.A., 2002. Detection of forest harvest type using multiple dates of Landsat TM imagery. Remote Sensing of Environment 80, 385–396.

Woodcock, C.E., Allen, R., Anderson, M., Belward, A., Bindschadler, R., Cohen, W., Gao, F., Goward, S.N., Helder, D., Helmer, E., Nemani, R., Oreopoulos, L., Schott, J., Thenkabail, P.S., Vermote, E.F., Vogelmann, J., Wulder, M.A., Wynne, R., 2008. Free Access to Landsat Imagery. Science 320, 1011–1011. doi:10.1126/science.320.5879.1011a

Wulder, M.A., Dymond, C.C., Erickson, B., 2004a. Detection and monitoring of the mountain pine beetle, Natural Resources Canada, Canadian Forest Service. Pacific Forestry Centre, Victoria, BC, Canada.

Wulder, M.A., Franklin, S.E., White, J.C., 2004b. Sensitivity of hyperclustering and labelling land cover classes to Landsat image acquisition date. International Journal of Remote Sensing 25, 5337–5344. doi:10.1080/0143116042000192385

Wulder, M.A., Masek, J.G., Cohen, W.B., Loveland, T.R., Woodcock, C.E., 2012. Opening the archive: How free data has enabled the science and monitoring promise of Landsat.

Remote Sensing of Environment 122, 2–10. doi:10.1016/j.rse.2012.01.010

Xian, G., Homer, C., Fry, J., 2009. Updating the 2001 National Land Cover Database land cover classification to 2006 by using Landsat imagery change detection methods. Remote Sensing of Environment 113, 1133–1147. doi:10.1016/j.rse.2009.02.004

Xu, Q., Hou, Z., Tokola, T., 2012. Relative radiometric correction of multi-temporal ALOS AVNIR-2 data for the estimation of forest attributes. ISPRS Journal of Photogrammetry and Remote Sensing 68, 69–78. doi:10.1016/j.isprsjprs.2011.12.008

Zeileis, A., 2005. A Unified Approach to Structural Change Tests Based on ML Scores, F Statistics, and OLS Residuals. Econometric Reviews 24, 445–466. doi:10.1080/07474930500406053

Zeileis, A., Leisch, F., Hornik, K., Kleiber, C., 2002. strucchange: An R Package for Testing for Structural Change in Linear Regression Models. Journal of Statistical Software 7, 1–38.

Zha, Y., Gao, J., Ni, S., 2003. Use of normalized difference built-up index in automatically mapping urban areas from TM imagery. International Journal of Remote Sensing 24, 583–594. doi:10.1080/01431160304987

Zhang, X., Friedl, M.A., Schaaf, C.B., Strahler, A.H., Hodges, J.C.F., Gao, F., Reed, B.C., Huete, A., 2003. Monitoring vegetation phenology using MODIS. Remote Sensing of Environment 84, 471–475. doi:10.1016/S0034-4257(02)00135-9

Zhang, Y., Odeh, I.O.A., Han, C., 2009. Bi-temporal characterization of land surface temperature in relation to impervious surface area, NDVI and NDBI, using a sub-pixel image analysis. International Journal of Applied Earth Observation and Geoinformation 11, 256–264. doi:10.1016/j.jag.2009.03.001

Zhu, Z., Woodcock, C.E., 2012. Object-based cloud and cloud shadow detection in Landsat imagery. Remote Sensing of Environment 118, 83–94. doi:10.1016/j.rse.2011.10.028

Zhu, Z., Woodcock, C.E., 2014. Continuous change detection and classification of land cover using all available Landsat data. Remote Sensing of Environment 144, 152–171. doi:10.1016/j.rse.2014.01.011

Zhu, Z., Woodcock, C.E., Olofsson, P., 2012. Continuous monitoring of forest disturbance using all available Landsat imagery. Remote Sensing of Environment 122, 75–91. doi:10.1016/j.rse.2011.10.030

# Appendix

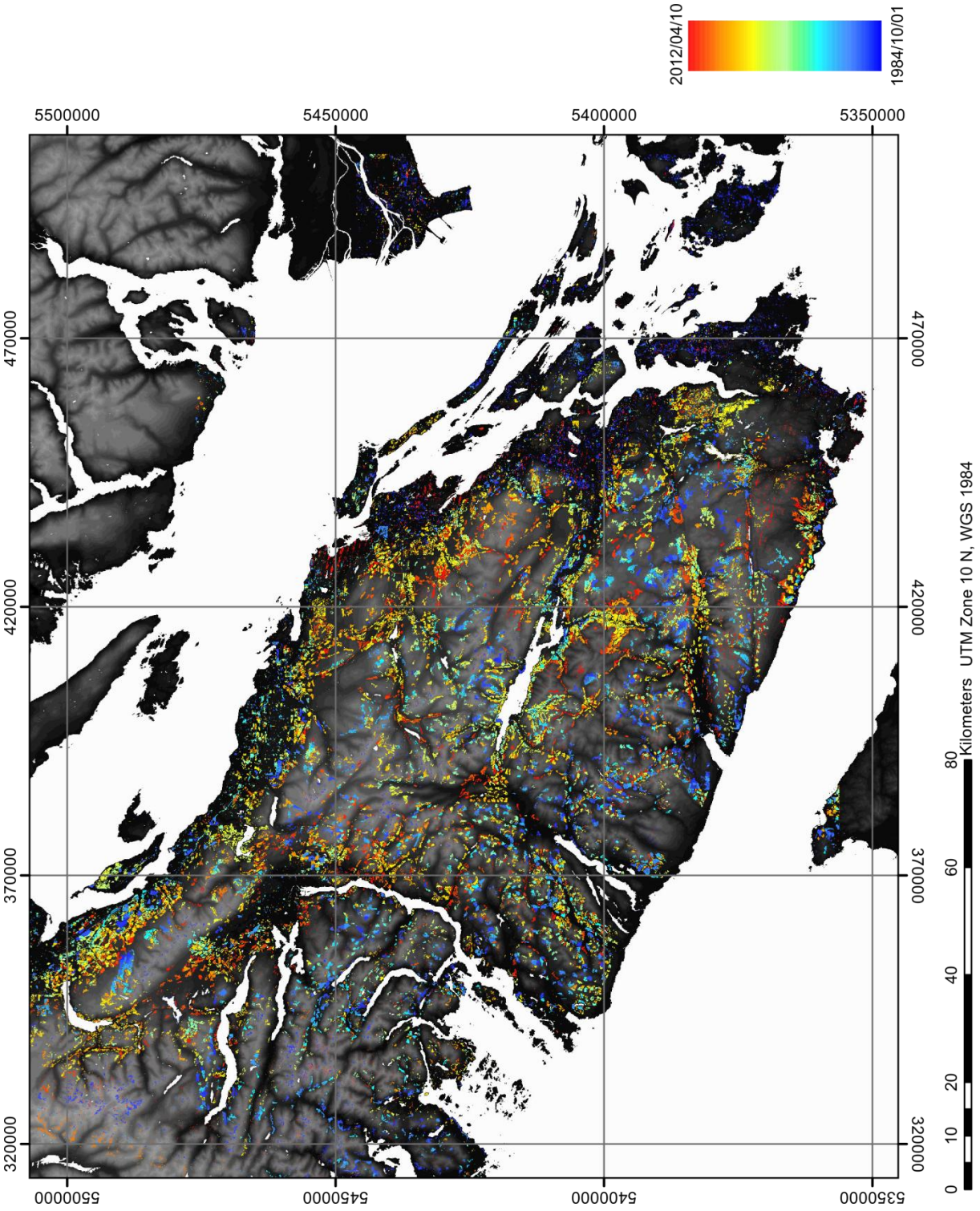


Fig. A.1: Map of detected clearcuts on southern Vancouver Island (rotated 90°, colors refer to timing of major changes).